NMR Spectroscopy of Exotic Quadrupolar Nuclei in Solids

by

Alexandra Faucher

A thesis submitted in partial fulfillment of the requirements for the degree of

Doctor of Philosophy

Department of Chemistry
University of Alberta

**Abstract**

This thesis is concerned with NMR studies of solids containing NMR-active quadrupolar nuclei typically overlooked due to their unfavorable NMR properties, particularly moderate to large nuclear electric quadrupole moments. It is shown that $^{75}$As, $^{87}$Sr, and $^{121/123}$Sb NMR spectra of a wide range of solid materials can be obtained. Traditional 1D pulse sequences (e.g., Bloch pulse, spin echo, QCPMG) are used alongside new methods (e.g., WURST echo, WURST-QCPMG) to acquire the NMR spectra; the advantages of these new methods are illustrated. Most of these NMR spectra were acquired at an external magnetic field strength of $B_0 = 21.14$ T. Central transition ($m_I = 1/2$ to $-1/2$) linewidths of half-integer quadrupolar nuclei of up to a breadth of ca. 32 MHz are obtained at $B_0 = 21.14$ T, demonstrating that nuclear sites with large nuclear quadrupolar coupling constants can be characterized. Many of the NMR spectra contained in this research depict situations in which the nuclear quadrupolar interaction is on the order of or exceeds the magnitude of the Zeeman interaction, thus rendering the high-field approximation invalid and requiring exact treatment in which the full Zeeman-quadrupolar Hamiltonian is diagonalized in order to properly simulate the NMR spectra and extract NMR parameters. It is also shown that both direct ($R_{\text{eff}}$) and indirect ($J$) spin-spin coupling between quadrupolar nuclei can be quantified in some circumstances, and that the signs of the isotropic indirect spin-spin coupling and the nuclear quadrupolar coupling constants can be obtained experimentally in cases of high-field approximation breakdown. This research represents a relatively large and valuable contribution to the available $^{75}$As, $^{87}$Sr, and $^{121/123}$Sb NMR data in the literature. For example, experimentally determined chemical shift anisotropy is reported for the $^{87}$Sr nucleus in a powdered solid for the first time, and the NMR parameters for $^{11}$B-$^{75}$As spin-spin coupling constants reported here add to a sparse collection of information on

quadrupolar spin-pairs.  Overall, this research is a step towards the goal of utilizing the entire

NMR periodic table for the characterization of molecular and crystallographic structure as well

as structural dynamics.

**Preface**

This thesis is an original work by Alexandra Faucher.

Chapter 3 of this thesis has been reprinted with permission from Faucher, A.; Terskikh, V. V.; Wasylishen, R. E. Assessing distortion of the $AF_6^-$ (A = As, Sb) octahedra in solid hexafluorometallates(V) via NMR spectroscopy. *Can. J. Chem*. **2015**, *93*, 938-944.

Chapter 4 of this thesis has been reprinted with permission from Faucher, A.; Terskikh, V. V.; Wasylishen, R. E. Feasibility of arsenic and antimony NMR spectroscopy in solids: An investigation of some group 15 compounds. *Solid State Nucl. Magn. Reson*. **2014**, *61-62*, 54-61. Copyright 2014 Elsevier.

Chapter 5 of this thesis has been reprinted with permission from Faucher, A.; Terskikh, V. V.; Wasylishen, R. E. Spin-spin coupling between quadrupolar nuclei in solids: $^{11}$B-$^{75}$As spin pairs in Lewis acid-base adducts. *J. Phys. Chem. A*. **2015**, *119*, 6949-6960. Copyright 2015 American Chemical Society.

For the above publications, I acquired all NMR data at $B_0$ = 7.05 and 11.75 T. Some of the $^{75}$As and $^{121/123}$Sb NMR experiments performed at $B_0$ = 21.14 T were also performed by me during my visits to the National Ultrahigh-Field NMR Facility for Solids in Ottawa, ON, Canada. The majority of the NMR spectra acquired at $B_0$ = 21.14 T were collected by Victor V. Terskikh, the manager of our ultrahigh-field NMR facility. Data analysis was made by me, with the exception of the variable temperature NMR spectra acquired at $B_0$ = 21.14 T shown in Chapter 3 and the

[75]As NMR spectrum of arsenobetaine bromide shown in Chapter 4. I have prepared all of the above manuscripts for publication.

Chapter 6 of this thesis has been reprinted with permission from Faucher, A.; Terskikh, V. V.; Ye, E.; Bernard, G. M.; Wasylishen, R. E. Solid-State [87]Sr NMR Spectroscopy at Natural Abundance and High Magnetic Field Strength. *J. Phys. Chem. A*, **2015**, *119*, 11847-11861. Copyright 2015 American Chemical Society. Data were collected for this project by each listed author, analysis of the data was made by Victor V. Terskikh, Eric Ye, and myself, and I prepared the manuscript for publication.

The published abstracts for these articles have been used in Chapter 1 as a summary of each project.

Minor details (e.g., symbols) have been modified from their original published appearance for the sake of consistency throughout this thesis.

*To my family*

*~~narrow~~ broad is beautiful*



| | | | | |
2.0          0.0          -2.0          -4.0      MHz
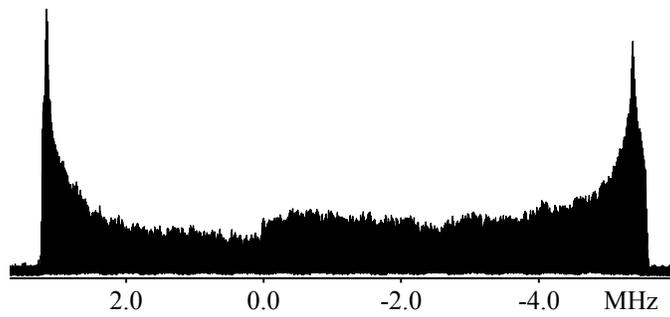
**Acknowledgements**

I would like to acknowledge Rod Wasylishen for giving me the opportunity to study solid-state NMR spectroscopy in his laboratory. Rod's encouragement, enthusiasm, and dedication to scientific rigor were a large part of what made working in this lab so enjoyable. I thank him for his guidance and support throughout my studies at the University of Alberta.

I would like to thank my supervisory committee, Alex Brown and Jonathan Veinot, for inspiring and assisting me throughout my studies. I also thank Rob Schurko and Nils Petersen for serving on my Ph.D. examination committee.

I thank all of the present and former members of the Wasylishen group. Specifically, I thank Tom Nakashima and Kris Harris for their guidance during my early days in the group, and Guy Bernard for his much-appreciated assistance over the years. I owe a huge thank you to my office-mate and friend, Rosha Teymoori, for keeping me sane over the last few years.

My studies here would not have been possible without the help of the support staff and facilities in our Department. I am incredibly grateful to Mark Miskolzie, Ryan McKay, and Nupur Dabral for their training, troubleshooting assistance, and helpful conversations. I would also like to thank Mark for taking the time to teach me many things about NMR spectrometer maintenance. I thank Dieter Starke and Allan Chilton for their time/assistance fixing electronics and other equipment, Robert McDonald and Stanislav Stoyko for their assistance in X-ray crystallography, and Wayne Moffat for many other analytical services.

Klaus Eichele and David Bryce are thanked for the development and maintenance of NMR simulation programs WSolids and QUEST, without which this work could not have been completed. Frédéric Perras is thanked for writing QUEST and providing me with the program used to simulate the RDC NMR spectra in Chapter 5. I also thank Victor Terskikh at the

* "I am sure your food poisoning was from that chip dip dated Feb 5 as I was pretty sick after eating some from that container last night!" – Don Palech, February 26, 2012

**Table of Contents**

**List of Tables**

Ph$_3$As.

**List of Figures**

90° pulse values is likely due to magnetic susceptibility differences between samples.

*a*-axis, whereas $V_{ZZ}$ and $\sigma_{11}$ are parallel to the *c*-axis in $SrCl_2 \cdot 6H_2O$. $SrCl_2 \cdot 6H_2O$ has axially symmetric EFG and magnetic shielding tensors.

**List of Symbols**

| | |
|---|---|
| $\bar{\bar{A}}$ | 3×3 tensor |
| $\bar{\bar{A}}^{PAS}$ | 3×3 tensor in its principal axis system |
| $\hat{A}$ | Eigenfunction (general) |
| $A$ | Amplitude |
| $A_{mn}$ | Element of tensor $\bar{\bar{A}}$ ($m, n = x, y, z$) |
| $A_{MM}$ | Element of tensor $\bar{\bar{A}}^{PAS}$ (M = X, Y, Z) |
| $A_{iso}$ | Isotropic value of $\bar{\bar{A}}^{PAS}$ |
| $\Delta A$ | Anisotropy in $A$ |
| $a$ | Eigenvalue (general) |
| $B_0$ | Applied static magnetic field strength |
| $B_1$ | Applied dynamic magnetic field strength |
| $B_{local}$ | Magnetic field strength at a specific location |
| $b_{mn}$ | Constant |
| $C$ | Constant |
| $C_Q$ | Nuclear quadrupolar coupling constant |
| $c_{mn}$ | Constant |
| $\bar{\bar{D}}$ | Direct dipolar coupling tensor |
| $\bar{\bar{D}}^{PAS}$ | Direct dipolar coupling tensor in its principal axis system |
| $E$ | Energy |
| $e$ | Elementary charge |
| $eq$ | Electric field gradient |

| | |
|---|---|
| $\mathcal{H}_{\mathrm{DD}}$ | Direct dipolar Hamiltonian |
| $\mathcal{H}_{\mathrm{J}}$ | Indirect spin-spin Hamiltonian |
| $\mathcal{H}_{\mathrm{MS}}$ | Magnetic shielding Hamiltonian |
| $\mathcal{H}_{\mathrm{NMR}}$ | NMR Hamiltonian |
| $\mathcal{H}_{\mathrm{Q}}$ | Quadrupolar Hamiltonian |
| $\mathcal{H}_{\mathrm{Q}}^{1}$ | First-order correction to the Zeeman energy due to the quadrupolar interaction |
| $\mathcal{H}_{\mathrm{Q}}^{2}$ | Second-order correction to the Zeeman energy due to the quadrupolar interaction |
| $\mathcal{H}_{\mathrm{RF}}$ | Radiofrequency Hamiltonian |
| $\mathcal{H}_{\mathrm{Z}}$ | Zeeman Hamiltonian |
| $\mathcal{H}_{\mathrm{ZQ}}$ | Zeeman-quadrupolar Hamiltonian |
| $h$ | Planck constant |
| $\hbar$ | Reduced Planck constant, $h/2\pi$ |
| $I$ | Moment of inertia |
| $I$ | Nuclear spin quantum number |
| $\bar{I}$ | Angular momentum operator (vector) for $I$ nuclei |
| $\hat{I}_n$ | $n^{\mathrm{th}}$ component of the angular momentum operator for $I$ nuclei |
| $\hat{I}_+$ | Raising operator for $I$ nuclei |
| $\hat{I}_-$ | Lowering operator for $I$ nuclei |
| $\bar{\bar{J}}$ | Indirect spin-spin coupling tensor |
| $\bar{\bar{J}}^{PAS}$ | Indirect spin-spin coupling tensor in its principal axis system |
| $^{x}J$ | Indirect spin-spin coupling constant over $x$ bonds |
| $J_{iso}$ | Isotropic indirect spin-spin coupling constant |

| | |
|---|---|
| $\Delta J$ | Anisotropy in $J$ |
| $k$ | Boltzmann constant |
| $\vec{L}_{classical}$ | Classical angular momentum |
| $\hat{L}$ | Operator for the total angular momentum |
| $\hat{L}_n$ | Operator for the $n^{th}$ component of the total angular momentum ($n = x, y, z$) |
| $l$ | Angular quantum number |
| $\bar{M}$ | Bulk (net) magnetization |
| $M_0$ | Magnitude of the net magnetization at equilibrium |
| $M_n$ | Magnitude of the net magnetization in the $n$-direction ($n = x, y, z$) |
| $M_{xy}$ | Magnitude of the net magnetization in the $x$-$y$ plane |
| $m$ | Mass |
| $m$ | Azimuthal/magnetic quantum number |
| $m_I$ | Nuclear spin state |
| $n$ | Principal quantum number |
| $Q$ | Nuclear electric quadrupole moment |
| $r$ | Distance |
| $\vec{r}$ | Distance (vector quantity) |
| $\bar{\bar{R}}$ | Rotation matrix |
| $R(\alpha, \beta, \gamma)$ | Rotation matrix |
| $R_{DD}$ | Direct dipolar coupling constant |
| $R_{eff}$ | Effective dipolar coupling constant |
| $\bar{S}$ | Angular momentum operator (vector) for $S$ nuclei |

| | |
|---|---|
| $\hat{S}_n$ | $n^{\text{th}}$ component of the angular momentum operator for $S$ nuclei |
| $\hat{S}_+$ | Raising operator for $S$ nuclei |
| $\hat{S}_-$ | Lowering operator for $S$ nuclei |
| $T$ | Temperature |
| $T_1$ | Spin-lattice relaxation time constant |
| $T_2$ | Spin-spin relaxation time constant |
| $T_2^*$ | Effective spin-spin relaxation time constant |
| $t$ | Time |
| $\vec{v}$ | Velocity |
| $\bar{\bar{V}}$ | Electric field gradient tensor |
| $\bar{\bar{V}}^{PAS}$ | Electric field gradient tensor in its principal axis system |
| $V$ | Electrostatic potential |
| $V_{mn}$ | Element of the electric field gradient tensor, $\bar{\bar{V}}$ ($m, n = x, y, z$) |
| $V_{ii}$ | Element of the electric field gradient tensor, $\bar{\bar{V}}^{PAS}$ ($i = $ X, Y, Z) |
| $\Delta V$ | Anisotropy in the electric field gradient |
| $x$ | Position |
| $x, y, z$ | Principal Cartesian directions (laboratory frame) |
| $\overline{\overline{ZQ}}$ | Zeeman-quadrupolar matrix |
| $zq_{IS}$ | Elements of the Zeeman-quadrupolar matrix |
| $\alpha, \beta, \gamma$ | Euler angles relating principal directions of two NMR interaction tensors |
| $\beta$ | Angle between NMR sample rotor and $B_0$ |
| $\gamma$ | Gyromagnetic ratio |

| | |
|---|---|
| $\Delta$ | Sweep range of WURST pulse |
| $\delta$ | Chemical shift |
| $\bar{\bar{\delta}}$ | Chemical shift tensor |
| $\bar{\bar{\delta}}^{PAS}$ | Chemical shift tensor in its principal axis system |
| $\delta_{mn}$ | Element of the chemical shift tensor, $\bar{\bar{\delta}}$ ($m, n = x, y, z$) |
| $\delta_{jj}$ | Element of the chemical shift tensor, $\bar{\bar{\delta}}^{PAS}$ ($j = 1, 2, 3$) |
| $\delta_{\mathrm{iso}}$ | Isotropic chemical shift |
| $\delta_{\mathrm{aniso}}$ | Anisotropy in chemical shift |
| $\eta$ | Asymmetry parameter |
| $\Theta$ | Angle between NMR interaction principal direction(s) and the axis of sample rotation (MAS) |
| $\theta$ | Angle between NMR interaction principal direction(s) and $B_0$ |
| $\theta_j$ | Angle between the magnetic shielding tensor principal directions and $B_0$ |
| $\theta_{\mathrm{p}}$ | Tip angle |
| $\vartheta$ | Polar angle between the dipolar vector and $B_0$ |
| $\kappa$ | Skew of the chemical shift or magnetic shielding tensor |
| $\lambda$ | Wavelength |
| $\mu$ | Nuclear magnetic moment |
| $\mu_0$ | Magnetic constant (permeability of free space) |
| $\nu$ | Frequency |
| $\nu_0$ | Larmor frequency |
| $\nu_1$ | Nuclear precession frequency about $B_1$ |
| $\nu_{\mathrm{a}}$ | Nuclear precession frequency in the rotating frame of reference |

| | |
|---|---|
| $\nu_{\text{off}}$ | Centre frequency of WURST pulse |
| $\nu_{\text{Q}}$ | Quadrupolar frequency |
| $\nu_{\text{reference}}$ | Reference resonance frequency |
| $\nu_{\text{sample}}$ | Sample resonance frequency |
| $\nu_{\text{T}}$ | Transmitter frequency |
| $\Delta\nu_{\text{CT}}$ | Central transition breadth |
| $\bar{\bar{\sigma}}$ | Magnetic shielding tensor |
| $\bar{\bar{\sigma}}^{PAS}$ | Magnetic shielding tensor in its principal axis system |
| $\sigma_{mn}$ | Element of the magnetic shielding tensor, $\bar{\bar{\sigma}}$ ($m, n = x, y, z$) |
| $\sigma_{jj}$ | Element of the magnetic shielding tensor, $\bar{\bar{\sigma}}^{PAS}$ ($j = 1, 2, 3$) |
| $\sigma_{\text{iso}}$ | Isotropic magnetic shielding |
| $\sigma_{\text{aniso}}$ | Anisotropy in magnetic shielding |
| $\tau$ | Time delay (in pulse sequences) |
| $\tau_{\text{p}}$ | Pulse length |
| $\varphi$ | Azimuthal angle between the dipolar vector and $B_0$ |
| $\phi$ | Phase |
| $\Psi$ | Wave function |
| $\Omega$ | Span of the chemical shift or magnetic shielding tensor |
| $\omega$ | Angular velocity |
| $\omega$ | Frequency (in radians) |
| $\omega_0$ | Larmor frequency |
| $\omega_1$ | Pulse amplitude |

$\omega_{max}$    Maximum pulse amplitude


**List of Abbreviations**

ADF            Amsterdam density functional

CASTEP        Cambridge serial total energy package

CS            Chemical shift

CSA            Chemical shift anisotropy

DFT            Density functional theory

EFG            Electric field gradient

GIPAW          Gauge-including projector augmented wave

QCPMG          Quadrupolar Carr-Purcell Meiboom-Gill

QUEST          Quadrupolar exact software

MAS            Magic angle spinning

MS            Magnetic shielding

NMR            Nuclear magnetic resonance

NQR            Nuclear quadrupole resonance

PAS            Principal axis system

RDC            Residual dipolar coupling

RF            Radio frequency

WURST          Wideband, uniform rate, smooth truncation

ZQ            Zeeman-quadrupolar

# Chapter 1

## Introduction

### 1.1 Background and Motivation

Though I worked on many different projects with different goals throughout my time in the Wasylishen lab, my focus shifted to one problem in particular. That is, the acquisition and interpretation of NMR spectra of traditionally difficult quadrupolar nuclei. NMR spectroscopy has long since been established as an invaluable characterization technique in the fields of chemistry and physics, but the majority of NMR experiments are still performed on a relatively small subset of elements. In part, this is due to the ubiquity of some elements in nature and chemistry (e.g., hydrogen, carbon, nitrogen, oxygen and silicon), and in part, this is due to the relative difficulty of studying many NMR-active nuclei. There exist several NMR-active nuclei for which few, if any, NMR data are reported. Over the past ten years, many advances in NMR software and pulse sequences have opened up new opportunities to expand the NMR literature to include more of the NMR periodic table. Ultimately, one would like to be able to study virtually

any NMR-active nucleus in any molecular or crystallographic environment and obtain NMR parameters useful for the determination of structure, bonding, and symmetry.

The majority of stable, NMR-active elements are quadrupolar,[1] meaning that in addition to interacting with the external magnetic field and the magnetic moments of other, nearby nuclei, they also possess a nuclear electric quadrupole moment, $Q$, which interacts with the surrounding electric field gradient (EFG). The nuclear quadrupolar coupling constant is dependent on the product of the nuclear quadrupole moment and the magnitude of the EFG. This interaction is often much larger in magnitude than nuclear spin-spin interactions, causing significant spectral broadening and increasing nuclear relaxation rates. This can make spectral acquisition challenging, if not impossible.

The main purpose of the research contained in this thesis is to demonstrate the feasibility of studying traditionally "challenging" quadrupolar nuclei, which have historically been largely overlooked due to unfavorable NMR properties, e.g., large nuclear electric quadrupole moments or low gyromagnetic ratios. Thus, initial studies of nuclei possessing large $Q$ values (e.g., $^{75}$As, $^{121/123}$Sb) in favorable environments, e.g., highly symmetric environments with small EFG tensor parameters, are highlighted at the beginning of this thesis. Following this, the work is extended to nuclei in non-symmetric environments in which the EFG is relatively large. Finally, the $^{87}$Sr nucleus is studied in a variety of crystallographic environments. This nucleus presents the additional challenges of possessing low natural abundance and a low gyromagnetic ratio in addition to possessing a moderate nuclear quadrupole moment. In this research, it is demonstrated that several traditionally challenging nuclei (e.g., $^{75}$As, $^{87}$Sr, $^{121/123}$Sb) can now be studied with relative ease, and under the right circumstances, a variety of nuclear spin interactions for these nuclei may be quantified. That being said, it is also apparent based on this

body of literature that the ability to successfully study these nuclei is contingent on the availability of the most modern NMR technology, i.e., broadband signal-to-noise enhancing pulse sequences and high magnetic field strengths. The majority of the work collected in this thesis would have been extremely difficult, if not impossible, to carry out without access to the $B_0 = 21.14$ T magnet at the Canadian National Ultrahigh-Field NMR Facility for Solids in Ottawa, ON.[2]

As such little NMR data exist on the majority of the nuclei featured in this thesis, spectroscopic parameters obtained via other methods of spectroscopy and by means of quantum chemistry calculations were extremely valuable. In particular, I made use of nuclear quadrupolar coupling constants determined experimentally from microwave and nuclear quadrupole resonance (NQR) spectroscopy, as well as nuclear spin-rotation and nuclear magnetic shielding constants obtained from microwave and molecular beam resonance spectroscopy. Calculated estimates of NMR parameters based on X-ray crystal structures of potential molecules for study were necessary in order to gauge the feasibility of acquiring NMR spectra in many cases. Quantum chemistry calculations were also necessary in most cases to determine the signs of NMR parameters. The aforementioned NMR parameters obtained from other fields of spectroscopy served as benchmark values with which to test my computational methods. Occasionally, the results of microwave or NQR experiments were used to verify experimental NMR spectroscopy results. It soon became obvious that though my research focused specifically on the NMR spectroscopy of solids, my knowledge of spectroscopy would have to be multidisciplinary. To this end, I have co-authored a book chapter on the connection between microwave, molecular beam resonance, and NMR spectroscopy.[3]

The nuclei that I have chosen as examples to explore the capabilities of modern NMR spectroscopy were selected first and foremost for their NMR properties, but consideration was also given to their role in the field of chemistry as a whole. For example, the arsenic nucleus is featured heavily in this thesis. This element has a unique place in human history, pop culture, and environmental chemistry. It is my hope that the insights gained in this research will be later applied to studying arsenic- and/or strontium-containing species which play a larger role in the environment and in human health.

## 1.2 Overview of Projects

### 1.2.1 Assessing Distortion of the $AF_6^-$ (A = As, Sb) Octahedra in Solid Hexafluorometallates(V) via NMR Spectroscopy

Arsenic and antimony hexafluoride salts have played an important role in the history of both solution and solid-state NMR spectroscopy. Here, solid polycrystalline $KAsF_6$ and $KSbF_6$ have been studied via high-resolution variable temperature $^{19}F$, $^{75}As$, $^{121}Sb$, and $^{123}Sb$ solid-state NMR spectroscopy at high magnetic field ($B_0 = 21.14$ T). Both $KAsF_6$ and $KSbF_6$ undergo solid-solid phase transitions at approximately 375 and 301 K, respectively. We use variable temperature NMR experiments to explore the effects of crystal structure changes on NMR parameters. $C_Q(^{75}As)$ values for $KAsF_6$ at 293, 323, and 348 K are $-2.87 \pm 0.05$ MHz, $-2.58 \pm 0.05$ MHz, and $-2.30 \pm 0.05$ MHz, respectively. The signs of these values are determined via DFT calculations. In the higher temperature cubic phase, $C_Q(^{75}As) = 0$ Hz, consistent with the point-group symmetry at the arsenic nucleus in this phase. In contrast, $C_Q$ values for $^{121}Sb$ and $^{123}Sb$ in the cubic phase of $KSbF_6$ are nonzero; e.g., at 293 K, $C_Q(^{121}Sb) = 6.42 \pm 0.10$ MHz, and $C_Q(^{123}Sb) = 8.22 \pm 0.10$ MHz. In the higher temperature tetragonal phase (343 K) of $KSbF_6$,

these values are 3.11 ± 0.20 MHz and 4.06 ± 0.20 MHz, respectively. CASTEP calculations performed on the cubic and tetragonal structures support this trend. Isotropic indirect spin-spin coupling constants are $^1J(^{75}As,^{19}F) = -926 \pm 10$ Hz (293 K) and $-926 \pm 3$ Hz (348 K), and $^1J(^{121}Sb,^{19}F) = -1884 \pm 3$ Hz (293 K), and $-1889 \pm 3$ Hz (343 K). Arsenic-75 and antimony-121,123 chemical shift values show little variation over the studied temperature ranges.

**1.2.2 Feasibility of Arsenic and Antimony NMR Spectroscopy in Solids: An Investigation of Some Group 15 Compounds**

The feasibility of obtaining $^{75}$As and $^{121/123}$Sb NMR spectra for solids at high and moderate magnetic field strengths is explored. Arsenic-75 nuclear quadrupolar coupling constants and chemical shifts have been measured for arsenobetaine bromide and tetraphenylarsonium bromide. Similarly, $^{121/123}$Sb NMR parameters have been measured for tetraphenylstibonium bromide and potassium hexahydroxoantimonate. The predicted pseudo-tetrahedral symmetry at arsenic and the known trigonal bipyramidal symmetry at antimony in their respective tetraphenyl-bromide "salts" are reflected in the measured $^{75}$As and $^{121}$Sb nuclear quadrupole coupling constants, $C_Q(^{75}As) = 7.8$ MHz and $C_Q(^{121}Sb) = 159$ MHz, respectively. Results of density functional theory quantum chemistry calculations for isolated molecules using ADF and first-principles calculations using CASTEP, a gauge-including projector augmented wave (GIPAW) method to deal with the periodic nature of solids, are compared with experiment. Although the experiments can be time consuming, measurements of $^{75}$As and $^{121}$Sb NMR spectra (at 154 and 215 MHz, respectively, i.e., at $B_0 = 21.14$ T) with linewidths in excess of 1 MHz are feasible using uniform broadband excitation shaped pulse techniques (e.g., WURST and WURST-QCPMG).

### 1.2.3 Spin-spin Coupling Between Quadrupolar Nuclei in Solids: $^{11}$B-$^{75}$As Spin Pairs in Lewis Acid-Base Adducts

Solid-state $^{11}$B NMR measurements of Lewis acid–base adducts of the form $R_3AsBR'_3$ (R = Me, Et, Ph; R′ = H, Ph, $C_6F_5$) were carried out at several magnetic field strengths (e.g., $B_0$ = 21.14, 11.75, and 7.05 T). The $^{11}$B NMR spectra of these adducts exhibit residual dipolar coupling under MAS conditions, allowing for the determination of effective dipolar coupling constants, $R_{eff}(^{75}As,^{11}B)$, as well as the sign of the $^{75}$As nuclear quadrupolar coupling constants. Values of $R_{eff}(^{75}As,^{11}B)$ range from 500 to 700 Hz. Small isotropic $J$-couplings are resolved in some cases, and the sign of $^1J(^{75}As,^{11}B)$ is determined. Values of $C_Q(^{75}As)$ measured at $B_0$ = 21.14 T for these triarylborane Lewis acid–base adducts range from $-82 \pm 2$ MHz for $Et_3AsB(C_6F_5)_3$ to $-146 \pm 1$ MHz for $Ph_3AsBPh_3$. For $Ph_3AsBH_3$, two crystallographically nonequivalent sites are identified with $C_Q(^{75}As)$ values of $-153$ and $-151 \pm 1$ MHz. For the uncoordinated Lewis base, $Ph_3As$, four $^{75}$As sites with $C_Q(^{75}As)$ values ranging from 193.5 to $194.4 \pm 2$ MHz are identified. At these applied magnetic field strengths, the $^{75}$As quadrupolar interaction does not satisfy high-field approximation criteria, and thus, an exact treatment was used to describe this interaction in $^{11}$B and $^{75}$As NMR spectral simulations. NMR parameters calculated using the ADF and CASTEP program packages support the experimentally derived parameters in both magnitude and sign. These experiments add to the limited body of literature on solid-state $^{75}$As NMR spectroscopy and serve as examples of spin–spin-coupled quadrupolar spin pairs, which are also rarely treated in the literature.

**1.2.4 Solid-State $^{87}$Sr NMR Spectroscopy at Natural Abundance and High Magnetic Field Strength**

Twenty-five strontium-containing solids were characterized via $^{87}$Sr NMR spectroscopy at natural abundance and high magnetic field strength ($B_0 = 21.14$ T). Strontium nuclear quadrupole coupling constants in these compounds are sensitive to the strontium site symmetry and range from 0 to 50.5 MHz. An experimental $^{87}$Sr chemical shift scale is proposed, and available data indicate a chemical shift range of approximately 550 ppm, from −200 to +350 ppm relative to $Sr^{2+}$ (aq). In general, magnetic shielding increased with strontium coordination number. Experimentally measured chemical shift anisotropy is reported for stationary samples of solid powdered $SrCl_2 \cdot 6H_2O$, $SrBr_2 \cdot 6H_2O$, and $SrCO_3$, with $\delta_{aniso}(^{87}Sr)$ values of +28, +26, and −65 ppm, respectively. NMR parameters were calculated using CASTEP, a gauge including projector augmented wave (GIPAW) DFT-based program which addresses the periodic nature of solids using plane-wave basis sets. Calculated NMR parameters are in good agreement with those measured.

# Chapter 2
## Theoretical Background

### 2.1 Nuclear Spin Angular Momentum

#### 2.1.1 Classical Angular Momentum

Given an object that is rotating about an external origin, the angular momentum, $\vec{L}_{classical}$, is described by the vector cross product[4]

$$\vec{L}_{classical} = \vec{r} \times m\vec{v} \qquad\qquad 2.1$$

where $\vec{r}$ is the distance between the object and the centre of rotation, $m$ is the mass of the object, and $\vec{v}$ is the linear velocity of the object (Fig. 2.1a).
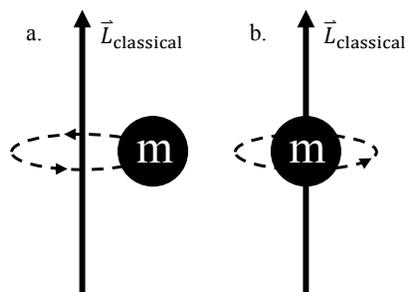


**Figure 2.1.** Classical angular momentum of a) an object rotating about an external rotation axis, and b), an object rotating about an internal rotation axis corresponding to the object's centre of mass.

Alternatively, one can have an object rotating about its centre of mass (Figure 2.1b). In this case, $\vec{L}_{classical}$ is defined as[4]

$$\vec{L}_{classical} = I\omega \qquad\qquad 2.2$$

where $I$ is the moment of inertia of the object, and $\omega$ is the angular velocity of the object. In this scenario, the angular momentum of the object is referred to as classical spin angular momentum. These two descriptions of classical angular momentum are interchangeable.

### 2.1.2 Quantum (Orbital) Angular Momentum

The term *quantum* (plural *quanta*) refers to the discrete nature of the energy of small objects, such as nuclei or electrons. Small objects can only possess specific values of angular momentum; their angular momentum is *quantized*.[4,5] This is illustrated by the solutions to the Schrödinger equation[6]

$$\hat{A}\psi = a\psi \qquad\qquad 2.3$$

where $\hat{A}$ is a quantum mechanical operator, $\psi$ is an eigenfunction that satisfies the conditions of the Schrödinger equation, and $a$ is the eigenstate corresponding to $\hat{A}$. The quantum mechanical operators we are concerned with for determining angular momentum are the square of the total angular momentum, $\hat{L}^2$, and the $z$-component of the total angular momentum vector, $\hat{L}_z$. The eigenfunctions used in the Schrödinger equation with these operators are spherical harmonic functions, and the calculated eigenstates for these two operators are as follows,[4]

$$\hat{L}^2|l,m\rangle = \hbar^2 l(l+1)|l,m\rangle \qquad (l = 0, 1, 2, \dots) \qquad 2.4$$

$$\hat{L}_z|l,m\rangle = \hbar m|l,m\rangle \qquad (m = l, l-1, l-2, \dots, -l) \qquad 2.5$$

where $\hbar$ is the reduced Planck constant, $h/2\pi$ or $1.054\ 571\ 726(47) \times 10^{-34}$ J·s. The quantum numbers $l$ and $m$ indicate the quantized nature of the angular momentum. The quantum number

$m$, which represents the projection of the total angular momentum vector onto the $z$-axis, ranges from $l$ to $-l$. The magnitude (length) of the total angular momentum vector is equal to $\hbar[l(l+1)]^{1/2}$, or the square root of the eigenvalue for $\hat{L}^2$. As indicated in Equation 2.5, there are $2l+1$ possible values of $m$.

### 2.1.3 Quantum Spin Angular Momentum

Quantum mechanical treatment of spin angular momentum is mathematically similar to what we have described for orbital angular momentum. That is, the solutions to the Schrödinger equation are of the same form. Here, $I$ represents the nuclear spin quantum number (analogous to $l$), and $m_I$ represents the nuclear spin state (analogous to $m$). For quantum numbers $I$ and $m_I$, the eigenvalues of the operators $\hat{I}^2$ and $\hat{I}_z$ are analogously $\hbar^2[I(I+1)]$, $I = 0, 1/2, 1, 3/2, \dots$, and $\hbar m_I$, $m_I = I, I-1, I-2, \dots, -I$, respectively (see Figure 2.2).[4] Colloquially, $I$ is called the "spin" or "spin number" of the particle. Leptons, protons, and neutrons possess $I = 1/2$, photons possess unit spin, and atomic nuclei possess a range of integral and half-integral spin numbers (vide infra).[7] Classical spin is not perfectly analogous to the corresponding quantum mechanical descriptions, and the concept of spin is difficult to grasp.[8-10] It is widely accepted that spin angular momentum is an intrinsic property of a quantum mechanical object.
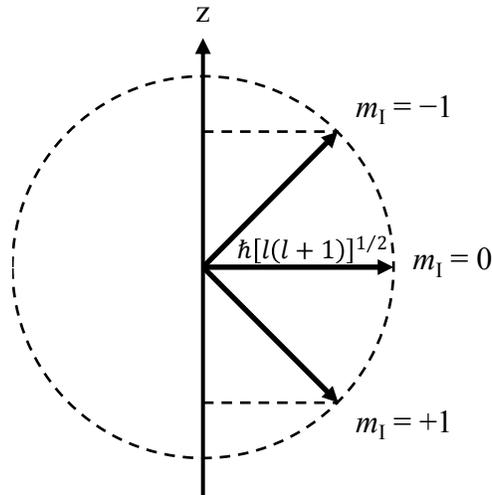
**Figure 2.2.** Spatial quantization of spin angular momentum for a particle with spin $I = 1$.

### 2.1.4 Origin of Nuclear Spin Number

There is no straightforward method to determine the ground state nuclear spin number for a given nuclide, though there are a few rules when it comes to this.

1. If the number of protons and the number of neutrons are both even, $I = 0$.

2. If the number of neutrons is odd and the number of protons is even, or vice versa, $I$ will be half-integer.

3. If the number of both protons and neutrons is odd, $I$ will be integer.

Collectively, the known elements feature nuclear spin quantum numbers ranging from $I = 0$ to $I = 9/2$ (half-integer spins), or $I = 7$ (integer spins). See Figure 2.3 for more details.

| | | | | | | | | | | | | | | | | | |
|---|---|---|---|---|---|---|---|---|---|---|---|---|---|---|---|---|---|
| 1/2 | | | | | | | | | | | | | | | | | 1/2 |
| 3/2 | 3/2 | | | | | | | | | | | 3/2 | 1/2 | 1 | 5/2 | 1/2 | 3/2 |
| 3/2 | 5/2 | | | | | | | | | | | 5/2 | 1/2 | 1/2 | 3/2 | 3/2 | |
| 3/2 | 7/2 | 7/2 | 5/2 | 7/2 | 3/2 | 5/2 | 1/2 | 7/2 | 3/2 | 3/2 | 5/2 | 3/2 | 9/2 | 3/2 | 1/2 | 3/2 | 9/2 |
| 5/2 | 9/2 | 1/2 | 5/2 | 9/2 | 5/2 | 6 | 5/2 | 1/2 | 5/2 | 1/2 | 1/2 | 9/2 | 1/2 | 5/2 | 1/2 | 5/2 | 1/2 |
| 7/2 | 3/2 | 7/2 | 7/2 | 7/2 | 1/2 | 5/2 | 3/2 | 3/2 | 1/2 | 3/2 | 1/2 | 1/2 | 1/2 | 9/2 | 1/2 | 5 | |
| 3/2 | | 3/2 | | | | | | | | | | | | | | | |

| | | | | | | | | | | | | | |
|---|---|---|---|---|---|---|---|---|---|---|---|---|---|
| | 5/2 | 7/2 | 5/2 | 7/2 | 5/2 | 3/2 | 3/2 | 5/2 | 7/2 | 7/2 | 1/2 | 5/2 | 7/2 |
| | 3/2 | 7/2 | 5/2 | 1/2 | 5/2 | 9/2 | | | 7/2 | | | | |

**Figure 2.3.** Nuclear spin periodic table depicting the nuclear spin quantum numbers of the NMR-active isotopes with the highest natural abundance. The most stable NMR-active nuclides of synthetic elements are also included. Spin-1/2 isotopes are highlighted for clarity.

### 2.1.5 Nuclear Magnetic Moments and the Gyromagnetic Ratio

Atomic nuclei are charged particles, thus a nucleus that possesses nuclear spin angular momentum also possesses a nuclear magnetic dipole moment.[7] The magnetic moment of a nucleus is quantized analogously to the nuclear spin angular momentum. For a spin-1/2 nucleus, this magnetic moment can be oriented either parallel or antiparallel to the nuclear spin angular momentum. These two quantities are related by the equation,

$$\bar{\mu} = \gamma \hbar \bar{I} \qquad\qquad 2.6$$

where $\bar{\mu}$ is the magnetic dipole moment of the nucleus, and $\gamma$ is the gyromagnetic ratio. The magnitude of the gyromagnetic ratio is an intrinsic property of the nuclide, and $\gamma$ is most often positive, denoting parallel alignment of the magnetic moment and spin angular momentum.

## 2.2 The NMR Hamiltonian

The Hamiltonian is the quantum mechanical operator corresponding to the total energy of a system. The NMR Hamiltonian consists of several terms that describe the way a nucleus interacts with its environment,[11,12]

$$\mathcal{H}_{NMR} = \mathcal{H}_Z + \mathcal{H}_{RF} + \mathcal{H}_Q + \mathcal{H}_{MS} + \mathcal{H}_{DD} + \mathcal{H}_J \qquad 2.7$$

where these terms, in order, represent the Zeeman interaction, the interaction between an oscillating magnetic field and the nucleus, the quadrupolar interaction, magnetic shielding, and the direct dipolar and indirect spin-spin interactions.

With the exception of the quadrupolar interaction, which does not affect nuclei with a spin number of $I = 1/2$, these interactions may affect every magnetically active nucleus in an NMR experiment to some extent. The Zeeman and RF interactions are referred to as external interactions as they are under the control of the experimentalist. The remaining interactions are referred to as internal interactions, and depend on the properties of the system under study, e.g., bond distances, molecular symmetry, and the intrinsic properties of the nuclides present. Internal interactions are orientation-dependent (anisotropic), i.e., they depend on the orientation of the crystallographic unit cell with respect to the applied magnetic (Zeeman) field. In a solid powder, crystallites are oriented randomly and the NMR spectrum consists of contributions from all orientations. In solution, rapid molecular tumbling changes the instantaneous orientation of molecules, and the magnitude of internal interactions contributing to NMR spectra are in most cases an average over every possible orientation, i.e., an isotropic value. Exceptions include partially ordered solutions such as liquid crystalline materials[13] and molecules with anisotropic magnetic susceptibilities in high magnetic fields.[14]

In general, terms in the NMR Hamiltonian can be written in Cartesian coordinates in the laboratory frame as[12]

$$\mathcal{H}_\mathrm{A} = C\bar{I} \cdot \bar{\bar{A}} \cdot \bar{S} \qquad\qquad 2.8$$

$$\mathcal{H}_\mathrm{A} = C(\hat{I}_x, \hat{I}_y, \hat{I}_z) \begin{bmatrix} A_{xx} & A_{xy} & A_{xz} \\ A_{yx} & A_{yy} & A_{yz} \\ A_{zx} & A_{zy} & A_{zz} \end{bmatrix} \begin{pmatrix} \hat{S}_x \\ \hat{S}_y \\ \hat{S}_z \end{pmatrix} \qquad\qquad 2.9$$

where $C$ is a constant, $\bar{I}$ and $\bar{S}$ are vectors, and $\bar{\bar{A}}$ is a 3 × 3 tensor. The vector $\bar{I} = (\hat{I}_x, \hat{I}_y, \hat{I}_z)$ corresponds to the spin angular momentum of the observed nuclei, the vector $\bar{S}$ describes what these nuclei are coupled to (e.g., the spin angular momentum of neigbouring nuclei $S$), and $\bar{\bar{A}}$ represents the manner in which they are coupled. In the case of internal NMR interactions, the elements of $\bar{\bar{A}}$ are molecular properties. The symmetric component of every internal NMR interaction tensor has a special axis system called the principal axis system (PAS) in which the tensor $\bar{\bar{A}}$ is diagonal.

$$\bar{\bar{A}}^{PAS} = \begin{bmatrix} A_{\mathrm{XX}} & 0 & 0 \\ 0 & A_{\mathrm{YY}} & 0 \\ 0 & 0 & A_{\mathrm{ZZ}} \end{bmatrix} \qquad\qquad 2.10$$

Note that both the magnetic shielding and indirect spin-spin coupling tensors also possess an antisymmetric component.[15] $\bar{\bar{A}}^{PAS}$ has a specific orientation within the molecular or crystallographic reference frame, which can be described by three Euler angles.[16] The ZYZ convention[12] is used in this thesis. This involves, starting with the axes of $\bar{\bar{A}}^{PAS}$ coincident with the laboratory axes, rotation about $z$ by the angle $\alpha$, followed by rotating about the (new) $y$ axis by the angle $\beta$ and again about the new $z$ direction by the angle $\gamma$ (see Figure 2.4). Mathematically, this is equivalent to multiplication of the tensor by the rotation matrix $R(\alpha,\beta,\gamma)$,[17,18]

$$R(\alpha,\beta,\gamma) = \begin{bmatrix} \cos\alpha\cos\beta\cos\gamma - \sin\alpha\sin\gamma & \sin\alpha\cos\beta\cos\gamma + \cos\alpha\sin\gamma & -\sin\beta\cos\gamma \\ -\cos\alpha\cos\beta\sin\gamma - \sin\alpha\cos\gamma & -\sin\alpha\cos\beta\sin\gamma + \cos\alpha\cos\gamma & \sin\beta\sin\gamma \\ \cos\alpha\sin\beta & \sin\alpha\sin\beta & \cos\beta \end{bmatrix} \qquad 2.11$$

if the laboratory frame is rotated away from the NMR interaction tensor (passive rotation).

The QUEST program[19] is used to simulate the majority of the NMR spectra in this thesis. To quantify the Euler angles describing the relative orientation of the EFG and CS tensors, this program holds the EFG tensor coincident with the applied magnetic field, and rotates the applied magnetic field away from the chemical shift tensor using Equation 2.13.
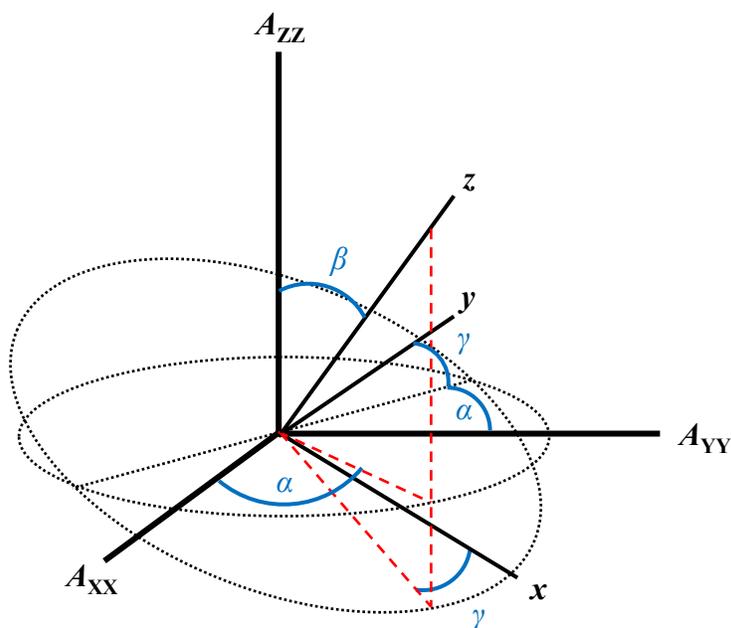


**Figure 2.4.** Illustration of the ZYZ convention for tensor rotation.

The elements of $\bar{\bar{A}}^{PAS}$ are often represented using the Haeberlen-Mehring-Spiess convention,[20] though other conventions may be used (see Section 2.2.4). Note the magnitudes of the elements of $\bar{\bar{A}}^{PAS}$ are defined as $|A_{ZZ} - A_{iso}| \geq |A_{XX} - A_{iso}| \geq |A_{YY} - A_{iso}|$.

$$A_{iso} = \frac{1}{3}Tr\bar{\bar{A}} = \frac{1}{3}(A_{XX} + A_{YY} + A_{ZZ}) \qquad 2.12$$

$$\Delta A = A_{ZZ} - \frac{(A_{XX} + A_{YY})}{2} \qquad 2.13$$

$$\eta = \frac{3}{2}\frac{(A_{YY} - A_{XX})}{\Delta A} \qquad 2.14$$

Here, $A_{iso}$ is the isotropic value of $A$, $\Delta A$ is the anisotropy in $A$, and $\eta$ is the asymmetry parameter. In special cases where nuclei occupy molecular or crystallographic sites of high symmetry, NMR interaction tensor components are confined. E.g., in the presence of a $C_n$, $n \geq 3$ rotation axis at the nucleus, the interaction tensors are axially symmetric, and $\bar{\bar{A}}^{PAS}$ contains only two unique components (i.e., either $A_{XX} = A_{YY}$ or $A_{YY} = A_{ZZ}$). For nuclei at sites with, e.g., $T_d$ or $O_h$ point-group symmetry, $A_{XX} = A_{YY} = A_{ZZ}$.

## 2.2.1 The Zeeman Interaction

In the absence of an external magnetic field, spin states of the same absolute value are degenerate in energy (e.g., $\pm 1/2$, $\pm 3/2$, etc.). When nuclear spins couple to an external magnetic field this degeneracy is broken, and all spin states possess a unique energy dependent on the magnitude of the applied magnetic field (Figure 2.5). Most importantly, the $m_I = 1/2$ to $m_I = -1/2$ transition, which is the only available transition for nuclei with $I = 1/2$ and the most easily studied transition for half-integer quadrupolar nuclei, becomes accessible to spectroscopists. The latter case makes up the bulk of this work. The Zeeman interaction is described by its Hamiltonian,[12]

$$\mathcal{H}_Z = -\gamma(\hat{I}_x, \hat{I}_y, \hat{I}_z)\begin{bmatrix} 1 & 0 & 0 \\ 0 & 1 & 0 \\ 0 & 0 & 1 \end{bmatrix}\begin{pmatrix} B_{0,x} \\ B_{0,y} \\ B_{0,z} \end{pmatrix} \qquad 2.15$$

16

where $B_0$ is the strength of the static magnetic field. If the direction of this field is defined as the $+z$ direction in the laboratory frame, i.e., $\bar{B}_0 = (0,0,B_0)$, the Hamiltonian is simplified.

$$\mathcal{H}_Z = -\gamma B_0 \hat{I}_Z \qquad 2.16$$
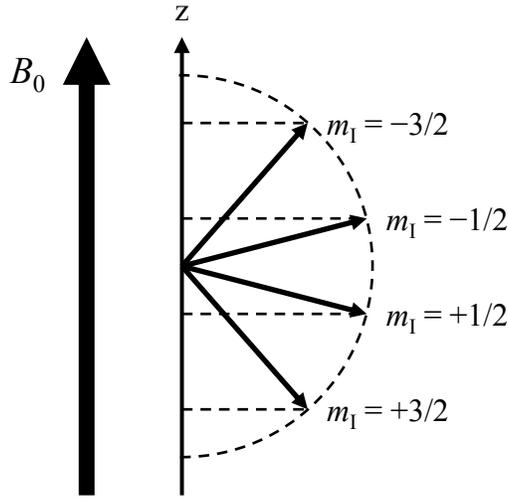


**Figure 2.5.** Nuclear spin angular momentum orientations ($I = 3/2$, positive $\gamma$) in a magnetic field as a result of the Zeeman interaction. Arrow indicates direction of $B_0$.

After operating with the Zeeman Hamiltonian on $|m_\mathrm{I}\rangle$, it is apparent that the energy levels of each spin state are unique,[11]

$$E_Z = -m_I \gamma \hbar B_0 \qquad 2.17$$

and that these energy levels have even spacing. The selection rule for NMR transitions is $\Delta m_\mathrm{I} = \pm 1$.

$$\Delta E_Z = \gamma \hbar B_0 = h\nu \qquad 2.18$$

$$\nu_0 = \frac{\gamma B_0}{2\pi} \qquad 2.19$$

Equation 2.19 is referred to as the Larmor equation, and it is the basis for the NMR experiment. It describes the magnetic field oscillation frequency required to perturb the ensemble of nuclear

spins from equilibrium. Note that the total angular momentum vector is offset from the $z$-direction (Figure 2.5), thus, according to the classical model of spin, torque supplied by the external magnetic field causes nuclear spin precession about the direction of $B_0$. This occurs at frequency $v_0$ for the bare nucleus, which falls in the radio frequency range at typical magnetic field strengths.

**2.2.2 The Boltzmann Distribution and the Net Magnetization**

The relative population of spin states at equilibrium is determined by the Boltzmann distribution,[11]

$$\frac{n_{\text{upper}}}{n_{\text{lower}}} = e^{-\Delta E/kT} = e^{-\gamma \hbar B_0/kT} \qquad \qquad 2.20$$

where $n_{\text{upper}}$ and $n_{\text{lower}}$ are the populations of spin states with higher and lower energy, respectively, $\Delta E$ is the energy difference between the two states, $k$ is the Boltzmann constant, and $T$ is the temperature in Kelvin.

The significance of this relationship becomes apparent when one considers the relative populations of nuclear spin states during a routine experiment (e.g., performed at moderate field strength, $B_0 = 11.75$ T, at room temperature). A typical sample used for a solid-state NMR experiment contains on the order of $10^{20}$ nuclei under observation. If these are $^1$H nuclei, $v_0 = 500.3$ MHz and $\Delta E = 3.3 \times 10^{-25}$ J, making the ratio $n_{\text{upper}}/n_{\text{lower}} = 0.99992$. That is, for every $10^{20}$ nuclei in the $m_I = -1/2$ state, there are $1.00008 \times 10^{20}$ nuclei in the $m_I = +1/2$ state, a difference of approximately 0.004 %. Since the observed NMR signal is collected from all nuclei simultaneously, the amplitude of the detected signal is proportional to the difference in population between the two states. Note that at NMR transition frequencies, spontaneous emission is negligible.[21]

NMR spectroscopy is performed on a bulk sample with many nuclei, so it is convenient to consider the *net magnetization*, or the vector sum of the individual nuclear spin angular momenta. At equilibrium, for nuclei with positive $\gamma$, the net magnetization is aligned parallel to the applied static magnetic field, i.e., in the $+z$ direction (laboratory frame), as this corresponds to the slight excess of nuclei in the ground spin state. At equilibrium, our vector model indicates that the precession of the nuclear spin angular momentum has no preferred phase, therefore the net magnetic moment in the $x$- and $y$-directions is zero. The bulk effects of applying a dynamic magnetic field are modeled by the behaviour of the net magnetization vector, $\bar{M}$.

### 2.2.3 Radiofrequency Pulses

The nuclear spin system is perturbed from equilibrium by a dynamic magnetic field which oscillates at radio frequency. This magnetic field is applied for a short duration of time, referred to as a pulse. The simplest commonly-used pulse is a Bloch pulse,[22] which is rectangular in shape and consists of a single oscillation frequency and phase. The combination of a series of pulses and delays with one or more oscillation frequency is called a pulse sequence. Some relevant pulse sequences will be reviewed later in this chapter.

The time-dependent, secondary magnetic field, $B_1$, arises primarily from Faraday induction near the transmitting coil due to the oscillating electrical current applied to the coil.[23] The RF Hamiltonian is[12]

$$\mathcal{H}_{\text{RF}} = -\gamma\left(\hat{I}_x, \hat{I}_y, \hat{I}_z\right)\begin{bmatrix} 1 & 0 & 0 \\ 0 & 1 & 0 \\ 0 & 0 & 1 \end{bmatrix}\begin{pmatrix} B_{1,x}(t) \\ B_{1,y}(t) \\ B_{1,z}(t) \end{pmatrix}. \tag{2.21}$$

For a rectangular pulse applied in the $x$-direction in the laboratory frame, $B_{1,x}(t) = 2B_1 \cos 2\pi\nu_{\text{T}}t$, while $B_{1,y}(t)$ and $B_{1,z}(t)$ are zero, making the RF Hamiltonian

19

$$\mathcal{H}_{\text{RF}} = -2\gamma B_1 \cos 2\pi\nu_{\text{T}} t\, \hat{I}_x.$$

<div align="right">2.22</div>

This is mathematically equivalent to two counter-rotating vectors of length $B_1$ (Figure 2.6). In this case only the resonant component (the vector precessing in the same direction as the nuclear spin angular momenta, depicted here as counter clockwise for nuclei with a positive gyromagnetic ratio) is considered.[24]
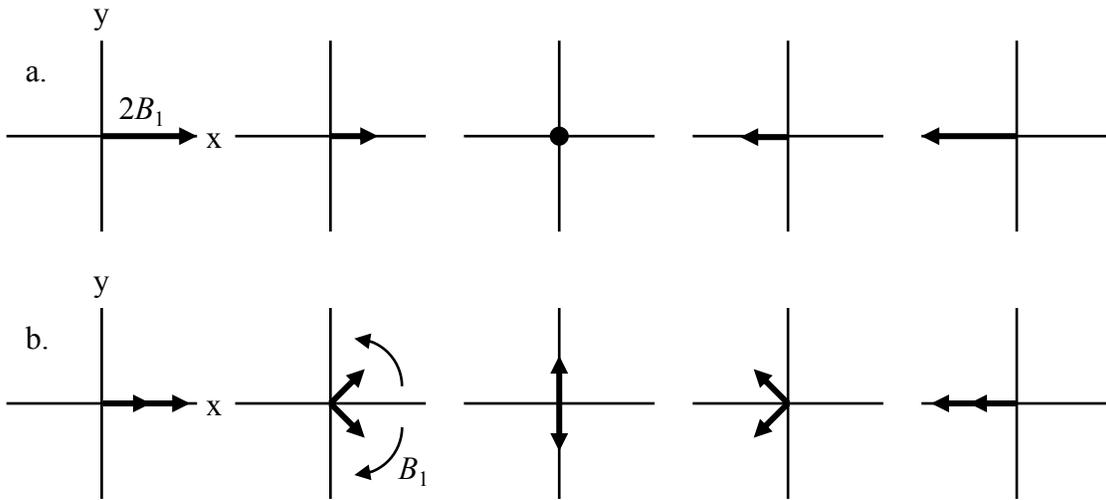


**Figure 2.6.** Dynamic magnetic field ($B_1$) in the *x-y* plane represented by a) a plane wave, and b) two counter-rotating vectors.

In the rotating frame of reference,

$$\nu_{\text{a}} = \nu_0 - \nu_{\text{T}}$$

<div align="right">2.23</div>

where $\nu_0$ is the nuclear resonance frequency in the laboratory frame, $\nu_{\text{T}}$ is the transmitter (RF) frequency, and $\nu_{\text{a}}$ is the nuclear resonance frequency in the rotating frame, which often falls in the audio frequency range. In the rotating frame, the RF Hamiltonian becomes

$$\mathcal{H}'_{\text{RF}} = -\gamma B_1 \hat{I}_x$$

<div align="right">2.24</div>

for a pulse applied along the *x*-axis. During an RF pulse, the net magnetization will undergo precession about the $B_1$ direction at frequency $\nu_1$.

$$v_1 = \frac{\gamma B_1}{2\pi}$$
2.25

RF pulse lengths are in the μs to ms range, and the net magnetization may not undergo a full rotation about the $B_1$ direction during this time. The tip angle, $\theta_p$, is

$$\theta_p = \gamma B_1 \tau_p$$
2.26

where $\tau_p$ is the pulse width, in units of time. $B_1$ magnitude is optimized to achieve specific tip angles, often 90° or less for a Bloch pulse.
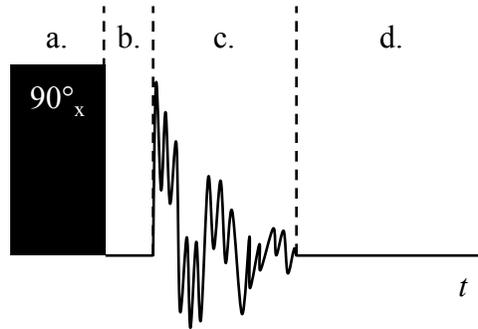


**Figure 2.7.** The Bloch pulse sequence, including a) the RF pulse (≈ μs), b) a short delay to allow for probe ringdown (≈ μs), c) FID acquisition (≈ ms to s), and d) a recycle delay allowing the Boltzmann equilibrium to re-establish (≈ ms to hours).

After the pulse is applied, the free-induction decay (FID) is observed. The FID is the graphical representation of the induced electrical current in a receiver coil caused by the magnetic moments of the observed nuclei. According to our model, the amplitude of the FID is thus proportional to the net sum of the nuclear magnetic moments in the $x$-$y$ plane; this quantity is time-dependent. If the transmitter frequency is offset from the resonance frequency of the observed nuclei, the FID will contain oscillations at $v_a$. Following FID acquisition, a time delay long enough to allow the spin system to return to Boltzmann equilibrium occurs before the

21

sequence is repeated. Signal from individual transients are added together to produce the final FID, which undergoes Fourier transformation to produce the NMR spectrum in the frequency-domain. The signal-to-noise ratio of the final NMR spectrum is proportional to $\sqrt{N}$, where $N$ is the number of transients.

**2.2.4 Magnetic Shielding and Chemical Shift**

The total magnetic field strength at a nucleus is dependent on the local electronic environment at that nucleus. Electrons experience a torque in the $B_0$ direction, causing them to circulate perpendicular to $B_0$. This movement induces a secondary local magnetic field, either opposing or augmenting the applied magnetic field ($B_0$). The magnetic shielding Hamiltonian[12] describes the correction to the Zeeman energy as a result of this process.

$$\widehat{\mathcal{H}}_{MS} = \gamma \left( \hat{I}_x, \hat{I}_y, \hat{I}_z \right) \begin{bmatrix} \sigma_{xx} & \sigma_{xy} & \sigma_{xz} \\ \sigma_{yx} & \sigma_{yy} & \sigma_{yz} \\ \sigma_{zx} & \sigma_{zy} & \sigma_{zz} \end{bmatrix} \begin{pmatrix} 0 \\ 0 \\ B_0 \end{pmatrix} \qquad 2.27$$

$$\widehat{\mathcal{H}}_{MS} = \gamma \left[ \hat{I}_x \sigma_{xz} B_0 + \hat{I}_y \sigma_{yz} B_0 + \hat{I}_z \sigma_{zz} B_0 \right] \qquad 2.28$$

One only considers terms of the Hamiltonian which commute with the Zeeman Hamiltonian, as these terms describe the NMR spectrum.

$$\widehat{\mathcal{H}}_{MS} = \gamma \sigma_{zz} B_0 \hat{I}_z \qquad 2.29$$

The magnitude of the local magnetic field at a nucleus is thus

$$B_{local} = (1 - \sigma_{zz}) B_0 \qquad 2.30$$

where the induced magnetic field is proportional to the applied magnetic field, $B_0$. Correcting for magnetic shielding, the Larmor equation becomes,

$$\nu = \frac{\gamma B_0}{2\pi} \left( 1 - \sigma_{zz}(\theta) \right) \qquad 2.31$$

22

where the value of $\sigma_{zz}(\theta)$ depends on the orientation of the chemical shift tensor within the applied magnetic field. For a given nucleus in a powder sample, the values of the shielding constant $\sigma_{zz}$ are determined by[11]

$$\sigma_{zz}(\theta) = \frac{1}{3}Tr\bar{\bar{\sigma}}^{PAS} + \frac{1}{3}\sum_{j=1}^{3}(3\cos^2\theta_j - 1)\sigma_{jj} \qquad 2.32$$

where $Tr\bar{\bar{\sigma}}^{PAS}$ is the trace of the magnetic shielding tensor, and $\theta_j$ ($j = 1, 2, 3$) is the angle between the magnetic shielding tensor axis and the applied magnetic field. The elements of $\bar{\bar{\sigma}}^{PAS}$ are often written with numeric subscripts.

$$\bar{\bar{\sigma}}^{PAS} = \begin{bmatrix} \sigma_{11} & 0 & 0 \\ 0 & \sigma_{22} & 0 \\ 0 & 0 & \sigma_{33} \end{bmatrix} \qquad 2.33$$

In the PAS, the three magnetic shielding tensor components are defined such that $\sigma_{11} \leq \sigma_{22} \leq \sigma_{33}$. In other words, $\sigma_{11}$ is the component in the direction of minimum shielding and $\sigma_{33}$ is in the direction of the greatest shielding.

Obtaining magnetic shielding values is not a straightforward task, as precise values for $B_0$ and $\gamma$ are generally not known. Instead, spectroscopists use the chemical shift (CS) to quantify this interaction. The chemical shift is defined as,[1]

$$\delta = \frac{(\nu_{\text{sample}} - \nu_{\text{reference}})}{\nu_{\text{reference}}} \times 10^6 \qquad 2.34$$

where $\nu_{\text{sample}}$ and $\nu_{\text{reference}}$ are the resonance frequencies for the sample peak and a standard reference peak, respectively, measured in the same magnetic field, and $\delta$ is in units of ppm. Note that in some NMR software, the denominator used to calculate the chemical shift is actually the nominal transmitter frequency of the observed nucleus, and not the frequency of the reference peak, which can introduce errors for nuclei with large chemical shift ranges. The elements of $\bar{\bar{\delta}}^{PAS}$ are defined such that $\delta_{11} \geq \delta_{22} \geq \delta_{33}$ (the magnetic shielding and chemical shift scales run

in opposite directions, i.e., $\delta \approx \sigma_{reference} - \sigma_{sample}$ for nuclei with small values of $\sigma$). For all

practical cases, chemical shift values expressed in units of ppm are independent of external

magnetic field strength.

It is common to represent the chemical shift tensor elements using the Maryland

convention,[25] whose terms are outlined below.

$$\delta_{iso} = \frac{(\delta_{11} + \delta_{22} + \delta_{33})}{3} \qquad 2.35$$

$$\Omega = \delta_{11} - \delta_{33} \qquad 2.36$$

$$\kappa = \frac{3(\delta_{22} - \delta_{iso})}{\Omega} \qquad 2.37$$

Here, $\Omega$ is the span and $\kappa$ is the skew, where $-1 \leq \kappa \leq 1$. For an axially symmetric site, $\kappa$ will

be either 1, where $\delta_{11} = \delta_{22}$, or $-1$, where $\delta_{22} = \delta_{33}$. See Figure 2.8 for examples of NMR spectra

of powdered solids for which the magnetic shielding interaction is the only contributor to the

NMR line shape.

a. $\kappa = 0.0$

b. $\kappa = 0.5$

c. $\kappa = 1.0$
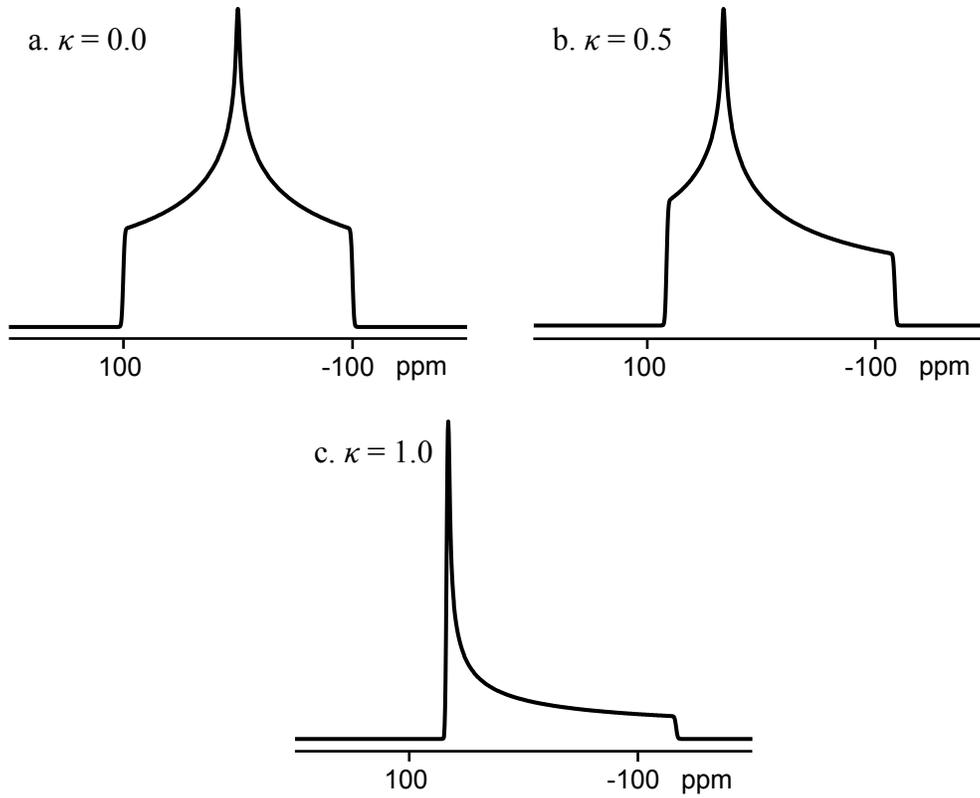
**Figure 2.8.** Solid-state NMR powder patterns due to anisotropic magnetic shielding. Simulation parameters are $\delta_{iso} = 0$ ppm and $\Omega = 200$ ppm. Figure shows cases with three unique tensor components in $\bar{\bar{\sigma}}^{PAS}$ (a and b), as well as the case of axial symmetry (c).

### 2.2.5 Direct Dipolar Coupling

Dipolar coupling occurs when the nuclear magnetic moment of a nucleus couples to the magnetic moments of surrounding nuclei. The direct dipolar Hamiltonian for an isolated spin pair, which describes this through-space coupling, is[12]

$$\mathcal{H}_{DD} = R_{DD}(\hat{I}_x, \hat{I}_y, \hat{I}_z) \begin{bmatrix} (r^2 - 3x^2)/r^2 & -3xy/r^2 & -3xz/r^2 \\ -3xy/r^2 & (r^2 - 3y^2)/r^2 & -3yz/r^2 \\ -3xz/r^2 & -3yz/r^2 & (r^2 - 3z^2)/r^2 \end{bmatrix} \begin{pmatrix} \hat{S}_x \\ \hat{S}_y \\ \hat{S}_z \end{pmatrix} \qquad 2.38$$

where $R_{DD}$ is the dipolar coupling constant, $x$, $y$, and $z$ are components of the vector $\bar{r}$ (i.e.,

$r = [x^2 + y^2 + z^2]^{1/2}$), which is the internuclear distance between spins $I$ and $S$, and $r$ is the

length of $\bar{r}$.

$$R_{DD} = \frac{\mu_0 \gamma_1 \gamma_2 \hbar}{8\pi^2} \langle \frac{1}{r_{1,2}^3} \rangle \tag{2.39}$$

Here, $\mu_0$ is the magnetic constant and $\gamma_n$ ($n = 1, 2$) are the gyromagnetic ratios of the coupled

nuclei. Assuming $\bar{r}$ lies along the laboratory $z$-axis (i.e. in the PAS), the dipolar tensor is axially

symmetric and traceless, except in some cases due to vibrational effects.[26]

$$\bar{\bar{D}}^{PAS} = \begin{bmatrix} 1 & 0 & 0 \\ 0 & 1 & 0 \\ 0 & 0 & -2 \end{bmatrix} \tag{2.40}$$

In spherical coordinates, the direct dipolar Hamiltonian is,[12]

$$\mathcal{H}_{DD} = R_{DD}[\hat{A} + \hat{B} + \hat{C} + \hat{D} + \hat{E} + \hat{F}] \tag{2.41}$$

$$\hat{A} = -(3\cos^2\vartheta - 1)\hat{I}_z\hat{S}_z \tag{2.42}$$

$$\hat{B} = -\frac{1}{2}(3\cos^2\vartheta - 1)(\hat{I}_z\hat{S}_z - \bar{I}\cdot\bar{S}) \tag{2.43}$$

$$\hat{C} = -\frac{3}{2}\sin\vartheta\cos\vartheta\, e^{-i\varphi}(\hat{I}_z\hat{S}_+ + \hat{I}_+\hat{S}_z) \tag{2.44}$$

$$\hat{D} = -\frac{3}{2}\sin\vartheta\cos\vartheta\, e^{i\varphi}(\hat{I}_z\hat{S}_- + \hat{I}_-\hat{S}_z) \tag{2.45}$$

$$\hat{E} = -\frac{3}{4}\sin^2\vartheta\, e^{-i2\varphi}\hat{I}_+\hat{S}_+ \tag{2.46}$$

$$\hat{F} = -\frac{3}{4}\sin^2\vartheta\, e^{i2\varphi}\hat{I}_-\hat{S}_- \tag{2.47}$$

where $\vartheta$ and $\varphi$ are the polar and azimuthal angles between the dipolar vector and the applied

magnetic field (laboratory $z$-axis), respectively, $\hat{I}_+$ and $\hat{S}_+$ are the raising operators for the $I$ and $S$

spins, and $\hat{I}_-$ and $\hat{S}_-$ are the lowering operators for those spins. In cases of residual dipolar

coupling between quadrupolar nuclei, all six terms of the "dipolar alphabet" must be considered to accurately model NMR spectra.[27]

**2.2.6 Indirect Spin-Spin Coupling**

Indirect spin-spin coupling, often referred to as *J*-coupling, describes the through-bond coupling of nuclear magnetic moments. This Hamiltonian is of the same form as the direct dipolar Hamiltonian,[12] as it too represents coupling of the *I* and *S* spins. Both direct and indirect spin-spin coupling result in field-independent peak splitting of the resonances of the coupled nuclei under typical conditions, though there are rare examples of field dependence in these parameters.[28]

$$\mathcal{H}_{\mathrm{J}} = (\hat{I}_x, \hat{I}_y, \hat{I}_z) \begin{bmatrix} J_{xx} & J_{xy} & J_{xz} \\ J_{yx} & J_{yy} & J_{yz} \\ J_{zx} & J_{zy} & J_{zz} \end{bmatrix} \begin{pmatrix} \hat{S}_x \\ \hat{S}_y \\ \hat{S}_z \end{pmatrix} \qquad 2.48$$

The isotropic *J*-coupling is most often measured in high-resolution NMR spectra. Anisotropy in *J* is typically negligibly small for light nuclei but can be important for heavier nuclides. Effects from $\Delta J$ on the NMR spectrum generally cannot be experimentally distinguished from those from direct dipolar coupling, leading to an experimentally measured effective dipolar coupling constant, $R_{\mathrm{eff}}$.

$$R_{\mathrm{eff}} = R_{\mathrm{DD}} - \frac{\Delta J}{3} \qquad 2.49$$

**2.2.7 Quadrupolar Interaction**

Quadrupolar nuclei have a non-spherical charge distribution, and therefore possess a nuclear electric quadrupole moment, $Q$. The magnitude of the quadrupole moment describes the extent to which the nuclear charge distribution is distorted from spherical symmetry. A

quadrupolar nucleus can have either an oblate (disc-like) or prolate (roughly cylindrical) charge distribution (Figure 2.9). Nuclei with prolate and oblate charge distributions have positive and negative nuclear quadrupole moments, respectively.
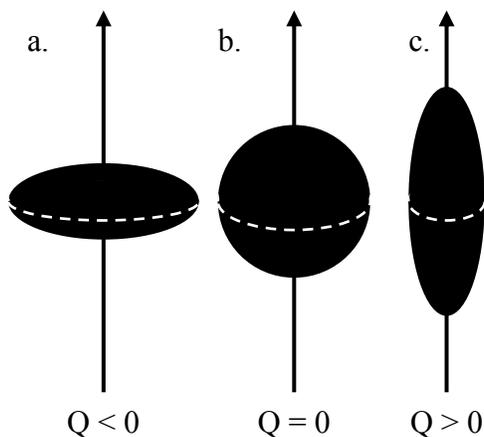


**Figure 2.9.** Oblate (a), spherical (b), and prolate (c) nuclear charge distributions. Quadrupolar nuclei are (a) and (c), while (b) represents a spin-1/2 nucleus.

What makes quadrupolar nuclei unique is that, in addition to the other internal NMR interactions which are magnetic in nature, quadrupolar nuclei interact electrically with their surroundings. A charged object possesses an associated local electric potential. For a point charge, the electrostatic potential is

$$V = \frac{e}{r}$$ 2.50

where $e$ is the elementary charge, and $r$ is the distance from the point charge. The electric field is the distance derivative of the electric potential.

$$E = \frac{-e}{r^2}$$ 2.51

The electric field gradient is the distance derivative of the electric field, or

$$eq = \frac{2e}{r^3}$$

<div align="right">2.52</div>

where $eq$ is the electric field gradient. All charged particles in a molecule or crystal contribute to the electric field gradient at a particular nucleus. The electric field gradient (EFG) at a nucleus is represented by the tensor $\bar{\bar{V}}$, which in its principal axis system has three components (the principal components).

$$\bar{\bar{V}}^{PAS} = \begin{bmatrix} V_{XX} & 0 & 0 \\ 0 & V_{YY} & 0 \\ 0 & 0 & V_{ZZ} \end{bmatrix}$$

<div align="right">2.53</div>

where $eq_{ii} = V_{ii}$ ($i$ = X, Y, Z), and $V_{XX}$, $V_{YY}$, and $V_{ZZ}$ are defined such that $|V_{XX}| \leq |V_{YY}| \leq |V_{ZZ}|$. The full quadrupolar Hamiltonian is[12]

$$\mathcal{H}_Q = \frac{eQ}{2I(2I-1)\hbar} \left( \hat{I}_x, \hat{I}_y, \hat{I}_z \right) \begin{bmatrix} V_{xx} & V_{xy} & V_{xz} \\ V_{yx} & V_{yy} & V_{yz} \\ V_{zx} & V_{zy} & V_{zz} \end{bmatrix} \begin{pmatrix} \hat{I}_x \\ \hat{I}_y \\ \hat{I}_z \end{pmatrix}$$

<div align="right">2.54</div>

where the $I$ spins correspond to the observed quadrupolar nucleus. The EFG tensor is traceless and symmetric, so the terms in the Haeberlen representation of the elements of $\bar{\bar{V}}^{PAS}$ are $V_{iso} = 0$ (not considered), $\Delta V = \frac{3}{2} V_{ZZ}$, and $\eta_Q = (V_{XX} - V_{YY})/V_{ZZ}$. The anisotropy in $\bar{\bar{V}}^{PAS}$ is most commonly represented by the nuclear quadrupolar coupling constant, $C_Q$, which is proportional to $\Delta V$.

$$C_Q = \frac{eQV_{ZZ}}{h}$$

<div align="right">2.55</div>

The quadrupolar Hamiltonian is typically rewritten in spherical polar coordinates,[29,30]

$$\mathcal{H}_Q = \frac{eQ}{4I(2I-1)\hbar}\left[\frac{1}{3}\sqrt{6}\left(3\hat{I}_z^2 - I(I+1)\right)V_0 + \left(\hat{I}_z\hat{I}_+ + \hat{I}_+\hat{I}_z\right)V_{-1}\right.$$

$$\left. - \left(\hat{I}_z\hat{I}_- + \hat{I}_-\hat{I}_z\right)V_1 + \hat{I}_+^2 V_{-2} + \hat{I}_-^2 V_2\right]$$

2.56

where the elements $V_{(2,q)}$ are as follows.

$$V_0 = 3\sqrt{\frac{1}{6}}V_{zz}$$

2.57

$$V_1 = -V_{xz} - iV_{yz}$$

2.58

$$V_{-1} = V_{xz} - iV_{yz}$$

2.59

$$V_2 = \frac{1}{2}\left(V_{xx} - V_{yy}\right) + iV_{xy}$$

2.60

$$V_{-2} = \frac{1}{2}\left(V_{xx} - V_{yy}\right) - iV_{xy}$$

2.61

In the high-field approximation, one assumes that internal NMR interactions are small in magnitude compared to the Zeeman interaction and can be described using perturbation theory. Accurately describing the NMR spectra of quadrupolar nuclei often requires consideration of the first- and second-order energy corrections to the Zeeman energy levels, though as will be discussed later in this chapter, the high-field approximation is not valid for the quadrupolar interactions of some of the nuclei in this work. The first- and second-order energy corrections are as follows.

$$\mathcal{H}_Q^1 = \frac{eQ}{4I(2I-1)\hbar}\frac{\sqrt{6}}{3}\left[3\hat{I}_z^2 - I(I+1)\right]V_0$$

2.62

$$\mathcal{H}_Q^2 = -\frac{1}{2\pi\nu_0}\left[\frac{eQ}{4I(2I-1)\hbar}\right]^2\left[2V_{-1}V_1\hat{I}_z\left(4I(I+1) - 8\hat{I}_z^2 - 1\right)\right.$$

$$\left. + 2V_{-2}V_2\hat{I}_z\left(2I(I+1) - 2\hat{I}_z^2 - 1\right)\right]$$

2.63
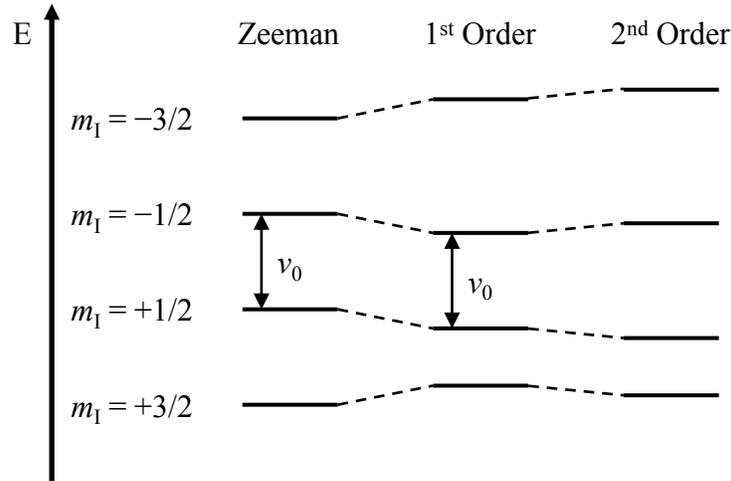
**Figure 2.10.** Energy levels of a spin-3/2 nucleus in a strong magnetic field. The $m_I = 1/2$ to $m_I = -1/2$ transition is affected by the second-order perturbative correction to the Zeeman energy. Note the perturbations to the Zeeman energy are not shown to scale.

The central transition is not affected by the first-order energy correction. The breadth of the central transition, $\Delta v_{CT}$, of the quadrupolar powder pattern is determined by the second-order correction to the energy (Figure 2.10),[31]

$$\Delta v_{CT} = \frac{(25 + 22\eta + \eta^2)}{144}\left(\frac{v_Q^2}{v_0}\right)[I(I+1) - 3/4] \qquad 2.64$$

where $\eta$ is the asymmetry parameter, and $v_Q$ is the quadrupolar frequency.

$$v_Q = \frac{3C_Q}{2I(2I-1)} \qquad 2.65$$

The central transition undergoes a second order quadrupolar shift, $v''_{CT}$,

$$v''_{CT} = \left(\frac{v_Q^2}{v_0}\right)\frac{[A\sin^4\beta - (2A+B)\sin^2\beta + 4\eta^2]}{144}[I(I+1) - 3/4] \qquad 2.66$$

31

where $\alpha$ and $\beta$ are angles describing the orientation of the applied magnetic field with respect to the principal axes of the EFG tensor, and $A$ and $B$ are as follows.

$$A = 9(3 - \eta \cos 2\alpha)^2 \hspace{4cm} 2.67$$

$$B = 12\eta^2 - 90 + 48\eta \cos 2\alpha - 18\eta^2 \cos^2 2\alpha \hspace{2cm} 2.68$$

Examples of quadrupolar powder NMR lineshapes are given in Figure 2.11.
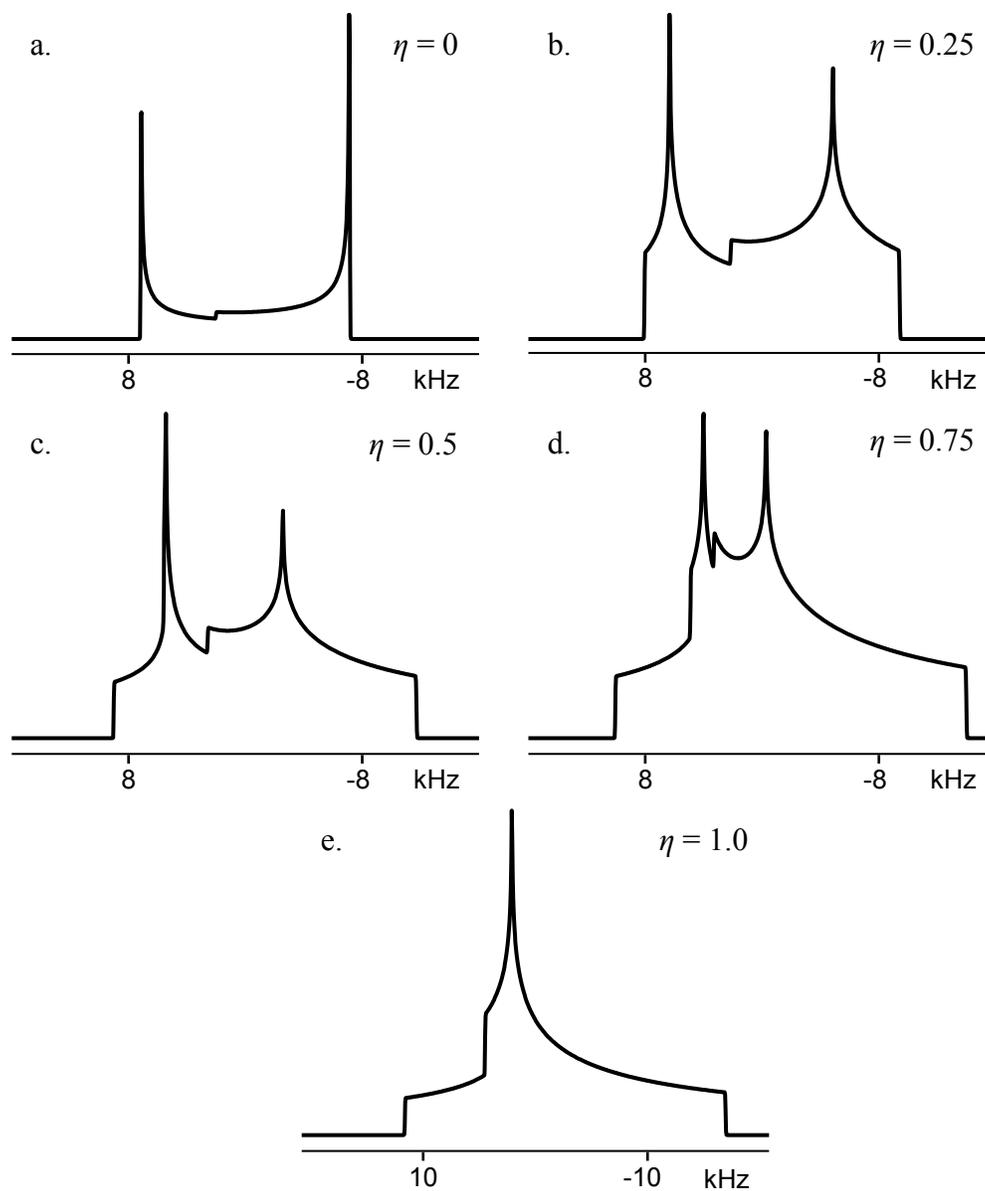
**Figure 2.11.** Solid-state NMR powder patterns of the central transition of a half-integer quadrupolar nucleus expected based on the 2$^{\text{nd}}$ order perturbation of the Zeeman energy. NMR parameters are as follows: $I = 3/2$, $C_Q = 3.0$ MHz, $\delta_{\text{iso}} = 25$ ppm, $v_0 = 80$ MHz, 50 Hz line broadening.

## 2.2.8 Exact Calculations for Large Quadrupolar Interactions

The key assumption in the high-field approximation is that the magnitudes of the internal NMR interactions are small compared to the magnitude of the Zeeman interaction. This is not always the case. In fact, it is common for some nuclei, such as $^{75}$As and $^{121/123}$Sb (featured heavily in this work) to have $\nu_Q$ values that are on the order of or exceed the Larmor frequency. In these cases, the full Zeeman-quadrupolar Hamiltonian must be considered. The elements of the Zeeman-quadrupolar matrix are[19]

$$zq_{IS} = \langle m_I | \mathcal{H}_{ZQ} | m_S \rangle \tag{2.69}$$

where $m_I$ and $m_S$ are the nuclear spin states. For a spin-3/2 nucleus such as $^{75}$As, the Zeeman-quadrupolar matrix is

$$\overline{\overline{ZQ}} = \begin{bmatrix} \langle +\frac{3}{2}|\mathcal{H}_{ZQ}|+\frac{3}{2}\rangle & \langle +\frac{3}{2}|\mathcal{H}_{ZQ}|+\frac{1}{2}\rangle & \langle +\frac{3}{2}|\mathcal{H}_{ZQ}|-\frac{1}{2}\rangle & \langle +\frac{3}{2}|\mathcal{H}_{ZQ}|-\frac{3}{2}\rangle \\ \langle +\frac{1}{2}|\mathcal{H}_{ZQ}|+\frac{3}{2}\rangle & \langle +\frac{1}{2}|\mathcal{H}_{ZQ}|+\frac{1}{2}\rangle & \langle +\frac{1}{2}|\mathcal{H}_{ZQ}|-\frac{1}{2}\rangle & \langle +\frac{1}{2}|\mathcal{H}_{ZQ}|-\frac{3}{2}\rangle \\ \langle -\frac{1}{2}|\mathcal{H}_{ZQ}|+\frac{3}{2}\rangle & \langle -\frac{1}{2}|\mathcal{H}_{ZQ}|+\frac{1}{2}\rangle & \langle -\frac{1}{2}|\mathcal{H}_{ZQ}|-\frac{1}{2}\rangle & \langle -\frac{1}{2}|\mathcal{H}_{ZQ}|-\frac{3}{2}\rangle \\ \langle -\frac{3}{2}|\mathcal{H}_{ZQ}|+\frac{3}{2}\rangle & \langle -\frac{3}{2}|\mathcal{H}_{ZQ}|+\frac{1}{2}\rangle & \langle -\frac{3}{2}|\mathcal{H}_{ZQ}|-\frac{1}{2}\rangle & \langle -\frac{3}{2}|\mathcal{H}_{ZQ}|-\frac{3}{2}\rangle \end{bmatrix} \tag{2.70}$$

where the zero-, single-, double-, and triple-quantum terms are as follows.

$$\langle m | \mathcal{H}_{ZQ} | m \rangle = -\nu_0 + \frac{\sqrt{6}C_Q}{12I(2I-1)}(3m^2 - I(I+1))V_0 \tag{2.71}$$

$$\langle m \pm 1 | \mathcal{H}_{ZQ} | m \rangle = \frac{\pm C_Q}{4I(2I-1)}\left[(2m \pm 1)\sqrt{I(I+1) - m(m \pm 1)}\right]V_{\mp 1} \tag{2.72}$$

$$\langle m \pm 2 | \mathcal{H}_{ZQ} | m \rangle = \frac{C_Q}{4I(2I-1)}\left[\sqrt{I(I+1) - m(m \pm 2)}\sqrt{I(I+1) - m(m \pm 1)}\right]V_{\mp 2} \tag{2.73}$$

$$\langle m \pm 3 | \mathcal{H}_{ZQ} | m \rangle = 0 \tag{2.74}$$

If the Zeeman states $|m_I\rangle$ are eigenfunctions of the Zeeman-quadrupolar Hamiltonian, a diagonal matrix would be obtained, with non-zero elements corresponding to the Zeeman-quadrupolar

eigenvalues. In order to obtain the eigenvalues of this Hamiltonian, as well as the Zeeman-quadrupolar eigenfunctions, $|n\rangle$, which are written as linear combinations of Zeeman states,

$$|n\rangle = \sum_{m=-I}^{I} (b_{mn} + ic_{mn})|m\rangle \qquad 2.75$$

where $b_{mn}$ and $c_{mn}$ are constants, the Zeeman-quadrupolar matrix must be diagonalized. Programs such as QUEST[19] carry out this procedure. After diagonalization, the diagonal ZQ tensor elements (eigenvalues) are used to simulate the NMR spectrum. When modelling other nuclear interactions such as dipolar or indirect spin-spin coupling, the Zeeman-quadrupolar eigenfunctions, $|n\rangle$, are used in place of the Zeeman states for the nucleus with the large quadrupolar interaction. The other NMR interactions are then treated as perturbations to the Zeeman-quadrupolar energy.

## 2.3 Nuclear Spin Relaxation

Spin-lattice relaxation requires a fluctuating field with a frequency approximately equal to the Larmor frequency. These fluctuating fields are provided by molecular motion modulating the instantaneous magnitude of the internal NMR interactions, which are orientation dependent. Spin-lattice ($T_1$) relaxation occurs when the system interacts with and loses energy to the "lattice," e.g., by the emission of a phonon. This type of relaxation is what restores the equilibrium magnetization in the $z$ ($B_0$) direction. Following an RF pulse, spin-spin ($T_2$) relaxation decreases magnetization in the $x$ and $y$ directions. Both $T_1$ and $T_2$ relaxation occur simultaneously, until the nuclear spin ensemble reaches equilibrium. In liquids, this process is described by the Bloch equations.[32] For $T_1$ relaxation,

$$\frac{dM_z}{dt} = \frac{-(M_z - M_0)}{T_1}$$

2.76

where $M_z$ is the magnetization in the $z$ direction, and $M_0$ is the magnitude of the net

magnetization at equilibrium. This equation is rewritten below.

$$M_z(t) = M_0 \left(1 - e^{-t/T_1}\right)$$

2.77

Spectroscopists typically recycle pulse sequences after anywhere from 1.5 to 5 $T_1$, depending on

experimental requirements.
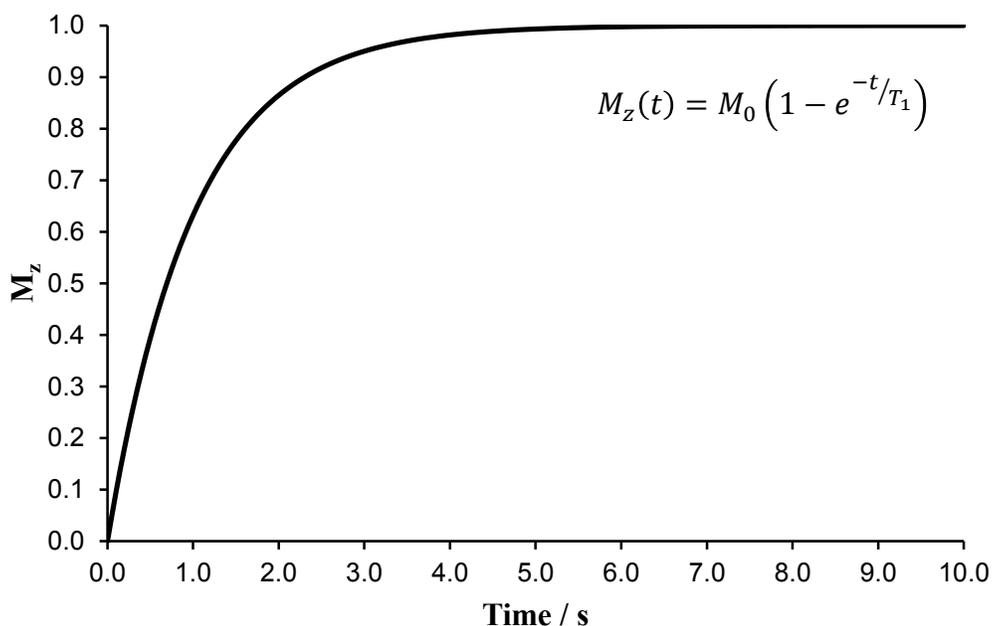


**Figure 2.12.** Spin-lattice relaxation of nuclei with $T_1 = 1.0$ s. After 5 $T_1$, $M_z = 0.993\ M_0$.

Note that nuclear relaxation in solids can be much more complicated, e.g., requiring multiple

exponential terms to accurately model. Magnetization decay in the $x$-$y$ plane due to spin-spin

relaxation is described by,[32]

$$\frac{dM_x}{dt} = \frac{-M_x}{T_2} \tag{2.78}$$

$$\frac{dM_y}{dt} = \frac{-M_y}{T_2} \tag{2.79}$$

where $M_x$ and $M_y$ are the magnetization in the $x$ and $y$ directions, respectively. The net

magnetization in the $x$-$y$ plane is described below.

$$M_{xy}(t) = M_0 e^{-t/T_2} \tag{2.80}$$

In an NMR experiment, $T_2$ determines the rate of decay in the FID.
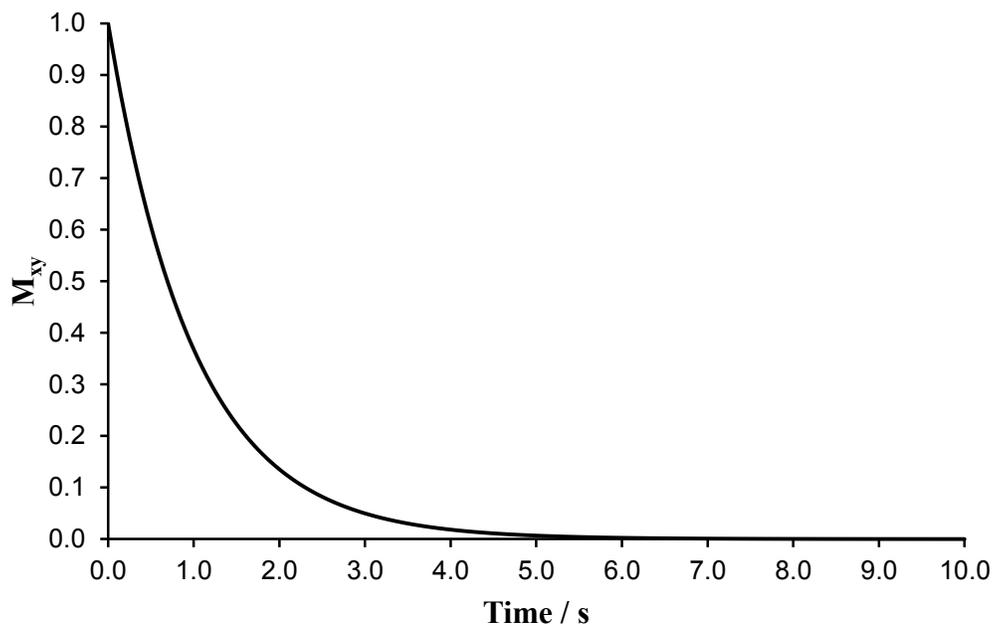


**Figure 2.13.** Spin-spin relaxation of nuclei with $T_2 = 1.0$ s.

In reality, magnetic field inhomogeneity over the sample volume also contributes to the

dephasing of nuclear spin magnetization in the $x$-$y$ plane, and the total decay rate of $M_{xy}$ is

represented by the time constant $T_2^*$.
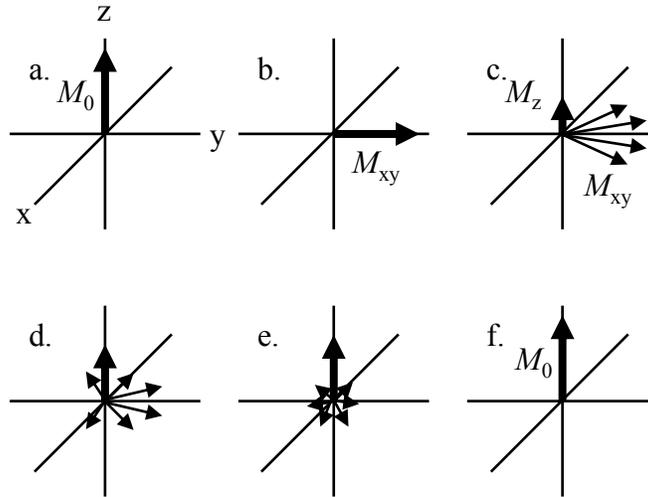
**Figure 2.14.** Vector diagram depicting simultaneous $T_1$ and $T_2$ relaxation. The system is at equilibrium (a) and is perturbed by a $90_x°$ pulse (b). After a period of time much less than 5 $T_1$, $M_z$ has begun to recover, whilst $M_{xy}$ begins to dephase (c). This continues over time (d) until $M_{xy}$ reaches zero (e). It is typical for $M_{xy}$ to reach zero before $M_z$ fully recovers. After a period of time greater than 5 $T_1$, $M_z$ has effectively reached equilibrium once more (f).

## 2.4 The Fourier Transform

A function is periodic if it meets the condition[33]

$$f(x + P) = f(x) \qquad 2.81$$

where $P$ is a constant equal to the function's period. The general form of a sinusoidal periodic function is

$$f(x) = A \sin(\omega x + \phi) \qquad 2.82$$

where $A$ is the amplitude of the waveform, $\omega$ is the angular frequency of the waveform, and $\phi$ is the initial phase. This function has a period of $2\pi/\omega$. The above equation is equivalent to

$$f(x) = A[a \sin(\omega x) + b \cos(\omega x)]$$

<div align="right">2.83</div>

where $a = \cos\phi$ and $b = \sin\phi$. Any periodic function can be represented by an infinite series of simpler sine and cosine functions, i.e., a Fourier series.[33] In NMR spectroscopy, each nucleus excited by the RF pulse(s) contributes to the observed time-domain signal (FID), resulting in an often complicated waveform that is not straightforward to analyze visually. The FID is treated as a Fourier series, and Fourier transformation is used to generate a frequency-domain spectrum which depicts all of the individual contributions to the FID. The Fourier transform and its inverse are written below.[34]

$$F(v) = \int_{-\infty}^{\infty} f(t)e^{-i2\pi vt} dt$$

<div align="right">2.84</div>

$$f(t) = \int_{-\infty}^{\infty} F(v)e^{i2\pi vt} dv$$

<div align="right">2.85</div>

In this equation, $f(t)$ is a function in the time domain, and $F(v)$ is a function in the frequency domain. If we recall Euler's formula,

$$e^{i2\pi vt} = \cos(2\pi vt) + i\sin(2\pi vt)$$

<div align="right">2.86</div>

it becomes clear that if $f(t)$ is real, $F(v)$ consists of both a real and an imaginary component.

$$Re[F(v)] = \int_{-\infty}^{\infty} f(t)\cos(2\pi vt)\, dt$$

<div align="right">2.87</div>

$$Im[F(v)] = \int_{-\infty}^{\infty} f(t)\sin(2\pi vt)\, dt$$

<div align="right">2.88</div>

In NMR spectroscopy, the real data set is referred to as "absorptive," and the imaginary data set is referred to as "dispersive." These two data sets differ in phase by 90 degrees. Note that for experimental NMR data sets, the collected data is digital, and a discrete Fourier transform is carried out via the fast Fourier transform (FFT) algorithm. There are many relationships

between time-domain and frequency-domain variables that are of importance in NMR spectroscopy, e.g., the inverse relationships between data sampling intervals (dwell time) and spectral width, acquisition time and digital resolution, and RF pulse length and excitation bandwidth in the frequency domain.

## 2.5 Experimental NMR Techniques

### 2.5.1 Magic Angle Spinning (MAS)

Rapid rotation of solid NMR samples about an axis 54.74° from the applied magnetic field direction removes or modulates NMR line shapes caused by the orientation dependence of internal NMR interactions.  MAS can be used to simplify NMR spectra, improve signal-to-noise ratio, and, in some cases, results in NMR spectra that mimic those of compounds in solution. This phenomenon arises because the values of internal NMR interaction constants (e.g., $\sigma_{zz}$) have $(3 \cos^2 \theta - 1)$ dependence on the angle between the axes of $\bar{\bar{A}}^{\mathrm{PAS}}$ and the applied magnetic field; at an angle of 54.74°, this expression is equal to zero.  Note that the angle $\theta$, defined as the angle between relevant principal axes and $B_0$, does not refer to the same angle as that between the rotor and the applied magnetic field ($\beta$), but that these two angles are related by the equation below.[35]

$$\langle \tfrac{1}{2}(3 \cos^2 \theta - 1)\rangle = \tfrac{1}{2}(3 \cos^2 \beta - 1) \times \tfrac{1}{2}(3 \cos^2 \Theta - 1) \qquad 2.89$$

Here, $\Theta$ is the angle between the principal axis direction and the axis of sample rotation.  If the sample rotation frequency exceeds the spectral breadth, the resulting MAS NMR spectrum mimics the NMR spectrum of a compound in solution, whereas slower spinning frequencies result in an isotropic peak flanked by spinning side bands separated by the rotor frequency.[36] Thus this technique is typically the most useful when the total NMR spectral breadth is smaller

in magnitude than the available MAS rotor frequencies.  Note that the orientation-dependent splitting described by the $2^{nd}$-order term for the quadrupolar interaction is not completely removed by MAS, but instead reduced in breadth by approximately 1/3.

### 2.5.2 Spin Echo

The spin echo pulse sequence[37] begins with a rectangular 90° pulse along the x-axis followed by a short time delay, $\tau_1$.  Following this period, a 180° pulse is applied (along either the x- or y-axis). The 180° pulse inverts the magnetization which has dephased in the x-y plane. After another delay $\tau_2$, the spins re-phase in the x-y plane, either along the –y-axis or the +y-axis, depending on the direction of the 180 degree pulse.
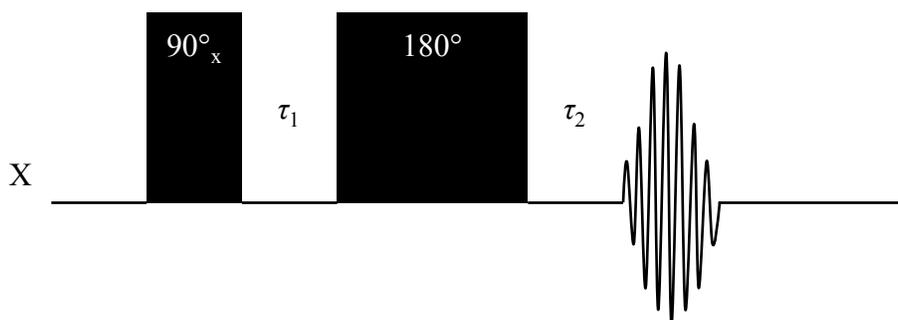


**Figure 2.15.** The spin echo pulse sequence.

### 2.5.3 QCPMG

The quadrupolar Carr-Purcell Meiboom-Gill (QCPMG) pulse sequence[38-40] is a method of obtaining NMR spectra with enhanced signal-to-noise ratio.  In essence, it is a "train" of spin echoes, where x-y magnetization is refocused periodically a set number of times.  Consequently, the frequency-domain consists of a series of spikelets mimicking the stationary powder NMR spectrum.  The overall decay of the echo manifold in the time-domain is determined by the $T_2$

relaxation constant. The signal-to-noise enhancement is especially important for the acquisition of wideline NMR powder patterns where the signal is spread out over a broad frequency range.
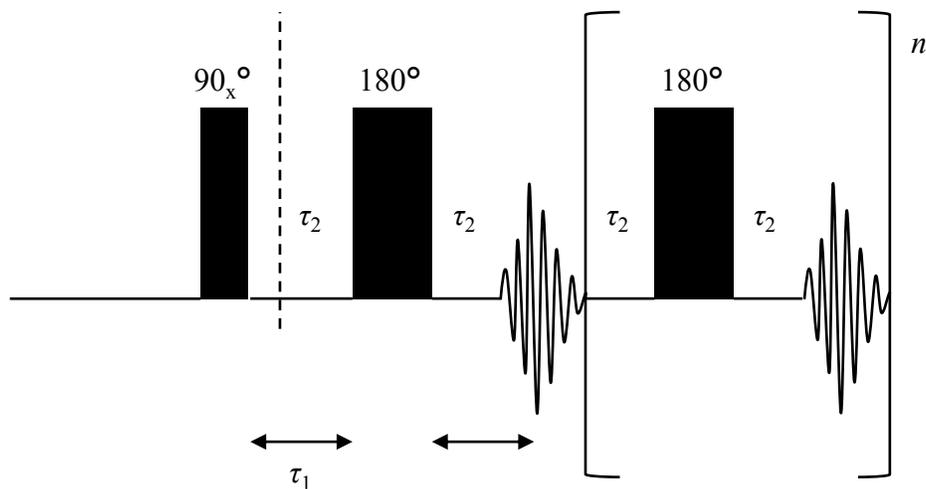


**Figure 2.16.** The QCPMG pulse sequence.

### 2.5.4 WURST

WURST (wideband, uniform rate, and smooth truncation) pulses were introduced by Kupče and Freeman in 1995[41] for the purpose of the adiabatic inversion of nuclear spin magnetization, and were later applied to the acquisition of broadband NMR spectra of quadrupolar nuclei using a spin-echo-like pulse sequence (WURST echo) by Bhattacharyya and Frydman.[42] WURST pulses consist of a sausage-shaped pulse amplitude profile in the time domain and are quadratic in phase.[43] The effective frequency of a WURST pulse varies linearly in time over the frequency range $\Delta$, often ca. 1 to 2 MHz in the experiments documented in this thesis. The WURST pulse is generated using the equations

$$\omega_1(t) = \omega_{\text{max}}\left(1 - \left|\cos\left(\frac{\pi t}{\tau_w}\right)\right|^N\right) \tag{2.90}$$

$$\phi(t) = \pm \left\{ \left( \nu_{\text{off}} + \frac{\Delta}{2} \right) t - \left( \frac{\Delta}{2\tau_w} \right) t^2 \right\} \qquad 2.91$$

where $\omega_1(t)$ is the pulse amplitude in the time domain, $\omega_{\text{max}}$ is the maximum pulse amplitude, $\tau_w$ is the pulse duration, $\phi(t)$ is the pulse phase, $\nu_{\text{off}}$ is the centre frequency of the sweep, and $\Delta$ is the total sweep range in Hz.

In the adiabatic regime, the net magnetization is spin-locked to the effective magnetic field, $\bar{B}_{\text{eff}}$, as it traverses from the +z to -z axis, thus inverting the net magnetization over a broad frequency range. A WURST pulse which meets the condition[43]

$$\left| \frac{d\theta}{dt} \right| < |\gamma \bar{B}_{\text{eff}}| \qquad 2.92$$

is considered to fall in the adiabatic regime. Here, $\theta$ is the angle between $\bar{B}_{\text{eff}}$ and the laboratory *x*-axis in the accelerating rotating frame of reference.[43] In the non-adiabatic regime, isochromats are excited in a linear sequence from the initial to the final pulse frequency, as though successive $\pi/2$ pulses of linearly varying frequencies were applied. In essence, in the non-adiabatic regime, a WURST pulse is used as a chirp pulse.[44] A WURST-echo is comprised of two WURST pulses separated by a time delay, analogous to the quadrupolar echo pulse sequence (Figure 2.17).
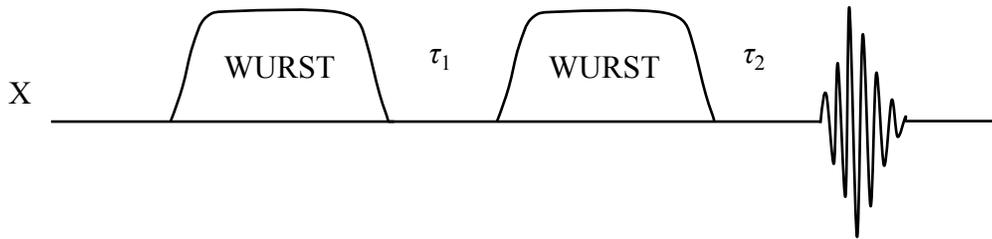


**Figure 2.17.** The WURST echo pulse sequence.

### 2.5.5 WURST-QCPMG

The WURST-QCPMG pulse sequence was first reported by Luke O'Dell in 2008.[45,46] It features a WURST pulse repeated in a CPMG-like echo train. This pulse sequence provides broadband excitation analogous to a WURST pulse, whilst also offering the improvements to signal-to-noise ratio available via QCPMG experiments. The intensity of the frequency-domain NMR spectrum, like in a QCPMG experiment, is distributed into spikelets whose frequency separation is inversely proportional to the time between echoes.

### 2.5.6 Acquiring Ultrawideline NMR Spectra

Many of the NMR spectra in this thesis feature central transition line breadths on the order of MHz. The breadth of these NMR spectra exceed available pulse excitation bandwidths and digitization rates (i.e., dwell times necessary to meet Nyquist criteria).[34] Thus the technique of frequency stepping[47-49] is used to acquire the NMR spectra. Frequency stepping involves systematically moving the transmitter offset frequency over the frequency range of the NMR spectrum to acquire the entire spectrum in separate pieces. The intervals between transmitter offset frequencies are determined primarily by the pulse excitation bandwidth. It is desirable for the overall collection of pulses to exhibit a flat excitation profile over the entire NMR spectrum. In QCPMG-like pulse sequences, transmitter offset steps should be integer multiples of the spikelet spacing, thus when multiple pieces of the total NMR spectrum are displayed simultaneously, the spikelets overlap and, if added together (vide infra), increase the signal-to-noise ratio in the final NMR spectrum.

Nuclear relaxation can lead to difficulties in acquiring broadband NMR spectra. Some of the $^{87}$Sr NMR spectra featured in Chapter 6 were acquired at a single transmitter offset frequency using a broadband, frequency-swept pulse (i.e., WURST or WURST-QCPMG). In these cases, NMR spectra were often distorted (i.e., spectral intensity was more intense on one side of the NMR powder pattern). Distortions in NMR powder patterns are possibly due to nuclear relaxation occurring over the duration of the frequency-swept pulse, though other factors such as $T_2$ anisotropy may also contribute to spectral distortions. In these cases, NMR spectra acquired with multi-directional sweeps (both low-to-high and high-to-low frequency) were added together to reduce distortions.

### 2.5.7 Assembling Ultrawideline NMR Spectra

The two techniques used in this thesis to assemble frequency-stepped NMR spectra are the skyline projection technique[50] and a simple co-added sum. The skyline projection technique involves overlaying the partial NMR spectra and taking the most intense points to define the line shape of the final NMR spectrum. This is analogous to how the shadow of a cityscape mimics the maximum "intensity" (or height) of the buildings. To construct a co-added sum, the partial NMR spectra are added together to produce the final spectrum (i.e., the final signal intensity at a given frequency is a sum of all signal intensities recorded at that resonance frequency). This can be advantageous as it leads to an increase in signal-to-noise ratio, but can sometimes lead to less-well-defined spectral features and/or spectral distortions.

### 2.5.8 Computational Methods

### 2.5.8.1 Amsterdam Density Functional (ADF)

Amsterdam Density Functional[51-53] is a DFT-based program for calculating molecular properties. In this thesis, the ADF program package is used to perform calculations on isolated ("gas phase") molecules, though it is noted that the ADF modelling suite includes methods for dealing with periodic solids (BAND). BAND was not used in this research, as use of the CASTEP code (*vide infra*) is more established in the solid-state NMR literature. Unless otherwise noted, calculations of NMR properties carried out with ADF feature relativistic corrections using the zeroth-order regular approximation (ZORA) to the Dirac equation, including effects from spin-orbit coupling. The inclusion of relativistic effects is important for the computation of both EFG and magnetic shielding parameters. All electrons are correlated in these calculations. The majority of the ADF calculations carried out in this research use the ZORA/QZ4P basis set, a basis set composed of Slater-type orbitals tailored for relativistic calculations. The GGA functional BP86 is used to describe the exchange-correlation energy. Example input files for ADF calculations are included in Appendix A.


### 2.5.8.2 Cambridge Serial Total Energy Package (CASTEP)

CASTEP[54-57] is a DFT-based program used to perform first-principles calculations of molecular and crystallographic properties. The version of CASTEP used in this thesis calculates molecular/crystallographic properties in the non-relativistic limit. CASTEP simulates the periodic nature of crystalline solids by the use of plane-wave basis sets and periodic boundary conditions. Pseudopotentials are used to approximate the potential arising from the atomic nuclei and core electrons. Ultrasoft pseudopotentials describing core-valence interactions are

calculated on-the-fly, and the PBE functional in the generalized gradient approximation[58,59] is used to describe the exchange-correlation energy. The basis set size is specified by setting a maximum cutoff energy; plane waves with this and lower energy are used to construct the total basis set. The cutoff energy thus depends on the desired accuracy of the calculation as well as the size of the crystallographic unit cell. The Materials Studio 4.4 environment was used to generate input files for CASTEP calculations.

# Chapter 3

## Assessing Distortion of the $AF_6^-$ (A = As, Sb) Octahedra in Solid Hexafluorometallates(V) via NMR Spectroscopy

### 3.1 Introduction

Naturally occurring NMR-active isotopes of arsenic and antimony include $^{75}$As, $^{121}$Sb, and $^{123}$Sb. These nuclei are quadrupolar, with $I$ = 3/2, 5/2, and 7/2, respectively.[60] The NMR properties of these nuclei are for the most part favorable; all three nuclei have moderate to high natural abundance and moderate magnetogyric ratios. The large nuclear quadrupole moments of these nuclei,[60,61] $Q(^{75}$As$)$ = 30.0 ± 5.0 fm$^2$, $Q(^{121}$Sb$)$ = −54.3 ± 1.1 fm$^2$, and $Q(^{123}$Sb$)$ = −69.2 ± 1.4 fm$^2$, result in the nuclear quadrupolar coupling constant, $C_Q$, being highly sensitive to structural changes at the arsenic or antimony crystal sites.[62] It is therefore possible to use experimental arsenic and antimony quadrupolar parameters as a probe of crystal symmetry. Note that the large quadrupole moments of these nuclei can also present challenges to the NMR spectroscopist; $C_Q$ values and hence the breadth of the NMR powder pattern can be very large for nuclei at sites with large local electric field gradient, e.g., for antimony or arsenic atoms which occupy crystallographic positions with low point-group symmetry.

Quadrupolar parameters are of particular use in monitoring changes in the symmetry at specific nuclear sites of solids that undergo phase transitions. Abrupt changes in these

parameters upon changes in temperature are a clear indicator that the phase transition has occurred, as the magnitude of $C_Q$ and the quadrupolar asymmetry parameter, $\eta_Q$, in each phase can be indicative of the point group symmetry about a particular crystallographic site, in this case a site occupied by either an arsenic or antimony atom. Both the hexafluoroarsenate(V) and hexafluoroantimonate(V) anions have played a significant role in pioneering work in the field of nuclear magnetic resonance, and both of these ions were among the first compounds to be studied via $^{75}$As, $^{121}$Sb, and $^{123}$Sb NMR spectroscopy (vide infra). In view of this historic importance, we have measured the arsenic-75 (natural abundance = 100%), antimony-121 (natural abundance = 57.2%), and antimony-123 (natural abundance = 42.8%) NMR spectra of solid polycrystalline samples of $KAsF_6$ and $KSbF_6$ at several temperatures. Both solids undergo phase transitions above room temperature, and the high-resolution spectra presented here show that the antimony nucleus in both the cubic and tetragonal phases experiences a nonzero electric field gradient (EFG). Furthermore, our measurements of the cubic phase of $KSbF_6$ highlight the advantages of studying many non-integer spin quadrupolar nuclei at the highest possible magnetic field strengths. This work is a fitting contribution to the recent special issue of the *Canadian Journal of Chemistry* dedicated to Dr. J.A. Ripmeester, who studied related systems early in his career.[63]


## 3.2 Background

NMR studies involving arsenic and antimony have been few and far between, in part owing to the large nuclear quadrupole moments of these nuclides. The first accurate determination of the $^{75}$As nuclear magnetic moment via an NMR experiment was published in 1951 by Dharmatti and Weaver,[64] and again in a more comprehensive study in 1953.[65] Here the

$^{75}$As NMR resonance frequency in an aqueous solution of 2 mol/L $Na_2HAsO_4$ and 2 mol/L

NaOH (i.e., to observe the $AsO_4^{3-}$ anion) was observed, and the magnetic moment of $^{75}$As was

determined to be +1.4347(3) nuclear magnetons ($\mu_N$).  A similar value, +1.4350(3) $\mu_N$, was

obtained by Jeffries and Loeliger in 1952.[66]  These values are close to the currently accepted

value of +1.43948(7) $\mu_N$.[60]  The $^{121}$Sb and $^{123}$Sb nuclear magnetic moments were determined via

NMR spectroscopy by Proctor and Yu and reported in 1951.[67]  Experiments were performed on

an aqueous solution of $NaSbF_6$, and values for the $^{121}$Sb and $^{123}$Sb nuclear magnetic moments

were reported to be +3.3427(6) and +2.5341(4) $\mu_N$, respectively.  The currently accepted values

are +3.3634(3) and +2.5498(2) $\mu_N$ for $^{121}$Sb and $^{123}$Sb, respectively.[60]

Despite these three nuclides receiving relatively little attention from the NMR

spectroscopy community on the whole, the hexafluoroarsenate(V) and hexafluoroantimonate(V)

anions have an important place in the history of NMR spectroscopy.  $KAsF_6$ was one of the first

compounds to be studied in the solution phase using Fourier transform $^{75}$As NMR

spectroscopy.[68]  These early experiments were performed by Balimann and Pregosin on a series

of tetrahedral arsenic salts in solution, at which time aqueous $K^+AsF_6^-$ was chosen as the

reference compound for the $^{75}$As chemical shift scale.  Previous to this, $^{19}$F NMR measurements

shed light on the indirect spin-spin coupling and relaxation behavior of the $^{75}$As nucleus in the

hexafluoroarsenate ion.  Arnold and Packer[69,70] studied the $^{75}$As spin-lattice relaxation time of

the hexafluoroarsenate ion via $^{19}$F NMR spectroscopy in nonaqueous solutions and reported

$^1J(^{75}As,^{19}F)$ = 933 Hz.  Andrew, Farnell, and Gledhill reported $^1J(^{75}As,^{19}F)$ to be 905 Hz in solid

$KAsF_6$, determined via $^{19}$F MAS NMR spectroscopy.[71]  This 1967 study was the first publication

to report the observation of resolved splittings due to indirect spin-spin coupling constants in

solids.  Spectra were acquired at a field strength of 0.6 T and a magic angle spinning (MAS)

frequency of 5.5 kHz. The $AsF_6^-$ ion received more attention recently in a comprehensive multinuclear magnetic resonance and powder X-ray diffraction study of the phase transition in solid $NaAsF_6$.[72]

The hexafluoroantimonate(V) ion was the first species reported to exhibit splittings that could be attributed to indirect spin-spin coupling, or $J$-coupling in solution. In their efforts to measure magnetic moments of various NMR-active nuclei, Proctor and Yu[67] noticed that the antimony-121 resonance of the $SbF_6^-$ anion, measured in solution, consisted of five lines, each separated by 1.90 G. This structure was initially attributed to direct magnetic dipole interactions between the antimony and the surrounding fluorine nuclei. This initial interpretation was supported by Andrew[73] who predicted that the $^{121}Sb$ NMR spectrum should consist of nine lines; however in 1952, Dharmatti and Weaver[74] showed that the antimony resonance of $SbF_6^-$ in fact consisted of seven equally spaced peaks with relative intensity 1:6:15:20:15:6:1. On the basis of earlier work by the research groups of Gutowsky,[75-77] Hahn,[78] and of Ramsey and Purcell,[79] Dharmatti and Weaver concluded that the spin-spin coupling must take place via the intervening electrons – a so-called indirect spin-spin coupling mechanism. Andrew and co-workers[71] resolved splittings from $J(^{121}Sb,^{19}F)$ and $J(^{123}Sb,^{19}F)$ in $^{19}F$ NMR spectra of solid potassium hexafluoroantimonate(V), which, along with their measurement of $^1J(^{75}As,^{19}F)$ discussed above, marked the first reported measurement of indirect spin-spin couplings in solid materials. The value of $J(^{121}Sb,^{19}F)$ was found to be 1820 Hz, somewhat smaller than the value of 1945 Hz reported in solution NMR studies.[80,81] In a follow-up study, Andrew and co-workers[82] found that by spinning the solid sample at 7 kHz, the spectral resolution could be improved sufficiently to permit direct $^{19}F$ NMR measurement of both $^1J(^{121}Sb,^{19}F)$ and $^1J(^{123}Sb,^{19}F)$. The values obtained were $1914 \pm 20$ Hz and $1018 \pm 10$ Hz, respectively. In 1987, Kozlova, Kriger, and Goncharuk

investigated the phase transition in $KSbF_6$ via variable temperature $^{19}F$ and $^{121}Sb$ NMR spectroscopy.[83]  Fluorine-19 relaxation data presented in their study shed light on the reorientation behavior of the $SbF_6^-$ octahedra.  $C_Q(^{121}Sb)$ values were determined at several temperatures between 120 and 360 K, however $^{121}Sb$ NMR spectra were acquired on a continuous wave NMR spectrometer, the spectra were not shown, and the precision of individual experimental $C_Q(^{121}Sb)$ values was not mentioned.

## 3.3 Crystal Structure and Dynamics

### 3.3.1 KAsF$_6$

Potassium hexafluoroarsenate(V) exists in two stable crystalline solid phases at atmospheric pressure, a rhombohedral phase (II) at lower temperature and a cubic phase (I) at higher temperature,[84] with the phase transition occurring at around 375 K.[85]  Differential thermal analysis (DTA) shows that the phase transition occurs at 378 K when heated and at 372 K when cooled.  The space group of the room temperature phase was originally reported to be either $R\bar{3}$ (No. 148) or $R\bar{3}m$ (No. 166),[86,87] though was later confirmed to be $R\bar{3}$.[85,88,89]  In this phase, the arsenic atoms are surrounded by six fluorine atoms at a nearly octahedral site that possesses $C_3$ point-group symmetry.  According to the most recently determined structure,[89] the As–F bond distance is 1.712 Å.  The space group of the high temperature phase is $Fm\bar{3}m$, wherein the arsenic atoms occupy a site of octahedral point-group symmetry.[85]  This phase change is accompanied by an increase in cell volume, which at the transition temperature is 116.06 Å$^3$ in the rhombohedral phase and 129.88 Å$^3$ in the cubic phase.[85]  The reorientation behavior of the As anions in $KAsF_6$ was studied by Niemelä in 1973.[90]  Data in that work show greater hysteresis than do the DTA data mentioned above, with the phase transitions taking place at

391.7 and 362.8 K upon heating and cooling, respectively. The $^{19}$F $T_1$ data exhibit a discontinuity at the phase-transition temperature. Fluorine-19 $T_1$ relaxation times in the high temperature phase of KAsF$_6$ decreased with increasing temperature, indicative of the spin-rotation relaxation mechanism dominating due to rapid isotropic rotational reorientation of the As octahedra. Using the $^{19}$F $T_1$ data of Niemelä in the low temperature phase,[90] the rotational correlation time, $\tau_c$, of this reorientational motion is calculated to be $3.7 \times 10^{-7}$, $4.9 \times 10^{-8}$, and $1.2 \times 10^{-8}$ s at 293, 323, and 348 K, respectively. Relaxation behavior in the related hexafluoride salt IF$_6$AsF$_6$ has been studied via variable temperature solid-state $^{19}$F NMR spectroscopy by Albert and Ripmeester.[63] These data show similar trends, with $T_1(^{19}\text{F})$ in the high temperature phase being essentially independent of temperature.


### 3.3.2 KSbF$_6$

Potassium hexafluoroantimonate(V) occurs in two stable crystalline forms at ambient pressure, a tetragonal form stable above 301 K (phase I) and a cubic form stable below 301 K (phase II).[84] This is particularly interesting, as it is rare for a crystal to exhibit cubic symmetry in a lower temperature phase.[91] DTA has shown that the cubic-to-tetragonal phase transition occurs at 301 K, while the tetragonal-to-cubic phase transition occurs at 277 K.[92] The cubic phase belongs to space group $I2_13$ (No. 199),[92-94] wherein the antimony atoms lie at a site with $C_3$ point-group symmetry, though the available X-ray crystallography data are refined in space group $Ia\overline{3}$ (No. 206).[95] Note that although KSbF$_6$ belongs to a cubic space group, the antimony atoms do not occupy an octahedral lattice position. The Sb ions, according to X-ray crystallographic data,[95] are distorted octahedra with F-Sb-F bond angles between 84.5° and 95.2°. The tetragonal higher temperature phase belongs to space group $P\overline{4}2m$ (No. 111),[96]

wherein the antimony atoms lie at a distorted octahedral site with $C_{2v}$ symmetry.[94] It was

proposed in 1975 that reorientation of the Sb ions caused nuclear spin-lattice relaxation in

$NaSbF_6$ and $KSbF_6$.[97] Based on that work, the rotational correlation times for reorientation of

the Sb octahedra are $1.6 \times 10^{-8}$, $5.9 \times 10^{-11}$, and $3.5 \times 10^{-11}$ s at 293 (low temperature phase),

308, and 348 K, respectively. Early $^{19}$F NMR investigations of solid $KSbF_6$ indicated that at

temperatures above 260 K, the Sb octahedra reorientate "isotropically."[93] Based on $^{19}$F NMR

relaxation data, Kozlova et al. later suggested that the reorientation may be strongly anisotropic

and involved motion about either the $C_3$ or $C_4$ axes of the Sb ion.[83] On the basis of a more recent

infrared study, Heyns and co-workers[94] have suggested that the reorientation of the anions is

more complex.


## 3.4 Experimental Section

$KAsF_6$ and $KSbF_6$ were obtained commercially and used without further purification.

NMR experiments were performed at $B_0 = 21.14$ T on a Bruker Avance II NMR spectrometer at

the Canadian National Ultrahigh-Field NMR Facility for Solids in Ottawa, Ontario[2] on phase II

of $KAsF_6$ and phases I and II of $KSbF_6$. Note that a solids probe, both operational above the

$KAsF_6$ phase transition temperature and capable of $^{19}$F decoupling, was not available at $B_0 =$

21.14 T. The sample spinning frequency was 15 kHz using a 2.5 mm double resonance Bruker

MAS probe. Arsenic-75 NMR spectra were recorded at a resonance frequency of 154.1 MHz,

using a 1 μs RF pulse ($\pi/2$ solid pulse) and a 1 s relaxation delay using single pulse acquisition.

For each $^{75}$As NMR spectrum with $^{19}$F decoupling, 256 transients were acquired, and 1024

transients were acquired for spectra without $^{19}$F decoupling. Arsenic-75 NMR spectra were

referenced to 0.5 mol/L $KAsF_6$ in MeCN at $\delta_{iso} = 0.0$ ppm. Antimony-121 NMR spectra were

recorded at a resonance frequency of 215.5 MHz, using a 1 μs RF pulse (π/2 solid pulse) and a 1 s relaxation delay. For each $^{121}$Sb spectrum with $^{19}$F decoupling, 256 transients were acquired, and 1024 transients were acquired for spectra without $^{19}$F decoupling. Antimony-123 NMR spectra were recorded at a resonance frequency of 116.7 MHz, using a 1 μs RF pulse (π/2 solid pulse) and a 1 s relaxation delay. For each $^{123}$Sb spectrum with $^{19}$F decoupling, 1024 transients were acquired, and 4096 transients were acquired for spectra without $^{19}$F decoupling. Antimony NMR spectra were referenced to 0.5 mol/L KSbF$_6$ in MeCN at $\delta_{iso}$ = 0.0 ppm. Fluorine-19 NMR spectra were recorded at a resonance frequency of 847.0 MHz, using a 2 μs RF pulse (π/4) and a 5 s relaxation delay. For each $^{19}$F spectrum, 32 transients were acquired. Fluorine-19 NMR spectra were referenced to external CF$_3$COOH at $\delta_{iso}$ = 0.0 ppm. Broadband $^{19}$F decoupling in $^{75}$As, $^{121}$Sb, and $^{123}$Sb NMR experiments was applied using 50 kHz decoupling power. The sample temperature was controlled with a Bruker BVT 3000 temperature control unit. The actual sample temperature under MAS conditions was calibrated using a $^{207}$Pb signal in Pb(NO$_3$)$_2$[98] with estimated accuracy of ±2 K. Spectral simulations were performed using the WSolids1[99] and the DMFit programs.[100] Arsenic-75 NMR spectra of phase I of KAsF$_6$ were acquired at $B_0$ = 9.39 T on an Agilent/Varian Inova 400 MHz spectrometer running VNMRJ 4.2A with a double-channel broadband switchable probe designed for experiments on solutions. The $^{75}$As resonance frequency was 68.5 MHz. The solid sample was packed in a 5 mm o.d. glass tube and remained stationary for all experiments at this magnetic field strength, as magic angle spinning was not available. A 0.5 s recycle delay was used, and 76 transients were acquired. Fluorine-19 decoupling was applied using a WURST-40 pulse and a maximum decoupling frequency of 2.84 kHz. Decoupling schemes typically used in experiments on solid samples were unavailable due to the pulse width and maximum power limitations of the probe. A $^{19}$F

NMR spectrum of $KAsF_6$ was obtained in phase I, which consisted of 8 transients that were acquired with a recycle delay of 2 s at a resonance frequency of 376.3 MHz. The sample temperature for experiments performed at 9.39 T was controlled with a Highland Technology Model L900 NMR temperature controller. The actual sample temperature was determined via the chemical shift difference between the methylene and hydroxyl protons in a sample of neat ethylene glycol, with an estimated accuracy of ±1 K.

EFG and CS tensor parameters were calculated using the CASTEP[54-57] program (Materials Studio 4.4). Atom positions in the unit cell for phases I and II of $KSbF_6$ and phase II of $KAsF_6$ were calculated using geometry optimizations in which the initial atomic coordinates were at the experimental geometry.[89,95,96] The geometry optimization of atom positions was necessary due to significant residual forces on the fluorine atoms caused by short As–F and Sb–F bond lengths in the experimental crystal structures. During the geometry optimization, the unit cell dimensions were kept constant. Since a crystal structure was not available for phase I of $KAsF_6$, unit cell parameters determined through X-ray powder diffraction experiments[92] along with atom positions in reported isostructural cubic $NaSbF_6$[101] were used to create an initial structure for $KAsF_6$. Final atom positions in this unit cell were determined via a geometry optimization. NMR parameter calculations for $KAsF_6$ in phase II and $KSbF_6$ in phase I were performed with a plane wave basis set cutoff energy of 550 eV using a fine accuracy basis set, and calculations of parameters in $KSbF_6$ in phase II used a cutoff energy of 500 eV with a medium accuracy basis set. Calculations were carried out using "on-the-fly" pseudopotentials, and the generalized gradient approximation (GGA) was used with the Perdew, Burke, and Ernzerhof (PBE) functionals to calculate the exchange correlation energy.[58,59]

## 3.5 Results and Discussion

Experimental $^{75}$As, $^{121}$Sb, and $^{123}$Sb NMR data are summarized in Tables 3.1 and 3.2. Results of CASTEP calculations are summarized in Table 3.3. Experimental and simulated $^{75}$As NMR spectra of phase II of $KAsF_6$ are shown in Figure 3.1, and $^{121/123}$Sb NMR spectra are shown in Figures 3.2 and 3.3. Fluorine-19 NMR spectra of $KSbF_6$ are shown in Figure 3.4. Arsenic-75 NMR spectra of phase I of $KAsF_6$ are shown in Figure 3.5. At high field, $^{121/123}$Sb NMR spectra were obtained for $KSbF_6$ in both phases I and II, whilst $^{75}$As NMR data were acquired at several temperatures for phase II of $KAsF_6$. High temperature NMR data for $KAsF_6$, i.e., above the phase transition at 375 K, were not obtained at $B_0 = 21.14$ T due to hardware limitations. High temperature $^{75}$As NMR nutation data for phase I of a stationary sample of powdered $KAsF_6$ were acquired at $386 \pm 1$ K on a 9.39 T NMR spectrometer. The $^{19}$F NMR spectrum acquired for phase I of $KAsF_6$ consisted of a single broad resonance similar to that reported by Gabuda et al.[102] and is not shown.

**Table 3.1.** NMR parameters determined for $KAsF_6$ at 21.14 T.

| | 0.5M $KAsF_6$/MeCN | Phase II 293 K | Phase II 323 K | Phase II 348 K | Phase I 386 K |
|---|---|---|---|---|---|
| $\delta(^{19}F)$ / ppm[a] | $12.60 \pm 0.05$ | $12.70 \pm 0.30$ | $12.70 \pm 0.05$ | $13.00 \pm 0.05$ | - |
| $^1J(^{75}As,^{19}F)$ / Hz[b] | $-930 \pm 5$ | $-926 \pm 10$ | $-926 \pm 3$ | $-926 \pm 3$ | - |
| $^1K(As,F)$ / $10^{20}$ N A$^{-2}$ m$^{-3}$ | $-47.9 \pm 0.1$ | $-47.7 \pm 0.1$ | $-47.7 \pm 0.1$ | $-47.7 \pm 0.1$ | - |
| $\delta(^{75}As)$ / ppm | $0.0^c$ | $-3.5 \pm 0.1$ | $-3.2 \pm 0.1$ | $-3.1 \pm 0.1$ | $-2.5 \pm 1$ |
| $C_Q(^{75}As)$ / MHz[b] | - | $-2.87 \pm 0.05$ | $-2.58 \pm 0.05$ | $-2.30 \pm 0.05$ | 0.0 |
| $\eta(^{75}As)$ | - | 0.00 - 0.05 | 0.00 - 0.05 | 0.00 - 0.05 | - |

[a] Referenced to external $CF_3COOH$.

[b] Signs of $^1J(^{75}As,^{19}F)$ and $C_Q(^{75}As)$ values were determined from DFT calculations (see text).

[c] Used as a chemical shift reference.

**Table 3.2.** NMR parameters determined for $KSbF_6$ at 21.14 T.

| | 0.5M $KSbF_6$/MeCN | Phase II 293 K | Phase I 308 K | Phase I 343 K |
|---|---|---|---|---|
| $\delta(^{19}F)$ / ppm[a] | $-45.35 \pm 0.05$ | $-47.05 \pm 0.03$ | $-46.86 \pm 0.03$ | $-46.07 \pm 0.03$ |
| $^1J(^{121}Sb,^{19}F)$ / Hz[b] | $-1929 \pm 10$ | $-1884 \pm 3$ | $-1885 \pm 3$ | $-1889 \pm 3$ |
| $^1J(^{123}Sb,^{19}F)$ / Hz[b] | $-1042 \pm 10$ | $-1019 \pm 3$ | $-1023 \pm 3$ | $-1026 \pm 3$ |
| $^1K(Sb,F)$ / $10^{20}$ N A$^{-2}$ m$^{-3}$ | $-70.8 \pm 0.1$ | $-69.2 \pm 0.1$ | $-69.3 \pm 0.1$ | $-69.5 \pm 0.1$ |
| $\delta(^{121}Sb,^{123}Sb)$ / ppm | $0.0^c$ | $-17.6 \pm 0.2$ | $-17.5 \pm 0.2$ | $-16.5 \pm 0.3$ |
| $C_Q(^{121}Sb)$ / MHz | - | $6.42 \pm 0.10$ | $4.30 \pm 0.10$ | $3.11 \pm 0.20$ |
| $C_Q(^{123}Sb)$ / MHz | - | $8.22 \pm 0.10$ | $5.48 \pm 0.10$ | $4.06 \pm 0.20$ |
| $\eta(^{121}Sb,^{123}Sb)$ | - | 0.00 - 0.10 | 0.32 - 0.37 | 0.40 - 0.60 |

[a] Referenced to external $CF_3COOH$.

[b] Signs of $^1J(^{121}Sb,^{19}F)$ and $^1J(^{123}Sb,^{19}F)$ values were determined from DFT calculations (see text).

[c] Used as a chemical shift reference.

**Table 3.3**. CASTEP calculated parameters for [75]As and [121]Sb in $KAsF_6$ and $KSbF_6$. $Q(^{75}As) =$ 31.1 fm$^2$, $Q(^{121}Sb) = -54.3$ fm$^2$.

|  | $C_Q$ / MHz | $\eta$ | $\sigma_{iso}$ / ppm | $\Omega$ / ppm[a] | $\kappa$[b] |
|---|---|---|---|---|---|
| $KAsF_6$ Phase II | −2.562 | 0.01 | 1531.7 | 1.7 | 0.960 |
| $KAsF_6$ Phase I | 0.00 | - | 1594.4 | 0.0 | - |
| $KSbF_6$ Phase II | 12.42 | 0.00 | 3115.8 | 0.9 | −1 |
| $KSbF_6$ Phase I | 2.695 | 0.63 | 3121.1 | 27.8 | −0.960 |

[a] $\Omega = \delta_{11} - \delta_{33}$

[b] $\kappa = 3(\delta_{22} - \delta_{iso})/\Omega$
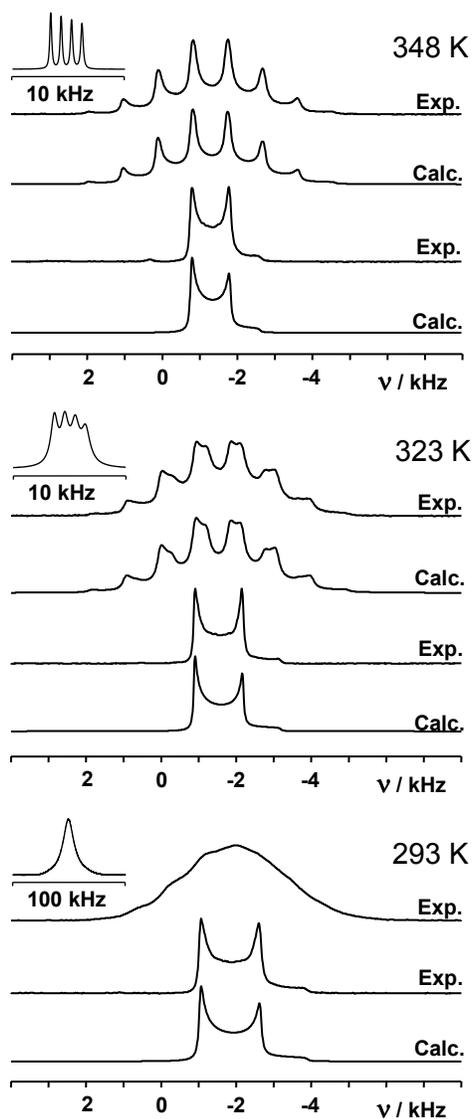
**Figure 3.1.** $^{75}$As MAS NMR spectra of $KAsF_6$ recorded at different temperatures. Spectra were recorded with (lower traces) and without (upper traces) $^{19}$F decoupling. Spectra are shown together with simulated spectra calculated using parameters contained in Table 3.1. Insets show corresponding $^{19}$F MAS NMR spectra.
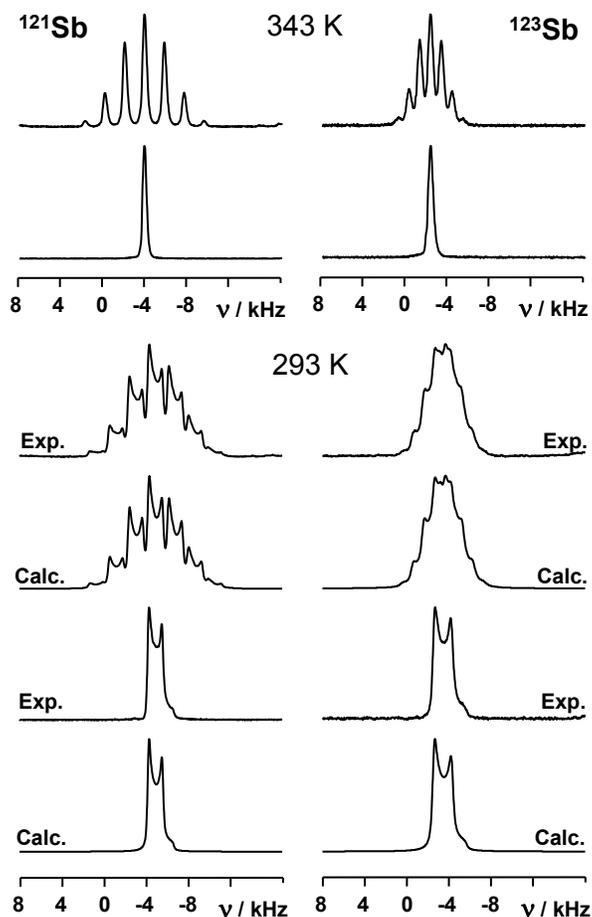
**Figure 3.2.** $^{121}$Sb and $^{123}$Sb MAS NMR spectra of KSbF$_6$ recorded for the low temperature phase (II) at 293 K and for the high temperature phase (I) at 343 K. Spectra were recorded with (lower traces) and without (upper traces) $^{19}$F decoupling. Experimental spectra are shown together with simulated spectra calculated using parameters contained in Table 3.2.
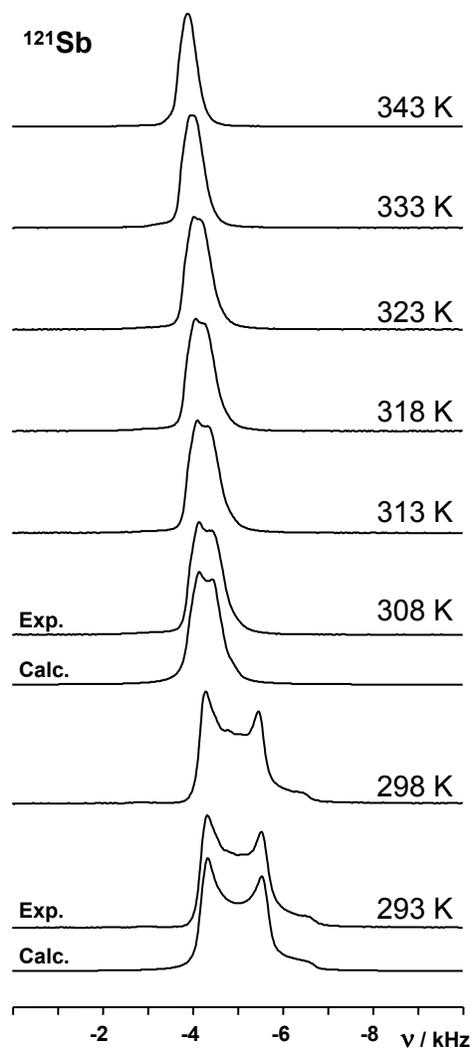
**Figure 3.3.** $^{121}$Sb MAS NMR spectra recorded with broadband $^{19}$F decoupling upon gradual heating of the KSbF$_6$ sample. (II → I) phase transition occurs at 301 K and is accompanied by abrupt changes both in $C_Q$ and $\eta$ (see Table 3.2 for NMR parameters used in simulations). Similar effects were observed in corresponding $^{123}$Sb MAS NMR spectra of this compound (not shown).
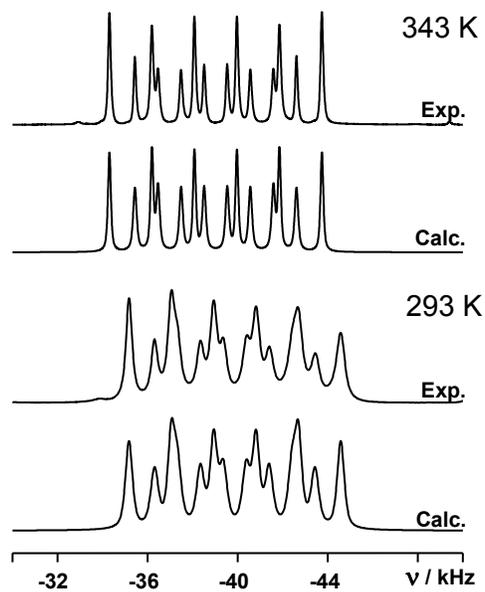
**Figure 3.4.** $^{19}$F MAS NMR spectra of KSbF$_6$ recorded for the low temperature phase (II) at 293 K and for the high temperature phase (I) at 343 K. Both spectra are shown together with simulated spectra calculated using parameters contained in Table 3.2.
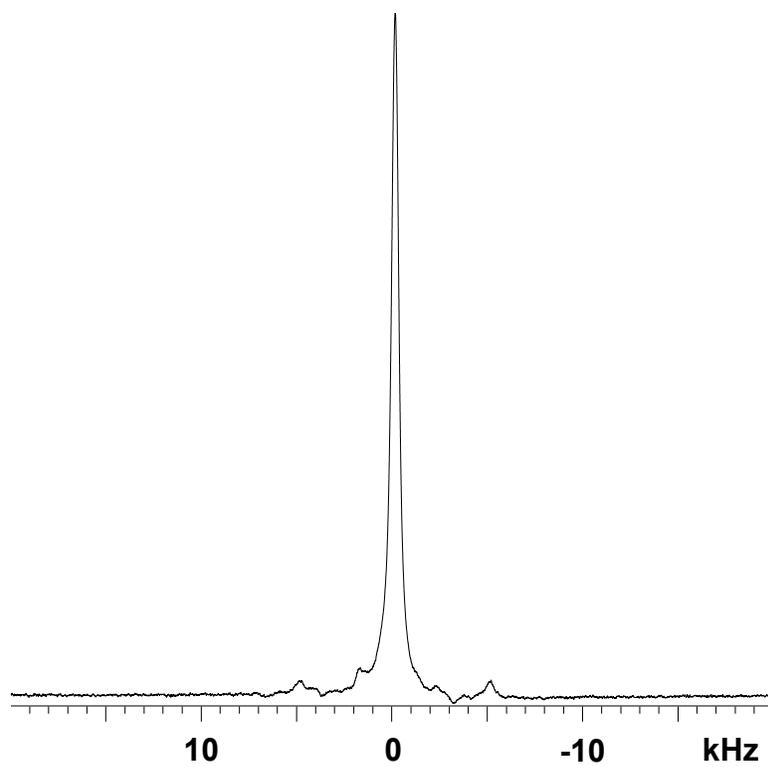
**Figure 3.5.** Arsenic-75 NMR spectrum of solid polycrystalline KAsF$_6$ at 386 ± 1 K acquired with $^{19}$F decoupling at $B_0$ = 9.4 T. The distortions on either side of the peak are decoupling artifacts.

### 3.5.1 KAsF$_6$

As mentioned above, the arsenic site in phase II of KAsF$_6$ possesses $C_3$ point-group symmetry, which confines the arsenic electric field gradient tensor parameters such that $V_{XX} = V_{YY}$, in other words, the tensor must be axially symmetric. In phase I, the octahedral symmetry about arsenic requires that the electric field gradient in all directions is zero, meaning the nuclear quadrupolar coupling constant for $^{75}$As will also have a value of zero, and a solution-like spectrum that includes signal contribution from the central transition ($m_I = 1/2 \leftrightarrow -1/2$) and the satellite transitions ($m_I = -3/2 \leftrightarrow -1/2$, and $1/2 \leftrightarrow 3/2$) should be obtained. We have found that in phase II at 293 K, $C_Q(^{75}$As$) = -2.87 \pm 0.05$ MHz (Table 3.1). $C_Q(^{75}$As$)$ values in phase II show some temperature dependence, with a variation of 570 kHz over a 55 K range in temperature. $|C_Q(^{75}$As$)|$ values decreased with increasing temperature. As $V_{ZZ}(^{75}$As$)$ lies along a three-fold rotation axis, the $^{75}$As electric field gradient tensor in this phase is axially symmetric, and the quadrupolar asymmetry parameter is zero. CASTEP calculations performed on phase II of KAsF$_6$ predict $C_Q(^{75}$As$) = -2.562$ MHz, close to our experimental values, which lie between $-2.30$ and $-2.87$ MHz. Note that signs of quadrupolar coupling constants are typically unavailable from NMR experiments, and thus only the absolute value of $C_Q(^{75}$As$)$ is available from the line shape simulations. We have chosen to include the signs predicted by the DFT calculations. In phase I of KAsF$_6$, $C_Q(^{75}$As$)$ is zero. This was confirmed by nutation experiments at a sample temperature of 386 K, which showed that the $^{75}$As nuclei contributing to the NMR spectrum of solid KAsF$_6$ possessed the same nutation behavior as those in the room temperature setup sample, 0.5 mol/L NaAsF$_6$ in CD$_3$CN (see Figure 3.6). In agreement with previous studies,[68-70] the solution value of $^1J(^{75}$As$,^{19}$F$)$ in 0.5 mol/L KAsF$_6$ in MeCN is $-930 \pm 5$ Hz. In the solid, $^1J(^{75}$As$,^{19}$F$)$ did not exhibit any temperature dependence in phase II, remaining,

within error, at a value of −926 Hz over the temperature range studied. The sign of $^1J(^{75}\text{As},^{19}\text{F})$

for the hexafluoroarsenate ion is unavailable from experiment, however, on the basis of previous

DFT calculations[103] the sign is negative. Splitting due to indirect spin-spin coupling was not

resolved in $^{19}\text{F}$ or $^{75}\text{As}$ NMR spectra (acquired without $^{19}\text{F}$ decoupling) of phase I at 386 K.

Arsenic-75 isotropic chemical shift values showed little variation over the temperature range

studied, with $\delta_{\text{iso}}(^{75}\text{As}) = -3.5 \pm 0.1$ ppm at 293 K and $-3.1 \pm 0.1$ ppm at 348 K.

Previous attempts at $^{75}\text{As}$ NMR measurements of $\text{KAsF}_6$ were carried out by Niemelä,[90]

though the experiments were unsuccessful, and spectra of neither the low nor the high

temperature phase were acquired. Gabuda et al. studied the phase transition in this solid in

1979,[102] but reported the transition at $355 \pm 1$ K, somewhat lower than the current literature value

of 375 K, suggesting that the sample may have been impure or that their reported temperatures

were not properly calibrated. In addition, $^{75}\text{As}$ NMR data were not collected below a

temperature of 347 K, and information about $C_\text{Q}(^{75}\text{As})$ values in the low temperature phase (II)

was ambiguous. The related hexafluoroarsenate salt $\text{NaAsF}_6$ was investigated previously via

variable temperature solid-state $^{23}\text{Na}$, $^{75}\text{As}$, and $^{19}\text{F}$ NMR spectroscopy.[72] Like $\text{KAsF}_6$, $\text{NaAsF}_6$

belongs to space group $R\bar{3}$ at low temperature and $Fm\bar{3}m$ at high temperature. The transition

between these two phases takes place at approximately 310 K, though like $\text{KAsF}_6$, the actual

transition temperature depends on whether the sample is being heated or cooled. Biswal et al.[72]

reported this transition taking place at 325 and 309 K upon heating and cooling, respectively.

$C_\text{Q}(^{75}\text{As})$ in the high temperature phase of $\text{NaAsF}_6$ (343 K) was reported[72] to be 0 Hz, like

$\text{KAsF}_6$. In the low temperature phase at 308 K, the experimental $C_\text{Q}(^{75}\text{As})$ value in $\text{NaAsF}_6$ was

$-820 \pm 20$ kHz, much smaller in magnitude than our $C_\text{Q}(^{75}\text{As})$ values for $\text{KAsF}_6$, which fell

between −2 and −3 MHz at around the same temperature. Based on these values, it is evident

that subtle changes in the structure caused by the substitution of sodium atoms with potassium atoms can lead to significant changes in the $^{75}$As quadrupolar coupling constant. As mentioned, the sensitivity of $C_Q(^{75}$As) values to crystal structure changes is due to the large quadrupole moment of $^{75}$As, which leads to large $C_Q(^{75}$As) values even in the presence of small electric field gradient tensor parameters. The small $C_Q(^{75}$As) value in NaAsF$_6$ also made it possible to obtain high-quality spectra at $B_0 = 7$ T.[72] The $^{19}$F-$^{75}$As isotropic spin-spin coupling constants measured for NaAsF$_6$ were $^1J(^{75}$As,$^{19}$F$) = 910 \pm 5$ Hz (from the $^{19}$F NMR spectra) and $900 \pm 20$ Hz (from the $^{75}$As NMR spectra) for both phases. This is similar to our $^1J(^{75}$As,$^{19}$F$)$ value of $-926$ Hz. Fluorine-19 isotropic chemical shift values differ by ca. 15 ppm between the NaAsF$_6$ and KAsF$_6$ salts, and $^{75}$As isotropic chemical shift values differ by less than 10 ppm.

The discussion of NMR spectroscopy of KAsF$_6$ would not be complete without commenting on the present $^{19}$F NMR spectra in comparison to that of Andrew et al. published in 1967.[71] As one can see from the previous data,[71] the $^{19}$F NMR spectrum acquired at room temperature with $B_0 = 0.6$ T, $v_0(^{19}$F$) = 24.0$ MHz shows well-resolved splitting due to indirect spin-spin coupling to $^{75}$As. In our work the $^{19}$F NMR spectrum of KAsF$_6$ acquired at 293 K and 21.14 T, however, does not show any resolved splitting (Figure 3.1). This effect can be attributed to a distribution of $^{19}$F chemical shift values across the bulk of the sample. Line broadening mechanisms such as this are well-known, and possible causes for chemical shift distributions in solids include crystal defects and effects from the bulk magnetic susceptibility.[104] Note that at $B_0 = 0.6$ T, a chemical shift spread of 1 ppm corresponds to 24 Hz, whereas at our experimental field strength of $B_0 = 21.14$ T, 1 ppm corresponds to 847 Hz. Therefore, the splitting resulting from $^1J(^{75}$As,$^{19}$F$) = 926$ Hz is approximately 39 ppm at low field and just over 1 ppm at $B_0 = 21.14$ T. Differences in chemical shifts of even a few ppm in the latter case

obscure the expected splitting pattern. Preliminary CASTEP dynamics simulations in $KAsF_6$ predict that at 293 K the $^{19}F$ chemical shift distribution can be as broad as 10 to 12 ppm, or 8.5 to 10.2 kHz at $B_0 = 21.14$ T. The *J*-splitting is clearly observed in $^{19}F$ NMR spectra at $B_0 = 21.14$ T recorded at elevated temperatures due to increased dynamics of As octahedra and more effective averaging of intermolecular dipolar interactions (Figure 3.1).
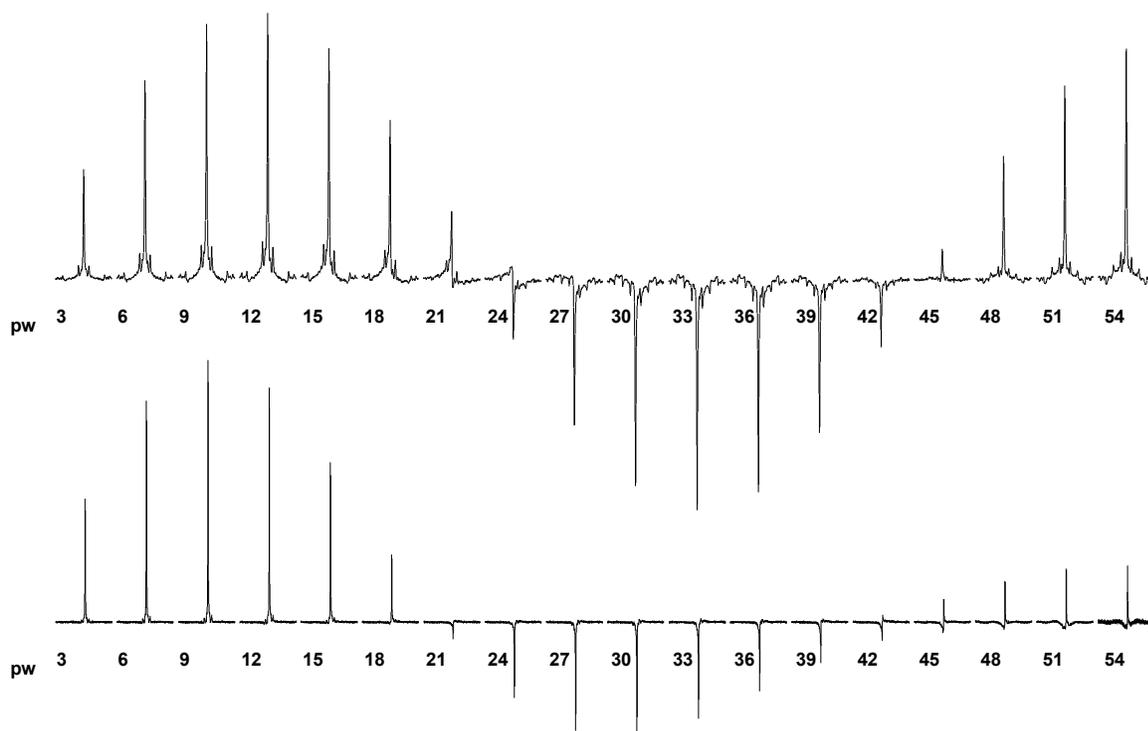


**Figure 3.6.** Nutation curves for 0.5 M $NaAsF_6$ in $CD_3CN$ at room temperature (upper trace) and solid polycrystalline $KAsF_6$ at 393 K (lower trace). Pulse widths are in µs. The 90° pulse widths were determined to be 10.75 µs and 10.5 µs, respectively. Note that if the spectrum of solid $KAsF_6$ included signal from the central transition only, the determined 90° pulse width would be approximately half of that determined in solution. The slight discrepancy between the solid and solution 90° pulse values is likely due to differences in magnetic susceptibility between samples.

**3.5.2 KSbF$_6$**

Measurements performed at $B_0 = 21.14$ T and $v_0(^{121}\text{Sb}) = 215.5$ MHz, both with and

without $^{19}\text{F}$ decoupling, show clearly resolved $^{121}\text{Sb}$ quadrupolar powder patterns, whose

breadths are approximately 3 kHz at 293 K (phase II) under MAS conditions (Figure 3.2).

Measured $C_Q(^{121}\text{Sb})$ values at 293 K (phase II) and at 343 K (phase I) are $6.42 \pm 0.10$ and $3.11 \pm$

0.20 MHz, respectively. Abrupt changes in $C_Q(^{121,123}\text{Sb})$ values between spectra acquired at 298

and 308 K are indicative of the phase transition at 301 K (see Figure 3.3). The nonzero

$C_Q(^{121,123}\text{Sb})$ values along with the determined $\eta_Q(^{121,123}\text{Sb})$ value of zero are in agreement with

the literature point-group symmetry of $C_3$ at the antimony crystal site in phase II of KSbF$_6$. In

phase I, $\eta_Q(^{121,123}\text{Sb}) = 0.50 \pm 0.10$, a value consistent with a non-axial EFG tensor (i.e., it is in

agreement with the literature point group, $C_{2v}$). CASTEP calculations support the experimental

trend, with calculated $C_Q(^{121}\text{Sb})$ values of 12.42 and 2.695 MHz in phases II and I, respectively.

Note that these CASTEP calculations do not include effects from vibrational motion, and the

temperature at which the crystal structure of phase II was obtained is unknown, possibly

accounting for the discrepancy between the calculated and experimental $C_Q(^{121}\text{Sb})$ values in

phase II of KSbF$_6$. Previous measurements of $C_Q(^{121}\text{Sb})$ in KSbF$_6$ were carried out by Kozlova

et al. on a continuous wave (CW) NMR spectrometer operating at an $^{121}\text{Sb}$ resonance frequency

of 20 MHz.[83] Temperature-dependent $C_Q(^{121}\text{Sb})$ values and their corresponding errors were not

explicitly reported, however, experimental $C_Q(^{121}\text{Sb})$ values were extrapolated to the low

temperature limit, i.e., at 0 K. Reported $C_Q(^{121}\text{Sb})$ values at this limit were $10.1 \pm 0.3$ and $15.1 \pm$

1 MHz for phases II and I, respectively. Antimony-121 NMR spectra were not shown. Based on

our experimental $C_Q(^{121}\text{Sb})$ value in KSbF$_6$ at 293 K, quadrupolar linewidths are predicted to be

ca. 70 kHz at an $^{121}$Sb resonance frequency of 20 MHz, neglecting the effects of $^{19}$F-$^{75}$As indirect spin-spin coupling.

Experimentally measured $^1J(^{121}Sb,^{19}F)$ values in the cubic and tetragonal phases are −1884 ± 3 Hz (293 K) and −1889 ± 3 Hz (343 K), and $^1J(^{123}Sb,^{19}F)$ values are −1019 ± 3 Hz (293 K) and −1026 ± 3 Hz (343 K). Again, based on DFT calculations performed previously,[103] $^1J(^{121}Sb,^{19}F)$ values are predicted to be negative. The reduced indirect spin-spin coupling, $^1K(Sb,F)$, in KSbF$_6$ is greater in magnitude than $^1K(As,F)$ in KAsF$_6$ in both solid phases and in solution (Tables 3.1 and 3.2). Values for one-bond reduced coupling constants in analogous molecules are known to increase as one moves down a group in the periodic table,[105] so this result is expected. Similar to that observed in KAsF$_6$, $^{121/123}$Sb and $^{19}$F chemical shift values vary little over the studied temperature range.


## 3.6 Conclusions

The present multinuclear magnetic resonance data on the hexafluoroarsenate(V) and hexafluoroantimonate(V) anions in KAsF$_6$ and KSbF$_6$ demonstrate some of the advantages of studying half-integer quadrupolar nuclei with large quadrupole moments at high field. Well-resolved $^{75}$As and $^{121}$Sb quadrupolar powder patterns were collected both with and without $^{19}$F decoupling, allowing for accurate determination of chemical shift and quadrupolar parameters as well as indirect spin-spin coupling constants. Fluorine-19 NMR parameters are in agreement with previous studies. Experimental and computed $^{121/123}$Sb quadrupolar coupling constants and asymmetry parameters support structures and symmetry determined via X-ray crystallography and Raman spectroscopy. The nonzero $^{121/123}$Sb nuclear quadrupolar coupling constants in cubic KSbF$_6$ show that antimony does not lie at a site of octahedral symmetry, despite its cubic crystal

structure. Current $^{121}$Sb NMR parameters provide a much needed update to the continuous wave experiments published in 1987. NMR parameters determined via CASTEP calculations are qualitatively in agreement with experimentally determined parameters.

## 3.7 Acknowledgements

# Chapter 4

Feasibility of Arsenic and Antimony NMR Spectroscopy in Solids: An Investigation of Some Group 15 Compounds

## 4.1 Introduction

Arsenic-75, antimony-121, and antimony-123 are not well explored in the NMR literature.[106-109] From the available NMR literature, the chemical shift (CS) ranges of arsenic-75 and antimony-121 are moderate, with the $^{75}$As chemical shifts spanning approximately 800 ppm, and the $^{121/123}$Sb chemical shifts spanning approximately 4000 ppm.[107] However, $^{75}$As and $^{121}$Sb CS anisotropies for AsP, SbN, and SbP have been calculated from nuclear spin rotation constants measured in high-resolution microwave spectroscopy[110,111] and are reported to be approximately 4070 ppm, 7770 ppm, and 8062 ppm, respectively (note that these are non-relativistic calculations and may be different from the actual values by several percent, vide infra). As it is not uncommon for CS anisotropies to span the chemical shift range of a given nucleus,[112] these results suggest that the chemical shift range of both $^{75}$As and $^{121}$Sb is much greater than what is reported in the NMR literature. Both NMR-active isotopes of antimony, $^{121}$Sb and $^{123}$Sb, as well as the NMR-active isotope of arsenic, $^{75}$As, are quadrupolar. They possess spin quantum numbers 3/2 for arsenic-75, 5/2 for antimony-121, and 7/2 for antimony-123 (Table 4.1). Despite the higher spin quantum number of antimony-123, the higher natural abundance and

larger magnetogyric ratio, as well as the smaller nuclear quadrupole moment of antimony-121 make it the favored isotope for NMR spectroscopy.[1]  All three of these isotopes have relatively large nuclear quadrupole moments.  It should be noted that the current (2007) IUPAC[60] values for the $^{121}$Sb and $^{123}$Sb quadrupole moments, −36.0 and −49.0 fm$^2$, respectively, are outdated. The ratio between the quadrupole moments of these two isotopes is known very precisely from microwave studies of diatomics[111,113] and a recent study conducted by Haiduke et al.[114] has provided the more accurate values of $Q = -54.3 \pm 1.1$ fm$^2$ for $^{121}$Sb, and $Q = -69.2 \pm 1.4$ fm$^2$ for $^{123}$Sb.  This is highlighted by Pyykkö,[61] and supported by work carried out in our group, in which the quadrupole moment of $^{121}$Sb was calculated to be $-53.8 \pm 2.0$ fm$^2$ (F. Chen and R. E. Wasylishen, unpublished).  Recently, a more precise value of the $^{75}$As quadrupole moment has been calculated,[115] $Q = 31.1 \pm 0.2$ fm$^2$, however, the accepted[60] value of $Q = 30.0 \pm 5.0$ fm$^2$ will be used in this work.

**Table 4.1.** Select properties for the nuclei $^{75}$As, $^{121}$Sb, and $^{123}$Sb.[1,60,61]

| Isotope | $^{75}$As | $^{121}$Sb | $^{123}$Sb |
|---|---|---|---|
| Natural Abundance / % | 100 | 57.21 | 42.79 |
| Spin Number, $I$ | 3/2 | 5/2 | 7/2 |
| Quadrupole Moment, $Q$ / fm$^2$ | 30.0 | -54.3 | -69.2 |
| Gyromagnetic Ratio, $\gamma$ / $10^7$ rad s$^{-1}$ T$^{-1}$ | 4.596 | 6.4435 | 3.4892 |
| Frequency Ratio, $\Xi$ / %$^a$ | 17.122 614 | 23.930 577 | 12.959 217 |
| Resonance Frequency (21.14 T) / MHz | 154.1 | 215.4 | 116.6 |
| Resonance Frequency (11.75 T) / MHz | 85.6 | 119.6 | 64.8 |

$^a$ Defined as $[\nu_{\text{reference}}(\text{X})]/[\nu_{\text{TMS}}(^1\text{H})]$ with TMS at infinite dilution.

The first determination of the magnetic moments of [121]Sb and [123]Sb were by Crawford and Bateson,[116] from the hyperfine structure observed in atomic spectra of gaseous antimony. The magnetic moment of arsenic-75 was first determined in 1933 by Crawford and Crooker.[117] Most of the early [75]As and [121]Sb NMR studies were carried out on samples in solution and involved either tetrahedral or octahedral species. This early literature is summarized in Chapter 11 of NMR and the Periodic Table[106] and Chapter 13 of Multinuclear NMR.[109] The large nuclear quadrupole moments of these three isotopes generally result in large quadrupolar coupling constants and broad or unobservable peaks in NMR spectra acquired for liquid (solution) samples due to efficient relaxation via the quadrupolar mechanism. In the solid state, the large nuclear quadrupolar coupling constants result in broad line shapes even in compounds that have near tetrahedral or octahedral symmetry at [75]As or [121/123]Sb. The small molecules arsine ($AsH_3$) and stibine ($SbH_3$) possess nuclear quadrupolar coupling constants of $C_Q(^{75}As) =$ −162.6 MHz and $C_Q(^{121}Sb) = 460.3$ MHz, respectively,[118] both of which would theoretically produce NMR quadrupolar central transition ($m_I = 1/2$ to $m_I = -1/2$) powder patterns spanning several MHz even if acquired on a high field NMR instrument. Such spectra typically exhibit low signal-to-noise ratios, particularly when nucleus concentration is low, and as shown, often require the use of frequency stepping to acquire the entire powder pattern. As a result, one of the most pervasive signal-enhancing techniques in solid-state NMR spectroscopy, magic angle spinning (MAS), is not useful in most cases as available spinning frequencies are much less than the breadth of the second-order quadrupolar linewidth of the central transition. These factors combined generally make acquiring [75]As, [121]Sb, and [123]Sb NMR spectra a difficult task. The majority of existing information on electric field gradients at antimony or arsenic nuclear sites has been determined from either microwave spectroscopy or nuclear quadrupole resonance

(NQR) studies.  However, these techniques have their limitations as well.  Microwave spectroscopy is performed on gas-phase samples and thus is limited in terms of which molecules can be characterized.  Furthermore, in cases where the asymmetry parameter $\eta_Q$ is not zero, it is difficult or may not be possible to characterize the EFG in its principal axis system.  NQR has been used extensively for the characterization of $^{121/123}$Sb compounds, however, since $^{75}$As has $I$ = 3/2, the parameters $C_Q$ and $\eta_Q$ cannot be obtained independently by NQR for this nucleus.[119]  Additionally, NQR studies can be challenging because one does not necessarily know where to look in terms of frequency in order to observe a transition.

Despite the difficulties encountered in acquiring $^{75}$As and $^{121/123}$Sb NMR data, there have been efforts in the past to obtain NMR spectra of these three isotopes.  Applications of antimony and arsenic in NMR spectroscopy include structural characterization in solution, notably of weakly coordinating anions, such as [M(OTeF$_5$)$_6$]− (M=As, Sb, Bi),[120-122] of heteropoly oxometalates,[123] and of alkali metal hydroxoantimonates.[124]  Glassy Ge–As–Se[125,126] and As$_2$Se$_3$,[127,128] as well as the synthetic semiconductor GaAs[129-131] have been studied via solid-state $^{75}$As NMR spectroscopy.  In 2002, $^{75}$As NMR experiments performed on powdered AsPh$_4$ReO$_4$ were included in a study of a series of compounds containing XO$_4{}^{-}$ groups.[132]  Arsenic oxysalts were studied in the solid state in 2007[133] in which NMR parameters were determined from QCPMG and spin echo experiments, with $C_Q$ values ranging from 2.85 ± 0.10 MHz in Li$_3$AsO$_4$ to 21.3 ± 0.2 MHz in As$_2$O$_5$.  A more recent study focused on the solid-state $^{75}$As NMR and NQR spectroscopy of four natural minerals, whose quadrupolar coupling constants range from 5.32 MHz in Cu$_3$AsS$_4$ to 161.7 MHz in FeAsS (the latter value determined from NQR).[134]  Arsenic-75 NMR spectroscopy was also utilized as part of a recent study of NaAsF$_6$, wherein $^{19}$F and $^{75}$As NMR results assisted in the structural characterization of $\beta$-NaAsF$_6$.[72]  This is by no

means an exhaustive list of references. For the most part, the compounds investigated via antimony and arsenic NMR spectroscopy to date have been fairly symmetric (pseudo-tetrahedral or -octahedral) where the EFGs are small.

Here we explore the application of high-field NMR spectroscopy along with the use of modern pulse programming for the acquisition of $^{75}$As and $^{121/123}$Sb NMR spectra of solids that do not exhibit perfect symmetry about the arsenic or antimony site. Four antimony- and arsenic-containing compounds, $KSb(OH)_6$, $SbPh_4Br$, $AsPh_4Br$, and $(CH_3)_3AsCH_2CO_2H^+Br^-$, were studied in the solid state. Arsenobetaine bromide, $(CH_3)_3AsCH_2CO_2H^+Br^-$, was first isolated from marine animals, and it is the primary arsenic species found in aquatic life commonly consumed by humans, e.g., lobster and many species of fish.[135,136] Although a crystal structure is unavailable for $AsPh_4Br$, evidence from related compounds suggest an "ionic" structure,[137,138] with tetrahedral symmetry about the arsenic atom. Tetraphenylammonium halides and tetraphenylphosphonium halides are known to be ionic salts, whereas $SbPh_4Br$ contains a covalent Sb−Br bond. This trend is seen in other pentavalent arsenic and antimony compounds.[139] Compounds with the composition $Ph_4SbX$ and $Ph_3SbX_2$ (X=OH, OR, halogen) have been characterized, and in most cases these compounds exhibit trigonal bipyrimidal geometry.[140] The solid-state NMR spectra of these compounds should reflect the local symmetry about the group 15 elements (vide infra).

## 4.2 Experimental Section

### 4.2.1 NMR Measurements

The compounds $KSb(OH)_6$ and $SbPh_4Br$ were purchased from Sigma-Aldrich. $AsPh_4Br$ was obtained from Alfa Aesar. $(CH_3)_3AsCH_2CO_2H^+Br^-$ (arsenobetaine bromide) was provided

by Dr. X. Chris Le (University of Alberta).  These compounds were characterized via $^{13}$C and/or $^{1}$H solution-phase NMR spectroscopy at a magnetic field strength of 11.75 T and were not further purified.  Arsenic-75 samples were referenced to 0.5 M NaAsF$_6$ in CH$_3$CN ($\delta_{iso} = 0.0$ ppm), and $^{121}$Sb and $^{123}$Sb samples were referenced to 0.5 M KSbF$_6$ in CH$_3$CN ($\delta_{iso} = 0.0$ ppm).  Note that SbF$_6^-$(aq) has a chemical shift $\delta = 88 \pm 3$ ppm with respect to the IUPAC $^{121/123}$Sb recommended reference, saturated KSbCl$_6$ in CH$_3$CN.[1]  90° pulse widths were calibrated using the reference samples.  For solid samples, a selective pulse was applied to excite only the central ($m_I = 1/2$ to $m_I = -1/2$) transition.  The selective pulse width was $PW_{90}/\left(I + \frac{1}{2}\right)$, where $PW_{90}$ is the 90° pulse width used for the solution phase reference sample, and $I$ is the spin number of the nucleus studied.[141]

Solid samples were packed in 4 mm o.d. zirconia rotors.  Solid-state $^{75}$As, $^{121}$Sb, and $^{123}$Sb NMR spectra were acquired at room temperature at field strengths of 11.75 T and 21.14 T.  These were acquired on either a Bruker Avance 500 MHz NMR spectrometer (University of Alberta), or a Bruker Avance II 900 MHz NMR spectrometer located in Ottawa, ON at the National Ultrahigh-Field NMR Facility for Solids.[2]  Spectra were obtained using 4 mm MAS probes operating in double-resonance mode.  $^{1}$H decoupling (CW) was applied during acquisition for all spectra acquired at 21.14 T.  Proton decoupling did not significantly affect the observed overall linewidths or lineshapes and therefore at 11.75 T most spectra were acquired without $^{1}$H decoupling.  Generally, compounds were first studied using the QCPMG[40,142] pulse sequence, followed by the WURST[41] and WURST-QCPMG[45,46] pulse sequences.  In some cases, single quadrupolar echoes were acquired.  WURST pulses used were 50 µs in duration.  Echo times used for spin echoes, QCPMG, and WURST-QCPMG varied between 40 and 50 µs.  All samples were stationary when spectra were acquired.  Detailed conditions are outlined below.

### 4.2.1.1 AsPh$_4$Br

Arsenic-75 NMR spectra were acquired at 21.14 T using both spin echo and WURST-QCPMG.  For the former, 5100 transients were acquired, with a recycle delay of 0.5 s and a spectral width of 500 kHz, for a total experiment time of 42.5 min.  The latter spectrum was obtained from 16 echoes, 7494 transients, a 0.5 s recycle delay, and a spectral width of 1 MHz.  This experiment required approximately 1 h to complete.  Both the spin echo and QCPMG experiments were also carried out at 11.75 T, the former with 985,750 transients using a recycle delay of 0.5 s, and the latter with 29,560 transients and the same recycle delay.  The QCPMG spectrum consisted of 20 echoes.  Though all of these spectra were acquired in a single spectral window, it took more than five days to complete the spin echo experiment at 11.75 T.

### 4.2.1.2 (CH$_3$)$_3$AsCH$_2$CO$_2$H$^+$Br$^-$

Arsenic-75 NMR spectra of arsenobetaine bromide were acquired at 21.14 T using the spin echo pulse sequence.  A total of 51,574 transients were acquired, with a recycle delay of 1.0 s and a spectral width of 1 MHz.  The spectrum took approximately 14.3 h to acquire.

### 4.2.1.3 KSb(OH)$_6$

The $^{121}$Sb NMR spectra of KSb(OH)$_6$ at 21.14 T were acquired using both a spin echo and WURST-QCPMG.  The WURST-QCPMG spectrum consisted of 30 echoes, with a recycle delay of 0.5 s, a bandwidth of 1 MHz, and 276 transients (less than 3 min).  The spin echo required 20,480 transients, with the same pulse delay.  Antimony-121 NMR spectroscopy was also carried out at 11.75 T, using WURST-QCPMG.  38,884 scans were acquired, with a 1 MHz

bandwidth and a 0.5 s recycle delay; a total of 5.5 h was required.  Antimony-123 NMR spectra

of KSb(OH)$_6$ were acquired at 21.14 T as well using the WURST-QCPMG pulse sequence.  This

consisted of 30 echoes, 1024 transients, and a 1 MHz bandwidth.  The recycle delay was

increased to 1.0 s for this nucleus, for a total experiment time of 17 min.

**4.2.1.4 SbPh$_4$Br**

Spin echo, QCPMG, and a WURST echo were used to acquire antimony-121 NMR

spectra of SbPh$_4$Br at 21.14 T.  These spectra required frequency stepping and were assembled

using the skyline projection technique.  The QCPMG NMR spectrum consisted of 32 steps with

a transmitter separation of 100 to 250 kHz, collecting 2048 transients with a recycle delay of 0.5

s, for a total experiment time of 9 h.  The spin echo spectra required anywhere from 30,000 to

120,000 transients per spectral window, each step requiring at least 4 h to complete.  This was

used in conjunction with the QCPMG spectrum to confirm the positions of the spectral shoulders

and discontinuities.  The WURST echo spectrum is comprised of a series of twelve frequency-

stepped WURST echoes.  This consisted of transmitter steps of 0.5 MHz, with 40,960 transients

per step and a recycle delay of 0.5 s.  The entire spectrum required approximately three days of

experiment time.  The spectral width for each window was 5 MHz.

Simulations used in conjunction with experimental data to determine the NMR

parameters for these compounds were carried out using the programs WSolids[99] and QUEST.[19]

WSolids uses perturbation theory to the second order to calculate quadrupolar powder patterns,

whereas QUEST diagonalizes the full Zeeman-quadrupolar Hamiltonian.  Spectra were

simulated by visual inspection and errors were determined by this method as well.  1000 to 5000

Hz of line broadening was used in the simulations to approximate the lineshape of the experimental spectra.

### 4.2.2 EFG and Magnetic Shielding Computations

Calculations performed on antimony- and arsenic-containing compounds were carried out using the Amsterdam Density Functional (ADF) software package, with the GGA functional BP86 and the ZORA/QZ4P basis set.[51-53] Where hydrogen positions were not given in the crystal structures (i.e., in the phenyl groups of $AsPh_4Br$ and $SbPh_4Br$), hydrogen atoms were added assuming planar geometry in the phenyl groups and a C−H bond length of 1.08 Å. Similarly, hydrogen coordinates were also modified if existing hydrogen positions were included in these structures. Since the crystal structure for $AsPh_4Br$ is not experimentally known, a five-coordinate structure was calculated by performing a geometry optimization using Gaussian 09,[143] the B3LYP functional and the basis set 6-311G*. The initial atomic parameters before optimization for the $AsPh_4Br$ structure was obtained from the known crystal structure of $SbPh_4Br$.[144,145] Calculation of the electric field gradient tensor was subsequently carried out using ADF. In addition, calculations were performed on the near-tetrahedral compound $AsPh_4I$ for comparison.

The CASTEP NMR program[54-57] in the Materials Studio 4.4 environment was used to calculate $^{121}Sb$ EFG tensor parameters in $SbPh_4Br$. Calculations were performed on a HP xw4400 workstation with a single Intel Dual-Core 2.67 GHz processor and 8 GB DDR RAM, using the structure model from reported crystallographic data.[144,145] Using the "on-the-fly" method provided in the CASTEP code, ultrasoft pseudopotentials were generated to calculate $^{121}Sb$ EFG tensor parameters with a plane wave basis set cutoff energy of 250 eV in a coarse

accuracy basis set limited by the large unit cell volumes; the Monkhorst-Pack k-space grid size was $1 \times 1 \times 1$. The Perdew, Burke, and Ernzerhof (PBE) functional was used in the generalized gradient approximation (GGA) for the exchange correlation energy.[58,59]

## 4.3 Results and Discussion

The experimental results for the compounds studied here are summarized in Table 4.2. No substantial improvements in the simulated spectra could be made by adding CS anisotropy except where noted. The relative orientation of the EFG and CS tensors (where CS anisotropy was simulated) was not determined as the sensitivity of the spectral line shape to these changes was relatively low. Simulations assumed the two tensors were coincident, though in reality this may not necessarily be the case.[146] The $C_Q$ values of a series of small molecules for which $C_Q$ is well known were calculated using the ADF program for proof of concept (Table 4.3). In general these calculated values of $C_Q$ corresponded with experimental values, however, the calculations for the larger molecules studied here were less accurate (see Table 4.3). CASTEP calculations performed on $SbPh_4Br$ gave more accurate results compared with those from ADF (Table 4.4).

**Table 4.2.** Experimental arsenic-75, antimony-121 and antimony-123 NMR parameters for AsPh$_4$Br, (CH$_3$)$_3$AsCH$_2$CO$_2$H$^+$Br$^-$, KSb(OH)$_6$, and SbPh$_4$Br, determined through simulation. Resonance frequencies of $^{75}$As, $^{121}$Sb, and $^{123}$Sb nuclei at 21.14 T were 154.1 MHz, 215.4 MHz, and 116.6 MHz, respectively. Where available, data acquired at $B_0 = 11.75$ T were used in addition to 21.14 T data to determine simulated fits.

| Compound | KSb(OH)$_6$ | | SbPh$_4$Br | AsPh$_4$Br | (CH$_3$)$_3$AsCH$_2$CO$_2$H$^+$Br$^-$ |
|---|---|---|---|---|---|
| Nucleus | $^{121}$Sb | $^{123}$Sb | $^{121}$Sb | $^{75}$As | $^{75}$As |
| $C_Q$ / MHz | 46.0 ± 0.1 | 58.6 ± 0.1 | 159.0 ± 0.5 | 7.8 ± 0.1 | 24.1 ± 0.1 |
| $\eta$ | | 0.46 ± 0.01 | 0.58 ± 0.01 | 0.97 ± 0.05 | 0.28 ± 0.01 |
| $\delta_{iso}$ / ppm | | 240 ± 3 | 490 ± 30 | 215 ± 5 | 220 ± 2 |
| $\Omega^a$ / ppm | | 150 ± 10 | - | 80 ± 10 | - |
| $\kappa^b$ | | 0.5 ± 0.1 | - | 0.9 ± 0.1 | - |

$^a$ $\Omega = \delta_{11} - \delta_{33}$

$^b$ $\kappa = 3(\delta_{22} - \delta_{iso})/\Omega$

**Table 4.3.** Antimony-121 and arsenic-75 electric field gradient parameters as calculated by ADF using the BP86 functional and the ZORA/QZ4P basis set.[a]

| Compound | Calculated | | | Experimental | | | |
|---|---|---|---|---|---|---|---|
| | $V_{ZZ}$ / a.u. | $C_Q$ / MHz | $\eta$ | $V_{ZZ}$ / a.u. | $C_Q$ / MHz | $\eta$ | Reference |
| SbN | −5.360 | 683.8 | 0 | −5.09 | 649.669 | 0 | 111 |
| SbP | −4.921 | 627.8 | 0 | −4.86 | 620.35 | 0 | 111 |
| SbF | 4.720 | −602.2 | 0 | 4.60 | −586.802 | 0 | 113 |
| SbCl | 4.364 | −556.7 | 0 | 4.05 | −516.3611 | 0 | 113 |
| $SbH_3$ | −3.498 | 446.3 | 0.00 | −3.61 | 460.31 | 0 | 118 |
| $SbPh_4Br$ | 0.4658 | −59.43 | 0.82 | 1.25[e] | 159.0[e] | 0.58 | This work |
| $Sb(OH)_6{}^{−b}$ | 0.2206 | −28.14 | 0.60 | 0.361[e] | 46.0[e] | 0.46 | This work |
| $SbPh_4I$ | −0.5157 | 65.79 | 0.75 | - | - | - | - |
| AsP | −3.409 | −240.3 | 0 | −3.52 | −247.9495 | 0 | 110 |
| $AsH_3$ | −2.160 | −159.4 | 0.00 | −2.31 | −162.63 | 0 | 118 |
| $AsPh_4I$ | −0.2591 | -18.26 | 0.70 | - | - | - | - |
| $AsPh_4Br$ (pentacoordinate)[c] | 0.3845 | 27.10 | 0.77 | 0.111[e] | 7.8[e] | 0.97 | This work |
| Arsenobetaine bromide[d] | −0.7282 | −51.33 | 0.81 | 0.342[e] | 24.1[e] | 0.28 | This work |

[a] A value of $Q(^{121}Sb) = −54.3$ fm$^2$ was used in these calculations.

[b] ADF calculations performed using the structure for the anion of the sodium salt, $NaSb(OH)_6$.

[c] Structure used in calculations of NMR parameters determined by performing a geometry optimization on the known structure for $SbPh_4Br$ using Gaussian 09, the B3LYP functional and the 6-311G* basis set.

[d] DFT calculations of NMR parameters performed on arsenobetaine hydrate.

[e] Absolute value.

**Table 4.4.** Antimony-121 electric field gradient parameters for the compound $SbPh_4Br$ as calculated by CASTEP.[a]

| | Calculated | | Experimental | |
|---|---|---|---|---|
| Reference Structure | $C_Q$ / MHz | $\eta$ | $|C_Q|$ / MHz | $\eta$ |
| 145[b] | −110.1 | 0.62 | | |
| 145[c] | −126.3 | 0.61 | | |
| 144[b] | −131.7 | 0.58 | 159.0 | 0.58 |
| 144[c] | −128.4 | 0.63 | | |

[a] The results have been corrected to reflect $Q = -54.3$ fm$^2$.

[b] Hydrogen atoms added where absent assuming a bond length of 1.08 Å.

[c] Full geometry optimization carried out pre-calculation.

### 4.3.1 Experimental NMR Parameters

### 4.3.1.1 AsPh$_4$Br

The spin echo spectrum acquired at 11.75 T (not shown) was used in conjunction with the data acquired at 21.14 T (see Figure 4.1) to determine the $^{75}$As NMR parameters for AsPh$_4$Br. Attempts to acquire QCPMG spectra at 11.75 T were unsuccessful. The central transition linewidth at 11.75 T is approximately 198 kHz, and at 21.14 T it is approximately 108 kHz. Since the second-order quadrupolar linewidth scales as $C_Q^2/\nu_0$, a linewidth of approximately 110 kHz is expected at 21.14 T based on the central transition linewidth at 11.75 T. The close agreement between the experimental and calculated values strongly suggests that CS anisotropy is not a significant contributor to line width or line shape. The parameters obtained for $^{75}$As in this compound are $C_Q(^{75}$As$) = 7.8 \pm 0.1$ MHz, $\eta_Q(^{75}$As$) = 0.97 \pm 0.05$, $\delta_{iso}(^{75}$As$) = 215 \pm 5$ ppm, $\Omega(^{75}$As$) = 80 \pm 10$ ppm, and $\kappa(^{75}$As$) = 0.9 \pm 0.1$.

### 4.3.1.2 (CH$_3$)$_3$AsCH$_2$CO$_2$H$^+$Br$^-$

The $^{75}$As spectrum of arsenobetaine bromide is shown in Figure 4.2. This spectrum was acquired using a single frequency offset resulting in minor distortion of the lineshape (attenuation of intensity) towards the outer edges due to limited excitation profile. This distortion does not affect the quality of the simulation since all of the singularities are clearly defined. The parameters used to simulate this spectrum are $C_Q(^{75}$As$) = 24.1 \pm 0.1$ MHz, $\eta_Q(^{75}$As$) = 0.28 \pm 0.1$, and $\delta_{iso}(^{75}$As$) = 220 \pm 2$ ppm. The simulation indicates that there is no significant CS anisotropy.
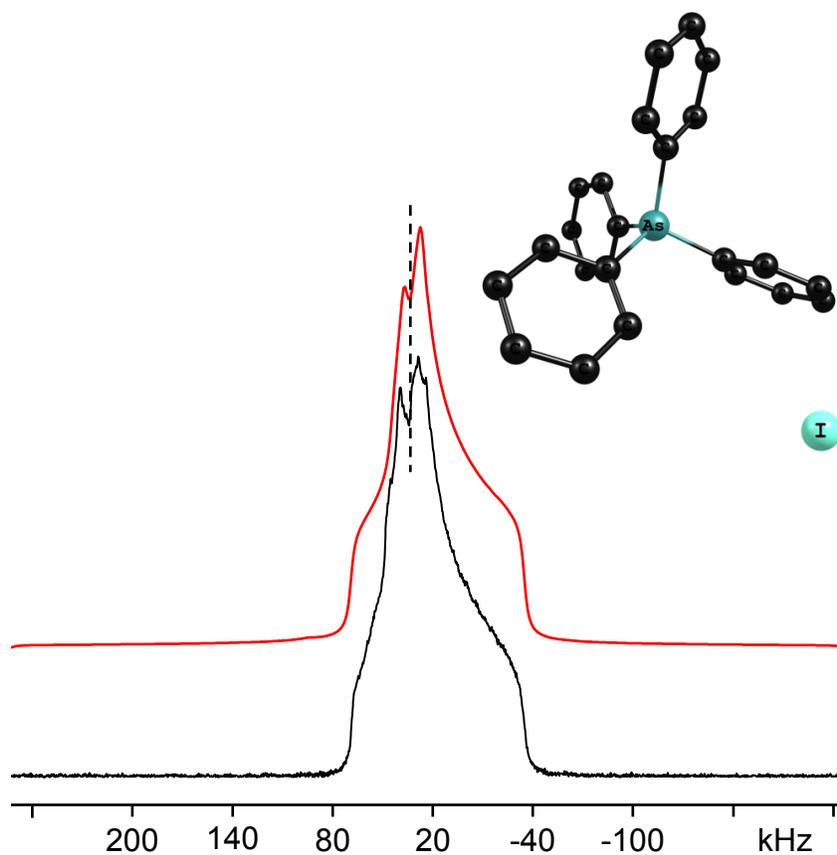
**Figure 4.1.** Experimental (lower trace) and simulated (upper trace) [75]As NMR spectra of

AsPh$_4$Br acquired at 21.14 T using the quadrupolar echo pulse sequence (90°-$\tau_1$-90°-$\tau_2$-acquire).

The same model parameters fit [75]As NMR spectra recorded for this compound at 11.75 T (not

shown).
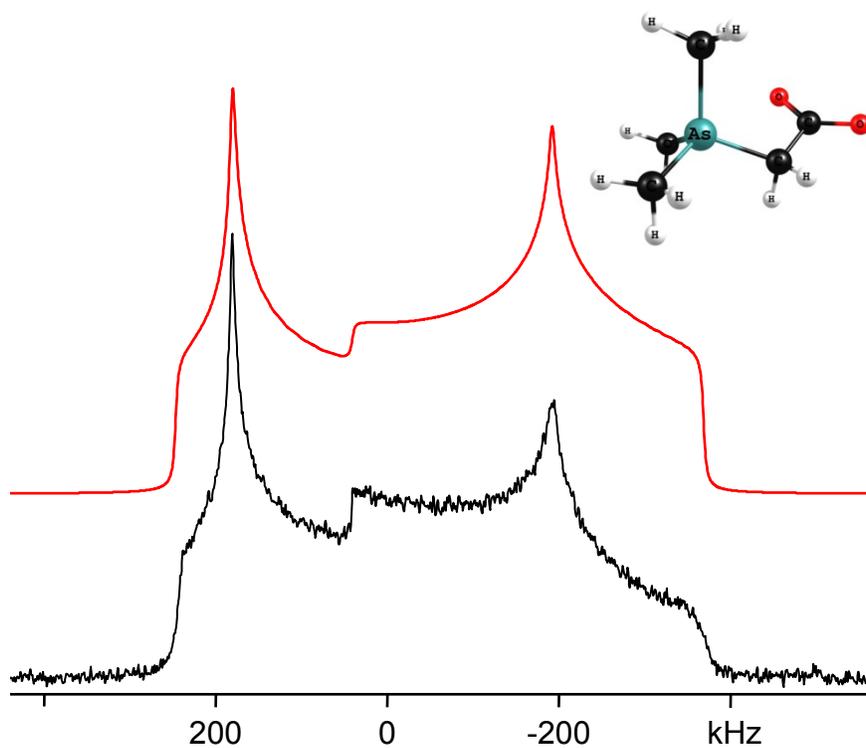
**Figure 4.2.** Experimental (lower trace) and simulated (upper trace) $^{75}$As NMR spectra of arsenobetaine bromide acquired at 21.14 T using the quadrupolar echo pulse sequence.

**4.3.1.3 KSb(OH)$_6$**

Solid KSb(OH)$_6$ was studied at 11.75 T and 21.14 T by both antimony-121 and antimony-123 NMR spectroscopy. Spin echo, QCPMG, and WURST-QCPMG spectra were obtained (see Figure 4.3 for $^{121}$Sb results, and Figure 4.4 for $^{123}$Sb results). Spectra were acquired at 21.14 T using a single frequency offset, resulting in somewhat distorted lineshapes. Nevertheless, all of the singularities are clearly visible. This compound was found through simulation to have $C_Q(^{121}\text{Sb}) = 46.0 \pm 0.1$ MHz and $C_Q(^{123}\text{Sb}) = 58.6 \pm 0.1$ MHz, with $\eta_Q = 0.46 \pm 0.01$. It was necessary to include the effects of CS anisotropy in the simulations (see Table 4.2). The overall central transition linewidth in the $^{121}$Sb spectrum is approximately 450 kHz at 21.14 T and approximately 820 kHz at 11.75 T. Simulated spectra were far less sensitive to changes in CS parameters than to changes in quadrupolar parameters.
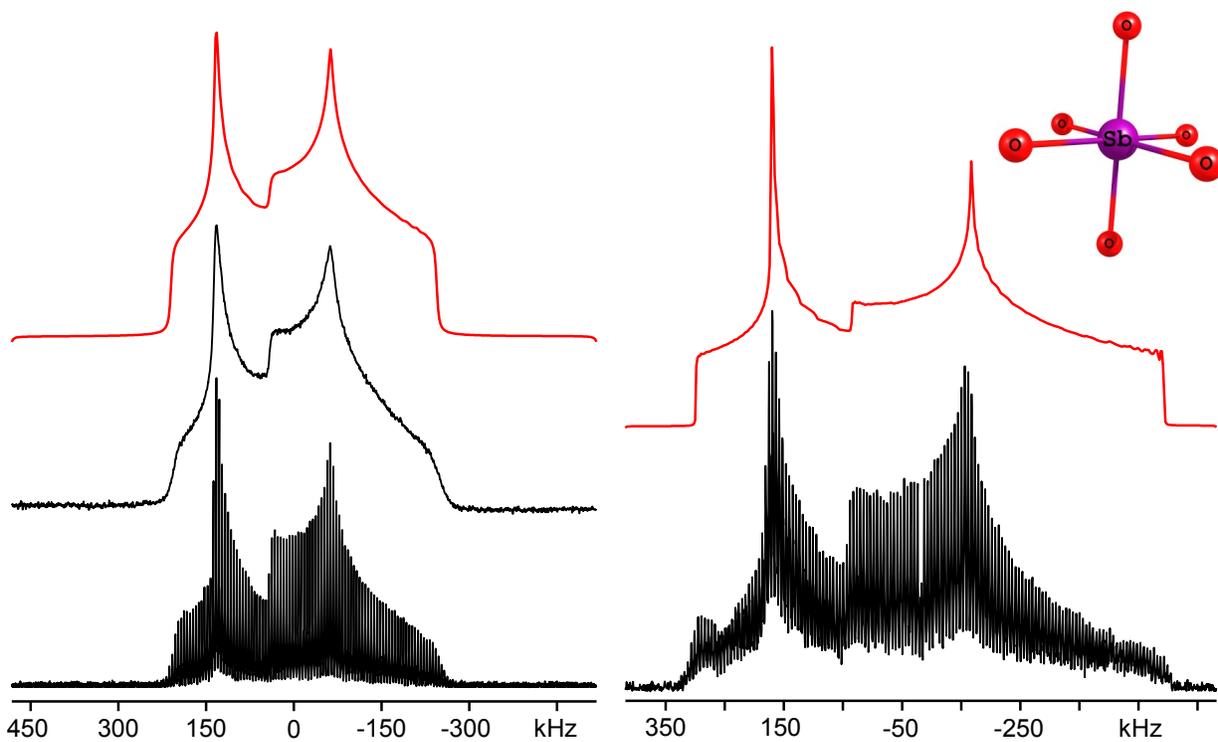
**Figure 4.3.** Experimental (middle left and lower traces) and simulated (upper traces) $^{121}$Sb NMR spectra of KSb(OH)$_6$ acquired at 21.14 T (left) and 11.75 T (right). Lower traces acquired using the WURST-QCPMG pulse sequence, middle trace acquired using a quadrupolar echo.
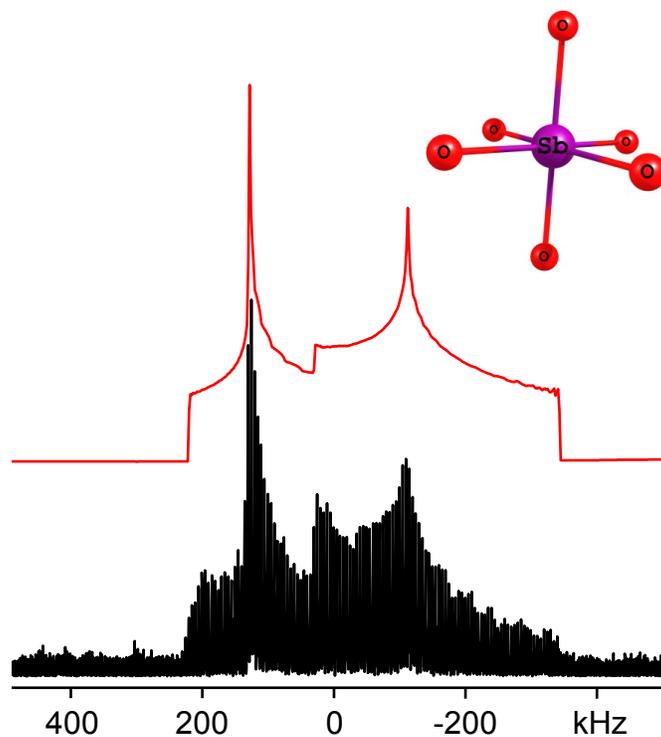
**Figure 4.4.** Experimental (lower trace) and simulated (upper trace) [123]Sb NMR spectra of KSb(OH)$_6$ acquired at 21.14 T using the WURST-QCPMG pulse sequence.

**4.3.1.4 SbPh₄Br**

The $^{121}$Sb NMR spectrum of this compound is quite remarkable, with a central transition linewidth spanning approximately 5.5 MHz at 21.14 T (see Figure 4.5). Due to the breadth of this powder pattern, studies were only carried out at 21.14 T. Chronologically, the first spectra acquired of this compound were the series of quadrupolar echoes and the QCPMG spectra shown in Figure 4.6. These data were valuable as they provided clear information about the discontinuities in the powder pattern. The WURST echo (Figure 4.5) provided the clearest results. Even at a relatively high field strength, spectral acquisition of this compound was difficult, with each of the twelve pieces in the skyline projection taking approximately 6 h to acquire. It should be noted, however, that the probe used in the acquisition of these spectra, a 4 mm double resonance MAS probe, was not ideally suited to acquiring wideline NMR powder patterns; the availability of a stationary probe with an RF coil oriented perpendicular to $B_0$ would have significantly decreased the experiment time given the same quality of spectra.
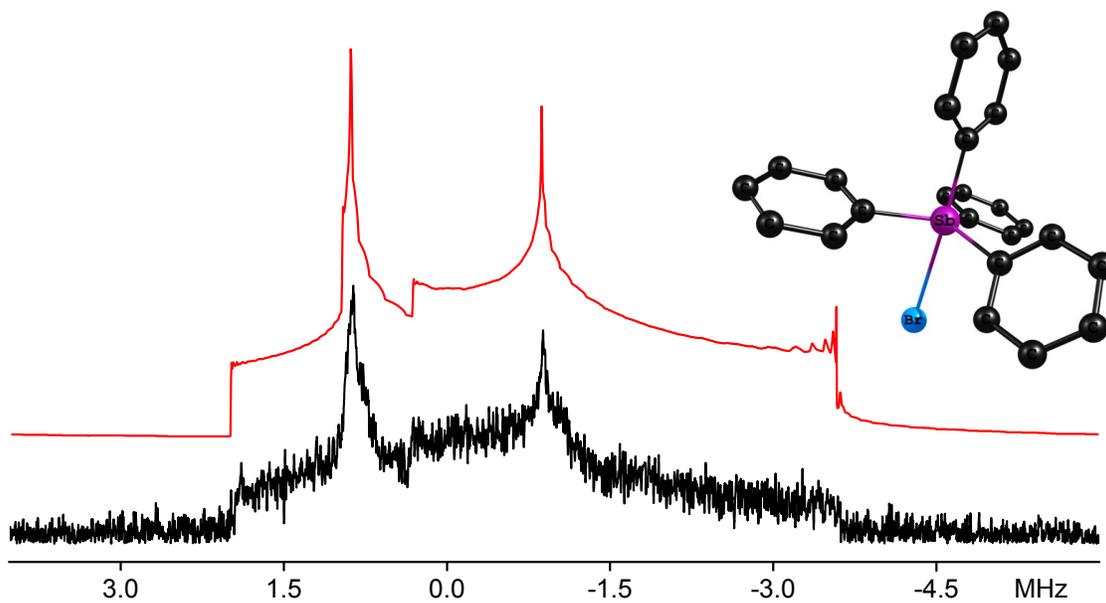
**Figure 4.5.** Antimony-121 NMR spectra of SbPh$_4$Br acquired at a field strength of 21.14 T. Experimental skyline projection created from WURST echo spectra (lower trace) and simulated spectrum (upper trace).
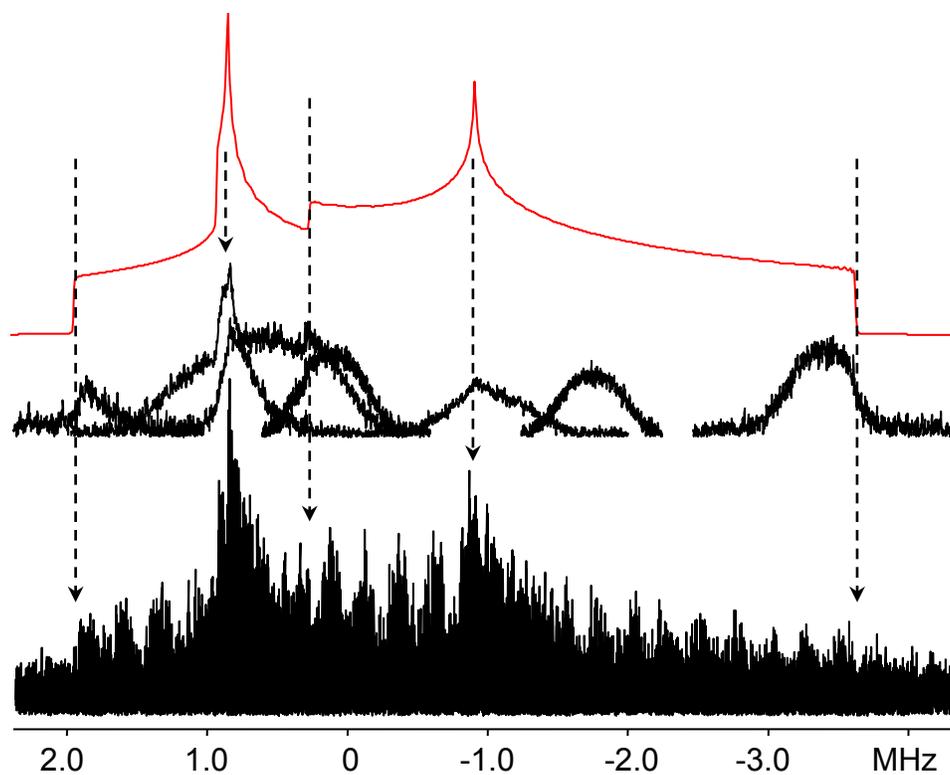
**Figure 4.6.** QCPMG (lower trace), spin echo (middle trace) and simulated (upper trace) [121]Sb NMR spectra of SbPh$_4$Br acquired at 21.14 T. The [121]Sb NMR spectrum was simulated using WSolids1.

Preliminary simulation parameters obtained in WSolids were $C_Q(^{121}\text{Sb}) = 159.0$ MHz, $\eta_Q(^{121}\text{Sb}) = 0.59$, $\Omega(^{121}\text{Sb}) = 0$ ppm, and $\delta_{\text{iso}}(^{121}\text{Sb}) = 380$ ppm. Due to the magnitude of $C_Q$, the program QUEST was employed in addition to WSolids for spectral simulation in order to determine if perturbation theory to second order is adequate to describe the line shape. The parameters determined using QUEST and all three SbPh$_4$Br spectra are $C_Q(^{121}\text{Sb}) = 159.0 \pm 0.5$ MHz, $\eta_Q(^{121}\text{Sb}) = 0.58 \pm 0.01$, $\delta_{\text{iso}}(^{121}\text{Sb}) = 490 \pm 30$ ppm, and $\Omega(^{121}\text{Sb}) = 0$ ppm. Minor adjustments were made to the parameters; clearly the spectrum of SbPh$_4$Br does not quite satisfy the assumptions made when using perturbation theory. In the simulations it was assumed that the quadrupolar interaction was the only interaction that contributed to the line shape. Given the lack of symmetry at the Sb site, some CS anisotropy must be present (see Table 4.5), but it is dwarfed by the magnitude of the quadrupolar interaction.

### 4.3.2 Calculated NMR Parameters and Crystal Structure

### 4.3.2.1 AsPh$_4$Br and SbPh$_4$Br

Examining the group trend (P, As, Sb), tetraphenylphosphonium halides, PPh$_4$X, exhibit structures involving a tetrahedral or near-tetrahedral tetraphenyl cation bonded ionically to the halide anion. Two crystal structures are available for tetraphenylphosphonium bromide, PPh$_4$Br, the phosphorous compound analogous to AsPh$_4$Br, both of which feature an ionic structure and a near-tetrahedral cation.[147,148] To date there is no crystal structure reported in the literature for AsPh$_4$Br. However, other tetraphenylarsonium halides and trihalides have been characterized, and like their phosphonium counterparts, they have approximately tetrahedral tetraphenylarsonium cations bonded ionically to the corresponding halide anions. Tetraphenylarsonium iodide, AsPh$_4$I, has been characterized via X-ray diffraction and it

crystallizes in the space group $I\bar{4}$ with cell parameters $a$ = 12.174(2) Å and $c$ = 6.885(2) Å.[149] Another tetraphenylarsonium halide for which the crystal structure is known is tetraphenylarsonium diiodobromide. This is isostructural with reported tetraphenylphosphonium interhalides, with space group $P2/n$.[138] These known structures suggest that in $AsPh_4Br$, the bonding environment about arsenic is likely tetrahedral.

Tetraphenylstibonium bromide, $SbPh_4Br$, has been characterized twice via X-ray crystallography, both reporting the space group $P21/n$.[144,145] The molecule is pentacoordinate about antimony and the Sb−Br bond is considered covalent. The antimony site displays distorted trigonal bipyrimidal symmetry with the bromine atom located in the axial position. The structure determined by Ferguson et al.[144] has cell parameters $a$ = 16.293(3) Å, $b$ = 10.616(3) Å, $c$ = 12.507(2) Å, and $\beta$ = 105.60(1)°. This structure has an Sb−Br bond distance of 2.965(1) Å, which is long for antimony(V), and Sb−C bond distances of 2.151(9) Å and 2.102(9) Å for the apical and equatorial phenyl groups, respectively. The structure determined by Knop et al.[145] has cell parameters $a$ = 12.282(2) Å, $b$ = 10.656(1) Å, $c$ = 16.156(1) Å, and $\beta$ = 104.92(7)° (note in this space group, $a$ and $c$ are interchangeable). The Sb−Br bond distance is 2.950(1) Å, and the Sb−C bond distances are 2.131(8) Å (apical) and 2.114(23) Å (equatorial). Both of these studies used $SbPh_4Br$ recrystallized from nitromethane and carried out the diffraction experiments at room temperature, and though the structures contain minor differences when compared, they can be considered essentially identical.

It is apparent that the value for $C_Q(^{121}Sb)$ calculated by ADF for an isolated $SbPh_4Br$ molecule using the structure by Knop et al. −59.4 MHz (see Table 4.3), is much smaller than the experimental value of (±)159.0 MHz. CASTEP (see Table 4.4) was more accurate, calculating the $C_Q(^{121}Sb)$ value to be −110.0 MHz for the original structure determined by Knop et al.[145] and

−126.3 MHz for the optimized structure, with asymmetry parameters of 0.62 and 0.61, respectively. For the structure determined by Ferguson et al.[144] CASTEP calculated $C_Q(^{121}Sb)$ and $\eta_Q(^{121}Sb)$ to be −131.7 MHz and 0.58 for the original structure, and −128.4 MHz and 0.63 for the optimized structure. Based on the improved $C_Q(^{121}Sb)$ accuracy observed in CASTEP, approximately a factor of two in magnitude greater than ADF, it seems that the lattice is contributing to the electric field gradient at antimony. ADF calculations (see Table 4.5) predict a CS span of approximately 320 ppm for this compound; inclusion of this parameter when simulating the experimental spectra causes only a slight variation from the original fit. The known crystal structure for $SbPh_4Br$ does not have higher-order symmetry about the antimony site, and therefore an appreciable local electric field gradient at that site is consistent with the structure.

**Table 4.5.** Antimony-121 and arsenic-75 magnetic shielding tensor parameters as calculated by ADF using the BP86 functional and the ZORA/QZ4P basis set.

| | Calculated | | | Experimental | |
| --- | --- | --- | --- | --- | --- |
| Compound | $\sigma_{iso}$ / ppm | $\Omega$ / ppm | $\kappa^d$ | $\Omega^e$ / ppm | Reference |
| SbN | 457.0 | 8442 | −1 | 7769.4 | 111 |
| SbP | 0.9947 | 9141 | −1 | 8061.6 | 111 |
| SbF | −928.4 | 9520 | −1 | - | - |
| SbCl | −374.4 | 8647 | −1 | - | - |
| SbPh$_4$Br | 2834 | 319.0 | −0.67 | - | This work |
| Sb(OH)$_6^{-a}$ | 3669 | 39.27 | 0.14 | 150 ± 10 | This work |
| AsP | −256.6 | 4997 | −1 | 4070 | 110 |
| AsPh$_4$I | 1469 | 888.7 | 0.65 | - | - |
| AsPh$_4$Br (pentacoordinate)$^b$ | 1249 | 179.9 | −0.33 | 80 ± 10 | This work |
| Arsenobetaine bromide$^c$ | 1304 | 188.0 | −0.66 | - | This work |

[a] Structure used in calculation is for the anion of the sodium salt, NaSb(OH)$_6$.

[b] Structure determined by performing a geometry optimization on the known structure for SbPh$_4$Br using the B3LYP functional and the 6-311G* basis set with Gaussian 09.

[c] Calculations performed on arsenobetaine hydrate.

[d] $\kappa = 3(\delta_{22} - \delta_{iso})/\Omega$

[e] $\Omega = \delta_{11} - \delta_{33}$

Since the crystal structure of AsPh$_4$Br is not known, DFT calculations to determine EFG

and CS parameters were carried out both on the near-tetrahedral iodide salt AsPh$_4$I, as well as on

a distorted trigonal bipyrimidal representation of AsPh$_4$Br created by performing a geometry

optimization with the initial atomic coordinates matching those of SbPh$_4$Br (see Table 4.3). The

fabricated trigonal bipyrimidal version of AsPh$_4$Br had a calculated $C_Q$($^{75}$As) of 27.1 MHz and

$\eta_Q$($^{75}$As) of 0.77, far larger than the experimental $C_Q$($^{75}$As) = 7.8 MHz. ADF also predicted the

$C_Q$($^{75}$As) of AsPh$_4$I to be much larger than what is measured experimentally for AsPh$_4$Br, with a

calculated $C_Q$($^{75}$As) of $-18.3$ MHz and $\eta_Q$($^{75}$As) of 0.70. Based on X-ray diffraction studies of

other tetraphenylarsonium halides, as well as the small $C_Q$($^{75}$As) found for AsPh$_4$Br, the

geometry about the arsenic site in this compound is likely near-tetrahedral. This conclusion is

supported by the calculated values of $V_{ZZ}$ (see Table 4.3) which show an order of magnitude

difference for the compounds AsPh$_4$Br and SbPh$_4$Br. The latter possesses a $V_{ZZ}$ of $-1.25$ au,

while $V_{ZZ}$ at the arsenic site in AsPh$_4$Br is only 0.106 au. Furthermore, comparison between $C_Q$s

of other analogous antimony and arsenic compounds show that it is unlikely compounds

SbPh$_4$Br and AsPh$_4$Br possess the same or a similar structure. As already mentioned,

isostructural AsH$_3$ and SbH$_3$ have $C_Q$($^{75}$As) $= -162.6$ MHz and $C_Q$($^{121}$Sb) = 460.3 MHz,

respectively.[118] The ratio between these two coupling constants, $C_Q$(SbH$_3$)/$C_Q$(AsH$_3$), is $-2.83$.

For the triphenylphosphines, AsPh$_3$ and SbPh$_3$, the ratio between the quadrupolar coupling

constants $C_Q$($^{75}$As)$_{NQR}$ $\approx$ 191.6 MHz (assuming $\eta_Q$ = 0) and $C_Q$($^{121}$Sb)$_{NQR}$ $\approx$ 503.4 MHz ($\eta_Q$ $\approx$

0.028) is $(-)2.63$.[150,151] The phosphides AsP and SbP (see Table 4.3) show similar results, with a

calculated ratio of $-2.50$. On the other hand, the ratio of the AsPh$_4$Br and SbPh$_4$Br $C_Q$ values is

$\approx$20.4, an order of magnitude larger, suggesting that the structures are not similar. It would

appear from the NMR data that, like other tetraphenylarsonium halides, AsPh$_4$Br is an ionic

compound in which the cation displays near tetrahedral symmetry, as opposed to the more covalent Sb−Br bonding and pentahedral coordination about antimony in SbPh$_4$Br.

**4.3.2.2 Arsenobetaine Bromide**

While the crystal structure of arsenobetaine bromide is unknown, arsenobetaine hydrate has been characterized via X-ray diffraction.[135] The arsenic atoms are located at a near-tetrahedral site, with As−C bond distances between 1.86 and 1.92 Å. The $^{75}$As NMR spectrum of arsenobetaine bromide actually shows a moderate $C_Q(^{75}$As$)$ even though the geometry about arsenic is near tetrahedral, a result of the large quadrupole moment of $^{75}$As. The geometry about arsenic is reflected by the small magnitude of $\Omega(^{75}$As$)$, i.e., it was not necessary to include effects from CS anisotropy in our simulated fit.

**4.3.2.3 Potassium Hexahydroxoantimonate(V)**

To date, there is no reported crystal structure for KSb(OH)$_6$. However, the structure for its sodium analogue, NaSb(OH)$_6$, is known.[152] NaSb(OH)$_6$ crystallizes in the tetragonal space group $P42/n$ with cell parameters $a = 8.029(2)$ Å and $c = 7.894(3)$ Å. In this structure, the antimony atoms reside in a near octahedral environment with Sb−O bond distances between 1.972 Å and 1.999 Å. Like AsPh$_4$Br, the Sb NMR spectra of KSb(OH)$_6$ give us insight into the crystal structure of this compound. The $C_Q(^{121}$Sb$)$ quadrupolar coupling constant determined here is moderate; clearly the antimony atoms do not reside in a crystallographic site with perfect octahedral symmetry. However, the electric field gradient in KSb(OH)$_6$ is similar in magnitude to what has been determined for the arsenic compounds AsPh$_4$Br and $(CH_3)_3AsCH_2CO_2H^+Br^-$ (Table 4.3), which deviate slightly from tetrahedral symmetry. The sensitivity of $C_Q$ to local

100

structure in the near-tetrahedral compounds indicates that though the antimony site in $KSb(OH)_6$ is not perfectly octahedral it is likely nearly so. The calculated EFG parameters of the $Sb(OH)6^-$ anion based on the crystal structure of $NaSb(OH)_6$ are $C_Q(^{121}Sb) = -28.1$ MHz and $\eta_Q(^{121}Sb) = 0.595$, close in magnitude to the experimental values for $KSb(OH)_6$ (Table 4.2).

## 4.4 Conclusions

There have been relatively few studies of antimony- and arsenic-containing compounds via $^{75}As$, $^{121}Sb$ and $^{123}Sb$ NMR spectroscopy. The spectra presented herein are the first published solid-state $^{121}Sb$ and $^{123}Sb$ NMR spectra for which $C_Q$ is appreciable, and an addition to the limited $^{75}As$ NMR data for solids. Insights were made into the solid-state structure of compounds $AsPh_4Br$, $KSb(OH)_6$, and $(CH_3)_3AsCH_2CO_2H^+Br^-$, while solid-state NMR data were consistent with the known structure of $SbPh_4Br$. From the NMR data it is clear that the arsenic compound $AsPh_4Br$, like other tetraphenylarsonium halides, bears more resemblance in the solid state to its phosphonium counterpart. This is shown by its relatively small value for $V_{ZZ}(^{75}As)$, especially when compared with the sizeable $V_{ZZ}(^{121}Sb)$ in the five-coordinate $SbPh_4Br$. The compound $KSb(OH)_6$ has an EFG comparable to the near-tetrahedral arsenic sites in $AsPh_4Br$ and $(CH_3)_3AsCH_2CO_2H^+Br^-$, suggesting that the symmetry about the antimony site is close to but deviates slightly from the predicted octahedral symmetry, similar to its sodium analogue, $NaSb(OH)_6$. Calculations performed using the programs ADF and CASTEP support these results. Through this work it is shown that characterization of both antimony and arsenic compounds via solid-state NMR spectroscopy is promising, though it does have its limitations. High magnetic field strengths and modern pulse engineering were pivotal in the acquisition of

these data, and with recent advances in hardware it is expected that acquiring $^{75}$As and $^{121,123}$Sb NMR spectra of solid-state compounds should become more practical.

## 4.5 Acknowledgments

# Chapter 5

## Spin-Spin Coupling Between Quadrupolar Nuclei in Solids: $^{11}$B$-^{75}$As Spin Pairs in Lewis Acid-Base Adducts

### 5.1 Introduction

Here, we present a $^{11}$B and $^{75}$As solid-state NMR study of five Lewis acid–base adducts containing triarylborane Lewis acids and a central boron–arsenic bond. These compounds were first synthesized and isolated by Conrad et al. in 2010[153] and are prototypical examples of arsenic-containing group 13–group 15 Lewis acid–base adducts. They are pseudotetrahedral at the arsenic and boron sites, with the general formula $R_3AsBR'_3$ (R = Me, Et, Ph; R′ = Ph, $C_6F_5$). We also re-examined the Lewis acid–base adduct $Ph_3AsBH_3$, previously studied via $^{11}$B NMR spectroscopy,[154] and report the first $^{75}$As NMR study of a Lewis base of the form $AsR_3$, the trigonal pyramidal $Ph_3As$. These arsenic-containing Lewis acid–base adducts may be of interest as group 13–group 15 adducts have been used for semiconductor fabrication via metal–organic chemical vapor deposition (MOCVD).[155] For the fabrication of semiconductors such as GaAs and InP, single-source adducts such as $Me_3GaAsMe_3$ have offered advantages over conventional MOCVD precursors (e.g., $AsH_3$ and $GaMe_3$), such as decreased precursor toxicity and improved stoichiometry control.[156] Though not routine for semiconductor production, use of Lewis acid–

base adducts has aided chemists in understanding surface growth mechanisms in these materials.[156]

Arsenic-75 and the most commonly studied NMR-active boron isotope, [11]B, are both quadrupolar nuclei ($I = 3/2$) and exist essentially as an isolated spin pair in these compounds. Pairs of quadrupolar nuclei[154,157-159] have not been studied nearly as extensively as spin-1/2 pairs or pairs that include one spin-1/2 and one quadrupolar nucleus.[160,161] However, a considerable amount of valuable information can be obtained from the NMR spectra of quadrupolar spin pairs. In any two-spin system that features spin–spin coupling to a quadrupolar nucleus that exhibits large $C_Q$ values, spectroscopists potentially have access to not only the magnitude of the quadrupolar, dipolar, and indirect spin–spin coupling interactions for both nuclei but also the signs of the quadrupolar and indirect spin–spin coupling constants.[162,163] In practice, in the case of pairs of two quadrupolar nuclei, quadrupolar line breadths and broadening often obscure spin–spin coupling information,[27,158,164] and interpreting the powder NMR spectrum arising from a quadrupolar spin-pair can be complicated due to the many parameters required to describe such spectra. In this study, samples were selected to minimize some of these complications. The Lewis acid–base adducts investigated here possess near-$C_3$ rotation symmetry about the As–B bond, the presence of which simplifies analysis of the resulting NMR powder spectra by confining the NMR tensor orientation within the molecular reference frame. These adducts therefore provide us the opportunity to study direct and indirect spin–spin coupling interactions between quadrupolar nuclei in detail.

We demonstrate that by using high magnetic field strengths and state-of-the-art pulse techniques one can carry out solid-state NMR measurements on isotopes which have been largely overlooked (e.g., [75]As). In addition to extracting relatively small values of spin–spin

coupling constants between quadrupolar nuclei, we demonstrate that $^{75}$As NMR spectra with central transition widths in excess of 30 MHz can be acquired (the largest NMR powder pattern width reported in the literature that we are aware of). While the focus of this chapter is on $^{11}$B and $^{75}$As NMR spectroscopy, the techniques illustrated here can be applied to many other quadrupolar nuclei that have large nuclear electric quadrupolar coupling constants (e.g., $^{121}$Sb, $^{209}$Bi). We sincerely hope that the methodology demonstrated here will encourage others to expand NMR studies of solids beyond traditional isotopes.

## 5.2 Background

The natural abundances of $^{75}$As and $^{11}$B, $C(^{75}$As$) = 100\%$ and $C(^{11}$B$) = 80.1(7)\%$, respectively, lend themselves favorably to the NMR experiment, as do their moderate frequency ratios, $\Xi(^{75}$As$) = 17.12\%$ and $\Xi(^{11}$B$) = 32.08\%$.[1] Table 5.1 provides a list of $^{75}$As and $^{11}$B NMR properties relevant to this study. Arsenic-75 has a moderate nuclear electric quadrupole moment and a fairly large Sternheimer antishielding factor ($\gamma_\infty = -7.09$)[165] which leads to generally large nuclear quadrupolar coupling constants (e.g., values on the order of 100 MHz or larger are common).[110,118,134,150,166-170] The muonic $Q(^{75}$As$) = 30.0(50)$ fm$^2$ currently recommended by IUPAC[60] is believed to be less precise than $Q(^{75}$As$) = 31.1(2)$ fm$^2$, recently determined from microwave spectroscopic data for AsP[110] and coupled-cluster calculations performed at the CCSD(T) level of theory.[115] The latter value will therefore be used in this work. Large $C_Q(^{75}$As$)$ values lead to broad and tedious-to-acquire $^{75}$As NMR spectra in solids as the breadth of the central transition ($m_I = 1/2$ to $m_I = -1/2$) can be on the order of MHz at the applied magnetic fields currently available (vide infra). In $^{75}$As NMR studies of liquids, large $C_Q(^{75}$As$)$ values lead to extremely efficient quadrupolar relaxation and broadening, limiting studies to $^{75}$As nuclei at

tetrahedral or octahedral sites since $C_Q \approx 0$ in those cases. Relatively few examples of $^{75}$As

NMR spectra of nonmetallic solids are documented in the NMR literature.[62,128-134,171-180] In

solids, $C_Q(^{75}$As$)$ values are mostly known from nuclear quadrupole resonance (NQR)[134,150,168-170]

and microwave spectroscopy experiments.[110,118,166,167] Note that information obtained from $^{75}$As

NQR studies of nonsymmetric molecules in powdered samples is limited, as $C_Q(^{75}$As$)$ and the

quadrupolar asymmetry parameter, $\eta_Q(^{75}$As$)$, are difficult to determine independently from

experiment due to $^{75}$As possessing a nuclear spin number of $I = 3/2$, giving the nucleus only one

NQR transition ($m_I = \pm 1/2 \leftrightarrow m_I = \pm 3/2$) dependent on both parameters in zero-field

conditions.[119] There are, however, techniques available to get around this limitation.[181] Arsenic-

75 NMR experiments both in solids and in the solution phase have primarily been focused thus

far on symmetric or pseudosymmetric compounds, i.e., those with approximate tetrahedral or

octahedral symmetry at arsenic.[68,106,107,109] Boron-11, on the other hand, has a relatively small

nuclear electric quadrupole moment,[60] making $^{11}$B NMR spectral acquisition a relatively easy

and straightforward process for both solid and liquid samples.

**Table 5.1.** ^{11}B and [75]As NMR properties.[1]

| Isotope | [11]B | [75]As |
|---|---|---|
| Natural Abundance, $C$ / % | 80.1 | 100 |
| Spin Number, $I$ | 3/2 | 3/2 |
| Quadrupole Moment, $Q$ / fm$^2$ | 4.07 | 31.1 |
| Gyromagnetic Ratio, $\gamma$ / 10$^7$ rad s$^{-1}$ T$^{-1}$ | 8.585 | 4.596 |
| Frequency Ratio, $\Xi$ / % | 32.083[a] | 17.122[b] |
| Resonance Frequency (21.14 T) / MHz | 288.8 | 154.1 |
| Resonance Frequency (11.75 T) / MHz | 160.4 | 85.6 |
| Resonance Frequency (7.05 T) / MHz | 96.2 | 51.4 |

[a] For 15% (by volume) $BF_3 \cdot Et_2O$ in $CDCl_3$.

[b] For 0.5 M $NaAsF_6$ in $CD_3CN$.

Under the *high-field approximation*, internal NMR interactions are assumed to be much smaller in magnitude than the Zeeman interaction and are therefore usually treated using perturbation theory.[30] Perturbation theory to second order has been used extensively to accurately produce simulated NMR spectra of quadrupolar nuclei;[108] third-order corrections only influence the satellite transitions[182] and have been measured.[183,184] However, the large $C_Q$([75]As) values of the adducts investigated here do not meet the high-field criteria. To describe a system using perturbation theory, the following relationship should be met[185]

$$\frac{|C_Q|}{4I(2I-1)|\nu_0|} \ll 1 \qquad 5.1$$

where $I$ is the spin quantum number of the quadrupolar nucleus and $|\nu_0|$ is the Larmor frequency of the quadrupolar nucleus. In the adducts considered in the present work, the smallest

$|C_Q(^{75}\text{As})|$ is 82 MHz (vide infra), which at $B_0 = 21.14$ T produces a ratio of approximately 0.04, while the largest experimentally determined $|C_Q(^{75}\text{As})| = 153$ MHz produces a ratio of approximately 0.08. At $B_0 = 7.05$ T, this ratio is 0.25. Clearly the high-field approximation is not valid for the quadrupolar interaction of the $^{75}$As nuclei at these external magnetic field strengths, and the influence of the quadrupolar interaction on NMR spectra cannot be modeled using perturbation theory. Since the Zeeman states are not true eigenfunctions of the Zeeman-quadrupolar (ZQ) Hamiltonian, the full ZQ Hamiltonian for the $^{75}$As quadrupolar interaction must be considered in order to properly analyze both $^{11}$B and $^{75}$As NMR spectra, since $^{11}$B is spin–spin coupled to $^{75}$As.[186] The Zeeman-quadrupolar Hamiltonian can be described, using the spherical tensor representation, as

$$\hat{\mathcal{H}}_{ZQ} = -\nu_0 \hat{I}_z + \frac{C_Q}{4I(2I-1)} \left[ \frac{1}{3}\sqrt{6}\left(3\hat{I}_z^2 - I(I+1)\right)V_0 + \left(\hat{I}_z\hat{I}_+ + \hat{I}_+\hat{I}_z\right)V_{-1} \right.$$
$$\left. - \left(\hat{I}_z\hat{I}_- + \hat{I}_-\hat{I}_z\right)V_1 + \hat{I}_+^2 V_{-2} + \hat{I}_-^2 V_2 \right]$$

5.2

where spherical tensor components $V_0$, $V_{\pm 1}$, and $V_{\pm 2}$ are

$$V_0 = 3\sqrt{\frac{1}{6}}V_{zz} \qquad\qquad 5.3$$

$$V_1 = -V_{xz} - iV_{yz} \qquad\qquad 5.4$$

$$V_{-1} = V_{xz} - iV_{yz} \qquad\qquad 5.5$$

$$V_2 = \frac{1}{2}\left(V_{xx} - V_{yy}\right) + iV_{xy} \qquad\qquad 5.6$$

$$V_{-2} = \frac{1}{2}\left(V_{xx} - V_{yy}\right) - iV_{xy} \qquad\qquad 5.7$$

following the work of Man[29] and Mehring.[30] From the diagonalization of the Zeeman-quadrupolar matrix, the eigenfunctions and eigenvalues of the ZQ Hamiltonian are obtained. The Zeeman-quadrupolar eigenfunctions are expressed in terms of Zeeman eigenfunctions

$$|n\rangle = \sum_{m=-I}^{I} (b_{mn} + ic_{mn})|m\rangle \qquad\qquad 5.8$$

where $b_{mn}$ and $c_{mn}$ are constants, $|m\rangle$ are the Zeeman states, and $|n\rangle$ represent the ZQ

eigenfunctions. These eigenfunctions are used in place of the Zeeman eigenfunctions for the

$^{75}$As nucleus in spin–spin coupling calculations, where the direct and indirect spin–spin coupling

is treated as a perturbation of $\hat{H}_{ZQ}$. The elements of the diagonalized matrix represent Zeeman-

quadrupolar energy levels and are used to simulate the $^{75}$As NMR powder spectra. This is

described in detail by Perras and Bryce.[27]

As the static magnetic field strength of commercially available instruments increases,

allowing faster acquisition of broad quadrupolar powder patterns, and as broadband pulse

sequences are developed,[46] the acquisition of solid-state NMR spectra that fall outside of the

high-field regime is becoming more practical. Recent examples of very broad quadrupolar

powder patterns in solids, acquired at $B_0 = 21.14$ T, include the $^{127}$I NMR spectrum of $SrI_2$, with

a breadth of approximately 10 MHz,[187] and the $^{185/187}$Re NMR spectrum of $NaReO_4$, spanning 15

MHz.[188] These two examples feature nuclear quadrupolar coupling constants of $C_Q(^{127}I) = 105.2$

MHz (site 1) and 214.0 MHz (site 2), $C_Q(^{185}Re) = 300.68$ MHz, and $C_Q(^{187}Re) = 284.54$ MHz,

with corresponding Larmor frequencies of $v_0(^{127}I) = 180.1$ MHz, $v_0(^{185}Re) = 202.7$ MHz, and

$v_0(^{187}Re) = 204.8$ MHz. In 2009, $^{209}$Bi NMR experiments were reported by Hamaed et al.,[189]

featuring compounds with $C_Q(^{209}Bi)$ values of up to 256 MHz. These NMR spectra span up to

4.5 MHz at $v_0 = 144.6$ MHz (21.14 T) and 15 MHz at $v_0 = 64.3$ MHz (9.4 T). A series of $^{35}$Cl

NMR spectra reported by Bryce and Perras in 2012 have central transition breadths of

approximately 7 MHz at 21.14 T, with $v_0(^{35}Cl) = 88.2$ MHz and $C_Q(^{35}Cl)$ between 66 and 75

MHz.[190] Finally, a recent study we have conducted features the $^{121}$Sb NMR spectrum of solid

Ph$_4$SbBr, whose central transition spans 5.5 MHz with a $C_Q$($^{121}$Sb) value of 159 MHz ($v_0$($^{121}$Sb)

= 215.4 MHz).[62] Note that the breadth of a quadrupolar powder pattern at a specific magnetic

field strength depends not only on the magnitude of the quadrupolar interaction (i.e., values of

$C_Q$ and $\eta_Q$), but also on the spin number of the nucleus, with the total width of the powder pattern

decreasing for increasing values of $I$.[146] The central transition NMR spectra featured in this

study are the broadest (in terms of MHz) reported in the current NMR literature for the $^{75}$As

nucleus, and among the broadest spectra reported in the NMR literature for any nucleus.

When it comes to relating experimental NMR spectra to molecular or crystallographic

structure, the direct dipolar interaction is uniquely useful since it depends on only one variable,

the internuclear distance between the coupled nuclei,[161]

$$R_{DD} = \frac{\mu_0 \gamma_1 \gamma_2 \hbar}{8\pi^2} \langle \frac{1}{r_{1,2}^3} \rangle \qquad 5.9$$

and hence can be used to determine structural information about the studied system. However,

dipolar couplings are rarely the dominant interaction contributing to solid-state NMR spectral

lineshapes of quadrupolar nuclei, and it is often difficult or impossible to quantify this interaction

in the presence of others. One method of determining the effective dipolar coupling constant,

$R_{eff}$, between quadrupolar nuclei (or one quadrupolar and one spin-1/2 nucleus), is to take

advantage of residual dipolar coupling under magic angle spinning (MAS) conditions.[160,191] In

MAS NMR spectra, residual dipolar coupling manifests itself as additional orientation-dependent

frequency shifts proportional to the magnitude of the quadrupolar interaction for the coupled

nucleus. Residual dipolar coupling arises from incomplete averaging of the direct dipolar

interaction under MAS conditions due to the off-Zeeman quantization axis of a quadrupolar

nucleus' nuclear spin angular momentum. Such spectra can also be utilized to obtain difficult-

to-extract information about other NMR interactions. The effective dipolar coupling constant, $R_{\text{eff}}$, is related to the direct dipolar coupling constant by

$$R_{\text{eff}} = R_{DD} - \frac{\Delta J}{3} \qquad\qquad 5.10$$

if the dipolar and $J$ tensors are coincident. See Harris and Olivieri[160] for a description of the case where they are not coincident. The Hamiltonian for the direct dipolar and indirect spin–spin interactions are of the same form,[30,192]

$$\hat{\mathcal{H}}_{DD} = R_{DD}\hat{I}_1 \cdot \overline{\overline{D}} \cdot \hat{I}_2 \qquad\qquad 5.11$$

and

$$\hat{\mathcal{H}}_J = \hat{I}_1 \cdot \overline{\overline{J}} \cdot \hat{I}_2. \qquad\qquad 5.12$$

As a consequence, the anisotropy in the indirect spin–spin coupling in general cannot be experimentally separated from the direct dipolar interaction. Internuclear distances between non-hydrogen atoms can usually be determined accurately from X-ray diffraction experiments allowing calculation of $R_{DD}$ (Equation 5.9), and therefore, it is sometimes possible, when $\Delta J$ is large, to extract its value from the experimental effective dipolar coupling constant (Equation 5.10). Where perturbation theory fails to describe the quadrupolar interaction of the coupled nucleus and an exact treatment is instead used, it is also possible to obtain the sign of $J_{\text{iso}}$.[27,162-164] In most cases, $C_Q$ values are obtained by observing the NMR powder pattern of the central transition of a nucleus, whose breadth is dependent on the square of $C_Q$ and the inverse of $\nu_0$. As such, the signs of nuclear quadrupolar coupling constants are typically unavailable from NMR experiments.[163,193] Since the residual dipolar splitting depends directly on the nuclear quadrupolar coupling constant of the coupled nucleus, it is sometimes possible to determine the sign of $C_Q$ of the coupled nucleus. In the systems studied here, ^{11}B NMR spectra acquired using the MAS technique exhibit residual dipolar coupling to [75]As. By examining ^{11}B NMR spectra of

As–B Lewis acid–base adducts, we demonstrate that it is possible to extract values for $R_{\text{eff}}(^{75}\text{As},^{11}\text{B})$, the sign of $C_Q(^{75}\text{As})$, and $^1J(^{75}\text{As},^{11}\text{B})$ values, including their sign.

Solid-state NMR measurements of residual dipolar couplings can be extremely useful for quantifying the above mentioned NMR parameters; however, these types of measurements have been applied mainly to systems involving one spin-1/2 and one quadrupolar nucleus.[160] Studies of quadrupolar spin pairs are relatively few in the literature, and even rarer for cases that fall outside of the high-field approximation. A $^{11}$B 3QMAS NMR study of the boron–arsenic spin pair of $H_3BAsPh_3$ was reported by Wi et al. in 2001.[154] In their work, the $^{75}$As nucleus was treated exactly using the full ZQ Hamiltonian whereas the high-field approximation was assumed for $^{11}$B, whose quadrupolar interaction was treated using perturbation theory. In 2011, Perras and Bryce published a solid-state NMR study of B-chlorocatecholborane under $^{11}$B MAS and DOR conditions.[164] The quadrupolar interaction for $^{11}$B was again treated using a perturbation theory approach, while the full ZQ interaction for $^{35}$Cl was considered. These authors published a subsequent study in 2013,[27] wherein spin–spin couplings between several different quadrupolar nuclei were measured. In 2013, Jakobsen et al. reported an $^{17}$O NMR study of $^{17}$O-$^{185/187}$Re spin pairs in $KReO_4$ and $NH_4ReO_4$.[194] The present contribution expands upon this little-investigated field of study, and as well is an addition to the relatively small body of NMR literature on the $^{75}$As nucleus.

## 5.3 Experimental Section

### 5.3.1 Materials

$Me_3AsB(C_6F_5)_3$, $Et_3AsB(C_6F_5)_3$, $Ph_3AsB(C_6F_5)_3$, $Me_3AsBPh_3$, and $Ph_3AsBPh_3$ were synthesized and characterized by Burford and co-workers[153] under an atmosphere of argon. The adduct $Ph_3AsBH_3$ was synthesized according to the literature[195] under an atmosphere of nitrogen and was characterized via ^{11}B NMR spectroscopy in a $C_6D_6$ solution. A sample of solid polycrystalline triphenylarsine was obtained from Sigma-Aldrich, characterized via ^{13}C solution NMR spectroscopy, and used without further purification. Lewis acid–base adducts were stored in a refrigerator when not in use. Crystal structures of $Et_3AsB(C_6F_5)_3$ and $Me_3AsBPh_3$ are available[153] and indicate near-$C_3$ rotation symmetry about the As–B bond. These two Lewis acid–base adducts belong to space groups $P21/n$ and $P\bar{3}$, respectively, and have As–B bond lengths of 2.1905(18) Å and 2.148(3) Å. The coordination about the As–B bond is close to eclipsed, with the smallest C–As–B–C angle of 9.89(13)° belonging to $Et_3AsB(C_6F_5)_3$.[153] The crystal structures of Lewis acid–base adducts $Me_3AsB(C_6F_5)_3$, $Ph_3AsB(C_6F_5)_3$, $Ph_3AsBPh_3$, and $Ph_3AsBH_3$ are not yet available. For the structures of the corresponding borane–phosphine adducts $Me_3PB(C_6F_5)_3$ and $Ph_3PB(C_6F_5)_3$, see Chase et al.[196] and Jacobsen et al.,[197] respectively. The phosphines, like the known arsines, possess near-$C_3$ symmetry and near-eclipsed conformation about the P–B bond. The C–P–B bond angles in $Ph_3PB(C_6F_5)_3$ range from 113.3° to 114.1°. For the structure of $Ph_3PBH_3$, see Huffman et al.[198] $Ph_3PBH_3$ crystallizes in space group $P\bar{1}$ and has two crystallographically nonequivalent molecules in the unit cell, both of which possess near-$C_3$ rotation symmetry about the P–B bond direction. The crystal structure of triphenylarsine, $Ph_3As$, indicates four nonequivalent arsenic sites within the unit cell.[199] Triphenylarsine crystallizes in the space group $P\bar{1}$, and the triphenylarsine molecules have near-

$C_3$ rotation symmetry at arsenic and As–C bond lengths that vary between 1.935 and 1.966 Å, with an average value of 1.957 Å.

### 5.3.2 NMR Measurements

All samples were packed in 4 mm o.d. zirconia rotors under an atmosphere of either argon or dry nitrogen, with the exception of triphenylarsine, which was packed under ambient atmosphere. Boron-11 NMR spectra were collected at magnetic field strengths of $B_0 = 7.05$ and 11.75 T using 4 mm MAS probes operating in double resonance mode. The sample spinning frequency was $v_{rot} = 10$ kHz, and the Bloch pulse sequence with a TPPM proton decoupling scheme at a frequency of ca. 60 kHz was used. Boron-11 chemical shifts were referenced to $BF_3$:$Et_2O$ ($\delta_{iso} = 0$ ppm) by setting the isotropic chemical shift of secondary reference $NaBH_4$(s) to $\delta_{iso} = -42.0$ ppm.[200] A recycle delay of 30 s was used for each sample. Note that some probe components include boron-containing materials, and thus a significant background signal is present in ^{11}B NMR spectra acquired using these probes. In our case, the desired signal overlapped with the background signal, and thus, a background correction was required. Spectra of the empty probe were acquired under experimental conditions identical to those used for each of the adducts and were subsequently subtracted from the spectra of each sample in order to produce the background-free spectra.

**Table 5.2.** Details of $^{11}$B and $^{75}$As NMR experiments.

| | $^{75}$As | | | | $^{11}$B | |
| --- | --- | --- | --- | --- | --- | --- |
| | No. Transients/step | No. Steps | Time/step | Probe | No. Transients ($B_0$ = 7.05 T) | No. Transients ($B_0$ = 11.75 T) |
| Me$_3$AsB(C$_6$F$_5$)$_3$ | 4096 | 16 | 35 minutes | H/X | 3280 | 1536 |
| Et$_3$AsB(C$_6$F$_5$)$_3$ | 49 152 | 3 | 7 hours | H/X | 2048 | 100 |
| Ph$_3$AsB(C$_6$F$_5$)$_3$ | 4096 | 17 | 35 minutes | H/X | 2048 | 400 |
| Me$_3$AsBPh$_3$ | 4096 | 1 | 35 minutes | H/X | 4096 | 3860 |
| Ph$_3$AsBPh$_3$ | 8192 | 7 | 70 minutes | H/X | 2752 | 2048 |
| Ph$_3$AsBH$_3$ | 2048 | 24 | 17 minutes | H/X | 628 | 102 |
| | 6144 | 12 | 26 minutes | X | - | - |
| Ph$_3$As | 4096 | 65 | 17 minutes | X | - | - |

Arsenic-75 NMR experiments were carried out at $B_0 = 21.14$ T at the National Ultrahigh-Field NMR Facility for Solids in Ottawa, ON.[2] These experiments were performed on a Bruker Avance II NMR spectrometer using either a home-built stationary 5 mm H/X or stationary 5 mm X (single-channel) NMR probe. Arsenic-75 NMR spectra were referenced using 1 M $KAsF_6$ in MeCN ($\delta_{iso} = 0$ ppm). All $^{75}$As NMR spectra were acquired using the WURST-QCPMG pulse sequence,[45] and those acquired on the H/X probe were acquired with proton decoupling. The decoupling frequency, $\gamma(^1H)B_1/2\pi$, was approximately 60 kHz. Applying $^1$H decoupling reduces effects on the $^{75}$As effective transverse relaxation time caused by the heteronuclear dipolar coupling relaxation mechanism, which is particularly relevant for these compounds. The bandwidth of the WURST-QCPMG pulse was 2 MHz, with a sweep from high to low frequency. For the Lewis acid–base adducts, 172 echoes were collected in the time domain for all samples except $Et_3AsB(C_6F_5)_3$, for which 48 echoes were acquired. The frequency domain spikelet separation was 8 kHz, and the recycle delays were 0.5 s (H/X probe) or 0.25 s (X probe). All spectra of triarylborane adducts were acquired on the double-channel H/X probe, whereas the low-frequency portion of the spectrum of $Ph_3AsBH_3$ was acquired on the single-channel probe. Systematic moving of the transmitter offset was employed to collect the entire frequency-domain spectrum,[47] which spanned several MHz in all cases. The transmitter offset was moved by 560 kHz for each step and the resulting spectra were added together to produce the final spectrum for each compound. For the compounds $Me_3AsBPh_3$ and $Ph_3AsBPh_3$, acquisition of the entire spectrum was not possible due to the limited tuning frequency range of the H/X probe and fast $T_2$ relaxation of $^{75}$As nuclei which prevented feasible spectral acquisition without proton decoupling. For the compound $Et_3AsB(C_6F_5)_3$, low signal-to-noise and lengthy experiment times due to rapid spin–spin relaxation prevented acquisition of the entire spectrum in a reasonable

time frame.  Thus, only the higher-frequency region of these spectra was collected (see discussion).  Arsenic-75 NMR spectra of triphenylarsine were collected in a manner similar to those for the adducts, using the single-channel probe with a recycle delay of 0.25 s, 96 echoes in the time domain, a 20 kHz spikelet separation in the frequency domain, and with transmitter steps of 500 kHz.  In addition, more detailed spectra of the high- and low-frequency discontinuities were acquired by using transmitter steps of 200 kHz.  The $^{75}$As NMR spectra of the high- and low-frequency discontinuities consisted of 14 and 22 steps, respectively.  The acquisition of each complete $^{75}$As NMR powder pattern required anywhere from 10 to 20 h of spectrometer time at $B_0 = 21.14$ T.  Further experimental details are given in Table 5.2.

### 5.3.3 Simulations and Calculations

Experimental $^{75}$As NMR spectra were simulated using QUEST,[19] which diagonalizes the full Zeeman-quadrupolar Hamiltonian and can accurately simulate both NMR and NQR spectra. Simulations of the experimental $^{11}$B NMR spectra were carried out using a program provided by the Bryce research group at the University of Ottawa.  This program treats the $^{75}$As quadrupolar interaction exactly, while retaining a perturbation theory approach for describing the $^{11}$B quadrupolar interaction, which is much smaller.  The specifics of these simulations, including a detailed description of the theory, are discussed by Perras and Bryce.[27,164]  Uncertainties in NMR parameters were determined by visual inspection of the agreement between simulated and experimental NMR spectra.

Relativistic DFT calculations using the zeroth order regular approximation (ZORA) to the Dirac equation were carried out on $Et_3AsB(C_6F_5)_3$ and $Me_3AsBPh_3$ to estimate the magnetic shielding and EFG tensors.  These were performed with the ADF program package[51-53] using the

BP86 functional in the generalized gradient approximation (GGA) and the ZORA/QZ4P basis

set. Calculations were carried out with hydrogen atom positions in the crystal structures

modified to $r_{CH} = 1.09$ Å (alkyl hydrogen atoms) or $r_{CH} = 1.08$ Å (aryl hydrogen atoms), and all

heavier atoms were at the positions given by the diffraction data. The CASTEP program[54-57] in

the Materials Studio 4.4 environment was used to calculate EFG and magnetic shielding tensor

parameters for these two compounds, as well as for $Ph_3As$ and several models of $Ph_3AsBH_3$.

The latter were created based on the known structure of $Me_3AsBPh_3$ and were set up by

exchanging the arsenic and boron atom positions, replacing the methyl groups with hydrogen

atoms, and adjusting the As–Ph and B–H bond lengths. After this preparation, a full geometry

optimization was carried out in three different scenarios using either a trigonal unit cell ($P\bar{3}$,

identical to that of $Me_3AsBPh_3$), a primitive unit cell ($P1$), or an isolated molecule (gas phase).

Note that the unit cell parameters for $Ph_3AsBH_3$ are not known, and thus, these models may not

reflect the true crystal packing of $Ph_3AsBH_3$ molecules. Due to large residual forces on arsenic

atoms in calculations using the experimental geometry of triphenylarsine, a full geometry

optimization of atom positions was carried out while the unit cell parameters were kept constant.

All CASTEP calculations used a coarse accuracy basis set due to the volume of the unit cells.

Cutoff energies for Lewis acid–base adducts were 250 eV, and the cutoff energy for

triphenylarsine was 200.0 eV. The Perdew, Burke, and Ernzerhof (PBE) functional in the

generalized gradient approximation was used to calculate the exchange-correlation energy.[58,59]

## 5.4 Results and Discussion

The main focus of this research involves analyzing the ^{11}B MAS NMR spectra of the

Lewis acid–base adducts in order to quantify arsenic–boron spin–spin coupling interactions, for

which knowledge of $^{75}$As quadrupolar parameters is necessary. It is therefore logical to first discuss the acquisition and analysis of $^{75}$As NMR spectra. Following this, the $^{11}$B NMR spectra will be discussed, and finally, the structure of the Lewis acid–base adducts in the solution and solid phases will be touched on. A summary of the experimental $^{11}$B and $^{75}$As NMR parameters for the Lewis acid–base adducts is given in Table 5.3, and experimental $^{75}$As NMR parameters for Ph$_3$As are given in Table 5.4. Boron-11 and arsenic-75 NMR spectral simulations fit the experimental spectra well. The $^{11}$B NMR spectra acquired at multiple magnetic field strengths were simulated with consistent parameters within the experimental errors given in Table 5.3.

**Table 5.3.** Experimental $^{11}$B and $^{75}$As NMR parameters for Lewis acid-base adducts.

| | Me$_3$AsB(C$_6$F$_5$)$_3$ | Et$_3$AsB(C$_6$F$_5$)$_3$ | Ph$_3$AsB(C$_6$F$_5$)$_3$ | Me$_3$AsBPh$_3$ | Ph$_3$AsBPh$_3$ | Ph$_3$AsBH$_3$ (site 1) | (site 2) |
|---|---|---|---|---|---|---|---|
| $C_Q(^{75}$As$)$ / MHz | $-91.8 \pm 0.5$ | $-82 \pm 2^a$ | $-101.7 \pm 1$ | $-125 \pm 1$ | $-146 \pm 1$ | $-151.4 \pm 1$ | $-153.2 \pm 1$ |
| $\eta(^{75}$As$)$ | $0 \pm 0.01$ | $0.08 \pm 0.01$ | $0.017 \pm 0.01$ | $0 \pm 0.01$ | $0.05 \pm 0.01$ | $0 \pm 0.01$ | $0 \pm 0.01$ |
| $\delta_{iso}(^{75}$As$)$ / ppm | $150 \pm 100$ | $0^b$ | $250 \pm 100$ | $0^b$ | $0^b$ | $475 \pm 100$ | $350 \pm 100$ |
| $C_Q(^{11}$B$)$ / MHz | $1.30 \pm 0.01$ | $1.34 \pm 0.02$ | $2.05 \pm 0.02$ | $2.0 \pm 0.1$ | $2.8 \pm 0.1$ | $1.85 \pm 0.05$ | |
| $\eta(^{11}$B$)$ | $0 \pm 0.06$ | $0 \pm 0.1$ | $0 \pm 0.05$ | $0 \pm 0.1$ | $0 \pm 0.1$ | $0 \pm 0.1$ | |
| $\delta_{iso}(^{11}$B$)$ / ppm | $-13.2 \pm 0.5$ | $-12.2 \pm 0.5$ | $-3.1 \pm 0.5$ | $-0.25 \pm 0.5$ | $9.3 \pm 0.5$ | $-34.6 \pm 0.5$ | |
| $R_{eff}(^{75}$As,$^{11}$B$)$ / Hz | $610 \pm 20$ | $-^c$ | $500 \pm 20$ | $590 \pm 40$ | $520 \pm 40$ | $700 \pm 40$ | |
| $^1J(^{75}$As,$^{11}$B$)$ / Hz | $50 \pm 15$ | $-^c$ | $25 \pm 10$ | $0 \pm 30$ | $0 \pm 40$ | $20 \pm 20$ | |

$^a$ Negative based on DFT calculations.

$^b$ Not determined. Error in $C_Q(^{75}$As$)$ determined from simulating $^{75}$As spectra at edges of $^{75}$As chemical shift range, see text.

$^c$ Not observed due to short $T_2(^{75}$As$)$, see text.

**Table 5.4.** Experimental $^{75}$As NMR parameters for Ph$_3$As.

|  | (site 1) | (site 2) | (site 3) | (site 4) |
|---|---|---|---|---|
| $C_Q(^{75}\text{As})$ / MHz | $193.5 \pm 2$ | $194.2 \pm 2$ | $194.2 \pm 2$ | $194.4 \pm 2$ |
| $\eta(^{75}\text{As})$ | $0.038 \pm 0.05$ | $0.022 \pm 0.05$ | $0.043 \pm 0.05$ | $0.03 \pm 0.05$ |
| $\delta_{\text{iso}}(^{75}\text{As})$ / ppm | $150 \pm 300$ | $150 \pm 300$ | $150 \pm 300$ | $150 \pm 300$ |

### 5.4.1 Arsenic-75 NMR Spectra

Experimental and simulated $^{75}$As NMR spectra of Ph$_3$As, Ph$_3$AsBH$_3$, and Ph$_3$AsB(C$_6$F$_5$)$_3$ are shown in Figure 5.1. Arsenic-75 NMR spectra of the remaining Lewis acid–base adducts are shown in Figure 5.2. Acquiring spectra with central transition line widths on the order of MHz is not routine and thus it is important to demonstrate that with the correct experimental conditions, acquisition of these spectra is feasible. Arsenic-75 NMR spectra of the triarylborane Lewis acid–base adducts acquired at $B_0 = 21.14$ T possessed total central transition breadths between 6.1 and 18.7 MHz, and that for Ph$_3$AsBH$_3$ was approximately 19.5 MHz (Figure 5.1). Though the acquisition of the $^{75}$As NMR spectra was expected to be a difficult task based on this breadth, the spectral quality is relatively high. This is especially noteworthy given several other challenges that were encountered, including rapid spin–spin relaxation in some samples, low sample volume (ca. 10 to 100 mg), and rather dilute $^{75}$As nuclei in each sample. Rapid spin–spin relaxation of $^{75}$As ($T_2$ values on the order of µs to ms) was observed even with proton decoupling, though this is not surprising given the magnitude of the experimental $C_Q(^{75}\text{As})$ values. Experimental spectra clearly show quadrupolar discontinuities ("horns") and the spectra of Ph$_3$AsB(C$_6$F$_5$)$_3$ and Ph$_3$AsBH$_3$ possess an unambiguous chemical shift discontinuity (Figure 5.1). Simulating the $^{75}$As NMR spectra was therefore a relatively straightforward task. The

$C_Q(^{75}$As) values for the triarylborane adducts ranged from $-82 \pm 2$ MHz to $-146 \pm 1$ MHz. These values belonged to the compounds $Et_3AsB(C_6F_5)_3$ and $Ph_3AsBPh_3$, respectively. The largest $C_Q(^{75}$As) values were for the two triphenylborane adducts, and the $C_Q(^{75}$As) values determined for the triphenylarsine adducts were the largest in their respective triarylborane series. The $^{75}$As NMR spectrum of $Ph_3AsBH_3$ (Figure 5.1) indicates that there are two crystallographically nonequivalent sites with axial electric field gradient tensors (i.e., $\eta_Q(^{75}$As) = $0.00 \pm 0.01$) and $C_Q(^{75}$As) values of $-151.4 \pm 1$ MHz and $-153.2 \pm 1$ MHz. Signs for all but the smallest $C_Q(^{75}$As) value were determined to be negative through simulation of the $^{11}$B NMR spectra (discussed below). It is reasonable to assume that the sign of $C_Q(^{75}$As) for $Et_3AsB(C_6F_5)_3$ is also negative based on DFT calculations, which agreed with the experimental $C_Q(^{75}$As) values for the other adducts (see Table 5.5). $\eta_Q(^{75}$As) values determined experimentally for $Me_3AsBPh_3$ and $Me_3AsB(C_6F_5)_3$ were zero, suggesting that the compounds possess $C_3$ or very close to $C_3$ symmetry about the As–B bond. Note that the angle between $V_{ZZ}(^{75}$As) and the arsenic–boron bond in $Me_3AsBPh_3$ calculated with the ADF program is $0.1°$, a negligible deviation from what would be expected in a perfect $C_3$ environment. The $^{75}$As NMR data indicate that arsenic atoms bonded to groups −Et and −Ph show nonzero asymmetry parameters, with $\eta_Q(^{75}$As) = 0.08, 0.017, and 0.05 for $Et_3AsB(C_6F_5)_3$, $Ph_3AsB(C_6F_5)_3$, and $Ph_3AsBPh_3$, respectively. Nevertheless, values of $\eta_Q(^{75}$As) < 0.10 point to near-axial symmetry about the As–B bond. Arsenic-75 isotropic chemical shift values determined for $Me_3AsB(C_6F_5)_3$ and $Ph_3AsB(C_6F_5)_3$ were $150 \pm 100$ ppm and $250 \pm 100$ ppm. The two sites in $Ph_3AsBH_3$ have $\delta_{iso}(^{75}$As) values of $350 \pm 100$ and $475 \pm 100$ ppm (see Table 5.3). With respect to the precision of these values, note that at $B_0$ = 21.14 T, 1.0 ppm in an $^{75}$As NMR spectrum covers approximately 154 Hz. Our uncertainty of 200 ppm in $\delta_{iso}(^{75}$As) values covers an area of approximately 30.8 kHz ($\approx$ four spikelets), small

compared to the overall $^{75}$As NMR central transition line widths, which are on the order of MHz. $\delta_{iso}(^{75}$As) values for $Et_3AsB(C_6F_5)_3$, $Me_3AsBPh_3$, and $Ph_3AsBPh_3$ were assumed to be zero. This assumption has negligible influence on our experimental values of $C_Q(^{75}$As) and $\eta_Q(^{75}$As) (vide infra).
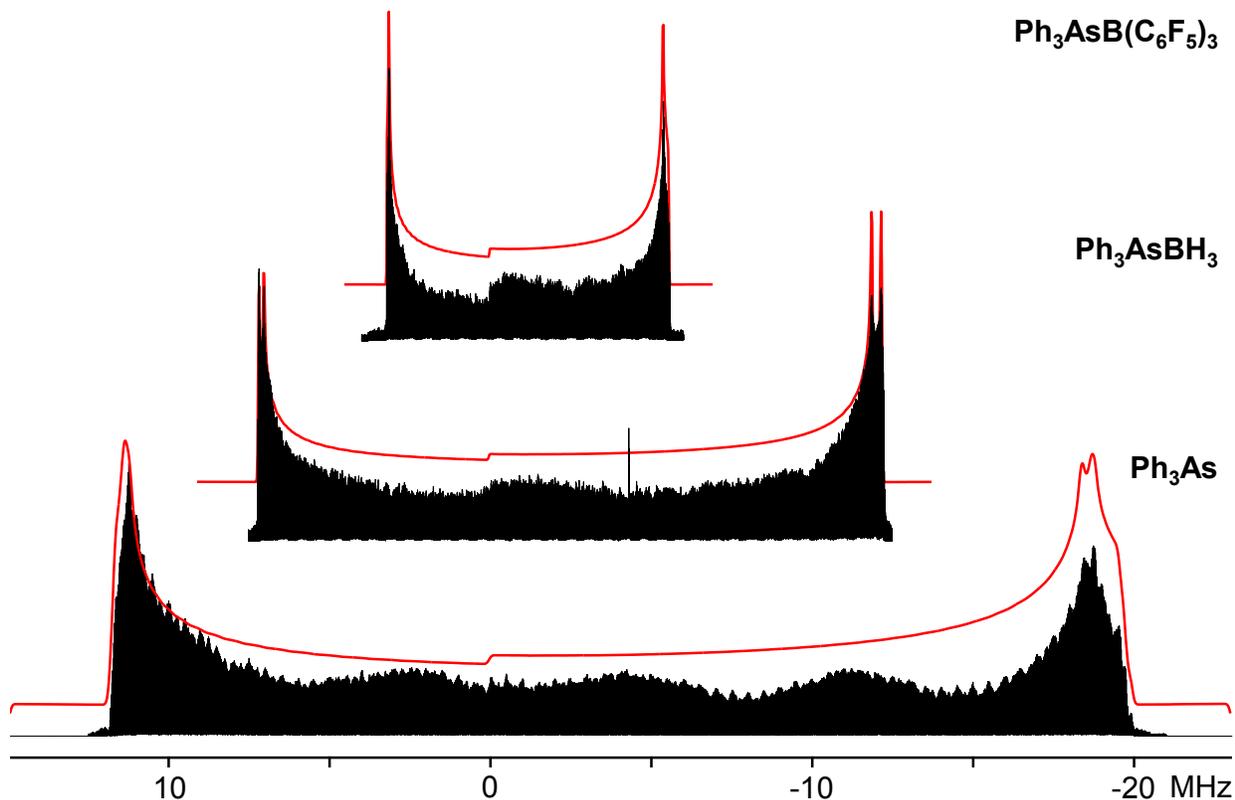


**Figure 5.1.** Experimental and simulated $^{75}$As NMR spectra of powdered $Ph_3AsB(C_6F_5)_3$, $Ph_3AsBH_3$, and $Ph_3As$ samples. Spectra were acquired using the WURST-QCPMG pulse sequence with proton decoupling at $B_0 = 21.14$ T and simulated using QUEST software. See Tables 5.3 and 5.4 for the simulation parameters.
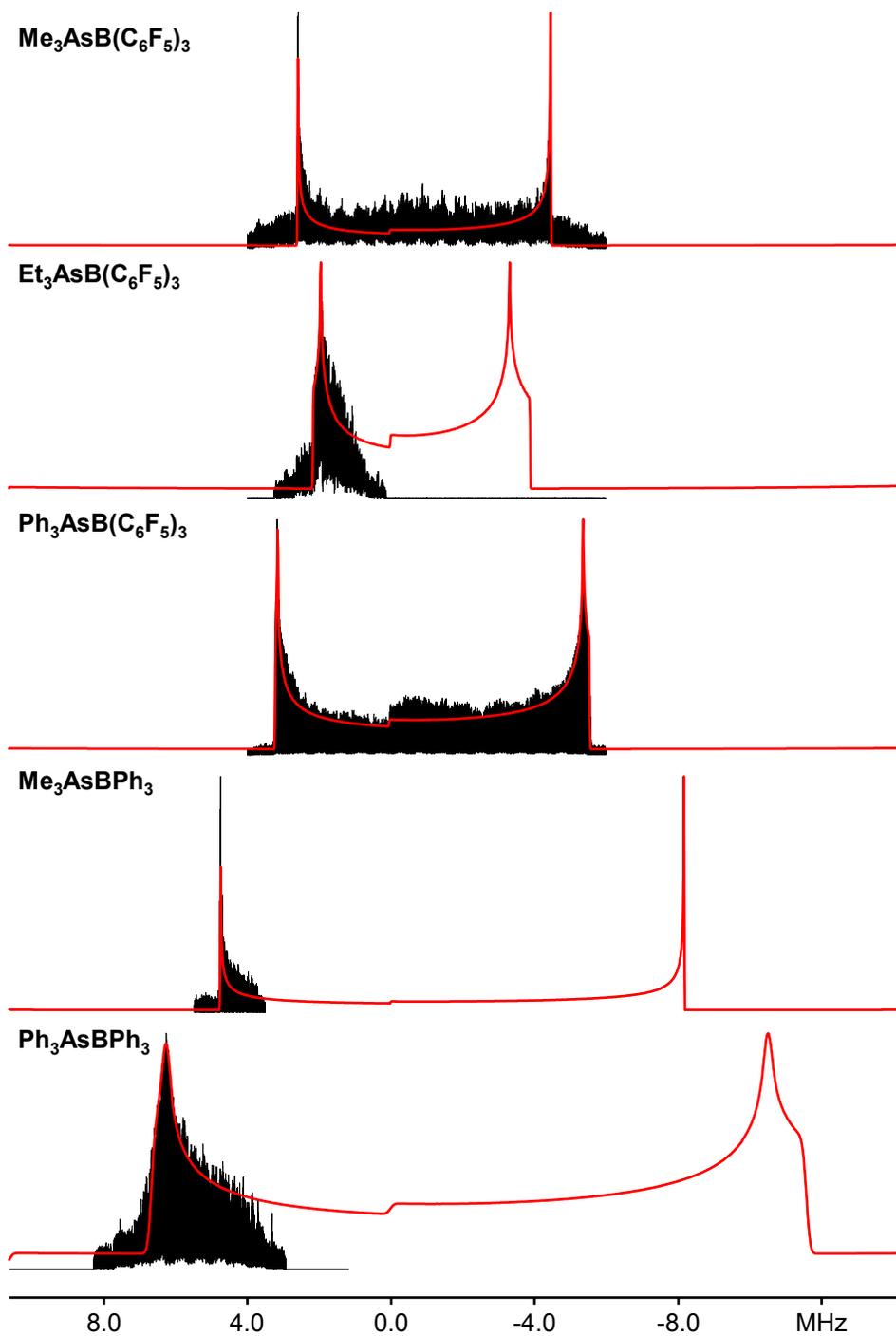
**Figure 5.2.** Experimental and simulated $^{75}$As NMR spectra of powdered $Me_3AsB(C_6F_5)_3$, $Et_3AsB(C_6F_5)_3$, $Ph_3AsB(C_6F_5)_3$, $Me_3AsBPh_3$, and $Ph_3AsBPh_3$ samples. Spectra were acquired using the WURST-QCPMG pulse sequence with proton decoupling at $B_0 = 21.14$ T and simulated using the QUEST program.

124

**Ph₃As**

| 14.0 | 10.0 | 6.0 | -16.0 | -20.0 | MHz |
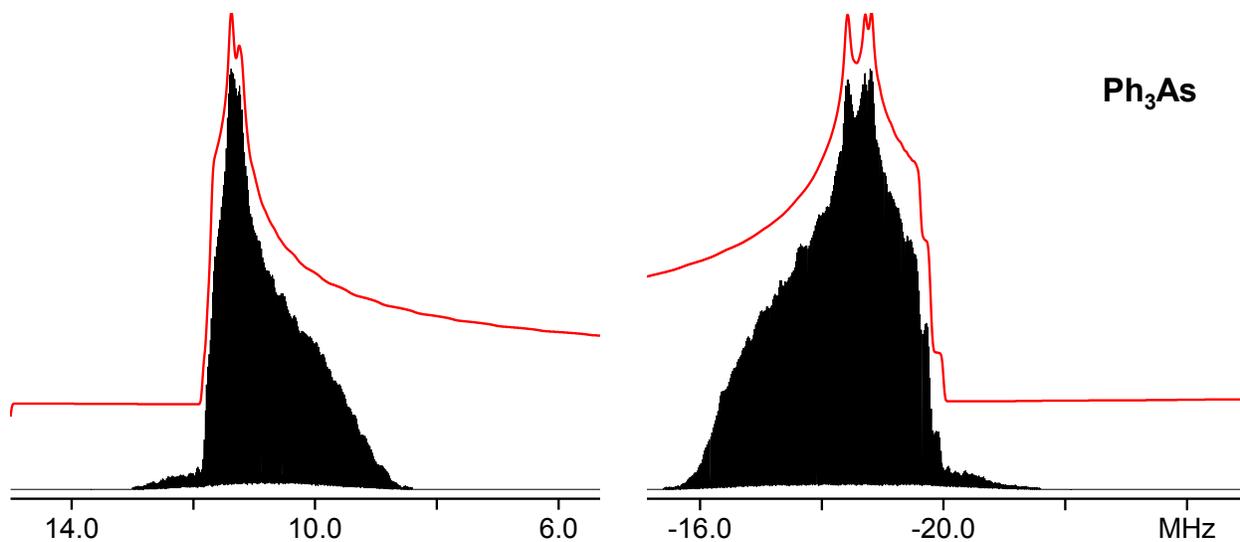
**Figure 5.3.** Experimental (lower traces) and simulated (upper traces) $^{75}$As NMR spectra of solid polycrystalline triphenylarsine acquired at $B_0 = 21.14$ T with higher definition quadrupolar singularities using the WURST-QCPMG pulse sequence. The QUEST program was used to carry out the simulation. The total spectral breadth is ca. 31.7 MHz

**Table 5.5.** Calculated NMR parameters for $Et_3AsB(C_6F_5)_3$, $Me_3AsBPh_3$, $Ph_3AsBH_3$, and $Ph_3As$.

| | | $C_Q(^{75}As)^a$ / MHz | $\eta(^{75}As)$ | $\sigma_{iso}(^{75}As)$ / ppm | $\Omega(^{75}As)$ / ppm | $C_Q(^{11}B)^a$ / MHz | $\eta(^{11}B)$ |
|---|---|---|---|---|---|---|---|
| $Et_3AsB(C_6F_5)_3$ | Exp. | $(\pm)82 \pm 2$ | $0.08 \pm 0.01$ | – | $< 800$ | $1.34 \pm 0.02$ | $< 0.1$ |
| | ADF | $-83.9$ | 0.03 | 1297 | 116 | 1.60 | 0.009 |
| | CASTEP | $-66.3$ | 0.06 | 1330 | 117 | 1.53 | 0.04 |
| $Me_3AsBPh_3$ | Exp. | $-125 \pm 1$ | $< 0.01$ | – | $< 800$ | $2.0 \pm 0.1$ | $< 0.1$ |
| | ADF | $-133.0$ | 0.01 | 1342 | 37 | 2.43 | 0.009 |
| | CASTEP | $-106.5$ | 0.01 | 1401 | 9 | 2.32 | 0.01 |
| $Ph_3AsBH_3$ | Exp. (site 1) | $-151.4 \pm 1$ | $< 0.01$ | – | $< 800$ | $1.85 \pm 0.05$ | $< 0.1$ |
| | Exp. (site 2) | $-153.2 \pm 1$ | $< 0.01$ | – | $< 800$ | – | – |
| | CASTEP ($P\bar{3}$) | $-135.4$ | 0.00 | 1224 | 77 | 2.40 | 0.01 |
| | CASTEP (P1, site 1) | $-138.5$ | 0.18 | 1223 | 87 | 2.35 | 0.01 |
| | CASTEP (P1, site 2) | $-138.5$ | 0.18 | 1223 | 87 | 2.35 | 0.01 |
| | CASTEP (gas phase) | $-143.2$ | 0.12 | 1238 | 136 | 2.39 | 0.01 |
| $Ph_3As^b$ | Exp. (site 1) | $193.5 \pm 2$ | 0.038 | – | $< 800$ | – | – |
| | Exp. (site 2) | $194.2 \pm 2$ | 0.022 | – | $< 800$ | – | – |
| | Exp. (site 3) | $194.2 \pm 2$ | 0.043 | – | $< 800$ | – | – |
| | Exp. (site 4) | $194.4 \pm 2$ | 0.03 | – | $< 800$ | – | – |
| | CASTEP (site 1) | 167.2 | 0.06 | 1257 | 64 | – | – |
| | CASTEP (site 2) | 168.3 | 0.10 | 1253 | 90 | – | – |
| | CASTEP (site 3) | 170.0 | 0.12 | 1241 | 154 | – | – |
| | CASTEP (site 4) | 170.8 | 0.13 | 1223 | 103 | – | – |

[a] The results of calculations have been corrected to $Q(^{75}As) = 31.1$ fm$^2$ and $Q(^{11}B) = 4.07$ fm$^2$.

[b] X-ray diffraction data indicate that there are four crystallographically nonequivalent arsenic atoms in the $Ph_3As$ unit cell.

The $^{75}$As NMR spectrum of triphenylarsine had a total central transition powder pattern breadth of 31.7 MHz at $B_0 = 21.14$ T (see Figure 5.1). Figure 5.3 shows the more detailed $^{75}$As NMR spectra of the quadrupolar discontinuities of Ph$_3$As, including four-site simulations of the spectra. Simulations that used only one arsenic site did not conform to the experimental line shape. This is especially evident at the low-frequency "horn", which is considerably less intense than theoretically expected for a single site. As previously mentioned, the structure of triphenylarsine from X-ray diffraction consists of four nonequivalent arsenic atoms in the unit cell; thus, the experimental $^{75}$As NMR spectrum should also consist of four overlapping quadrupolar powder patterns, each with different $^{75}$As NMR parameters. Indeed, the higher quality spectra of the horns (Figure 5.3), with closely spaced transmitter steps (i.e., 200 kHz apart) clearly showed four $^{75}$As sites with unique quadrupolar parameters (Table 5.4). Simulations that included four arsenic sites more accurately reproduced the experimental $^{75}$As NMR line shape (Figure 5.3). The $C_Q(^{75}$As$)$ values used in these simulations ranged from 193.5 to 194.4 ± 2 MHz, and all $\eta_Q(^{75}$As$)$ values were nonzero, ranging from 0.022 to 0.043 ± 0.05 (see Table 5.4). CASTEP calculations (Table 5.5) also indicate that the four arsenic sites possess slightly different values for $C_Q(^{75}$As$)$ and $\eta_Q(^{75}$As$)$, with a predicted range in $C_Q(^{75}$As$)$ values of approximately 3 MHz and $\eta_Q(^{75}$As$)$ values ranging from 0.06 to 0.13. We note the tendency in CASTEP to systematically underestimate $C_Q(^{75}$As$)$ values (Table 5.5), possibly because the calculations do not include relativistic effects. The quadrupolar frequency, $\nu_Q(^{75}$As$)$, determined for this compound via nuclear quadrupole resonance spectroscopy was reported as 97.05 MHz in 1972[201] and 95.81 MHz in 1974,[150] which if $\eta_Q(^{75}$As$)$ is zero, correspond to nuclear quadrupolar coupling constants of 194 and 191 MHz (both measured at $T = 300$ K), close to our experimental values. In the 1972 NQR study of Brill and Long,[201] the reported $\nu_Q(^{75}$As$)$ value is an average of

four observed resonances, consistent with the crystallographic data.  It does not appear as though

NQR resonances for four sites were resolved in the 1974 study.[150]

It is clear on the basis of the values of $C_Q(^{75}\text{As})$ and the breadth of the $^{75}\text{As}$ NMR central

transitions that the $^{75}\text{As}$ NMR line shapes are completely dominated by the quadrupolar

interaction.  Line shape contributions from the orientation-dependence of the $^{75}\text{As}$ chemical shift

were not observed.  Arsenic-75 NMR chemical shifts of near-tetrahedral and near-octahedral

compounds typically fall within a range of approximately 800 ppm, from 400 ppm to −400 ppm

relative to 0.5 M $\text{NaAsF}_6$ in $\text{CD}_3\text{CN}$,[107] though exceptions have been noted.[133,173]  Proof-of-

concept calculations using the ADF program package are shown in Table 5.6.  Calculations

performed on available experimental structures as well as model Lewis acid–base adducts (see

Tables 5.4 and 5.7) estimate that in the studied compounds the spans of the $^{75}\text{As}$ chemical shift

tensors, $\Omega = \delta_{11} - \delta_{33}$ where $\delta_{11} > \delta_{33}$, are less than 200 ppm.  The analogous adduct

$\text{Ph}_3\text{PB}(\text{C}_6\text{F}_5)_3$ was reported to have $\Omega(^{31}\text{P}) = 39$ ppm, covering ca. 5% of the $^{31}\text{P}$ chemical shift

range.[109,202]  Simulations of the $^{75}\text{As}$ NMR spectra that included a span of 800 ppm (123 kHz at

21.14 T) did not affect the determined $C_Q(^{75}\text{As})$ or $\eta_Q(^{75}\text{As})$ values within error.  $\delta_{\text{iso}}(^{75}\text{As})$ values

in $\text{Et}_3\text{AsB}(\text{C}_6\text{F}_5)_3$, $\text{Me}_3\text{AsBPh}_3$, and $\text{Ph}_3\text{AsBPh}_3$ (the partial $^{75}\text{As}$ NMR spectra) were assumed to

be zero, though they are probably closer to the values obtained for $\text{Me}_3\text{AsB}(\text{C}_6\text{F}_5)_3$ and

$\text{Ph}_3\text{AsB}(\text{C}_6\text{F}_5)_3$.  Calculations (Tables 5.4 and 5.7) predict $\sigma_{\text{iso}}(^{75}\text{As})$ values of the adducts fall

within a 200 ppm range, and $^{31}\text{P}$ NMR experiments performed on solid $\text{Ph}_3\text{PBH}_3$[203] and

$\text{Ph}_3\text{PB}(\text{C}_6\text{F}_5)_3$[202] indicated similar $\delta_{\text{iso}}(^{31}\text{P})$ values of 18.6 and 21.4 ppm, respectively.  For these

three compounds, we have estimated the error in $C_Q(^{75}\text{As})$ values by simulating the partially

acquired spectra with $\delta_{\text{iso}}(^{75}\text{As})$ values of −500 and 500 ppm, a range which comfortably includes

all of our experimentally determined $\delta_{\text{iso}}(^{75}\text{As})$ values.  The difference between the experimental

$C_Q(^{75}\text{As})$ values reported here and those determined at the edge of this range is less than 2 MHz.

The remaining NMR interactions contributing to the breadth of the NMR powder pattern that must be considered in the $^{75}$As NMR simulations are the direct dipolar coupling and indirect spin–spin coupling. These interactions are typically on the order of kHz or less and would not noticeably affect the $^{75}$As NMR powder line shape. This is supported by the $R_{\text{eff}}(^{75}\text{As},^{11}\text{B})$ and $^1J(^{75}\text{As},^{11}\text{B})$ values determined via analysis of the $^{11}$B NMR spectra (vide infra).

**Table 5.6.** Calculated and experimental NMR parameters for a series of arsenic-contaning molecules. Calculated parameters determined using the ADF program package, the BP86 functional, and the ZORA/QZ4P basis set.

| | $C_Q(^{75}As)$ / MHz | | $\Omega$ / ppm | | $\sigma_{iso}$ / ppm | | Reference |
|---|---|---|---|---|---|---|---|
| | Calc. | Expt. | Calc. | Expt. | Calc. | Expt. | |
| AsN | −282 | - | 4162 | - | 286 | 740.95[a] | 204 |
| AsP | −252 | −247.9495(46) | 4997 | 4070(110) | −256.64 | 25 | 110 |
| | - | - | - | - | −257 | 245.39[a] | 204 |
| AsAs | −216 | - | 5522 | - | −563 | −8.01[a] | 204 |
| AsH$_3$ | −159 | −162.63 ± 0.03 | 125 | - | 1982 | - | 118 |
| AsF$_3$ | −203 | −235 | 450 | - | 977 | - | 167 |
| AsMe$_3$ | −192 | −203.15 | 44 | - | 1535 | - | 166 |

[a] Calculated using CCSD(T)/cc-pV5Zs,p-unc with relativistic corrections included (see Ref. 204).

**Table 5.7.** Calculated $^{75}$As quadrupolar, magnetic shielding, and indirect spin-spin coupling NMR parameters for the model

compounds Me$_3$AsBH$_3$, Et$_3$AsBH$_3$, Me$_3$AsBMe$_3$, and Et$_3$AsBMe$_3$. DFT calculations were performed using the ADF program

package. Structures of these model compounds were determined via geometry optimization in the gas phase. All calculations were

carried out using the BP86 functional and the ZORA/QZ4P basis set (i.e., relativistic effects were included).

| | $C_Q$ / MHz | $\eta$ | $\sigma_{iso}$ / ppm | $\Omega$ / ppm | $^1J(^{75}\text{As},^{11}\text{B})$ / Hz | $\Delta J(^{75}\text{As},^{11}\text{B})$ / Hz |
|---|---|---|---|---|---|---|
| Me$_3$AsBH$_3$ | −155.6 | 0.00242 | 1266 | 138 | −48 | 105 |
| Et$_3$AsBH$_3$ | −147.0 | 0.02831 | 1204 | 171 | −45 | 99 |
| Me$_3$AsBMe$_3$ | −156.7 | 0.00005 | 1319 | 75 | −57 | 78 |
| Et$_3$AsBMe$_3$ | −148.9 | 0.02282 | 1278 | 106 | −54 | 73 |

### 5.4.2 Boron-11 NMR Spectra

Experimental and simulated $^{11}$B$\{^1$H$\}$ NMR spectra are given in Figure 5.4. An impurity contributing to $^{11}$B MAS NMR spectra for compounds Me$_3$AsBPh$_3$ and Ph$_3$AsBPh$_3$ is most evident in the spectra acquired at $B_0 = 7.05$ T, where a spinning sideband from the impurity overlaps with peaks from the adduct. Independent experiments (not shown) confirm the identity of the impurity to be free triphenylborane. No signals from impurities were detected in the $^{11}$B NMR spectra of the B(C$_6$F$_5$)$_3$-containing adducts.

The $^{11}$B NMR spectra are influenced by several different interactions, including the quadrupolar and magnetic shielding interactions for the $^{11}$B nuclei and spin–spin coupling interactions involving $^{75}$As. Values for $C_Q(^{75}$As$)$ and $\eta_Q(^{75}$As$)$ were determined from $^{75}$As NMR experiments as described above. The remaining parameters required to fit the $^{11}$B NMR spectra include the quadrupolar parameters $C_Q(^{11}$B$)$ and $\eta_Q(^{11}$B$)$, spin–spin interaction constants $R_{\text{eff}}(^{75}$As,$^{11}$B$)$ and $^1J(^{75}$As,$^{11}$B$)$, the isotropic chemical shift $\delta_{\text{iso}}(^{11}$B$)$, as well as Euler angles relating the EFG tensors of the two nuclei, $\alpha_Q$, $\beta_Q$, and $\gamma_Q$, and angles orienting the dipolar vector with respect to the $^{75}$As EFG tensor, $\alpha_D$ and $\beta_D$. Following the work of the Bryce group,[27] we have used the ZYZ convention to relate the two EFG tensors. Since these molecules have near-$C_3$ symmetry along the As–B bond, it was assumed in the simulations that $V_{ZZ}(^{11}$B$)$ and $V_{ZZ}(^{75}$As$)$ lie along the As–B bond axis and that the dipolar vector is coincident with $V_{ZZ}(^{75}$As$)$. In other words, the angles $\beta_Q$ and $\beta_D$ are zero, and $\alpha_D$ is undefined. Spectral simulations indicate $\beta_Q = 0 \pm 10°$. Varying angles $\alpha_Q$ and $\gamma_Q$ does not visibly affect our simulated spectra. The NMR parameters required to fit the $^{11}$B NMR spectra are therefore reduced to $C_Q(^{75}$As$)$ and $\eta_Q(^{75}$As$)$, determined accurately from high-field $^{75}$As NMR experiments, as well as $C_Q(^{11}$B$)$, $\eta_Q(^{11}$B$)$, $\delta_{\text{iso}}(^{11}$B$)$, $R_{\text{eff}}(^{75}$As,$^{11}$B$)$, and $^1J(^{75}$As,$^{11}$B$)$. In order to determine the remaining $^{11}$B NMR

parameters confidently, $^{11}$B NMR spectra acquired at both $B_0 = 7.05$ and 11.75 T were simulated. As the line width of the central transition due to the second-order quadrupolar interaction scales as the reciprocal of the magnetic field strength and the magnitude of the spin–spin interactions are independent of field strength, fitting spectra at both fields is expected to yield reliable results.

Simulations indicate that the $^{11}$B quadrupolar coupling constants fall in the range of 1.30 to 2.8 MHz (Table 5.3), which are within the expected range for tetracoordinate $^{11}$B in Lewis acid–base adducts.[202] Note that for the Lewis acids $B(C_6F_5)_3$ and $B(Mes)_3$ $C_Q(^{11}B)$ values are 4.26 and 4.75 MHz, respectively,[202,205] and $C_Q(^{11}B)$ values in the Lewis acid–base adducts are expected to be smaller. $C_Q(^{11}B)$ values for $R_3AsB(C_6F_5)_3$ range from approximately 1.3 MHz (R = Me, Et) to ca. 2.0 MHz (R = Ph). $C_Q(^{11}B)$ values for $R_3AsBPh_3$ show a similar trend, with $C_Q(^{11}B) = 2.0$ MHz when R = Me, and 2.8 MHz when R = Ph. DFT calculations reproduce this trend and show that $\eta_Q(^{11}B)$ values are very close to zero (Table 5.5). Simulations indicate $\eta_Q(^{11}B)$ values of $0 \pm 0.05$ to 0.1 (sample dependent). Experimental $R_{eff}(^{75}As,^{11}B)$ values for the triarylborane adducts varied from ca. 500 to 610 Hz (see Table 5.3). The expected $R_{DD}(^{75}As,^{11}B)$ values based on the experimental As–B bond lengths of $Et_3AsB(C_6F_5)_3$ and $Me_3AsBPh_3$ are 630 and 668 Hz, respectively. DFT calculations predict $\Delta J$ values of approximately 80 Hz for both $Et_3AsB(C_6F_5)_3$ and $Me_3AsBPh_3$ (see Table 5.8). Anisotropy in $J$ is theoretically possible to measure for the compound $Me_3AsBPh_3$, as we have experimental values for both $R_{DD}(^{75}As,^{11}B)$ and $R_{eff}(^{75}As,^{11}B)$. However, given the error in $R_{eff}(^{75}As,^{11}B)$ as well as the small calculated value of $\Delta J$, any meaningful conclusions regarding $\Delta J$ are beyond the scope of this research. It is possible that some anisotropy in $J$ is contributing to $R_{eff}(^{75}As,^{11}B)$ values for the remaining compounds, and thus calculated As–B bond lengths based on the assumption that $R_{DD} = R_{eff}$ are likely unreliable and will not be reported in this work.

For the adducts $Me_3AsB(C_6F_5)_3$ and $Ph_3AsB(C_6F_5)_3$, including contributions from isotropic $J$-coupling was necessary to reproduce experimental $^{11}B$ NMR spectral line shapes. The measured $^1J(^{75}As,^{11}B)$ values for these two compounds were $50 \pm 15$ and $25 \pm 10$ Hz, respectively. Note that $^1J(^{31}P,^{11}B)$ values in phosphine–boranes have been reported to be ca. 50 Hz,[202] and given the ratio $\gamma(^{75}As)/\gamma(^{31}P) \approx 0.42$, as well as group trends in $^1K$ magnitudes (i.e., $^1K$ values typically increase as one moves down a group),[109] we expect that $^{75}As$–$^{11}B$ one-bond $J$-coupling values will be similar in analogous molecules. Therefore, the measured $^1J(^{75}As,^{11}B)$ values reported in this work are reasonable. This contrasts with the value of $^1J(^{75}As,^{11}B) = 650$ Hz reported by Wi et al.[154] in the Lewis acid–base adduct $Ph_3AsBH_3$. This value, along with their reported value of $\Delta J = -300$ Hz, seems anomalous compared to our results for the series of triarylborane adducts. Furthermore, these values are not consistent with DFT calculations that we have carried out on model systems, which predict $^1J(^{75}As,^{11}B)$ values near zero and $\Delta J(^{75}As,^{11}B)$ values of approximately 70–100 Hz (see Table 5.8). Our $^{11}B$ MAS NMR spectra of $Ph_3AsBH_3$ were fit assuming a single site, as the $^{11}B$ NMR powder patterns of the two sites overlapped closely and the spectra did not possess discontinuities unique to only one site. As this was the case, our simulated fit (Figure 5.5) and the experimental line shape are slightly different. Our experimentally determined value for $^1J(^{75}As,^{11}B)$ in $Ph_3AsBH_3$ is $20 \pm 20$ Hz. This compares with $^1J(^{31}P,^{11}B) = 60$ Hz in $Ph_3PBH_3$[203] and is consistent with the values obtained for the other Lewis acid–base adducts in this work. For $Ph_3AsBH_3$, our $^{11}B$ NMR simulations indicate $R_{eff}(^{75}As,^{11}B) = 700 \pm 40$ Hz. There is no available X-ray diffraction data for this molecule, and the reported As–B bond distance in $Me_3AsBH_3$ used by Wi et al. (2.03 Å)[154] is less than that reported for $Me_3AsBPh_3$ (2.148 Å)[153] and our geometry optimized structures for $Ph_3AsBH_3$ (2.08 Å in the "gas phase" model). Thus, between the uncertainty in As–B bond

length and in the measured $R_{eff}(^{75}As,^{11}B)$ value, the value of $\Delta J$ is unclear. Quadrupolar and chemical shift parameters determined previously[154] for $^{11}B$ in $Ph_3AsBH_3$ are very close to our experimental values of $\delta_{iso}(^{11}B) = -34.6 \pm 0.5$ ppm, $C_Q(^{11}B) = 1.85 \pm 0.1$ MHz, and $\eta_Q(^{11}B) = 0$. However, $^{75}As$ quadrupolar parameters differ by several percent, and the sign of $C_Q(^{75}As)$ determined by Wi et al.[154] is in conflict with that determined here. The data presented here demonstrate the importance of acquiring NMR spectra for both quadrupolar nuclei in order to extract reliable spin–spin coupling information.

**Table 5.8.** Calculated indirect spin-spin coupling constants for compounds $H_3AsBH_3$, $Et_3AsB(C_6F_5)_3$, $Me_3AsBPh_3$, $H_3PBH_3$, and $Ph_3PBH_3$. DFT calculations were carried out with the ADF program package using the molecules' experimental geometries,[153,206-208] the BP86 functional, and the ZORA/QZ4P basis set.

| | $^1J(E,^{11}B)$, E = $^{31}P$, $^{75}As$ / Hz | $\Delta J(E,^{11}B)$, E = $^{31}P$, $^{75}As$ / Hz |
|---|---|---|
| $H_3AsBH_3$ | −44 | 103 |
| $Et_3AsB(C_6F_5)_3$ | 0.4 | 82 |
| $Me3AsBPh_3$ | −26 | 81 |
| $H_3PBH_3$ | −23 | 96 |
| $Ph_3PBH_3$ (site 1) | 10 | 90 |
| $Ph_3PBH_3$ (site 2) | 6 | 90 |
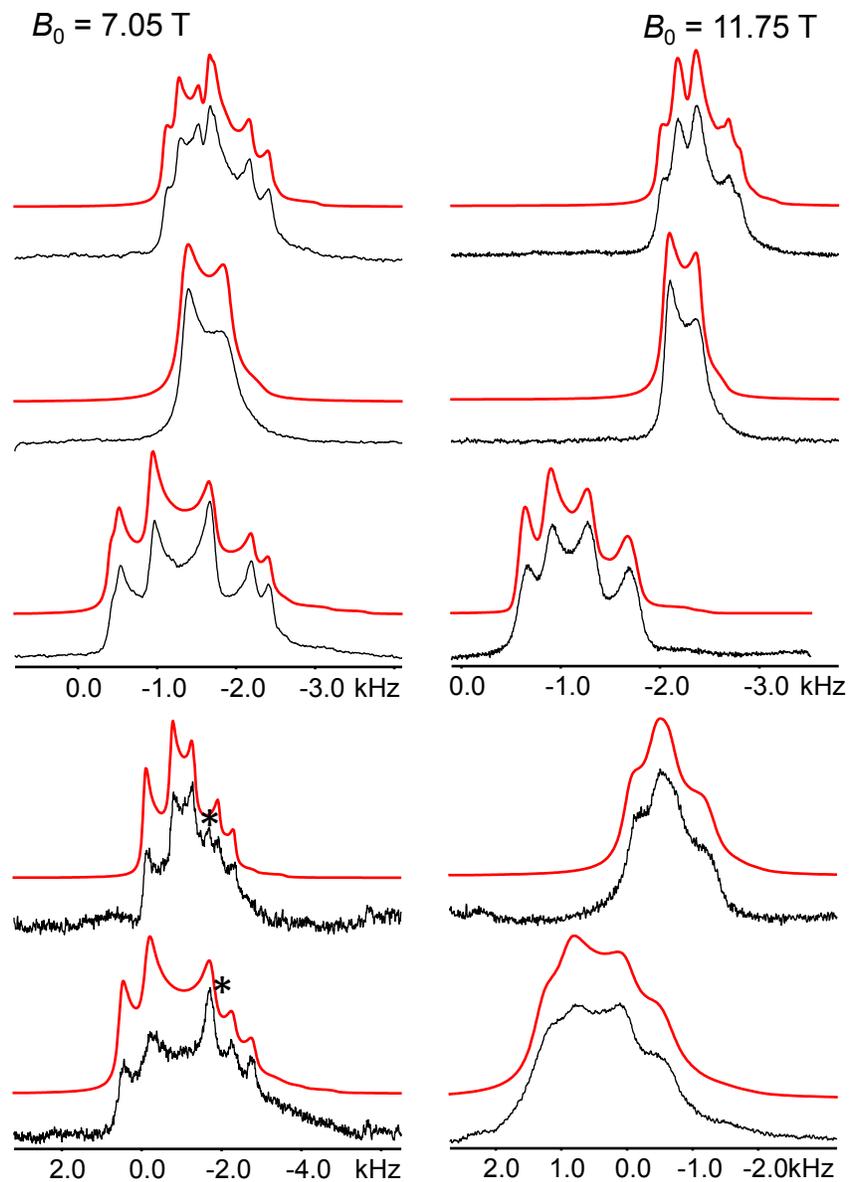
**Figure 5.4.** Experimental (lower traces) and simulated (upper traces) solid-state $^{11}$B MAS NMR spectra acquired at two magnetic field strengths using a Bloch pulse sequence with proton decoupling. From top to bottom, compounds studied are $Me_3AsB(C_6F_5)_3$, $Et_3AsB(C_6F_5)_3$, $Ph_3AsB(C_6F_5)_3$, $Me_3AsBPh_3$, and $Ph_3AsBPh_3$. See Table 5.3 for the simulation parameters. Asterisks on spectra of compounds $Me_3AsBPh_3$ and $Ph_3AsBPh_3$ indicate the position of a spinning sideband assigned to free $BPh_3$.
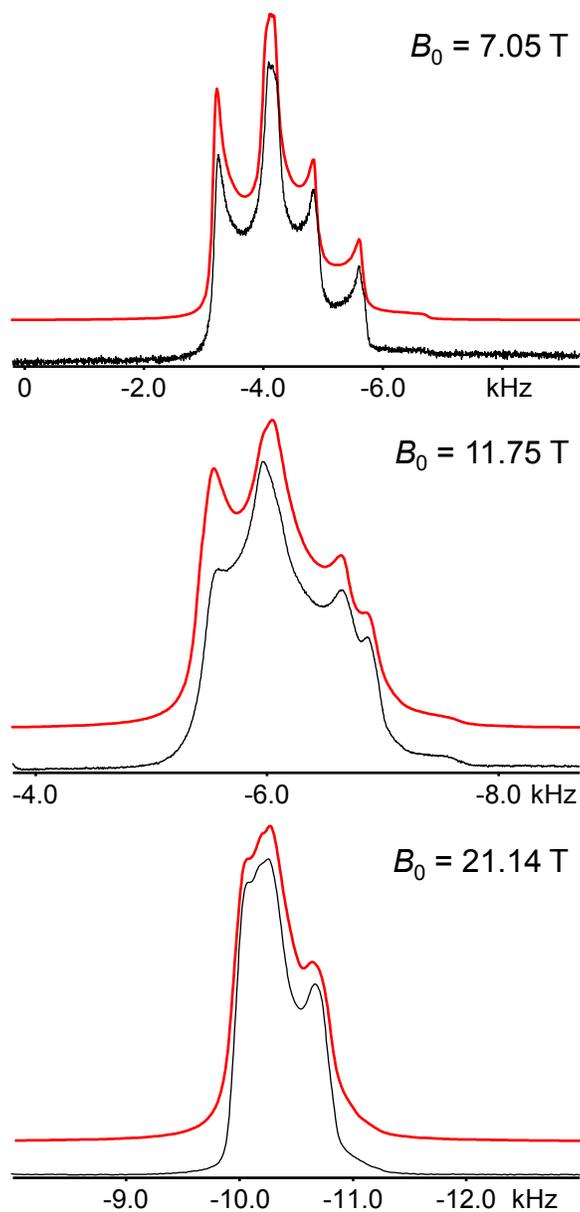
**Figure 5.5.** Experimental (lower traces) and simulated (upper traces) ^{11}B MAS NMR spectra of powdered $Ph_3AsBH_3$ acquired at three different magnetic field strengths. See Table 5.3 for simulation parameters.

The sign of $C_Q(^{75}As)$ was readily determined in five of six cases, as the $^{11}B$ NMR spectral line shapes were dependent on this value. The exception to this was the compound $Et_3AsB(C_6F_5)_3$, whose $^{75}As$ NMR free-induction decay showed complete relaxation in less than 1 ms. For this compound alone, the only resolved contribution to the $^{11}B$ NMR line shape is from the quadrupolar interaction of the boron nuclei (see Figure 5.4). Therefore, boron–arsenic spin–spin coupling constants as well as the sign of $C_Q(^{75}As)$ could not be determined experimentally for this compound. It is likely that the $^{75}As$ nuclei are self-decoupling from boron due to their short spin–spin relaxation times. The signs for the $C_Q(^{75}As)$ values in the five cases where information was experimentally available were determined to be negative. DFT calculations predict negative $C_Q(^{75}As)$ values for compounds $Et_3AsB(C_6F_5)_3$ and $Me_3AsBPh_3$, as well as for the model structures of $Ph_3AsBH_3$. The sign of $^1J(^{75}As,^{11}B)$ has been determined somewhat less confidently. Simulations are indeed sensitive to this sign, however, the small splittings due to this coupling in the case of $Ph_3AsB(C_6F_5)_3$ produce a less obvious difference between the simulated spectra with $+^1J(^{75}As,^{11}B)$ or $-^1J(^{75}As,^{11}B)$. That being said, the spectrum simulated using a positive value for the indirect spin–spin coupling produces a slightly better fit. The splitting features caused by indirect spin–spin coupling in $Me_3AsB(C_6F_5)_3$ are more obvious, and the sign of $^1J(^{75}As,^{11}B)$ was also determined to be positive. This is consistent with calculated $J_{iso}$ values in other group 13–group 15 Lewis acid–base adducts.[193,202,209] Computations performed on model compounds indicate $|^1J(^{75}As,^{11}B)|$ values are small ($< 50$ Hz), and the exact sign and magnitude is sensitive to the geometry (see Tables 5.9 to 5.12).

**Table 5.9.** Indirect spin-spin coupling constants for the compound $H_3AsBH_3$ (experimental geometry)[206] calculated using the ADF program package with the BP86 functional, both with and without the inclusion of relativistic effects. The basis sets used are indicated below.

| | TZP | | TZ2P | | QZ4P | |
| --- | --- | --- | --- | --- | --- | --- |
| | Rel. | Non-Rel. | Rel. | Non-Rel. | Rel. | Non-Rel. |
| $^1J(^{75}As,^{11}B)$/Hz | −33.865 | −27.760 | −33.842 | −27.538 | −44.203 | −35.001 |
| $^1J(^{75}As,^1H)$/Hz | 183.280 | 211.117 | 179.992 | 207.822 | 190.471 | 202.169 |
| $^1J(^{11}B,^1H)$/Hz | 101.787 | 101.454 | 99.005 | 98.658 | 102.723 | 102.376 |
| $^2J(^1H,^1H)_{As}$/Hz | 7.319 | 6.082 | 7.443 | 6.219 | 8.977 | 7.810 |
| $^2J(^1H,^1H)_B$/Hz | −8.599 | −8.885 | −8.397 | −8.677 | −8.397 | −8.633 |
| $^3J(^1H,^1H)_{trans}$/Hz | 27.221 | 26.673 | 28.323 | 27.770 | 29.400 | 28.809 |
| $^3J(^1H,^1H)_{gauche}$/Hz | −0.262 | 0.085 | −0.349 | −0.008 | −0.161 | 0.154 |

**Table 5.10.** Calculated spin-spin coupling constants for the adduct $H_3AsBH_3$ where the arsenic-boron bond distance was varied, using the ADF program package, the BP86 functional, and the QZ4P basis set, either with or without the inclusion of relativistic effects.

| $r_{AsB}$ / Å | 2.00 | | 2.05 | | 2.10 | | 2.15 | |
|---|---|---|---|---|---|---|---|---|
| | Rel. | Non-Rel. | Rel. | Non-Rel. | Rel. | Non-Rel. | Rel. | Non-Rel. |
| $^1J(^{75}As,^{11}B)$/Hz | −39.813 | −30.354 | −45.775 | −36.707 | −49.776 | −41.232 | −52.056 | −44.134 |
| $^1J(^{75}As,^1H)$/Hz | 193.597 | 204.449 | 189.058 | 201.120 | 184.084 | 197.353 | 178.780 | 193.249 |
| $^1J(^{11}B,^1H)$/Hz | 101.183 | 100.819 | 103.369 | 103.029 | 105.454 | 105.142 | 107.435 | 107.149 |
| $^2J(^1H,^1H)_{As}$/Hz | 9.339 | 8.149 | 8.825 | 7.668 | 8.333 | 7.210 | 7.862 | 6.775 |
| $^2J(^1H,^1H)_B$/Hz | −8.619 | −8.841 | −8.294 | −8.535 | −7.915 | −8.174 | −7.485 | −7.761 |
| $^3J(^1H,^1H)_{trans}$/Hz | 31.068 | 30.443 | 28.697 | 28.120 | 26.410 | 25.876 | 24.220 | 23.726 |
| $^3J(^1H,^1H)_{gauche}$/Hz | 0.063 | 0.397 | −0.250 | 0.058 | −0.515 | −0.235 | −0.734 | −0.481 |

**Table 5.11.** Calculated indirect spin-spin coupling constants for the compound $H_3AsBH_3$ (experimental geometry)[206] using the Gaussian 09 program.

| | cc-pVTZ | | cc-pVQZ | | cc-pV5Z | |
| --- | --- | --- | --- | --- | --- | --- |
| | RHF | B3LYP | RHF | B3LYP | RHF | B3LYP |
| $^1J(^{75}As,^{11}B)$/Hz | 30.0 | −19.5 | 37.9 | −12.8 | 41.3 | −13.6 |
| $^1J(^{75}As,^1H)$/Hz | 390.0 | 259.4 | 391.4 | 238.7 | 435.6 | 281.7 |
| $^1J(^{11}B,^1H)$/Hz | 122.2 | 114.0 | 123.5 | 112.5 | 130.2 | 120.0 |
| $^2J(^1H^1H)_{As}$/Hz | −6.8 | 3.6 | −6.3 | 4.5 | −6.3 | 5.4 |
| $^2J(^1H^1H)_B$/Hz | −20.6 | −9.9 | −20.8 | −10.7 | −22.7 | −11.7 |
| $^3J(^1H^1H)_{trans}$/Hz | 21.3 | 22.7 | 22.5 | 24.0 | 24.8 | 26.7 |
| $^3J(^1H^1H)_{gauche}$/Hz | −0.3 | 0.06 | −0.3 | 0.2 | −0.08 | 0.4 |

**Table 5.12.** Calculated spin-spin coupling constants for the adduct $H_3AsBH_3$ where the arsenic-boron bond distance was varied, using the Gaussian 09 program and the cc-pVQZ basis set.

| $r_{As-B}$/Å | 2.00 | | 2.05 | | 2.10 | | 2.15 | | 2.20 | |
|---|---|---|---|---|---|---|---|---|---|---|
| | RHF | B3LYP | RHF | B3LYP | RHF | B3LYP | RHF | B3LYP | RHF | B3LYP |
| $^1J(^{75}As,^{11}B)$/Hz | 48.7 | −60.2 | 33.4 | −15.4 | 19.4 | −23.2 | 6.8 | −29.4 | −4.2 | −34.0 |
| $^1J(^{75}As,^1H)$/Hz | 393.3 | 241.3 | 390.0 | 237.4 | 386.8 | 233.1 | 382.4 | 228.4 | 377.4 | 223.4 |
| $^1J(^{11}B,^1H)$/Hz | 121.3 | 110.6 | 124.5 | −3.9 | 127.7 | 115.9 | 130.8 | 118.3 | 133.9 | 120.7 |
| $^2J(^1H^1H)_{As}$/Hz | −5.7 | 4.8 | −6.5 | 4.3 | −7.2 | 3.8 | −7.9 | 3.3 | −8.5 | 2.9 |
| $^2J(^1H^1H)_B$/Hz | −21.3 | −10.9 | −20.6 | −10.5 | −19.9 | −10.1 | −19.2 | −9.6 | −18.5 | −9.1 |
| $^3J(^1H^1H)_{trans}$/Hz | 24.0 | 25.5 | 21.8 | 23.4 | 19.8 | 21.4 | 17.9 | 19.4 | 16.2 | 17.6 |
| $^3J(^1H^1H)_{gauche}$/Hz | 0.1 | 0.5 | −0.4 | 0.7 | −0.9 | −0.3 | −1.3 | −0.6 | −1.6 | −0.8 |

### 5.4.3 Structure in Solution

There is a notable discrepancy between the solid-state $\delta_{iso}(^{11}B)$ values and $\delta(^{11}B)$ determined for the samples in $CD_2Cl_2$ or $CD_3CN$ solution by Burford et al.[153] (see Table 5.13). Given the relatively small chemical shift range for $^{11}B$, approximately 250 ppm,[109] this difference is significant, particularly for $Me_3AsBPh_3$ and $Ph_3AsBPh_3$, whose chemical shifts in solution differ from the solid-state values by over 50 ppm. This disparity indicates that the structures in the two phases are dissimilar. Exchange phenomena are known to occur in Lewis acid–base adducts of triarylboranes and phosphines, where a free phosphine molecule replaces the phosphine in the adduct via a two-step mechanism.[210,211] It is possible that a similar process is occurring in these samples, and the $\delta(^{11}B)$ values obtained in solution are a weighted average of those of the free ligand and the coordinated adduct. In the studies conducted by Bradley et al.,[210,211] triphenylborane demonstrated a greater propensity to exchange versus its fluorinated analogue, tris(pentafluorophenyl)borane. This is expected as the Lewis acidity of triarylboranes increases as the hydrogen atoms in the phenyl rings are replaced with fluorine atoms.[211,212]

The chemical shifts in solution for $Me_3AsBPh_3$ and $Ph_3AsBPh_3$ are $\delta(^{11}B) = +53.6$ ppm and $+67.8$ ppm, respectively. These values lie within the expected range for tricoordinate boron, whereas those determined for the solid adducts lie within the range expected for tetracoordinate boron compounds.[109] Free triphenylborane has a literature chemical shift of $\delta(^{11}B) = 68$ ppm,[213] which corresponds within error to the value reported for $Ph_3AsBPh_3$ in solution. This suggests that $Ph_3AsBPh_3$ is completely dissociated into its tricoordinate constituents in solution, making it (not surprisingly) the least stable Lewis acid–base adduct of the five studied. The chemical shift of $Me_3AsBPh_3$ in solution is closer to its value in the solid state, suggesting it is spending some time as an adduct in solution. Free tris(pentafluorophenyl)borane has a literature chemical shift

between $\delta(^{11}B) = 59$ and 61 ppm.[202,210] The boron chemical shift values for $Me_3AsB(C_6F_5)_3$ and

$Et_3AsB(C_6F_5)_3$, $\delta(^{11}B) = -11.0$ ppm and $-11.8$ ppm, obtained in solution match closely with the

values obtained in the solid state, $\delta_{iso}(^{11}B) = -13.3 \pm 0.5$ ppm and $-12.2 \pm 0.5$ ppm, suggesting

these adducts remain intact in solution. The final compound, $Ph_3AsB(C_6F_5)_3$, had $^{11}B$ chemical

shift values in solution and in the solid state of $-11.6$ ppm and $-3.1 \pm 0.5$ ppm, respectively. In

this case, the $\delta_{iso}(^{11}B)$ value obtained in the solid is somewhat higher in frequency than the

solution-phase value. Note that the difference in chemical shift in the solid state between

$Me_3AsBPh_3$ and $Ph_3AsBPh_3$ is very similar to that between compounds $Me_3AsB(C_6F_5)_3$ and

$Ph_3AsB(C_6F_5)_3$, approximately 10 ppm in each case. As with the trends in $C_Q(^{11}B)$, this may

indicate that the solid-state environment about boron is influenced by the substituents on arsenic

in a systematic manner. Specifically, the shift to higher frequency is evidence for an increase in

the As–B bond length in the solid triphenylarsine adducts.[202]

**Table 5.13.** Solution-phase and solid-state values for $\delta(^{11}B)$.

| Compound | $\delta(^{11}B)$ / ppm | $\delta_{iso}(^{11}B)$ / ppm | |
|---|---|---|---|
| | Solution Phase (Burford et al.)[153] | Solid State (This Work) | \|Difference\| / ppm |
| $Me_3AsB(C_6F_5)_3$ | −11.0 | −13.2 | 2.2 |
| $Et_3AsB(C_6F_5)_3$ | −11.8 | −12.2 | 0.4 |
| $Ph_3AsB(C_6F_5)_3$ | −11.6 | −3.1 | 8.5 |
| $Me_3AsBPh_3$ | 53.6 | −0.25 | 53.9 |
| $Ph_3AsBPh_3$ | 67.8 | 9.3 | 58.5 |

## 5.5 Conclusions

Six boron–arsenic spin pairs in Lewis acid–base adducts were studied via ^{11}B and [75]As solid-state NMR spectroscopy.  The observation of boron–arsenic spin–spin coupling in ^{11}B MAS NMR spectra allowed for the determination of $R_{eff}$([75]As,[11]B) and $^1J$([75]As,[11]B), as well as the signs of the latter and of $C_Q$([75]As).  DFT calculations supported the experimental results. Despite several challenges, it was shown that [75]As NMR powder spectra with central transition line widths on the order of 30 MHz can be acquired in favorable systems and that if the quadrupolar interaction is significantly large for this nucleus, it is possible to reliably determine [75]As quadrupolar parameters based solely on the position and shape of the high-frequency discontinuity of the quadrupolar powder pattern.  This technique may be useful for fast NMR spectral acquisition for other nuclei that exhibit large quadrupolar coupling values.  This research also provided information about the chemical exchange behavior of the Lewis acid–base adducts in solution.  The relative Lewis acid strength of the triarylborane species observed here is consistent with what has been determined for related triarylborane adducts with phosphines in solution.

## 5.6 Acknowledgements

# Chapter 6

## Solid-State $^{87}$Sr NMR Spectroscopy at Natural Abundance and High Magnetic Field Strength

### 6.1 Introduction

Strontium-containing materials have many applications, some old and some new.[214-223] For example, strontium salts are widely used in pyrotechnics to produce deep red colors, strontium aluminate is used in phosphorescent ("glow-in-the-dark") paints, and $SrAl_2O_4$ nanoparticles are a potential source of photoluminescent probes for environmental and biological diagnostic testing.[214] Organic strontium compounds such as strontium citrate and strontium ranelate are used for the treatment of osteoporosis,[215] and tablets containing strontium compounds are available over-the-counter at many supermarkets and pharmacies in North America. As a calcium analogue, strontium ions are incorporated into bone tissue and regular ingestion of strontium supplements is purported to reduce the risk of bone fractures.[215] Strontium-containing bioactive glasses have also garnered a lot of interest in the medical and materials science communities.[216,224] Bioactive glasses are surgically implanted at defect bone sites to effect bone repair and regeneration, and the inclusion of strontium is thought to give additional antiosteoporotic benefits similar to those gained from taking strontium supplements.[216] Strontium ruthenate, $Sr_2RuO_4$, displays superconducting behavior,[217] as do several other

strontium-containing perovskites, e.g., BSCCO[219] and $La_{2-x}Sr_xCuO_4$ (LSCO).[218] $SrTiO_3$-based

perovskites such as $Pb_xSr_{1-x}TiO_3$, $Ba_xSr_{1-x}TiO_3$, and other materials such as $SrBi_2Ta_2O_9$ are of

interest for the manufacture of capacitors and other electronics.[220,221] Strontium-containing

perovskites have also recently been under investigation for use in fuel cells[222] and in hybrid

perovskite solar cells.[223] Arguably the most important naturally occurring form of strontium is

the mineral celestine, $SrSO_4$, as this is the primary source from which the metal is obtained.

Other naturally occurring strontium minerals include strontianite, $SrCO_3$, another important

strontium source, as well as the less-common mineral tausonite, $SrTiO_3$.[225]

Strontium-87 is the only naturally occurring isotope of strontium that is NMR-active.

Early optical hyperfine structure measurements reported by Heyden and Kopfermann indicate

that $^{87}$Sr has spin $I = 9/2$.[226] Strontium-87 has a natural abundance of 7.00 %, a gyromagnetic

ratio of $\gamma(^{87}Sr) = -1.164 \times 10^7$ rad T$^{-1}$ s$^{-1}$, and a quadrupole moment of $Q(^{87}Sr) = 30.5(2)$ fm$^2$.[1,61]

The moderate nuclear quadrupole moment, low natural abundance, and small gyromagnetic ratio

of this nucleus make it challenging to study via NMR spectroscopy, particularly in the case of

solid samples.

The first reported $^{87}$Sr NMR experiment was performed by Jeffries and Sogo and

published in 1953.[227] This experiment was carried out on a saturated aqueous solution of $SrBr_2$,

which resonated at 1.84 MHz in a field of $B_0 = 1.0$ T. Jeffries and Sogo reported the magnetic

moment of $^{87}$Sr to be $-1.0892 \pm 0.00015$ $\mu_N$. Weber and Allen reported the first $^{87}$Sr NMR

experiments performed on a solid compound in 1963, in a study of the phase transition at 110 K

in strontium titanate, $SrTiO_3$.[228] Published data on the $^{87}$Sr chemical shifts of $SrCl_2$, $SrBr_2$,

$Sr(ClO_4)_2$, and $Sr(NO_3)_2$ in aqueous solutions were reported ten years later by Banck and

Schwenk,[229] along with an updated value for the $^{87}$Sr magnetic moment, $-1.089273(9)$ $\mu_N$. Note,

however, that this magnetic moment is for $Sr^{2+}$ in aqueous solution, not the bare nucleus. Banck and Schwenk noted that the [87]Sr NMR signal in a 1 M aqueous solution of the strontium salts was about 6 orders of magnitude weaker than the ^{1}H NMR signal of protons in water. The first modern solid-state [87]Sr NMR measurements were included in a feasibility study of several low-$\gamma$ nuclei in 2000.[230] To a limited extent, [87]Sr NMR spectroscopy has been used to study strontium halides,[231] strontium-containing minerals,[232-234] perovskites,[220] and other simple inorganic strontium compounds.[230] Most recently, [87]Sr NMR spectroscopy has been applied to study bioactive glasses and the over-the-counter antiosteoporotic strontium malonate ([87]Sr-enriched).[224] For quadrupolar nuclides, in addition to NMR spectroscopy, nuclear electric quadrupolar coupling constants are often obtained via nuclear quadrupole resonance (NQR) or microwave spectroscopy. Microwave data are available for the diatomic molecules SrO and SrS in the gas phase,[235,236] with $C_Q$([87]Sr, SrO) = −42.729(37) MHz and $C_Q$([87]Sr, SrS) = −21.959(85) MHz in the ground vibrational state. As far as the authors are aware, no $C_Q$([87]Sr) values determined via NQR spectroscopy have been reported, and other determinations of $C_Q$([87]Sr) are few in the literature, the majority known from the aforementioned collection of solid-state [87]Sr NMR experiments.

As there are very little data available in the NMR literature concerning the [87]Sr nucleus, we present a collection of [87]Sr NMR parameters for several strontium-containing solids. Quadrupolar parameters for several strontium salts are quantified. We report the [87]Sr isotropic chemical shifts for studied compounds, and, for the first time, experimental evidence for [87]Sr magnetic shielding anisotropy in powdered samples is presented. Note that [87]Sr magnetic shielding anisotropy in NMR spectra of single crystal $Sr(NO_3)_2$ has been reported previously.[237] We also perform experiments on previously studied strontium-containing compounds to clarify

discrepancies in isotropic chemical shift values in the NMR literature. A [87]Sr absolute shielding scale, based on a recently calculated value for the magnetic shielding of the $Sr^{2+}$ ion coordinated to water molecules,[238] is proposed. The results of this research are discussed in the context of the other group II elements.


## 6.2 Experimental Section

### 6.2.1 Samples and NMR Measurements

Strontium malonate and strontium nitrite monohydrate, $Sr(NO_2)_2 \cdot H_2O$, were synthesized according to the literature.[239,240] The remaining compounds were acquired commercially and used without further purification. Karl Fischer analysis[241] was performed on bulk powdered samples of strontium acetylacetonate, strontium acetate, and strontium oxalate to determine the number of water molecules per formula unit.

All [87]Sr NMR spectra were acquired at natural abundance. Spectra were acquired at 39.0 MHz using a Bruker Avance II 900 MHz NMR spectrometer ($B_0 = 21.14$ T). Access to this spectrometer was provided by the National Ultrahigh-Field NMR Facility for Solids, located in Ottawa, ON, Canada.[2] Samples were packed in either 7 mm o.d. zirconia rotors or glass tubes. Hygroscopic samples (e.g., the strontium halides) were packed in a glovebox under argon. Experimental solid-state [87]Sr NMR spectra were acquired using either a 7 mm single channel (X) MAS Bruker probe for MAS samples, or a home-built single channel 7 mm solenoid probe for stationary samples. When required, 30 to 50 kHz proton decoupling was used in either a 7 mm H/X MAS Bruker probe or a 7 mm H/X home-built solenoid probe with a dual-coil design, although the decoupling effects were generally insignificant. Pulse sequences used include the Bloch pulse, quadrupolar echo ($90°$-$\tau_1$-$90°$-$\tau_2$-acquire), and the WURST-QCPMG[45,46] pulse

sequence. For experiments using rectangular pulses, a selective pulse with width,

$PW_{90}/(I + 1/2)$, was used to selectively excite the central transition ($m_I = 1/2$ to $m_I = -1/2$),

where $PW_{90}$ was the 90° pulse width calibrated using the reference solution. WURST pulses in

the WURST-QCPMG pulse sequence were 50 μs in length with a 1 MHz excitation bandwidth.

Most of the experimental spectra were acquired in one spectral window. Broader spectra

required the acquisition of multiple spectra for which the transmitter offset was adjusted

systematically to cover the entire spectral region.[47,48] These spectra were assembled either by

adding the pieces together (coadded sum) or by means of the skyline projection technique. The

DMFit program[100] was used to generate skyline projections.[50] Experiment times ranged from

approximately 10 min (SrO, SrS, SrTiO$_3$, and SrCl$_2$) to 62 h (SrBr$_2$). The delays between scans

were checked in each case to ensure adequate relaxation. Typically, the strontium spectra

featured here required on the order of hours to acquire, usually less than 1 day. Acquisition

details specific to each strontium compound are found in Table 6.1. Strontium-87 chemical shift

values were referenced with respect to a 0.5 M solution of SrCl$_2$ in D$_2$O ($\delta = 0.0$ ppm). Note that

the concentration dependence of $\delta(^{87}\text{Sr})$ in aqueous SrCl$_2$ has been measured by Banck and

Schwenk.[229] On the basis of molecular dynamics simulations and relativistic quantum chemistry

computations,[238] the absolute shielding of Sr$^{2+}$(aq) is $3536 \pm 106$ ppm. Using this value, Antušek

et al.[238] determined an updated value for the $^{87}$Sr magnetic moment, $-1.09316(11)\,\mu_N$.

**Table 6.1.** Experimental parameters used in the acquisition of $^{87}$Sr NMR spectra of stationary samples at $B_0 = 21.14$ T.

| Compound | Pulse sequence | Recycle delay /s | Number of frequency offset steps | Number of scans per step | Co-added sum or skyline projection | Total expt.time /hrs. |
|---|---|---|---|---|---|---|
| SrO | single pulse | 5 | 1 | 512 | - | 0.7 |
| SrS | single pulse | 5 | 1 | 128 | - | 0.2 |
| SrI$_2$ | quadrupole echo | 2 | 1 | 25 k | - | 14.3 |
| SrBr$_2$ | WURST-QCPMG | 1 | 1 | 8 k | - | 2.3 |
|  | quadrupole echo | 0.5 | 1 | 432 k | - | 62 |
| SrSnO$_3$ | WURST-QCPMG | 2 | 3 | 24 k | skyline projection | 41.0 |
| SrZrO$_3$ | WURST-QCPMG | 2 | 1 | 16 k | - | 9.1 |
| SrTiO$_3$ | single pulse | 5 | 1 | 128 | - | 0.2 |
| SrCl$_2$ | single pulse | 5 | 1 | 128 | - | 0.2 |
| SrF$_2$ | single pulse | 5 | 1 | 512 | - | 0.7 |
| SrWO$_4$ | WURST-QCPMG | 2 | 1 | 1024 | - | 0.6 |
| SrMoO$_4$ | quadrupole echo | 1 | 1 | 67 k | - | 19 |
| SrClO$_4$·3H$_2$O | QCPMG | 0.5 | 3 | 4 k | - | 1.7 |
| Sr(NO$_3$)$_2$ | quadrupole echo | 0.5 | 1 | 94 k | - | 13.4 |
| SrSO$_4$ | WURST-QCPMG | 1 | 3 | 8 k | skyline projection | 7.0 |
| (single crystal) | single pulse | 0.5 | 1 | 10 k | - | 1.4 |
| SrCrO$_4$ | WURST-QCPMG | 2 | 3 | 2 k | skyline projection | 3.4 |
| SrAl$_2$O$_4$ | WURST-QCPMG | 0.5 | 9 | 4 k | co-added sum | 5.1 |
| SrBr$_2$·6H$_2$O | quadrupole echo | 1 | 1 | 6.5 k | - | 1.9 |
| SrCl$_2$·6H$_2$O | quadrupole echo | 1 | 1 | 16 k | - | 4.6 |
| SrCO$_3$ | quadrupole echo | 0.5 | 1 | 101.5 k | - | 14.4 |

| | | | | | | |
|---|---|---|---|---|---|---|
| Sr(NO$_2$)$_2$·H$_2$O | WURST-QCPMG | 1 | 3 | 56 k | - | 49.2 |
| Sr(acac)$_2$·H$_2$O | WURST-QCPMG | 1 | 1 | 50 k | - | 14.2 |
| | quadrupole echo | 0.25 | 1 | 544 k | - | 38.7 |
| Sr(F-acac)$_2$ | QCPMG | 1 | 1 | 50 k | - | 14.2 |
| Sr(acetate)$_2$·½H$_2$O | WURST-QCPMG | 1 | 1 | 100 k | - | 28.5 |
| | quadrupole echo | 0.25 | 1 | 576 k | - | 42 |
| Sr(oxalate) | quadrupole echo | 2 | 1 | 24.1 k | - | 6.8 |
| Sr(malonate) | WURST-QCPMG | 1 | 2 | 40 k | co-added sum | 22.8 |

## 6.2.2 Spectral Simulations and First-Principles Calculations

Strontium-87 NMR parameters were determined by simulating the experimental spectra. Uncertainties in NMR parameters were determined via visual inspection of the simulated fits. The majority of the [87]Sr NMR spectra were simulated using the computer program QUEST,[19] which treats the Zeeman-quadrupolar (ZQ) interaction exactly (i.e., the full Zeeman-quadrupolar Hamiltonian is diagonalized to determine the ZQ eigenvalues). Note that due to the low resonance frequency of the [87]Sr nucleus (ca. 39 MHz at $B_0 = 21.14$ T), even samples with moderate to low $|C_Q|$ values may not meet the criteria of the high-field approximation.[185] Spectra acquired under both stationary and MAS sample conditions for the compounds SrCl$_2$·6H$_2$O, SrBr$_2$·6H$_2$O, and SrCO$_3$ were simulated with the program WSolids1.[99] This program treats all NMR interactions as perturbations of the Zeeman interaction and includes both first- and second-order corrections for the quadrupolar interaction. Note that $|C_Q(^{87}\text{Sr})|$ values for these three compounds are relatively small; the effects of their [87]Sr quadrupolar interactions are accurately described as second-order corrections to the Zeeman energy.

153

First-principles calculations of NMR parameters were performed using the CASTEP NMR program[54-57] running in the Materials Studio 4.4 environment using the experimental geometries[239, 242-262] determined via diffraction methods, "on-the-fly" pseudopotentials, and the Perdew, Burke, and Ernzerhof (PBE) functional in the generalized gradient approximation (GGA).[58,59] The gauge including projector augmented wave (GIPAW) method implemented in CASTEP provides accurate computed values of molecular properties and its use is well-established in the solid-state NMR literature.[263,264] See Table 6.2 for a summary of select crystallographic structure details for the strontium compounds. Cutoff energies ranged from 299 to 550 eV (Table 6.3) depending on the unit cell size. In some cases (where noted), calculations were carried out after a geometry optimization of all hydrogen atom positions, keeping the unit cell parameters and other atom positions constrained at their experimentally determined values. DFT calculations were carried out using the ADF program package[51-53] on isolated SrO, SrS, and SrCl$_2$ molecules. The NMR parameters calculated using ADF include a relativistic correction determined using the zeroth-order regular approximation (ZORA). Calculations were carried out using the GGA functional BP86 and the ZORA/QZ4P basis set.

## 6.3 Results and Discussion

This section begins with a discussion of $^{87}$Sr NMR spectral analysis and experimentally determined NMR parameters. We begin with strontium compounds for which the $^{87}$Sr NMR spectra are simulated as Zeeman-quadrupolar spectra; that is, anisotropic broadening effects from other NMR interactions (e.g., magnetic shielding) either are not present or are too small to quantify. Compounds with the highest point-group symmetry at the strontium crystallographic site are discussed first, as high-order symmetry confines the NMR interaction tensor orientation

and thus simplifies spectral acquisition and interpretation.  In order, compounds with cubic symmetry (no anisotropy), high-order rotational symmetry (axial interaction tensors), and those with no tensor parameter-confining symmetry elements are discussed.  Following this, the three compounds whose [87]Sr NMR spectra (stationary samples) show line shape effects from magnetic shielding anisotropy, $SrCl_2 \cdot 6H_2O$, $SrBr_2 \cdot 6H_2O$, and $SrCO_3$, are discussed.  After the [87]Sr NMR experiments are discussed, the results of first-principles CASTEP calculations are summarized and compared with experiment.  Trends in [87]Sr NMR isotropic chemical shift values are then discussed, followed by a discussion of how the [87]Sr chemical shift range and chemical shift values fit into the broader picture of NMR trends noted for other group II nuclei.

**Table 6.2.** Crystal structure information for strontium compounds.

| | Space group | Crystal system | Sr coordination number | Strontium bonding symmetry | Reference |
|---|---|---|---|---|---|
| SrO | $Fm\bar{3}m$ (no. 225) | cubic | 6 | octahedral | 258 |
| SrS | $Fm\bar{3}m$ (no. 225) | cubic | 6 | octahedral | 255 |
| $SrSnO_3$ | $Pbnm$ (no. 62) | orthorhombic | 8 | | 256 |
| $SrAl_2O_4$ | $P2_1$ (no. 4) | monoclinic | 9 | | 245 |
| $SrI_2$ | $Pnma$ (no. 62) | orthorhombic | 7 | monocapped trigonal prismatic | 243 |
| $SrZrO_3$ | $Pbnm$ (no. 62) | orthorhombic | 8 | | 254 |
| $SrBr_2$ | $P4/n$ | tetragonal | 8 | distorted square antiprismatic | 261 |
| $SrTiO_3$ | $Pm\bar{3}m$ (no. 221) | cubic | 12 | cuboctahedral | 253 |
| $SrCl_2$ | $Fm\bar{3}m$ (no. 225) | cubic | 8 | cubic | 242 |
| $Sr(NO_2)_2 \cdot H_2O$ | $P2_1$ (no. 4) | monoclinic | 9, 10 | | 247 |
| $SrWO_4$ | $I4_1/a$ (no. 88) | tetragonal | 8 | snub disphenoidal | 244 |
| $SrMoO_4$ | $I4_1/a$ (no. 88) | tetragonal | 8 | snub disphenoidal | 244 |

| | | | | | |
|---|---|---|---|---|---|
| Sr(oxalate) | $C2/c$ (no. 15) | monoclinic | 8 | distorted square antiprismatic | 252 |
| Sr(malonate) | $Pnan$ (no. 52) | orthorhombic | 9 | distorted tricapped trigonal prismatic | 239 |
| $SrCl_2 \cdot 6H_2O$ | $P321$ (no. 150) | trigonal | 9 | tricapped trigonal prismatic | 249 |
| $SrBr_2 \cdot 6H_2O$ | $P321$ (no. 150) | trigonal | 9 | tricapped trigonal prismatic | 251 |
| $SrCO_3$ | $Pmcn$ (no. 62) | orthorhombic | 9 | | 257 |
| $Sr(ClO_4)_2 \cdot 3H_2O$ | $P2_1/n$ (no. 14) | monoclinic | 9 | | 262 |
| $SrF_2$ | $Fm\bar{3}m$ (no. 225) | cubic | 8 | cubic | 242 |
| $Sr(NO_3)_2$ | $Pa\bar{3}$ (no. 205) | cubic | 12 | distorted cuboctahedral with broken square faces | 246 |
| $SrSO_4$ | $Pbnm$ (no. 62) | orthorhombic | 12 | | 250 |
| $SrCrO_4$ | $P2_1/n$ (no. 14) | monoclinic | 10 | | 248 |

**Table 6.3.** [87]Sr chemical shift tensors calculated using CASTEP.

| | $\sigma_{iso}$ | $\sigma_{aniso}$ | $\eta$ | Cutoff energy / eV | Crystal Structure Reference |
|---|---|---|---|---|---|
| SrO | 2620 | 0 | - | 550 | 258 |
| SrS | 2630 | 0 | - | 299 | 255 |
| $SrSnO_3$ | 2849 | 109.4 | 0.63 | 550 | 256 |
| $SrAl_2O_4$ | 2901 | −145.4 | 0.92 | 550 | 245 |
| | 2878 | 76.99 | 0.75 | - | |
| $SrI_2$ | 2767 | −111.6 | 0.68 | 299 | 243 |
| $SrZrO_3$ | 2886 | 115.2 | 0.48 | 550 | 254 |
| $SrBr_2$ | 2870 | −50.6 | 0.96 | 299 | 261 |
| | 2852 | 8.4 | 0 | - | |
| $SrTiO_3$ | 2941 | 0 | - | 550 | 253 |
| $SrCl_2$ | 2936 | 0 | - | 299 | 242 |
| $Sr(NO_2)_2 \cdot H_2O$ | 3004 | −142 | 0.31 | 550 | 247 |
| | 3018 | −83.8 | 0.74 | - | |
| $SrWO_4$ | 3002 | 26.7 | 0 | 550 | 244 |
| $SrMoO_4$ | 3014 | 34.3 | 0 | 550 | 244 |
| Sr(oxalate) | 3023 | 14.6 | 0.72 | 550 | 252 |
| Sr(malonate) | 3013 | −74.2 | 0.88 | 500 | 239 |
| $SrCl_2 \cdot 6H_2O$ | 2994 | −27.1 | 0 | 550 | 249 |
| $SrBr_2 \cdot 6H_2O$ | 2953 | −128.6 | 0 | 550 | 251 |
| $SrBr_2 \cdot 6H_2O$[a] | 2984 | −34.6 | 0 | 550 | 251 |

| | | | | | |
|---|---|---|---|---|---|
| SrCO$_3$ | 3009 | 77.2 | 0.46 | 550 | 257 |
| Sr(ClO$_4$)$_2$·3H$_2$O | 3038 | 73.4 | 0.43 | 300 | 262 |
| | 3069 | 69.1 | 0.47 | - | |
| SrF$_2$ | 3007 | 0 | - | 550 | 242 |
| Sr(NO$_3$)$_2$ | 3097 | 19.4 | 0 | 550 | 246 |
| SrSO$_4$ | 3113 | 106.8 | 0.52 | 550 | 250 |
| SrCrO$_4$ | 3168 | −167.9 | 0.63 | 550 | 248 |
| Sr(oxalate)·H$_2$O | 2899 | 108.9 | 0.23 | 550 | 259 |
| Sr(oxalate)·H$_2$O[a] | 2927 | 114.3 | 0.29 | 550 | 259 |
| Sr(oxalate)·2H$_2$O | 2899 | 46.8 | 0.19 | 500 | 259 |
| SrSe | 2620 | 0 | - | 310 | 242 |
| Sr(MnO$_4$)$_2$·3H$_2$O | 3022 | 58.2 | 0 | 550 | 260 |

[a] Calculation was performed after a geometry optimization for all hydrogen positions.

### 6.3.1 Spectral Acquisition and Analysis

Strontium-87 NMR spectra and parameters for 25 strontium-containing compounds are reported in this study (Tables 6.4-6.6). Eight of the compounds for which data are reported have been studied previously, SrO, $SrF_2$, $SrCl_2$, $Sr(NO_3)_2$, $SrMoO_4$, $SrSO_4$, $SrCO_3$, and Sr(malonate).[224,230-232,234] As our research focuses on characterizing [87]Sr chemical shift tensors and establishing [87]Sr chemical shift trends, and there are discrepancies between the reported [87]Sr chemical shift values, it was logical to repeat previous experiments in high-field conditions to determine isotropic [87]Sr chemical shift values. In many cases, short recycle delays, relatively narrow spectral breadth, and sufficient signal intensity allowed the acquisition of quadrupolar echo NMR spectra within a reasonable time frame. This allowed for more precise determination of the singularity positions versus what may be achieved from analysis of the QCPMG NMR spectra. A comparison of NMR spectral simulations carried out using QUEST and WSolids1 indicated that the high-field approximation begins to break down when $v_Q \approx 1$ MHz ($C_Q(^{87}Sr) = 24$ MHz), resulting in shifts of the quadrupolar discontinuity positions of ca. 5 ppm versus those predicted by the exact simulations at $v_0 = 39$ MHz. At $v_Q = 2$ MHz ($C_Q(^{87}Sr) = 48$ MHz), the discrepancies between singularity positions increase to ca. 45 ppm at $v_0 = 39$ MHz. The Haeberlen convention[20] is used here to report all chemical shift (CS) and electric field gradient (EFG) tensor parameters, however, occasionally in the text we cite the span of the chemical shift tensor ($\Omega = \delta_{11} - \delta_{33}$),[25] when it is relevant to the discussion.

**Table 6.4.** Experimental and calculated [87]Sr NMR parameters for inorganic strontium compounds.

| | | $\delta_{iso}$ / ppm[a] | $\sigma_{iso}$ / ppm | $|C_Q|$ / MHz[b] | $\eta_Q$ | Crystal Structure Ref. |
|---|---|---|---|---|---|---|
| SrO | Expt. | $340.8 \pm 0.5$ | - | 0 | - | - |
| | Ref. 231 | $340 \pm 1$ | - | 0 | - | - |
| | Calc. | - | 2620 | 0 | - | 258 |
| SrS | Expt. | $322.5 \pm 0.5$ | - | 0 | - | - |
| | Calc. | - | 2630 | 0 | - | 255 |
| SrSnO$_3$ | Expt. | $150 \pm 50$ | - | $31.6 \pm 0.2$ | $0.73 \pm 0.01$ | - |
| | Calc. | - | 2849 | $-30.9$ | 0.71 | 256 |
| SrAl$_2$O$_4$ | Expt. (site 1) | $130 \pm 100$ | - | $50.5 \pm 5$ | $0.70 \pm 0.04$ | - |
| | Expt. (site 2) | $150 \pm 100$ | - | $43.0 \pm 5$ | $0.88 \pm 0.04$ | - |
| | Calc. (site 1) | - | 2901 | $-46.1$ | 0.72 | 245 |
| | Calc. (site 2) | - | 2878 | 39.7 | 0.87 | |
| SrI$_2$ | Expt. | $100 \pm 50$ | - | $10.5 \pm 1$ | $0.90 \pm 0.05$ | - |
| | Calc. | - | 2767 | 11.8 | 0.68 | 243 |
| SrZrO$_3$ | Expt. | $91 \pm 50$ | - | $31.2 \pm 0.2$ | $0.62 \pm 0.02$ | - |
| | Calc. | - | 2886 | $-30.6$ | 0.47 | 254 |
| SrBr$_2$ | Expt. (site 1) | $80 \pm 30$ | - | $26.0 \pm 1.0$ | $0.30 \pm 0.02$ | - |
| | Expt. (site 2) | $85 \pm 10$ | - | $9.25 \pm 0.3$ | $0 \pm 0.01$ | - |
| | Calc. (site 1) | - | 2870 | 25.5 | 0.26 | 261 |
| | Calc. (site 2) | - | 2852 | 8.1 | 0 | |
| SrTiO$_3$ | Expt. | $63.4 \pm 0.5$ | - | 0 | - | - |
| | Calc. | - | 2941 | 0 | - | 253 |
| SrCl$_2$ | Expt. | $46.3 \pm 0.5$ | - | 0 | - | - |
| | Ref. 231 | $45.9 \pm 1.2$ | - | 0 | - | - |

| | | | | | |
|---|---|---|---|---|---|
| | Calc. | - | 2936 | 0 | - | 242 |

| Compound | | | | | | |
|---|---|---|---|---|---|---|
| | Calc. | - | 2936 | 0 | - | 242 |
| Sr(NO$_2$)$_2$·H$_2$O | Expt. | 40 ± 50 | - | 28.3 ± 0.2 | 0.31 ± 0.02 | - |
| | Calc. (site 1) | - | 3004 | 20.2 | 0.67 | 247 |
| | Calc. (site 2) | - | 3018 | 22.2 | 0.77 | |
| SrWO$_4$ | Expt. | 20 ± 50 | - | 22.4 ± 0.2 | 0 ± 0.01 | - |
| | Calc. | - | 3002 | −20.6 | 0 | 244 |
| SrMoO$_4$ | Expt. | 15 ± 5 | - | 22.8 ± 0.2 | 0 ± 0.01 | - |
| | Ref. 230 | −5 ± 5 | - | 22.7 ± 0.2 | 0.03 ± 0.05 | - |
| | Calc. | - | 3014 | −21.1 | 0 | 244 |
| Sr(ClO$_4$)$_2$·3H$_2$O | Expt. | 0 ± 50 | - | 25.5 ± 0.5 | 0.40 ± 0.03 | - |
| | Calc. (site 1) | - | 3038 | −30.6 | 0.34 | 262 |
| | Calc. (site 2) | - | 3069 | −27.8 | 0.31 | |
| SrF$_2$ | Expt. | −12.3 ± 1 | - | 0 | - | - |
| | Ref. 231 | −13 ± 1.2 | - | 0 | - | - |
| | Calc. | - | 3007 | 0 | - | 242 |
| Sr(NO$_3$)$_2$ | Expt. | −70 ± 5 | - | 15.3 ± 0.2 | 0 ± 0.01 | - |
| | Ref. 234 | −323 | - | 15.3 | 0.03 | - |
| | Ref. 230 | −84 ± 5 | - | 15.4 ± 0.2 | 0.03 ± 0.05 | - |
| | Ref. 224 | −70 ± 30 | - | 15.3 | 0.03 | |
| | Calc. | - | 3097 | −18.7 | 0 | 246 |
| SrSO$_4$ | Expt. | −87 ± 50 | - | 28.3 ± 0.2 | 0.70 ± 0.01 | - |
| | Ref. 234 | −47 | - | 28.1 | 0.71 | - |
| | Calc. | - | 3113 | 29.9 | 0.68 | 250 |
| SrCrO$_4$ | Expt. | −175 ± 50 | - | 35.0 ± 0.5 | 0.33 ± 0.03 | - |
| | Calc. | - | 3168 | 37.4 | 0.32 | 248 |

[a] The $^{87}$Sr NMR chemical shifts are referenced to 0.5 M SrCl$_2$ in D$_2$O at 0 ppm.

**Table 6.5.** Experimental and calculated $^{87}Sr$ NMR parameters for strontium compounds containing organic ligands.

| | | $\delta_{iso}$ / ppm | $|C_Q|$ / MHz[a] | $\eta_Q$ | Crystal Structure Ref. |
|---|---|---|---|---|---|
| Sr(acac)$_2$·H$_2$O | Expt. | $30 \pm 10$ | $14.1 \pm 0.2$ | $0.25 \pm 0.01$ | - |
| Sr(F-acac)$_2$ | Expt. | $-15 \pm 50$ | $15.4 \pm 0.2$ | $0.61 \pm 0.01$ | - |
| Sr(acetate)$_2$·½H$_2$O | Expt. (site 1) | $5 \pm 10$ | $14.9 \pm 0.3$ | $0.31 \pm 0.02$ | - |
| | Expt. (site 2) | $30 \pm 10$ | $15.9 \pm 0.3$ | $0.62 \pm 0.02$ | - |
| Sr(oxalate) | Expt. | $5 \pm 5$ | $13.6 \pm 0.2$ | $0.79 \pm 0.01$ | - |
| | Calc. | $-14.3^{b}$ | $-10.9$ | $0.54$ | 252 |
| Sr(malonate) | Expt. | $0 \pm 50$ | $31.6 \pm 0.2$ | $0.79 \pm 0.01$ | - |
| | Ref. 224 | $0 \pm 60$ | $31.5$ | $0.80$ | - |
| | Calc. | $-5.4^{b}$ | $30.1$ | $0.89$ | 239 |

[a] Experimental signs of $C_Q(^{87}Sr)$ are not available.  CASTEP calculated $C_Q(^{87}Sr)$ signs are indicated.

[b] The calculated chemical shifts were obtained by converting the calculated magnetic shielding values using the correlation in Figure 6.14.

**Table 6.6.** Experimental and calculated $^{87}$Sr NMR parameters for $SrBr_2 \cdot 6H_2O$, $SrCl_2 \cdot 6H_2O$ and $SrCO_3$. Estimated isotropic magnetic shielding values were calculated using CASTEP.

| | | $\delta_{iso}$ /ppm | $\sigma_{iso}$ /ppm | $\delta_{aniso}$ /ppm | $\eta_{CS}$ | $|C_Q|$ /MHz | $\eta_Q$ | Euler angles $\alpha, \beta, \gamma$ / ° | Crystal Structure Ref. |
|---|---|---|---|---|---|---|---|---|---|
| $SrBr_2 \cdot 6H_2O$ | Expt. | 1 ± 2 | - | 26 ± 5 | 0 ± 0.05 | 3.5 ± 0.3 | 0 ± 0.05 | $\alpha^b$, 90 ± 10, 180 ± 10 | - |
| | Calc. | - | 2953 | −129 | 0 | 20.3 | 0 | 182, 90, 180 | 251 |
| | Calc.[a] | - | 2984 | −35 | 0 | 2.8 | 0 | 97, 90, 180 | 251 |
| $SrCl_2 \cdot 6H_2O$ | Expt. | 1 ± 2 | - | 28 ± 5 | 0 ± 0.05 | 4.9 ± 0.3 | 0 ± 0.05 | $\alpha^b$, 90 ± 10, 0 ± 10 | - |
| | Calc. | - | 2994 | −27 | 0 | 3.4 | 0 | 181, 90, 0 | 249 |
| $SrCO_3$ | Expt. | 1 ± 5 | - | −65 ± 5 | 0.67 ± 0.05 | 8.4 ± 0.3 | 0.16 ± 0.05 | 0 ± 10, 25 ± 10, 90 ± 10 | - |
| | Ref. 232 | ≈500[c] | - | - | - | 8.6 ± 2 | 0.27 ± 0.03 | - | - |
| | Ref. 234 | −133 | - | - | - | 8.91 | 0.14 | - | - |
| | Ref. 224 | 0 ± 20 | - | - | - | 8.91 | 0.14 | - | - |
| | Calc. | - | 3009 | 77.2 | 0.46 | 5.6 | 0.1 | 0, 24, 90 | 257 |

[a] Calculation was performed after a geometry optimization for all proton positions.

[b] The angle $\alpha$ cannot be determined unambiguously for this compound.

[c] The chemical shift was referenced to solid $SrTiO_3$ at 0 ppm and has not been corrected (see text).

### 6.3.1.1 Strontium at Sites of Cubic Symmetry

The most readily studied strontium compounds are those with structures exhibiting high symmetry (e.g., cubic), as quadrupolar coupling and magnetic shielding anisotropy do not contribute to the NMR spectral line shape, leading to relatively narrow peaks and higher signal-to-noise ratios. These compounds are SrO, SrS, $SrTiO_3$, $SrF_2$, and $SrCl_2$. SrO and SrS are isostructural, crystallizing in space group $Fm\overline{3}m$ with the Sr and O or S atoms occupying the vertices of a cube, i.e., with octahedral coordination geometry.[255,258] Strontium chloride and strontium fluoride also belong to space group $Fm\overline{3}m$, and possess 8-coordinate, cubic coordination geometry about the strontium atoms.[242] $SrTiO_3$ is an example of an ideal cubic perovskite structure, with 12 oxygen atoms coordinating to each strontium atom in a cuboctahedral arrangement.[253] The [87]Sr NMR spectra of these compounds (Figure 6.1) consisted of a single peak centered at the isotropic chemical shift values found in Table 6.4. Our experimentally determined chemical shift values of $340.8 \pm 0.5$, $-12.3 \pm 1$, and $46.3 \pm 0.5$ ppm for SrO, $SrF_2$ and $SrCl_2$, respectively, are in excellent agreement with the previously reported values of $340 \pm 1$, $-13.0 \pm 1.2$, and $45.9 \pm 1.2$ ppm.[231]
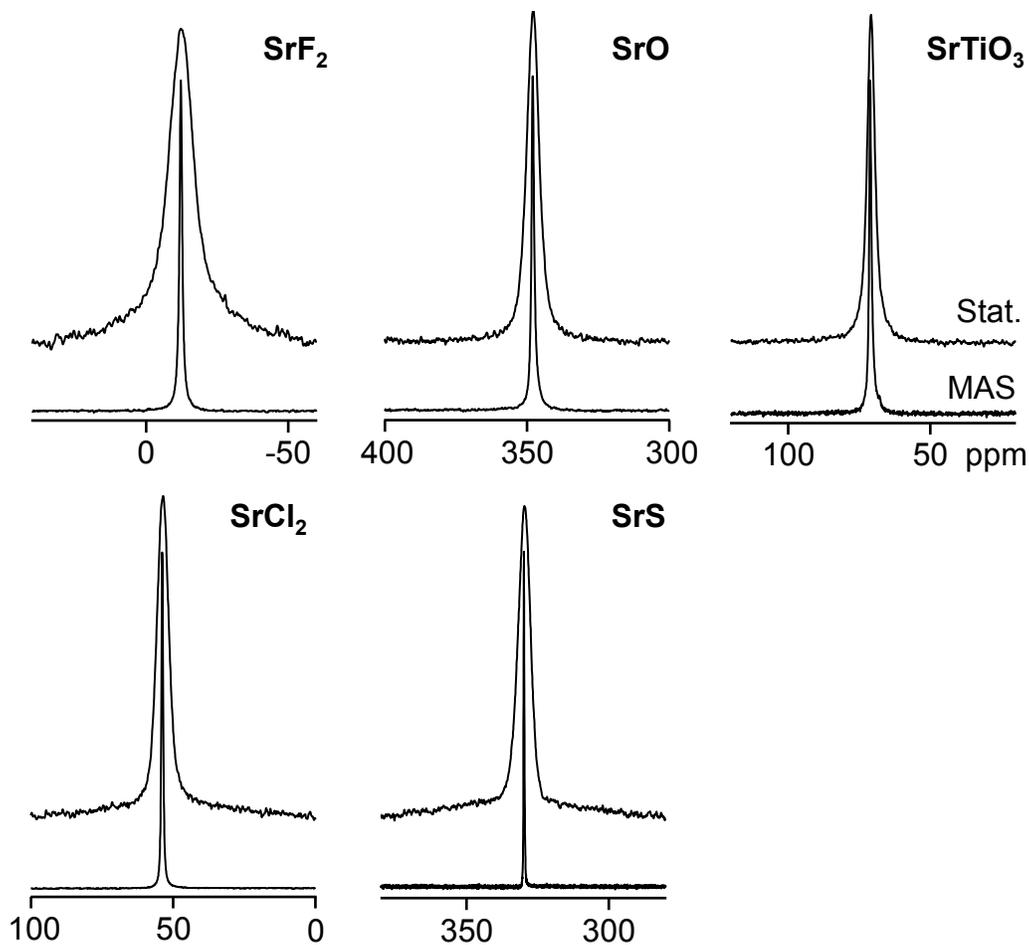
**Figure 6.1.** Strontium-87 NMR spectra of stationary (upper traces) and MAS (lower traces) $SrF_2$, $SrCl_2$, SrO, SrS, and $SrTiO_3$. Spectra were acquired at $B_0 = 21.14$ T. Parameters used to simulate these spectra (simulations not shown) are summarized in Table 6.4. All scales are in ppm. Note that with the exception of $SrF_2$, these spectra were referenced to 1 M $Sr(NO_3)_2$ (aq) at $\delta(^{87}Sr) = 0.0$ ppm. Parameters in Table 6.4 have been corrected to reflect $\delta(^{87}Sr)$ of 0.5 M $SrCl_2$ in $D_2O$ at 0.0 ppm.

### 6.3.1.2 Strontium at Sites of Axial Symmetry

Strontium-87 NMR spectra of $Sr(NO_3)_2$, $SrMoO_4$, and $SrWO_4$ are shown in Figure 6.2. Experimental and CASTEP calculated NMR parameters for these compounds are summarized in Table 6.4. $Sr(NO_3)_2$ possesses $C_3$ rotational symmetry at the strontium site,[246] whereas $SrMoO_4$ and $SrWO_4$ possess $C_{4h}$ point-group symmetry at the strontium site,[244] thus, in all three cases, the EFG tensor is confined to have axial symmetry (i.e., $|V_{XX}| = |V_{YY}| < |V_{ZZ}|$) with $V_{ZZ}$ along the axis of highest symmetry (see Figure 6.3). Therefore, $\eta_Q(^{87}Sr)$ is necessarily zero for these three compounds, which is in agreement with our experimental observations. $Sr(NO_3)_2$ has been investigated previously by several research groups.[224,230,234] Previously reported $C_Q(^{87}Sr)$ values[230,234] for $Sr(NO_3)_2$ of 15.3 and 15.4 MHz are in agreement with our experimental value of $15.3 \pm 0.2$ MHz. Previously reported[230,234] $\eta_Q(^{87}Sr)$ values were 0.03, close to the expected value of zero on the basis of the crystal structure of $Sr(NO_3)_2$. X-ray crystal diffraction data[244] indicate that $SrMoO_4$ and $SrWO_4$ are isostructural, with scheelite-type structures, where the $SrO_8$ coordination polyhedra assume snub disphenoidal geometry. $C_Q(^{87}Sr)$ values for $SrMoO_4$ and $SrWO_4$ are similar, with $C_Q(^{87}Sr) = 22.8$ and 22.4 MHz, respectively. The $V_{ZZ}$ direction in $SrMoO_4$ and $SrWO_4$ is along the 4-fold rotation axis, and is parallel to the $c$-axis of the unit cell. The $V_{ZZ}$ direction in $Sr(NO_3)_2$ lies parallel to the diagonal of the unit cell (Figure 6.3). Isotropic chemical shifts determined for $Sr(NO_3)_2$, $SrMoO_4$, and $SrWO_4$ are $-70 \pm 5$, $15 \pm 5$, and $20 \pm 50$, respectively. Note that the $^{87}Sr$ NMR spectrum of $SrWO_4$ was acquired with the WURST-QCPMG pulse sequence, rendering the location of the isotropic chemical shift less certain. Larsen et al.[230] reported $\delta_{iso}(^{87}Sr) = -84$ and $-5 \pm 5$ ppm for $Sr(NO_3)_2$ and $SrMoO_4$, respectively, both values in disagreement with our experimental values. The chemical shift values reported by Larsen et al. differ from ours systematically. Note that although Larsen et al.[230] report $\delta_{iso}(^{87}Sr)$

$= -84$ ppm for $Sr(NO_3)_2$ in their tables, determined from their $^{87}Sr$ QCPMG NMR spectrum, text

in their discussion mentions an additional fit of a quadrupolar echo NMR spectrum with $\delta_{iso}(^{87}Sr)$

$= -93$ ppm. Chemical shift values of $-323$ and $-70$ ppm were reported for $Sr(NO_3)_2$ by Bowers

et al.[234] and Bonhomme et al.,[224] respectively. In general (Table 6.4), the chemical shift values

reported by Bowers et al.[234] in their 2006 paper are in disagreement with our values. This

discrepancy is not systematic, with the absolute difference between their reported chemical shift

values and ours varying from 40 to 253 ppm. Our research and the recent study by Bonhomme

et al.[224] are in excellent agreement, supporting that of the three reported values for $\delta_{iso}(^{87}Sr)$ in

$Sr(NO_3)_2$, the most recently determined value of $-70 \pm 5$ ppm is the most accurate.
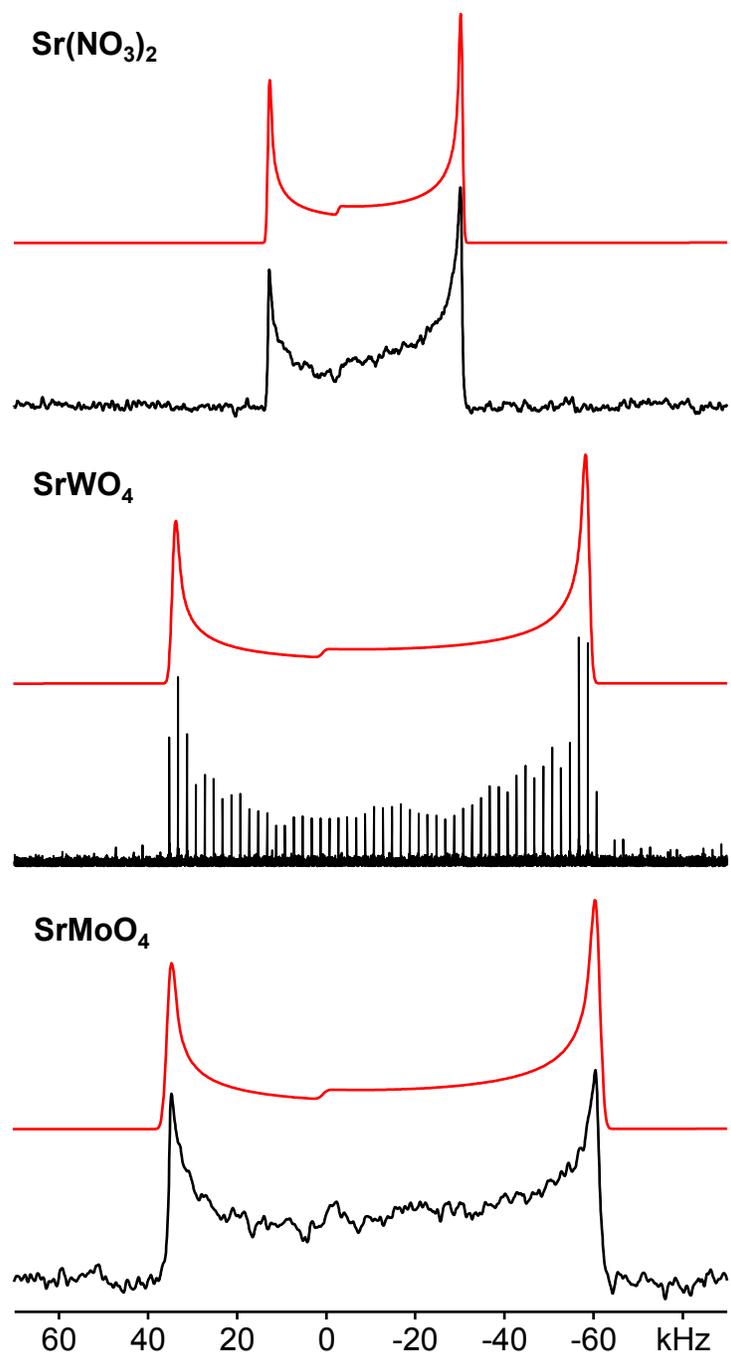
**Figure 6.2.** Experimental (lower traces) and simulated (upper traces) [87]Sr NMR spectra of stationary solid powdered samples of $Sr(NO_3)_2$, $SrWO_4$, and $SrMoO_4$. Experimental spectra were acquired at $B_0 = 21.14$ T using the quadrupolar echo or WURST-QCPMG pulse sequences. Simulations were performed with the QUEST program. Parameters used in the simulations are summarized in Table 6.4.
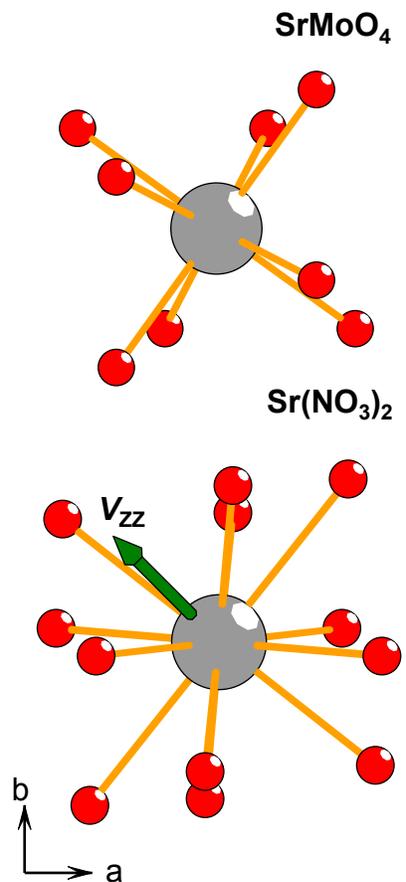
**SrMoO$_4$**

**Sr(NO$_3$)$_2$**

**Figure 6.3.** Strontium coordination geometry and electric field gradient tensor orientation for SrMoO$_4$ and Sr(NO$_3$)$_2$. $V_{ZZ}$($^{87}$Sr) in SrMoO$_4$ lies parallel to the $c$-axis, directed out of the plane of the page. $V_{ZZ}$ in Sr(NO$_3$)$_2$ lies along a 3-fold rotation axis (green arrow). SrMoO$_4$ and SrWO$_4$ are isostructural.

**6.3.1.3 Strontium at Sites with Low Symmetry**

Strontium-87 WURST-QCPMG NMR spectra of $SrSO_4$, $SrBr_2$, $SrI_2$, $Sr(NO_2)_2 \cdot H_2O$, $SrAl_2O_4$, $SrSnO_3$, $SrZrO_3$, $SrCrO_4$, and $Sr(ClO_4)_2 \cdot 3H_2O$ are shown in Figures 6.4−6.8. These inorganic strontium salts do not possess high-order symmetry at the strontium site, allowing nonzero $C_Q(^{87}Sr)$ values as well as nonaxial EFG tensors. These compounds possess $C_Q(^{87}Sr)$ values between 10.5 MHz and 50.5 MHz, with $\eta_Q(^{87}Sr)$ values between 0.31 and 0.89. Experimental NMR parameters for these compounds are summarized in Table 6.4.

In the mineral celestine, $SrSO_4$, which belongs to the orthorhombic space group *Pbnm*, the strontium atoms are coordinated by 12 oxygen atoms. The strontium atoms are, in pairs, related by a center of inversion, i.e., there are two sets of two strontium atoms that share inversion symmetry (see Figure 6.9). Crystal symmetry considerations indicate that all four strontium atoms in the $SrSO_4$ unit cell are crystallographically equivalent and must possess identical EFG and magnetic shielding tensor components. Note, however, that only the strontium atoms related by a center of inversion are magnetically equivalent,[265] and those that are not magnetically equivalent will possess different tensor orientations with respect to the crystallographic reference frame. The single-crystal $^{87}Sr$ NMR spectrum of $SrSO_4$ at one orientation in the laboratory frame is shown in Figure 6.10. As the EFG tensor orientation of each magnetically nonequivalent strontium site in celestine differs with respect to the crystallographic reference frame, their relative orientation also differs with respect to the applied magnetic field direction (laboratory $z$-axis), resulting in sets of two $^{87}Sr$ NMR peaks for each of the five observed $^{87}Sr$ spectroscopic transitions (e.g., $m_I = 5/2 \leftrightarrow m_I = 3/2$, $m_I = 3/2 \leftrightarrow m_I = 1/2$, etc). Note that $^{87}Sr$ has $I = 9/2$; the single-crystal NMR spectrum should consist of nine spectroscopic transitions for each site (not shown due to the breadth of the outer satellite

transitions, likely due to crystal imperfections). Examples of magnetic nonequivalence such as this have been discussed previously, for example, the $^{133}$Cs NMR spectrum of CsCd(SCN)$_3$ reported by Kroeker et al. in 1997.[266] The $^{87}$Sr NMR spectrum of solid, powdered celestine is shown in Figure 6.4. All orientations of the EFG tensor axes with respect to the applied magnetic field direction are represented in the $^{87}$Sr NMR spectrum of the powdered sample, resulting in an NMR powder spectrum consistent with a single strontium site, as further supported by CASTEP calculations. The $^{87}$Sr NMR spectrum of the central transition of the powdered sample was thus fit using a single $^{87}$Sr site, with $C_Q(^{87}$Sr$) = 28.3 \pm 0.2$ MHz, $\eta_Q(^{87}$Sr$) = 0.70 \pm 0.01$, and $\delta_{iso}(^{87}$Sr$) = -87 \pm 50$ ppm. Our quadrupolar parameters are in good agreement with the previous data of Bowers et al.[234] The isotropic chemical shift value of $-47$ ppm reported by Bowers et al.[234] is in agreement within error with our experimental value of $-87 \pm 50$ ppm.

The $^{87}$Sr NMR spectra of SrBr$_2$ and SrI$_2$ complete the strontium halide series that began above with cubic SrF$_2$ and SrCl$_2$. At room temperature, strontium fluoride and strontium chloride both possess cubic fluorite crystal structures.[242] Strontium bromide belongs to tetragonal space group $P4/n$, and possesses 8-coordinate strontium atoms with distorted square antiprismatic geometry.[261] Note that SrBr$_2$ undergoes a solid-solid phase transition at ca. 915-919 K,[261] adopting a cubic fluorite structure (space group $Fm\overline{3}m$), analogous to SrF$_2$ and SrCl$_2$. At room temperature, SrBr$_2$ possesses two crystallographically nonequivalent strontium sites, one with 4-fold rotation symmetry (i.e., with an axially symmetric EFG tensor), and the other lacking any high-order symmetry. The $^{87}$Sr NMR spectrum (Figure 6.6) correspondingly possesses two unique strontium NMR powder patterns, with $C_Q(^{87}$Sr$)$ and $\eta_Q(^{87}$Sr$)$ values of $26 \pm 1$ and $9.25 \pm 0.3$ MHz, and $0.30 \pm 0.02$ and $0 \pm 0.01$, respectively. Strontium iodide crystallizes

in space group *Pnma*, and is 7-coordinate, with monocapped trigonal prismatic coordination geometry.[243]  $SrI_2$ has one unique strontium site in the crystal structure, with $C_Q(^{87}Sr) = 10.5 \pm 1$ MHz and $\eta_Q(^{87}Sr) = 0.90 \pm 0.05$.  Chemical shifts for these two haldies are similar, with $\delta_{iso}(^{87}Sr)$ = 80 ± 30 and 85 ± 10 ppm for the two sites of $SrBr_2$, and $\delta_{iso}(^{87}Sr) = 100 \pm 50$ ppm for $SrI_2$. Isotropic chemical shift trends in the entire halide series are discussed below.

The crystal structure of strontium nitrite monohydrate, $Sr(NO_2)_2 \cdot H_2O$,[247] indicates two nonequivalent $^{87}Sr$ sites coordinated to a mixture of 9 or 10 oxygen and nitrogen atoms. CASTEP calculations estimate that the two sites possess different NMR parameters, e.g., $C_Q(^{87}Sr)$ values were estimated to be 20.2 and 22.2 MHz.  The experimental $^{87}Sr$ NMR spectrum of $Sr(NO_2)_2 \cdot H_2O$ did not have resolved discontinuities consistent with two $^{87}Sr$ sites, thus the NMR spectrum was fit using a single site.  This is not surprising, as the parameters estimated by CASTEP for the two sites were similar.  The crystal structure for strontium perchlorate trihydrate[262] indicates two nonequivalent strontium atoms, each coordinated to five oxygen atoms belonging to $H_2O$ molecules and four oxygen atoms belonging to perchlorate anions. CASTEP calculations predict similar NMR parameters for both sites.  The $^{87}Sr$ NMR spectrum of $Sr(ClO_4)_2 \cdot 3H_2O$ was fit with a single strontium site, with $C_Q(^{87}Sr)$ and $\eta_Q(^{87}Sr)$ values of 25.5 ± 0.5 MHz and 0.40 ± 0.03.  The $^{87}Sr$ NMR spectrum of $SrAl_2O_4$ (Figure 6.8) is also expected to consist of two overlapping powder patterns belonging to two crystallographically nonequivalent strontium sites.[245]  Simulations that included only one $^{87}Sr$ site did not conform to the experimental line shape, which displays discontinuities indicative of two quadrupolar NMR sites. $C_Q(^{87}Sr)$ values determined for $SrAl_2O_4$ were 50.5 and 43.0 ± 5 MHz, with $\eta_Q(^{87}Sr) = 0.70$ and 0.88 ± 0.04, respectively, and with $\delta_{iso}(^{87}Sr)$ values of 130 and 150 ± 100 ppm, respectively.  Our

two-site simulation is admittedly a poor fit; the parameters must be considered as preliminary

estimates until access to higher magnetic field strengths are available.

Strontium stannate and strontium zirconate are both examples of orthorhombic

perovskites with 8-coordinate strontium atoms.[244] $SrSnO_3$ and $SrZrO_3$ possess similar

quadrupolar parameters, with $C_Q(^{87}Sr) = 31.6 \pm 0.2$ and $31.2 \pm 0.2$ MHz, and $\eta_Q(^{87}Sr) = 0.73 \pm$

$0.01$ and $0.62 \pm 0.02$, respectively. Strontium chromate possesses a monazite-type structure,

though according to Effenberger and Pertlik,[248] the strontium atom is coordinated to ten

surrounding oxygen atoms with interatomic distances between 2.575(2) and 3.264(2) Å, rather

than the nine expected[267] for the classic monazite structure. $SrCrO_4$ has the most shielded $^{87}Sr$

nucleus of all the compounds investigated here, with a chemical shift of $-175 \pm 50$ ppm. Note

that the central discontinuity in our simulated NMR spectrum for $SrCrO_4$ does not fit perfectly

with that shown on the experimental spectrum when chemical shift anisotropy is disregarded,

suggesting that some CSA may be present. However, spectra simulated with the inclusion of

CSA, while giving a better fit for the central discontinuity, gave poorer fits for the two

quadrupolar "horns." It was thus assumed in our spectral simulation (Figure 6.4) that $\Omega(^{87}Sr) = 0$

ppm.
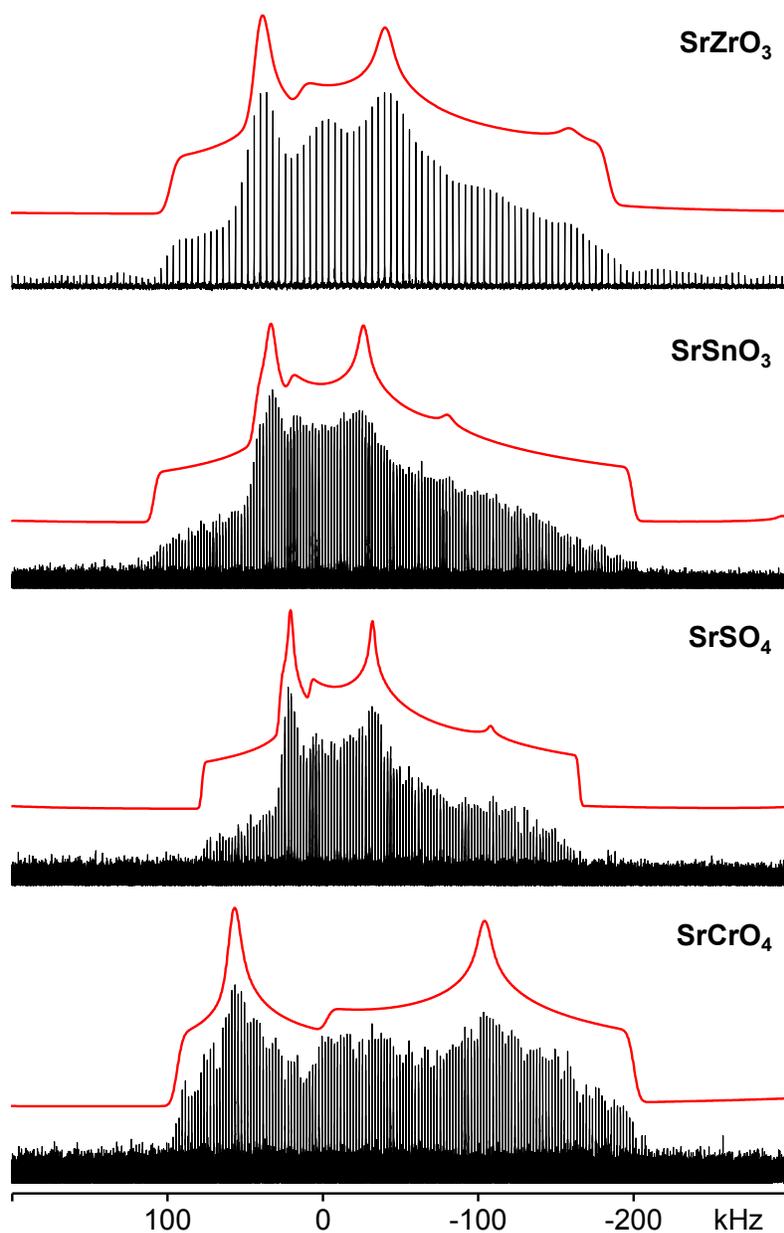
**Figure 6.4.** Experimental (lower traces) and simulated (upper traces) [87]Sr NMR spectra of stationary powdered samples of $SrZrO_3$, $SrSnO_3$, $SrSO_4$, and $SrCrO_4$. Experimental spectra were acquired at $B_0 = 21.14$ T with the WURST-QCPMG pulse sequence. Parameters used in the simulations are summarized in Table 6.4.
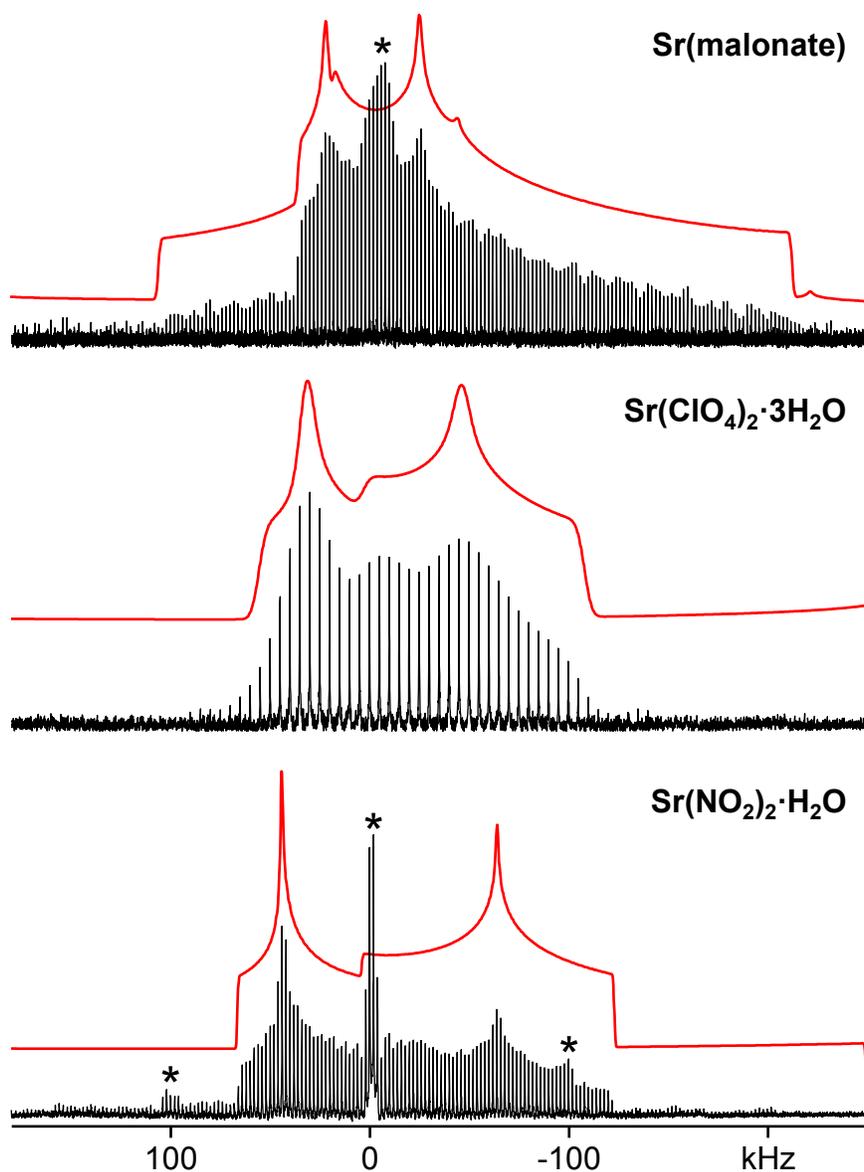
**Figure 6.5.** Experimental (lower traces) and simulated (upper traces) [87]Sr NMR spectra of stationary powdered samples of strontium malonate, $Sr(ClO_4)_2 \cdot 3H_2O$, and $Sr(NO_2)_2 \cdot H_2O$. Experimental spectra were acquired at $B_0 = 21.14$ T using the WURST-QCPMG pulse sequence. Asterisks show the location of impurities ($SrCO_3$ and $SrCl_2 \cdot 6H_2O$ for strontium malonate and strontium nitrite monohydrate, respectively). Parameters used in the simulations are summarized in Tables 6.4 and 6.5.
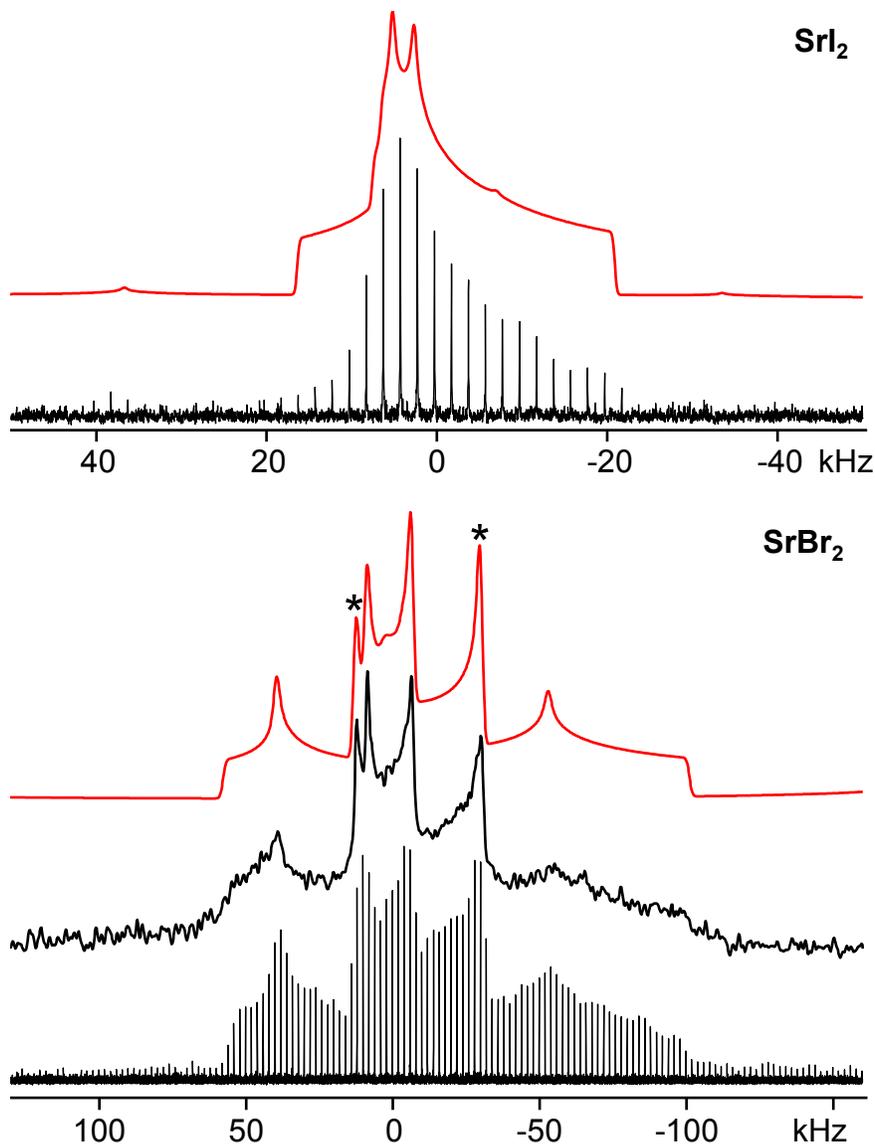
**Figure 6.6.** Experimental (lower traces) and simulated (upper traces) [87]Sr NMR spectra of stationary powdered samples of $SrBr_2$ and $SrI_2$. Experimental spectra were acquired at $B_0 = 21.14$ T with either the WURST-QCPMG or quadrupole echo pulse sequences. The [87]Sr NMR spectrum of $SrBr_2$ includes signal from the impurity $Sr(NO_3)_2$ (marked with asterisks).
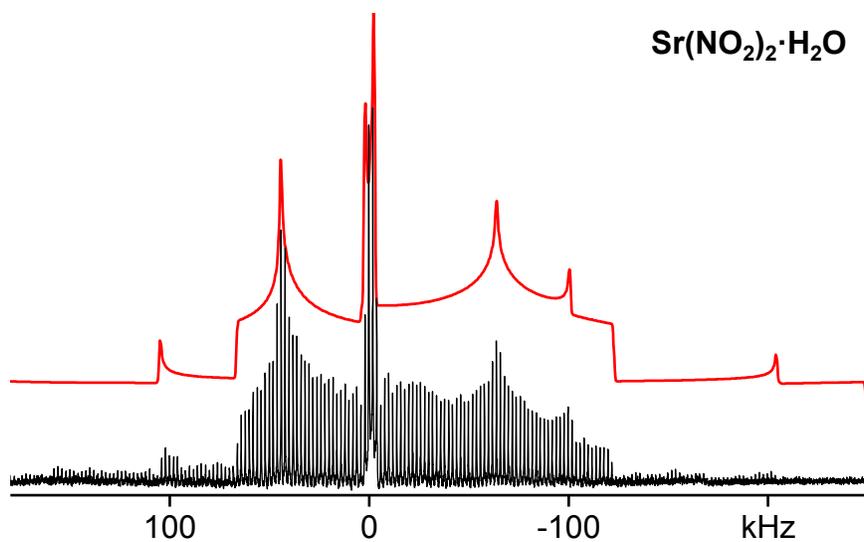
**Figure 6.7.** Experimental (lower trace) and simulated (upper trace) $^{87}$Sr NMR spectra of a stationary powdered sample of $Sr(NO_2)_2 \cdot H_2O$. The simulation includes the $^{87}$Sr NMR signal from $SrCl_2 \cdot 6H_2O$ (sample impurity) at 7% intensity. The $SrCl_2 \cdot 6H_2O$ central transition and a discontinuity from a satellite transition overlap with the $Sr(NO_2)_2 \cdot H_2O$ central transition.
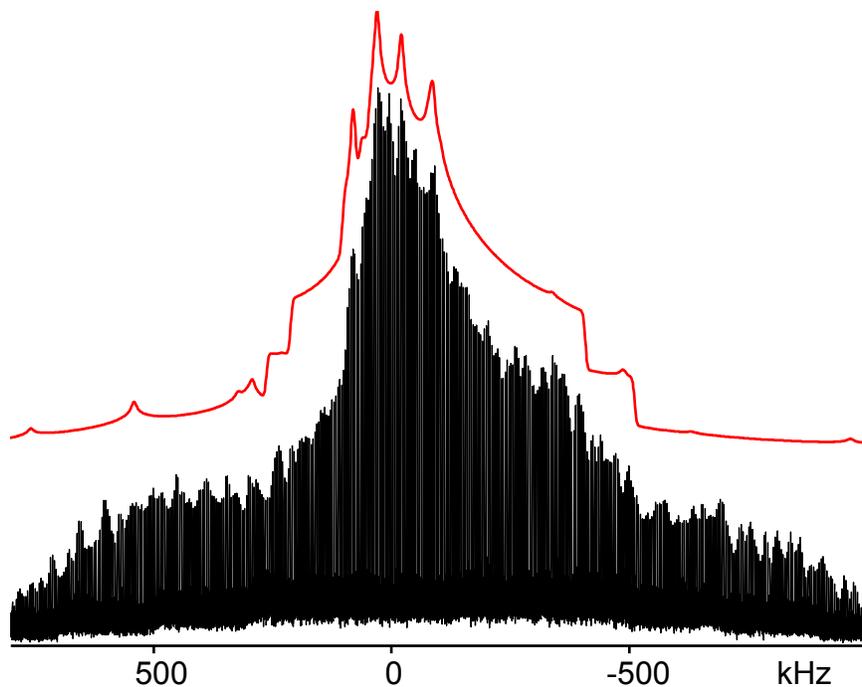
**Figure 6.8.** Experimental (lower trace) and simulated (upper trace) [87]Sr NMR spectra of SrAl$_2$O$_4$. The crystal structure for SrAl$_2$O$_4$ indicates two unique strontium sites, and the [87]Sr NMR spectrum is correspondingly a sum of two overlapping NMR powder patterns with similar EFG and CS tensor parameters. The simulated NMR spectrum was generated using QUEST and contains spectral contributions from the central ($m_I$ = 1/2 to −1/2) and satellite transitions.
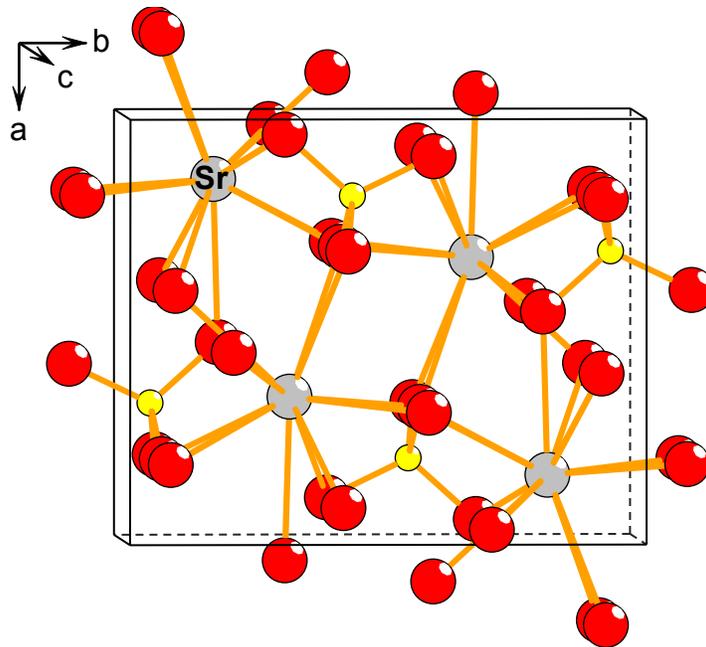
**Figure 6.9.** Unit cell for celestine, $SrSO_4$. Oxygen atoms are shown in red, and sulfur atoms are shown in yellow. Strontium atoms at the top left and bottom right of the figure are related by a center of inversion, as are the two strontium atoms at the top right and bottom left of the image.
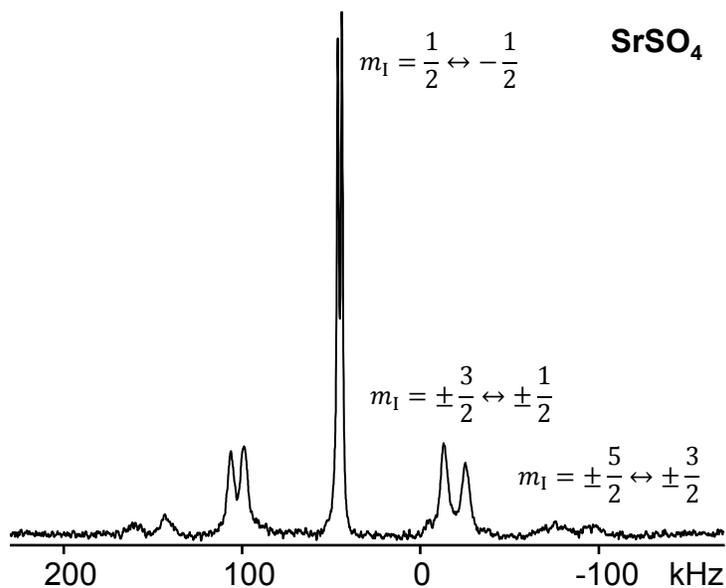
**Figure 6.10.** Central portion of the $^{87}$Sr NMR spectrum of a single crystal of celestine, SrSO$_4$, at a random orientation in $B_0$. The two peaks present for each spectroscopic transition correspond to two sets of magnetically nonequivalent strontium atoms in the celestine unit cell (Figure 6.9).

### 6.3.1.4 Strontium Salts with Organic Anions

Several strontium salts with monodentate or bidentate organic anions were also included in this research. These compounds include the antiosteoporotic drug strontium malonate, as well as strontium acetylacetonate, strontium hexafluoro-2,4-pentanedionate (Sr(F-acac)$_2$), strontium acetate, and strontium oxalate. Unfortunately, the crystal structures of strontium acetylacetonate and strontium acetate are not currently available in the literature. Karl Fischer analysis of our bulk powdered samples indicates approximately 0.8 water molecules per strontium acetylacetonate unit (i.e., the monohydrate), approximately 0.5 water molecules per strontium acetate unit (i.e., the hemihydrate), and that our sample of strontium oxalate is anhydrous. Spectra of some of these compounds are shown in Figure 6.11, whereas the $^{87}$Sr NMR spectrum of Sr(malonate) is shown in Figure 6.5, and the $^{87}$Sr NMR parameters are summarized in Table 6.5. Our experimental NMR parameters of $C_Q(^{87}$Sr$) = 31.6 \pm 0.2$ MHz, $\eta_Q(^{87}$Sr$) = 0.79 \pm 0.01$, and $\delta_{iso}(^{87}$Sr$) = 0 \pm 50$ ppm for Sr(malonate) are in excellent agreement with parameters reported by Bonhomme et al.[224] for their $^{87}$Sr-enriched sample. $C_Q(^{87}$Sr$)$ values for the remaining four strontium compounds with organic ligands fell between 13.6 and 15.9 MHz, and experimental $\delta_{iso}(^{87}$Sr$)$ values ranged from −15 to +30 ppm. The experimental $^{87}$Sr NMR spectra of strontium acetate hemihydrate (Figure 6.11) did not conform to a one-site powder pattern, so two $^{87}$Sr sites were used in the spectral simulation. The NMR parameters for these two sites were similar, with $C_Q(^{87}$Sr$) = 14.9$ and $15.9 \pm 0.3$ MHz, and $\delta_{iso} = 5$ and 30 ppm, for sites 1 and 2, respectively. The resulting simulated line shape accurately reproduces both the WURST-QCPMG and quadrupolar echo NMR spectra. These five organic anions are all coordinated to strontium through oxygen atoms, with Sr(oxalate) possessing an 8-coordinate strontium site, and Sr(malonate) possessing a 9-coordinate strontium site (Table 6.2). It is thus reasonable to expect similar coordination

environments for strontium acetate hemihydrate, strontium acetylacetonate hydrate, and strontium hexafluoro-2,4-pentanedionate, given their similarities in both isotropic chemical shifts and quadrupolar coupling constants.

**6.3.1.5 Salts with Experimentally Measureable $^{87}$Sr Chemical Shift Anisotropy**

Strontium-87 NMR spectra of $SrCl_2 \cdot 6H_2O$, $SrBr_2 \cdot 6H_2O$, and $SrCO_3$ (strontianite) were acquired under both MAS and stationary sample conditions (Figure 6.12). These spectra were simulated using the WSolids program[99] as $C_Q(^{87}Sr)$ values are relatively small (note also that the current version of QUEST is not able to simulate NMR spectra acquired under MAS conditions). A summary of the NMR parameters used in the simulations is available in Table 6.6. The parameters used to simulate both experimental conditions, stationary samples and samples undergoing MAS, agree within the reported error.

Both $SrCl_2 \cdot 6H_2O$ and $SrBr_2 \cdot 6H_2O$ have axially symmetric $^{87}$Sr NMR interaction tensors, meaning $\eta_{CS}$ and $\eta_Q$ are both zero. $C_Q(^{87}Sr)$ values are 4.9, 3.5, and 8.4 MHz, for $SrCl_2 \cdot 6H_2O$, $SrBr_2 \cdot 6H_2O$, and $SrCO_3$, respectively. Isotropic chemical shift values for all three compounds are approximately 1 ppm. Note that these compounds all feature strontium atoms coordinated to nine surrounding oxygen atoms, making their coordination geometry similar to that of the $Sr^{2+}$ ion in solution,[238] which is used as our chemical shift reference. Strontium malonate also possesses a similar coordination geometry and an isotropic chemical shift value of 0 ppm (see above). Chemical shift anisotropy was measured experimentally for all three compounds (Figure 6.12). As MAS NMR spectra do not exhibit broadening due to anisotropy in magnetic shielding, but retain some orientation-dependent broadening due to the quadrupolar interaction, MAS NMR spectra of these three compounds were used to characterize the electric field gradient tensors.

Orientation-dependent (anisotropic) broadening due to both the quadrupolar and magnetic shielding interactions contributes to the NMR line shapes of stationary $SrCl_2 \cdot 6H_2O$, $SrBr_2 \cdot 6H_2O$, and $SrCO_3$; the chemical shift tensors were characterized on the basis of the NMR line shapes of the stationary samples. Euler angles relating the EFG and CS tensor principal directions estimated by CASTEP calculations were used to simulate experimental NMR spectra (see Figure 6.13). Note we use the ZYZ convention.[30] The axial symmetry of the $^{87}$Sr CS and EFG tensors of $SrCl_2 \cdot 6H_2O$ and $SrBr_2 \cdot 6H_2O$ simplifies analysis by confining the possible Euler angles (i.e., $\beta$ = 0 or 90°). Simulated fits showed good agreement with experimental line shapes using the CASTEP calculated Euler angles. $\delta_{aniso}(^{87}Sr)$ values of +28, +26, and −65 ppm were measured for $SrCl_2 \cdot 6H_2O$, $SrBr_2 \cdot 6H_2O$, and $SrCO_3$, respectively. Note the latter corresponds to a span of ca. 80 ppm ($\eta_{CS}(^{87}Sr)$ = 0.67). These values are in good agreement with those estimated by CASTEP, with $\sigma_{aniso}(^{87}Sr)$ = −27, −35, and +77.2 ppm for $SrCl_2 \cdot 6H_2O$, $SrBr_2 \cdot 6H_2O$, and $SrCO_3$, respectively (an estimated span of 89 ppm for $SrCO_3$).

Strontianite, $SrCO_3$, has been studied via solid-state $^{87}$Sr NMR spectroscopy several times previously,[224,232,234] where NMR parameters were obtained under the assumption that the only source of spectral broadening was the quadrupolar interaction. $C_Q(^{87}Sr)$ values of 8.6 and 8.91 MHz were reported previously for $SrCO_3$, the former in agreement with our experimental value of 8.4 ± 0.3 MHz. As with $Sr(NO_3)_2$, reported isotropic chemical shifts for $SrCO_3$ vary greatly. The reported value of 0 ppm by Bonhomme et al.[224] is in agreement with our experimental value, whereas Bowers et al.[234] and Bastow[232] report $\delta_{iso}(^{87}Sr)$ = −133 and ≈ 500 ppm, respectively, in disagreement with our value. The value reported by Bastow[232] was referenced to $SrTiO_3$ at 0 ppm, which possesses a chemical shift of 63.4 ppm with respect to 0.5 M $SrCl_2$ in $D_2O$ (Table 6.4). The corrected value of ≈ 563 ppm is in even further disagreement

with ours. We are confident in our experimental $\delta_{iso}(^{87}Sr)$ value for $SrCO_3$ as it is consistent with

$\delta_{iso}(^{87}Sr)$ values for compounds with similar coordination environments as well as the 9-coordinate $Sr^{2+}$ ion in solution (our chemical shift reference), and because this value was

determined independently by Bonhomme et al.[224]

Though we have shown that chemical shift anisotropy can visibly contribute to $^{87}Sr$ NMR

spectra of solids, the $^{87}Sr$ NMR spectra of the stationary samples of $SrCl_2 \cdot 6H_2O$ and $SrBr_2 \cdot 6H_2O$

could easily be mistaken for pure Zeeman-quadrupolar spectra, as the intensity and position of

the spectral discontinuities are not drastically altered by the inclusion of CSA. Thus it may be

necessary to acquire $^{87}Sr$ NMR spectra under MAS conditions or, when MAS is not available, at

multiple magnetic field strengths to recognize CSA as a contributor to the $^{87}Sr$ NMR powder line

shape. Certainly, if one is only acquiring QCPMG spectra it may not be possible to resolve

effects from CSA; resolving these effects would be dependent on the NMR spectral resolution.

CASTEP calculations reported in this work as well as by Bonhomme et al.[224] indicate $\sigma_{aniso}$

values of up to $-170$ ppm (a maximum span of ca. 200 ppm), whereas the entire $^{87}Sr$ chemical

shift range available in the current literature spans approximately 550 ppm. This would suggest

that $^{87}Sr$ spans on the order of 500 ppm are possible (vide infra).
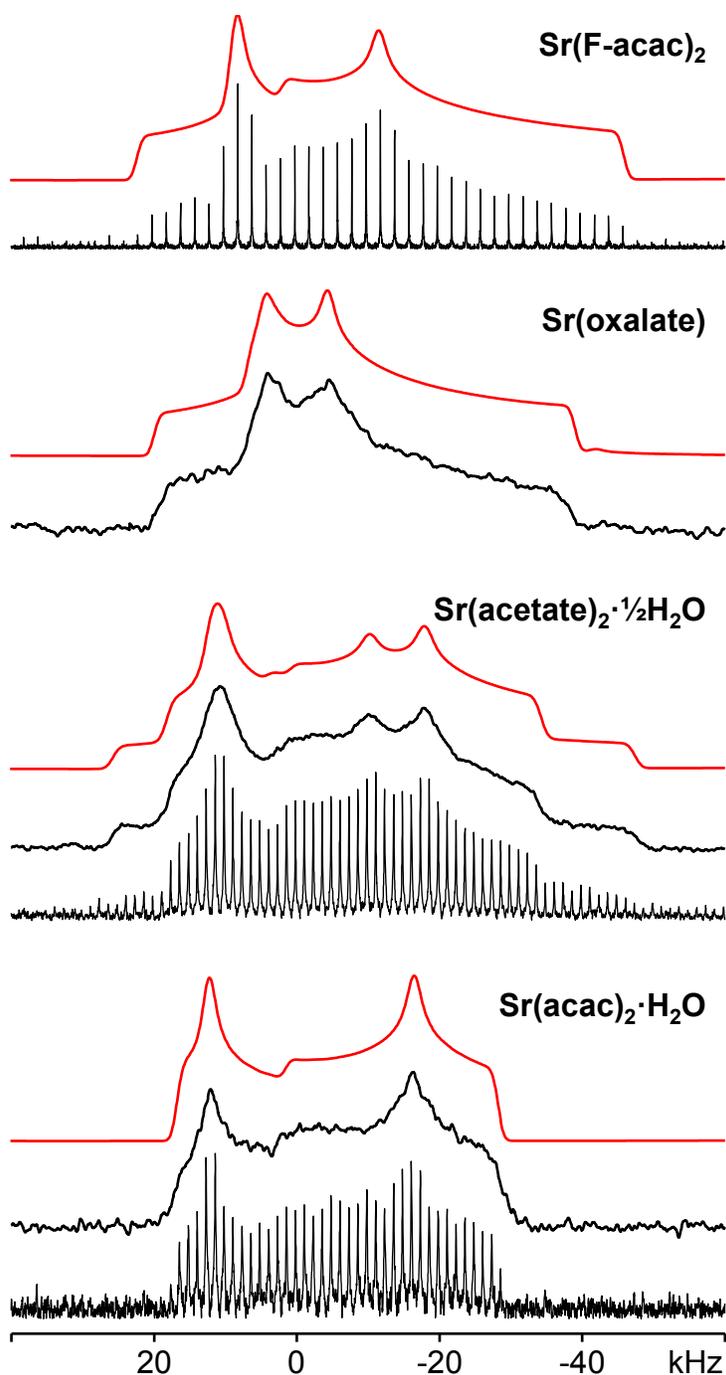
**Figure 6.11.** Experimental (lower traces) and simulated (upper traces) [87]Sr NMR spectra of stationary solid powdered samples of strontium hexafluoro-2,4-pentanedionate, strontium oxalate, strontium acetate hemihydrate, and strontium acetylacetonate monohydrate. Experimental spectra were acquired at $B_0 = 21.14$ T using the quadrupolar echo and WURST-QCPMG pulse sequences. Simulations were performed using the QUEST program. Parameters used in the simulation are summarized in Table 6.5.
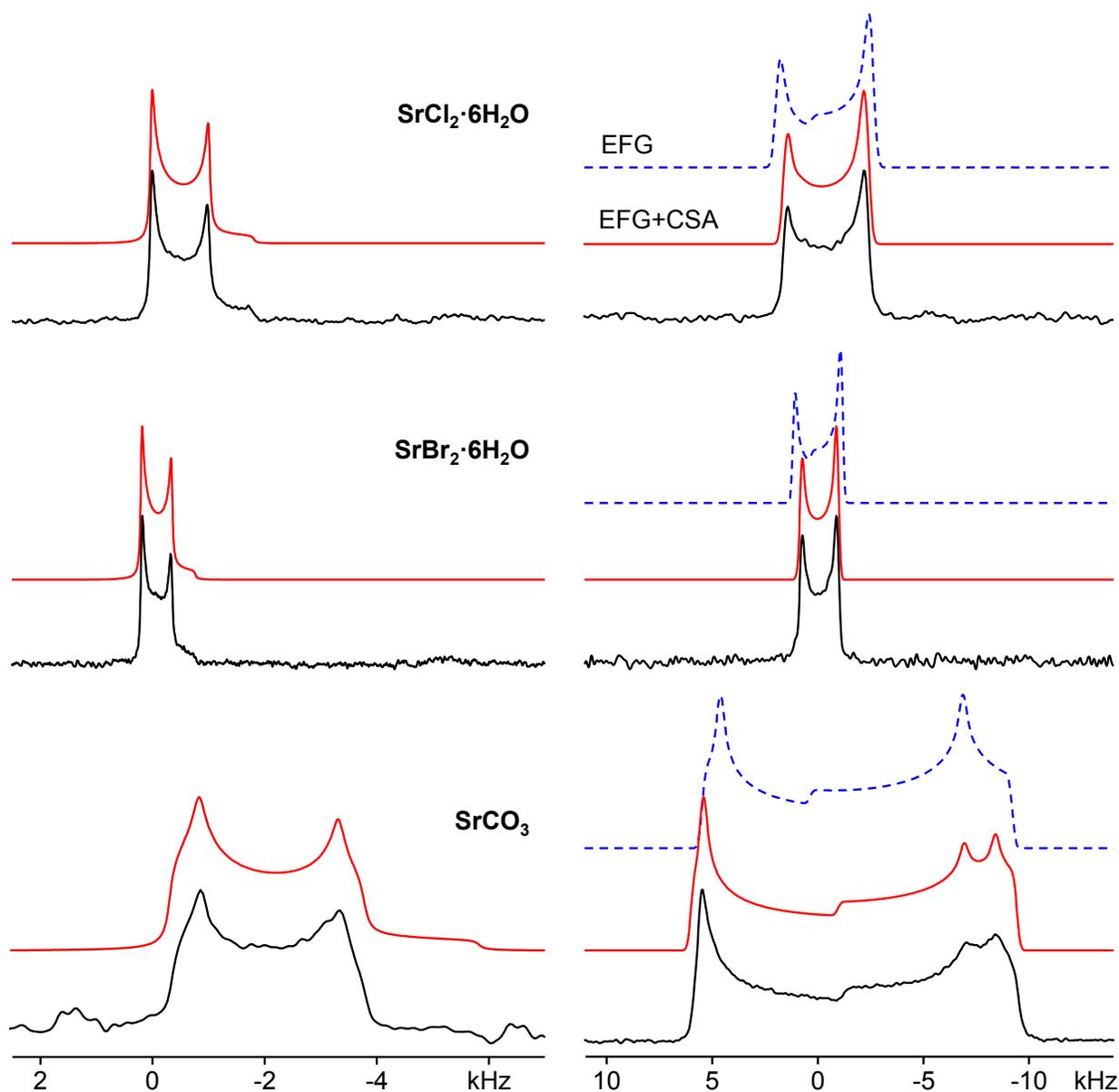
**Figure 6.12.** Experimental (lower traces) and simulated (upper traces) [87]Sr NMR spectra of solid powdered samples of $SrCl_2 \cdot 6H_2O$, $SrBr_2 \cdot 6H_2O$, and $SrCO_3$. Experimental spectra were acquired at $B_0 = 21.14$ T using a quadrupolar echo. Simulated spectra were generated using WSolids1. Spectra acquired under MAS conditions (left) show orientation-dependent line shape effects from the quadrupolar interaction (second-order correction to the Zeeman energy), whereas spectra of stationary samples (right) show line shape contributions from both quadrupolar coupling and chemical shift anisotropy. Blue dotted lines indicate simulated [87]Sr NMR spectra that only include quadrupolar effects derived from MAS spectra for comparison. Parameters used in the simulations are summarized in Table 6.6.
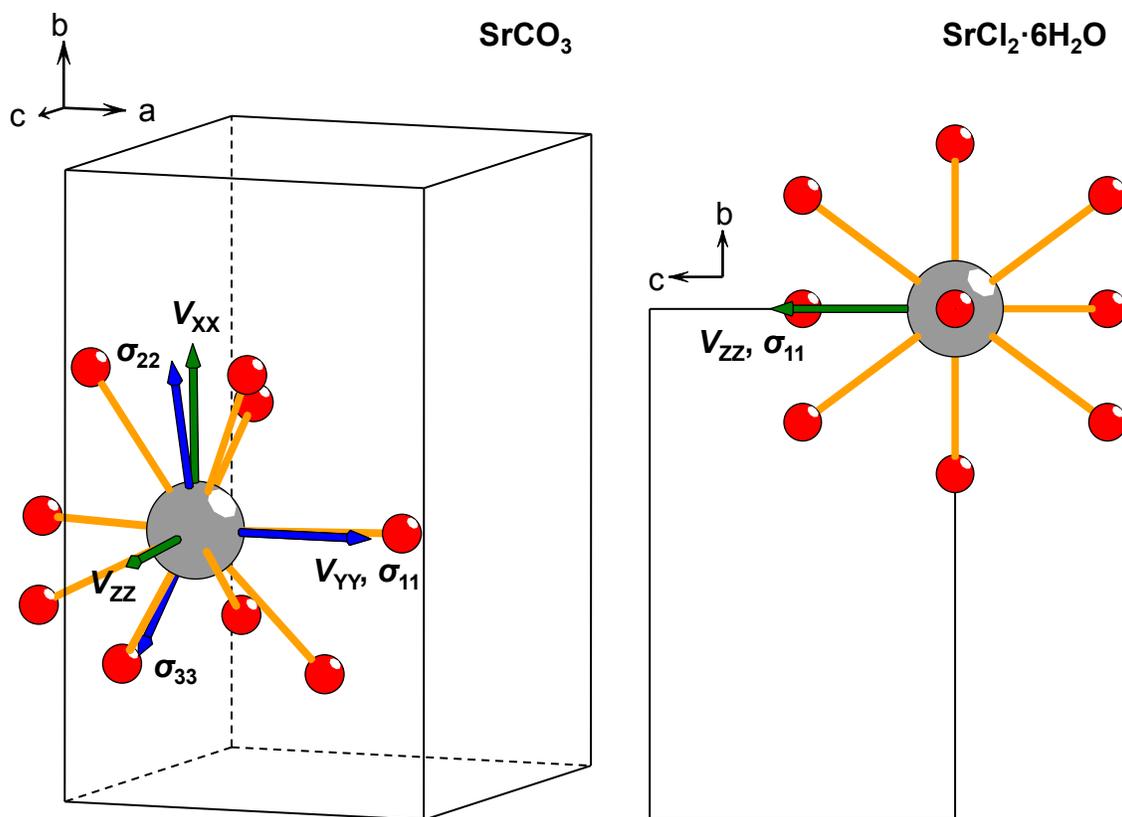
**Figure 6.13.** Strontium-87 EFG and magnetic shielding tensor orientations in $SrCO_3$ and $SrCl_2 \cdot 6H_2O$, as calculated by CASTEP. In $SrCO_3$, $V_{YY}$ and $\sigma_{11}$ are parallel to the $a$-axis, whereas $V_{ZZ}$ and $\sigma_{11}$ are parallel to the $c$-axis in $SrCl_2 \cdot 6H_2O$. $SrCl_2 \cdot 6H_2O$ has axially symmetric EFG and magnetic shielding tensors.

**6.3.1.6 Unsuccessful $^{87}$Sr NMR Experiments**

Attempts were made at acquiring $^{87}$Sr NMR spectra of solid powdered strontium gluconic acid, strontium oxalate monohydrate and dihydrate, strontium ranelate, strontium neodecanoate, strontium citrate pentahydrate, and strontium selenide, but no reliable NMR data were obtained. Strontium-87 NMR spectra of Sr(oxalate)·$H_2O$, Sr(oxalate)·$2H_2O$, and Sr(citrate)·$5H_2O$ were acquired with and without $^1$H decoupling.  Proton decoupling did not have any discernible effect on the NMR spectra of these compounds.  Strontium ranelate exists in the solid phase as a number of different hydrates, including a tetrahydrate, heptahydrate, octahydrate, and nonahydrate.[268,269]  Preparations of the nonahydrate were reported to dehydrate rapidly in atmosphere, e.g., larger crystals broke down into smaller crystals containing ca. five to seven hydrated water molecules per formula unit.[268]  It is thus not clear if our sample of strontium ranelate was pure or a mixture of hydrates, the latter being likely.  Each hydrate is expected to produce a unique $^{87}$Sr NMR spectrum, and the resulting multiple NMR powder patterns with weak intensity may account for why we were unable to observe $^{87}$Sr NMR signal for this compound.  Strontium selenide was likely nonstoichiometric and showed metallic behavior.

**6.3.2 CASTEP Results**

**6.3.2.1 Magnetic Shielding**

The correlation between calculated and experimental magnetic shielding and chemical shift values is shown in Figure 6.14.  This figure includes chemical shift and magnetic shielding values for all inorganic strontium compounds except $SrI_2$.  The version of the CASTEP program used does not include relativistic contributions to the magnetic shielding, and as the iodine atoms directly bonded to strontium are expected to introduce significant relativistic effects, $SrI_2$ was not

included in the correlation.  Indeed, the calculated value of $\sigma(^{87}Sr)$ for $SrI_2$ is a clear outlier. Values calculated by CASTEP and experimental values show strong correlation, with $R^2 =$ 0.9528 and a slope of $-1.118$.  As strontium is a fifth-period element, relativistic effects introduced by the mass of the strontium nuclei are expected to be important.[270]  The strong correlation indicates that relativistic contributions to the magnetic shielding are likely similar for all of the studied strontium salts.  The relationship found in the least squares linear regression was used to determine calculated isotropic chemical shift values for strontium oxalate and strontium malonate (Table 6.5).  Several CASTEP calculations estimating magnetic shielding values were performed for strontium-containing compounds that were not studied experimentally (Table 6.3).  As there is a strong correlation between calculated and experimental magnetic shielding and chemical shift values, these additional CASTEP calculations are expected to be reliable additions to the known $^{87}Sr$ chemical shift scale.  In addition, the CASTEP estimated values for the magnetic shielding anisotropy and asymmetry parameters are likely an accurate representation of the general magnitudes of chemical shift anisotropy and asymmetry parameters for the $^{87}Sr$ nucleus.
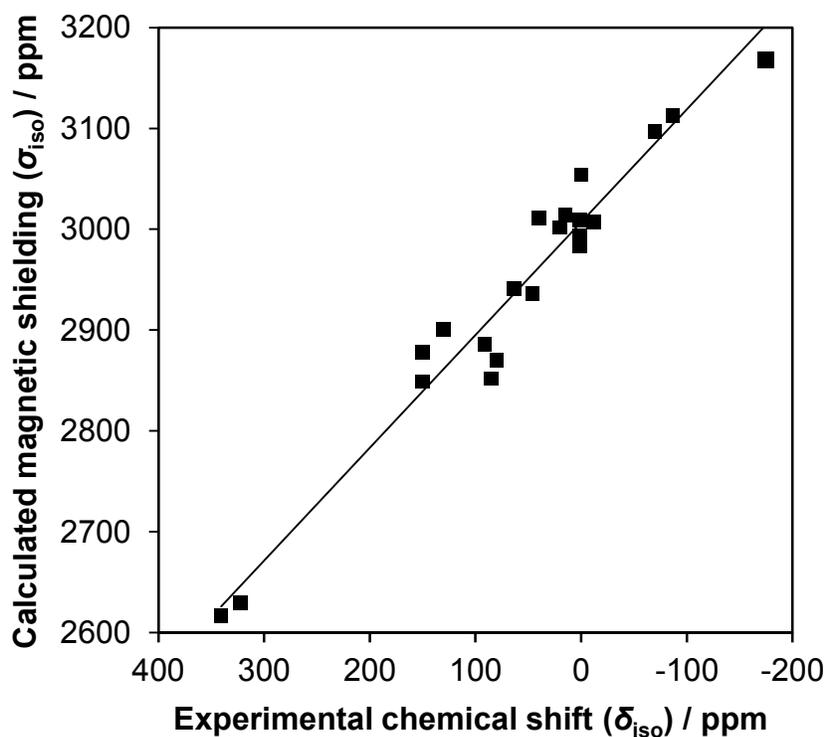
**Figure 6.14.** Correlation between calculated isotropic [87]Sr magnetic shielding constants and experimentally determined isotropic [87]Sr chemical shift values listed in Table 6.4 (Except SrI$_2$). $\sigma_{iso}(^{87}Sr) = 3007$ ppm $- 1.118\delta_{iso}(^{87}Sr)$, $R^2 = 0.9528$. The experimental [87]Sr NMR chemical shift values are referenced to 0.5 M SrCl$_2$ in D$_2$O at $\delta_{iso} = 0.0$ ppm.
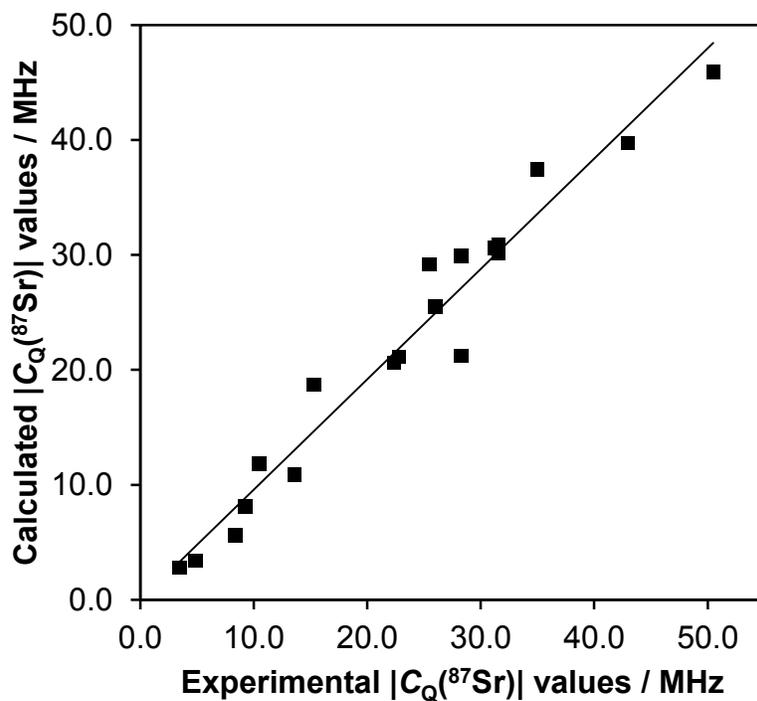
**Figure 6.15.** Correlation between calculated and experimental $C_Q(^{87}Sr)$ values. $C_Q(^{87}Sr)_{calc} = 0.9591 C_Q(^{87}Sr)_{expt} - 0.0105$ MHz, $R^2 = 0.9571$.
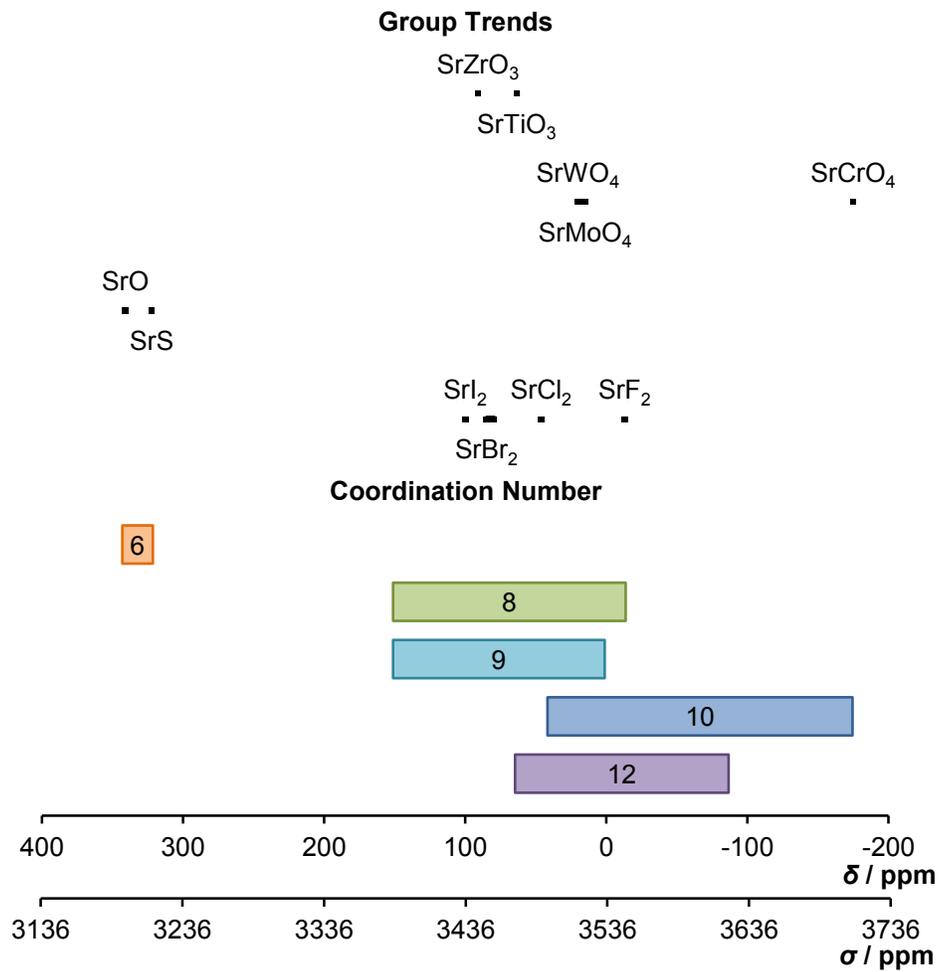
**Figure 6.16.** Trends in [87]Sr magnetic shielding. Coordination numbers for each compound are those given in the crystallography literature (see text).

### 6.3.2.2 Electric Field Gradients

The correlation between calculated and experimental $C_Q(^{87}Sr)$ values is shown in Figure 6.15. All nonzero $C_Q(^{87}Sr)$ values obtained in this work were used in this correlation. An average of the two calculated $C_Q(^{87}Sr)$ values for the two nonequivalent strontium sites in both $Sr(NO_2)_2 \cdot H_2O$ and $Sr(ClO_4)_2 \cdot 3H_2O$ were used in conjunction with the experimentally determined $C_Q(^{87}Sr)$ values for these compounds, as both experimental NMR spectra were fit with a single $^{87}Sr$ site. These data have $R^2 = 0.9571$ and a slope of 0.9591. Note, however, that the signs of $C_Q(^{87}Sr)$ are not available from experiment, and signs predicted by CASTEP vary (Tables 6.4-6.6). In general, the magnitudes of $C_Q(^{87}Sr)$ values predicted by CASTEP were in reasonable agreement with the experimental values.

### 6.3.3 Chemical Shift Trends

### 6.3.3.1 $^{87}Sr$ Chemical Shift Trends and Absolute Shielding Scale

Trends in chemical shifts based on the available $^{87}Sr$ isotropic chemical shift data are illustrated in Figure 6.16. The absolute shielding scale depicted in Figure 6.16 is based on the recently calculated value of $3536 \pm 106$ ppm for the absolute shielding of the $Sr^{2+}$ ion coordinated to nine water molecules,[238] corresponding to our $^{87}Sr$ chemical shift reference, 0.5 M $Sr^{2+}$ ions ($SrCl_2$) in aqueous solution. This value is fairly close to that predicted by the correlation of our experimental $\delta_{iso}(^{87}Sr)$ and CASTEP calculated values, which indicates $\sigma_{iso}(^{87}Sr) = 3007$ ppm at $\delta_{iso}(^{87}Sr) = 0$ ppm. Note that CASTEP performs nonrelativistic calculations for magnetic shielding values, and the relativistic contribution to the magnetic shielding of $Sr^{2+}$ is estimated to be ca. 400 ppm (i.e., $\sigma_{iso}(^{87}Sr)_{nonrel} = 3142$ ppm according to Antušek et al.).[238] As mentioned, some of the previous $^{87}Sr$ chemical shift data (e.g., for

194

Sr(NO$_3$)$_3$ and SrCO$_3$) are in conflict with those determined here and in Bonhomme et al.[224] Excluding data with large discrepancies to those in the present work and to those of Bonhomme et al.,[224] the [87]Sr isotropic chemical shifts currently available range from approximately −200 to 350 ppm, covering approximately 550 ppm. CASTEP calculations indicate a similar chemical shift range. Note that some of the chemical shift values, particularly those obtained from WURST-QCPMG NMR spectra, have large associated uncertainties (e.g., 50−100 ppm), as indicated in Tables 6.4-6.6.

Of course, the chemistry of the group II elements is mainly that of M$^{2+}$ ionic compounds; therefore, the chemical shift range discussed here is primarily relevant for Sr$^{2+}$ and its compounds. To estimate whether or not the [87]Sr chemical shift range differs significantly for strontium compounds with coordination geometry not found in solid strontium salts (e.g., one- and two-coordinate compounds in the gas phase), DFT calculations have been performed on small, isolated strontium-containing molecules (Table 6.7) using CASTEP and ADF. According to calculations performed using CASTEP, estimated [87]Sr isotropic chemical shifts of isolated SrO and SrS molecules are 3176 and 2956 ppm, respectively. These fall in the range of the most shielded [87]Sr nuclei we have studied in the solid state, e.g., CASTEP calculates $\sigma_{iso}$([87]Sr) values of 3097, 3113, and 3168 ppm for Sr(NO$_3$)$_2$, SrSO$_4$, and SrCrO$_4$, respectively. The calculated magnetic shielding anisotropy for the isolated diatomic molecules SrO and SrS, 604 and 933 ppm, respectively, is much greater than what is calculated for the solid strontium salts. These large spans suggest that the [87]Sr chemical shift range may cover closer to 1000 ppm, rather than the 550 ppm we have observed experimentally. DFT calculations of the magnetic shielding tensors in SrO and SrS performed using ADF provide estimates of $\sigma_{iso}$([87]Sr, SrO) = 3348 ppm and $\sigma_{iso}$([87]Sr, SrS) = 3090 ppm. These two $\sigma_{iso}$([87]Sr) values, calculated with the inclusion of

relativistic effects using a two-component approximation to the Dirac equation (ZORA), are approximately 150 ppm larger than those determined by CASTEP. DFT calculations were also carried out on the isolated triatomic molecule $SrCl_2$, at the experimental ground-state geometry as well as at the estimated equilibrium geometry[271] (Table 6.7) using ADF. The results of these calculations, which estimate $\sigma_{iso}(^{87}Sr) = 2931$ ppm for the ground-state model, also fall within the chemical shift range established by the solid compounds studied here. The magnetic shielding anisotropy for isolated ground-state $SrCl_2$ is estimated to be 1040 ppm, corresponding to a span of ca. 1102 ppm. It should be noted that all of the studied strontium salts as well as those structures used in additional DFT calculations are diamagnetic, nonmetallic materials, thus this chemical shift range does not include effects from paramagnetic (contact or pseudocontact) shifts or Knight shifts.

The acquisition of $^{87}Sr$ NMR spectra of several analogous compounds with substitutions down a group in the periodic table allows us to qualitatively assess group trends in $^{87}Sr$ isotropic chemical shift values. Readers are at this point reminded that the strontium environments in these crystal structures are not necessarily analogous within each set of compounds (Table 6.2). The sets of strontium titanate and strontium zirconate (group 4), strontium chromate, molybdate, and tungstate (group 6), as well as the halogen series of strontium fluoride, chloride, bromide, and iodide, display the same trend in $^{87}Sr$ isotropic magnetic shielding. That is, $^{87}Sr$ magnetic shielding decreases (chemical shift increases) as one increases the atomic number of the substituted element. The $^{43}Ca$ NMR chemical shifts of calcium analogues $CaF_2$, $CaCl_2$, and $CaBr_2$ also display inverse halogen dependence,[272] with chemical shifts of $\delta_{iso}(^{43}Ca, CaF_2) = -1.4 \pm 2.0$ ppm, $\delta_{iso}(^{43}Ca, CaCl_2) = 64.0 \pm 2.0$ ppm, and $\delta_{iso}(^{43}Ca, CaBr_2) = 83.5 \pm 2.0$ ppm. The isotropic $^{43}Ca$ NMR chemical shifts of $CaMoO_4$ and $CaWO_4$ are very close, at 1.1 and $2.6 \pm 2.0$

ppm, respectively,[272] analogous to what we observe for the corresponding strontium compounds. The $^{43}$Ca NMR magnetic shielding of CaTiO$_3$ and CaZrO$_3$ decreases from Ti to Zr. The magnesium-containing analogues display the opposite trend, with $\delta_{iso}(^{25}$Mg, MgMoO$_4$) = −10.6 and −8.3 ± 0.3 ppm (sites 1 and 2), and $\delta_{iso}(^{25}$Mg, MgWO$_4$) = −1.7 ± 1 ppm.[273] Note that room-temperature MgMoO$_4$ is not isostructural with MgWO$_4$, the former adopting space group $C2/m$,[274] and the latter $P2/c$.[275] Strontium-87 magnetic shielding values increase from strontium oxide to strontium sulfide. This is again consistent with what is observed for $^{43}$Ca in calcium(II) chalcogenides.[272]

As shown in Figure 6.16, $\sigma_{iso}(^{87}$Sr) tends to increase as the strontium coordination number increases, i.e., $6 < 8 \approx 9 \leq 10 \geq 12$. This is, however, very qualitative. As chemical shift data for $^{87}$Sr are still limited, we expect that the regions defining each coordination number will be updated in the future. Furthermore, in the crystallography literature there is no single agreed upon method of assigning coordination number. For the compounds featured in this research, the bond distance cutoff used to determine the size of the coordination sphere and the coordination number varied. For example, on the basis of a bond distance cutoff of 3.0 Å, Abrahams et al.[276] assigned a coordination number of 9 to one strontium site in Sr(NO$_2$)$_2$·H$_2$O, and a coordination number of 10 to the other strontium site. The strontium-oxygen and strontium-nitrogen bond distances in Sr(NO$_2$)$_2$·H$_2$O range from approximately 2.56 to 2.83 Å (site 1) or 2.54 to 2.88 Å (site 2) in intervals of less than 0.1 Å. The next nearest nitrogen atoms to each strontium site are 3.197(1) or 3.231(2) Å away, respectively. Therefore, the approximate 0.35 Å break in interatomic distances for each strontium site is a logical boundary for the coordination sphere. A cutoff distance of 3.5 Å from the central strontium ion was used to assign a coordination number of 10 for SrCrO$_4$.[248] Effenberger and Pertlik[248] concede that the matter of assigning the

coordination number of strontium in $SrCrO_4$ is not clear-cut. In $SrAl_2O_4$, Sr−O bond distances that exceed 3.5 Å are included in the coordination sphere,[245] and the two 9-coordinate strontium sites in $SrAl_2O_4$ have isotropic chemical shift values that are much less shielded than the 9-coordinate strontium atoms in other compounds. As the bonding circumstances such as interatomic distances and coordination geometry change from structure to structure, there is no simple way to standardize the determination of coordination number.[277] It would also be naïve to think $\delta_{iso}$ depends only on coordination number. It is with this consideration that we recommend that the trends in Figure 6.16 be treated as rough guidelines.

**Table 6.7.** Calculated $^{87}$Sr NMR parameters for small molecules in the gas phase. DFT calculations performed with ADF used the BP86 functional and the ZORA/QZ4P basis set. $Q(^{87}Sr) = 30.5$ fm$^2$.

| | | $\sigma_{iso}(^{87}Sr)$ / ppm | $\Delta\sigma(^{87}Sr)$ / ppm | $\eta_{MS}(^{87}Sr)$ | $C_Q(^{87}Sr)$ / MHz | $\eta_Q(^{87}Sr)$ | Structure Reference |
|---|---|---|---|---|---|---|---|
| SrO | CASTEP | 3176 | 604 | 0 | −47.6 | 0 | 235 |
| | ADF | 3348 | 571 | 0 | −64.7 | 0 | |
| | Expt. | - | - | | −42.729(37) | 0 | |
| SrS | CASTEP | 2956 | 933 | 0 | −30.2 | 0 | 236 |
| | ADF | 3090 | 963 | 0 | −39.6 | 0 | |
| | Expt. | - | - | - | −21.959(85) | 0 | |
| $SrCl_2$ | ADF | 2931 | 1040 | 0.18 | −171.9 | 0.11 | 271 |
| $SrCl_2$[a] | ADF | 2913 | 1073 | 0.17 | −178.0 | 0.11 | |

[a] Estimated equilibrium geometry from joint ED-SP analysis, see Ref. 271.

**6.3.3.2 Group II Periodic Trends in Magnetic Shielding**

At present, there exists relatively little NMR data on the NMR-active nuclei of group II elements in general. For the most recent literature survey, see Moudrakovski.[278] The gyromagnetic ratios of $^{25}$Mg, $^{43}$Ca, and $^{87}$Sr are all relatively low, and these nuclei also have relatively low natural abundances,[1] making spectral acquisition challenging. Magnesium-25, strontium-87, and barium-137 also have moderate nuclear electric quadrupole moments,[1,61] leading to broad NMR line shapes due to the quadrupolar interaction in solid samples. Beryllium and its compounds are highly toxic, a deterrent to spectroscopists. NMR properties of the group II elements are summarized in Table 6.8, and the currently known chemical shift ranges of the group II elements are shown in Figure 6.17. The CS ranges of these nuclei increase as one moves down the group. This is expected on the basis of similar trends in other element groups.[279]

The $^9$Be chemical shift range was reported to be ca. 50 ppm by Bryce and Wasylishen in 1999.[280] In their research, spans of 3.4 and 6.6 ppm were measured experimentally for two unique $^9$Be sites in Be(acac)$_2$. Available $^{25}$Mg data indicate a chemical shift range of approximately 200 ppm, from ca. −100 to +100 ppm,[273] though the isotropic chemical shifts of most molecules/compounds fall between −15 and +25 ppm. CASTEP calculations estimate magnesium spans of up to approximately 40 ppm in magnesium nitride, Mg$_3$N$_2$. The available solid-state NMR data for the $^{43}$Ca nucleus was summarized in a 2013 review by Laurencin and Smith,[272] and has been supplemented by recent studies by Widdifield et al.[281] and Burgess et al.[282] The available chemical shift data for $^{43}$Ca cover approximately 280 ppm, from −70 to +210 ppm. The largest experimentally determined span for $^{43}$Ca is 70 ppm for vaterite (CaCO$_3$), and CASTEP calculations indicate that spans are in general less than 110 ppm. Shielded

$\delta_{iso}(^{25}Mg)$ values exceed those of $^{43}Ca$, which is expected to have a larger chemical shift range than $^{25}Mg$.[279] This suggests that our picture of the $^{43}Ca$ chemical shift range may not be complete. Note that there is only one reported $\delta_{iso}(^{25}Mg)$ value below −15 ppm, for bis(cyclopentadienyl)magnesium at −91 ± 3 ppm,[283] and that no NMR data for a $^{43}Ca$ analogue are known to have been reported.

With little data,[284-286] our picture of the chemical shift range of $^{137}Ba$ is also likely incomplete. Some of the literature chemical shift data for $^{137}Ba$, like that for $^{87}Sr$, are in conflict. For example, the largest $\delta_{iso}(^{137}Ba)$ value reported in the solid-state NMR literature, to our knowledge, is that for $BaCO_3$, at 1070 ppm. This value was obtained in 2000 by MacKenzie and Meinhold.[287] However, in a more recent study by Hamaed et al.,[285] a value of 50 ppm is reported for the same compound. The majority of the large chemical shifts available for $^{137}Ba$ were reported in the year 2000 study. As evidence against a systematic referencing error by MacKenzie and Meinhold, their measured $\delta_{iso}(^{137}Ba)$ value for BaO of 748 ppm is in reasonable agreement with $\delta_{iso}(^{137}Ba) = 760$ ppm, reported by Dec et al.[288] in 1993. The $\delta_{iso}(^{137}Ba)$ values reported by Hamaed et al. are supported by the results of CASTEP calculations, which agree reasonably well with their experimental $\delta_{iso}(^{137}Ba)$ values. Note, though, that relativistic corrections to chemical shift values may be on the order of hundreds of ppm for sixth-row elements.[289,290] A recent calculation by Antušek et al.[238] suggests that the relativistic contribution to the $^{137}Ba$ magnetic shielding in aqueous $Ba^{2+}$ is ca. 1500 ppm. It is thus not clear exactly how broad the $^{137}Ba$ chemical shift range is, though on the basis of the available literature, we believe a value of 1500 ppm (ca. −500 to 1000 ppm) is a reasonable estimate.

Recent research by Antušek et al.[238] provide estimated values determined via careful ab initio quantum chemistry calculations for the isotropic magnetic shielding of all the group II

metal ions, $M^{2+}$, coordinated to a full solvation shell of water molecules.  Their calculated values

also include a relativistic correction based on $M^{2+}$ shielding values in smaller water-ion clusters.

In general, both the absolute shielding values for $M^{2+}$ in solution and the relativistic contribution

to the magnetic shielding increase as one moves down the group, the latter increasing by

approximately 4 orders of magnitude, from 0.38 to 1516 ppm, as one moves from $Be^{2+}$ to $Ba^{2+}$.

Isotropic magnetic shielding values for Be, Mg, Ca, Sr, and Ba in aqueous $M^{2+}$ were calculated

to be $112 \pm 3$, $602 \pm 18$, $1259 \pm 38$, $3536 \pm 106$, and $6854 \pm 206$ ppm, respectively.  As $M^{2+}$

solutions of each of these nuclei are commonly used as chemical shift references, these

calculated values are highly useful in relating the results of quantum chemistry calculations to

experimentally determined chemical shift values.


**Table 6.8.** Select NMR properties of the group II nuclei.[1,61]

| Isotope | Nuclear Spin Number, $I$ | Natural Abundance, $C$ / % | $\nu_0$ / MHz (21.14 T) | $Q$ / fm$^2$ | Chemical Shift Range / ppm |
|---|---|---|---|---|---|
| $^9$Be | 3/2 | 100 | 126.5 | 5.288 | 50[280] |
| $^{25}$Mg | 5/2 | 10.0 | 55.10 | 19.94 | 200[273] |
| $^{43}$Ca | 7/2 | 0.135 | 60.58 | -4.08(8) | 280[272] |
| $^{87}$Sr | 9/2 | 7.00 | 39.01 | 30.5(2) | 550 |
| $^{135}$Ba | 3/2 | 6.592 | 89.42 | 16.0 | 1500[284-286] |
| $^{137}$Ba | 3/2 | 11.232 | 100.0 | 24.6(1) | 1500[284-286] |
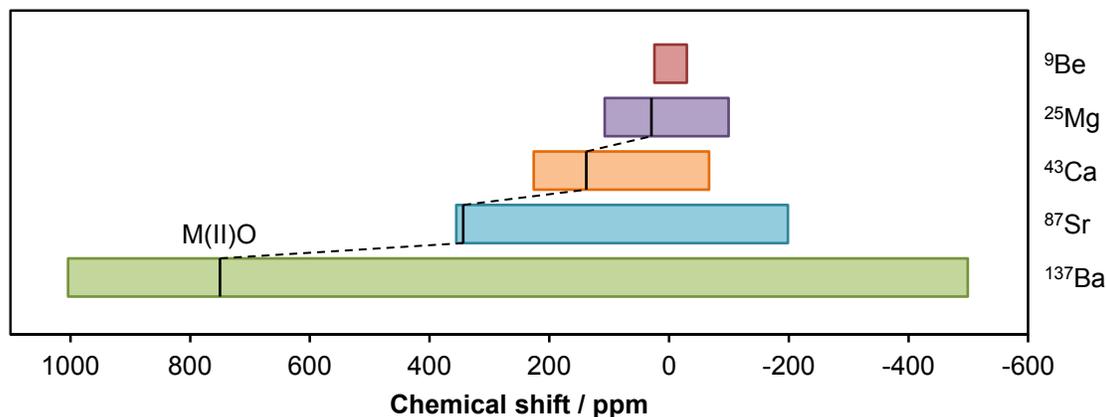
**Figure 6.17.** Chemical shift ranges of the primary NMR-active group II elements. The chemical shift of the group II metal oxide, M(II)O, is represented by a vertical black line. The isotropic chemical shift values for MgO, CaO, and BaO are with reference to a 1 M aqueous solution of the corresponding metal chloride, M(II)Cl$_2$ at $\delta_{iso}$ = 0 ppm. The isotropic chemical shift of SrO is with reference to a 0.5 M solution of SrCl$_2$ in D$_2$O at $\delta_{iso}$ = 0 ppm.

## 6.4 Conclusions

Strontium-87 quadrupolar and chemical shift parameters have been determined for 25 strontium salts. Though our samples were not [87]Sr-labeled, we achieved satisfactory signal intensity and were able to unambiguously determine NMR parameters. $C_Q$([87]Sr) values measured experimentally were up to 50.5 MHz in magnitude. We have shown experimental evidence for the existence of [87]Sr chemical shift anisotropy, as well as presented a case based on the results of CASTEP calculations that CSA should not be neglected in the fitting of some [87]Sr NMR spectra, particularly those with relatively small $C_Q$([87]Sr) values. For [87]Sr NMR spectra acquired with QCPMG-based pulse sequences on existing hardware, however, it is unlikely that chemical shift anisotropy can be easily quantified. Several [87]Sr experimental chemical shift

values for compounds previously featured in the literature were updated or confirmed, and a [87]Sr

magnetic shielding scale based on the current NMR literature was proposed.  Our experimental

[87]Sr chemical shift range is in line with what is expected on the basis of periodic trends in

chemical shifts, given the current data for other group II nuclei.  However, it must be stressed

that given the limited data available for the majority of the group II elements, the chemical shift

ranges for some of these nuclei may need amending as more data become available.  The

BRAIN-CP technique may be useful for acquiring [87]Sr NMR spectra in the future, provided that

the studied compounds are protonated.[291]  Our study indicates the importance of acquiring NMR

spectra at the highest possible magnetic field strengths if one wishes to observe quadrupolar

nuclei with unfavorable NMR properties like those in [87]Sr.  This work could not have been

completed without access to the Canadian National Ultrahigh-Field NMR Facility for Solids

(http://nmr900.ca/).


## 6.5 Acknowledgements

# Chapter 7

## Summary and Future Outlook

All of the projects presented in this thesis utilize current state-of-the-art NMR hardware and software, in conjunction with modern quantum chemistry computations, to tackle difficult problems in the field of NMR spectroscopy. Even in the recent past (i.e., ca. 5 to 10 years), experiments such as these were impractical, or, in some cases, even thought to be impossible. This research was focused on the acquisition of NMR spectra of exotic quadrupolar nuclei in solid materials. The exoticism of these nuclei stems primarily from their unfavorable NMR properties, e.g., low gyromagnetic ratios, low natural abundances, and/or moderate to large nuclear electric quadrupole moments, rendering them largely overlooked in the current NMR literature. Much of this research is foundational, and adds to limited literature on the studied nuclei (e.g., $^{75}$As, $^{87}$Sr, and $^{121/123}$Sb) or on the type of system studied (e.g., isolated pairs of spin-spin coupled quadrupolar nuclei where the quadrupolar interaction is large for one of the paired nuclei). Thus, much of the data presented in this work can be used as benchmark values for subsequent NMR experiments and quantum chemistry calculations.

Each of these projects required the use of the $B_0 = 21.14$ T NMR spectrometer located at our National Ultrahigh-Field NMR Facility for Solids,[2] demonstrating that access to high-field instruments is crucial to carrying out modern NMR research of this nature. Quantum chemistry calculations using the DFT-based programs ADF and CASTEP were used extensively to support

experimental results, to help establish trends in NMR parameters, as well as to gauge the feasibility of performing NMR experiments. The availability of more reliable quantum chemistry methods were a vital aspect of these projects. It is shown that DFT calculations carried out using both the CASTEP and ADF codes support experimental data, and the choice between the two program suites may come down to what is applicable to the system under study (e.g., relativistic effects, long-range interactions, etc.). The development of accurate NMR spectral simulation software has also played an important role in the growing utilization of NMR spectroscopy to address difficult systems such as these. QUEST and its residual dipolar coupling-oriented derivative were used extensively in this work to accurately model NMR spectra for which the high-field approximation is not valid.

Of course, there is a lot of potential work that can be carried out to continue the projects mentioned in this thesis. It may be interesting to extend the work on quadrupolar spin-pairs of boron and arsenic nuclei in Lewis acid-base adducts to other pairs of quadrupolar nuclei, including As-Al and As-Ga pairs in analogous adducts.[153] NMR parameters derived for the latter may be of particular use given that there is some interest in using Lewis acid-base adducts as precursors for the fabrication of GaAs semiconductors.[155,156] Many of the $v_Q(^{75}\text{As})$ values quantified in this work are moderate to large, thus nuclear quadrupole resonance experiments at zero field could be performed to verify the values determined via NMR spectroscopy, since $\eta_Q(^{75}\text{As})$ values are now known. Further work could also include a more detailed interpretation of EFG tensor orientations within the molecular reference frame, and how these tensor orientations as well as the signs of $C_Q$ values relate to or shed light on molecular or crystallographic structure.[292] In this thesis it is shown that high-field NMR experiments on spin-3/2 nuclei with $C_Q$ values of up to ca. 200 MHz are now clearly a feasible undertaking, opening

up possibilities of studying exotic quadrupolar nuclei in non-symmetric environments. For example, the techniques demonstrated in this thesis would be suitable for studying the structure of arsenic-containing hydrocarbons and fatty acids present in fish and other marine animals as well as marine oil supplements.[293] Exposure to arsenic through the environment and through the ingestion of food is a growing concern[294-296] and thus far there are few toxicological data on many organic arsenic compounds found in the environment.[297]

Strontium-87 NMR spectroscopy has the potential to be of importance in the field of materials chemistry as, for example, strontium-containing perovskites possess many interesting electrical properties and are currently being investigated for applications such as capacitors[221] and solid oxide fuel cells.[222,298,299] The use of strontium in devices is of particular interest due to its relatively low toxicity; there have even been recent efforts to synthesize a strontium-containing analogue for the lead halogen perovskite material $CH_3NH_3PbI_3$, which is currently being investigated for use in the production of solar cells.[300] The materials chemistry community has already shown interest in characterizing bioactive glasses using $^{87}Sr$ NMR spectroscopy,[224] and $^{87}Sr$ NMR spectroscopy could be incredibly useful for the characterization of many related strontium-containing glasses and ceramics.

The techniques demonstrated here are by no means limited to $^{75}As$, $^{87}Sr$, and $^{121/123}Sb$ NMR studies; it is hoped that our promising demonstration of the capabilities of NMR spectroscopy inspires spectroscopists to pursue studies of more challenging systems and nuclei. Having the option of studying almost any quadrupolar nucleus in the NMR periodic table gives scientists access to a potentially rich collection of structural information and hence to insights into the chemical properties of materials.

It is clear that the field of solid-state NMR spectroscopy still has a lot of room to grow. Newly developed pulse techniques such as BRAIN-CP (BRoadband Adiabatic INversion – Cross Polarization)[301] have been utilized for the acquisition of wideline NMR spectra of spin-1/2 and quadrupolar nuclei[302-304] and offer additional signal enhancements to the WURST and WURST-QCPMG methods demonstrated here. The field of dynamic nuclear polarization (DNP) NMR spectroscopy,[305-307] which involves the transfer of polarization from electrons to atomic nuclei, is a promising candidate for the study of quadrupolar nuclei. To this end, polarization transfer techniques such as PRESTO[308] may be of use for observing MAS NMR spectra of quadrupolar nuclei. New NMR hardware is also being developed; a 36 T series-connected hybrid magnet will soon be available for NMR users at the National High Magnetic Field Laboratory (NHFML) in Tallahassee, FL.[309] It is likely that the NMR spectroscopy of "challenging" quadrupolar nuclei in solids will continue to advance beyond what we have demonstrated here.

# References

[1] Harris, R. K.; Becker, E. D.; de Menezes, S. M. C.; Goodfellow, R.; Granger, P. *NMR Nomenclature. Nuclear Spin Properties and Conventions for Chemical Shifts. Pure Appl. Chem.* **2001**, *73*, 1795-1818.

[2] The National Ultrahigh-Field NMR Facility for Solids. http://nmr900.ca (Accessed October 21, 2015).

[3] Faucher, A.; Wasylishen, R. E. Obtaining Gas-Phase NMR Parameters from Molecular Beam and High-Resolution Microwave Spectroscopy. To be published as Chapter 2 in *Gas Phase NMR*; Jackowski, K., Jaszuński, M., Eds.; New Developments in NMR; RSC Publishing.

[4] Griffiths, D. J. *Introduction to Quantum Mechanics*, 2nd edition; Pearson Prentice Hall: Upper Saddle River, 2005.

[5] Atkins, P.; Friedman, R. *Molecular Quantum Mechanics*, 4th edition; Oxford University Press: Oxford, 2005.

[6] Schrödinger, E. An Undulatory Theory of the Mechanics of Atoms and Molecules. *Phys. Rev.* **1926**, *28*, 1049-1070.

[7] Levitt, M. H. *Spin Dynamics: Basics of Nuclear Magnetic Resonance*; Wiley: Chichester, 2001.

[8] Levitt, M. H. *Spin Dynamics: Basics of Nuclear Magnetic Resonance*; Wiley: Chichester, 2001; pp 6-17.

[9] Commins, E. D. Electron Spin and Its History. *Annu. Rev. Nucl. Part. Sci.* **2012**, *62*, 133-157.

[10] Ohanian, H. C. What is Spin? *Am. J. Phys*. **1986**, *54*, 500-505.

[11] Apperley, D. C.; Harris, R. K.; Hodgkinson, P. *Solid State NMR: Basic Principles & Practice*; Momentum Press: New York, 2012; pp 1−38.

[12] Mehring, M. *Principles of High Resolution NMR in Solids*, 2nd ed.; Springer-Verlag: New York, 1983; pp 8−62.

[13] Domenici, V. The Role of NMR in the Study of Partially Ordered Materials: Perspectives and Challenges. *Pure Appl. Chem*. **2011**, *83*, 67-94.

[14] Heist, L. M.; Poon, C.-D.; Samulski, E. T.; Photinos, D. J.; Jokisaari, J.; Vaara, J.; Emsley, J. W.; Mamone, S.; Lelli, M. Benzene at 1 GHz. Magnetic Field-Induced Fine Structure. *J. Magn. Reson*. **2015**, *258*, 17-24.

[15] Harris, K. J.; Bryce, D. L.; Wasylishen, R. E. NMR Line Shapes from AB Spin Systems in Solids – The Role of Antisymmetric Spin-Spin Coupling. *Can. J. Chem*. **2009**, *87*, 1338-1351.

[16] Apperley, D. C.; Harris, R. K.; Hodgkinson, P. *Solid State NMR: Basic Principles & Practice*; Momentum Press: New York, 2012; pp 97−101.

[17] Mueller, L. J. Tensors and Rotations in NMR. *Concepts Magn. Reson., Part A*, **2011**, *38*, 221-235.

[18] Schmidt-Rohr, K.; Spiess, H. W. *Multidimensional Solid-State NMR and Polymers*; Academic Press: London, 1994; pp 444−452.

[19] Perras, F. A.; Widdifield, C. M.; Bryce, D. L. QUEST−QUadrupolar Exact SofTware: A Fast Graphical Program for the Exact Simulation of NMR and NQR Spectra for Quadrupolar Nuclei. *Solid State Nucl. Magn. Reson*. **2012**, *45-46*, 36-44.

[20] Haeberlen, U. *High Resolution NMR in Solids: Selective Averaging*; Academic Press: London, 1976; p 9.

[21] Hollas, J. M. *Modern Spectroscopy*; Wiley: Chichester, 1987; pp 27−39.

[22] Bloch, F.; Hansen, W. W.; Packard, M. Nuclear Induction. *Phys. Rev*. **1946**, *69*, 127.

[23] Hoult, D. I. The Origins and Present Status of the Radio Wave Controversy in NMR. *Concepts Magn. Reson., Part A*, **2009**, *34*, 193-216.

[24] Keeler, J. *Understanding NMR Spectroscopy*, 2nd Edition; Wiley: Chichester, 2010.

[25] Mason, J. Conventions for the Reporting of Nuclear Magnetic Shielding (or Shift) Tensors Suggested by Participants in the NATO ARW on NMR Shielding Constants at the University of Maryland, College Park, July 1992. *Solid State Nucl. Magn. Reson*. **1993**, *2*, 285-288.

[26] Ishii, Y.; Terao, T.; Hayashi, S. Theory and Simulation of Vibrational Effects on Structural Measurements by Solid-State Nuclear Magnetic Resonance. *J. Chem. Phys*. **1997**, *107*, 2760-2774.

[27] Perras, F. A.; Bryce, D. L. Measuring Dipolar and *J* Coupling Between Quadrupolar Nuclei Using Double-Rotation NMR. *J. Chem. Phys*. **2013**, *138*, 174202.

[28] Raynes, W. T.; Stevens, S. J. Magnetic Field-Dependent Nuclear Spin-Spin Coupling. *Magn. Reson. Chem*. **1992**, *30*, 124-128.

[29] Man, P. P. Quadrupolar Interactions. In *NMR of Quadrupolar Nuclei in Solid Materials*; Wasylishen, R. E., Ashbrook, S. E., Wimperis, S., Eds.; Wiley: Chichester, West Sussex, 2012; pp 4−16.

[30] Mehring, M. *Principles of High Resolution NMR in Solids*, 2nd ed.; Springer-Verlag: Berlin, 1983.

[31] Amoureux, J. P.; Fernandez, C.; Granger, P. Interpretation of Quadrupolar Powder Spectra: Static and MAS Experiments. (Tutorial Session). In *Multinuclear Magnetic Resonance in Liquids and Solids – Chemical Applications*; Granger, P., Harris, R. K., Eds.; Kluwer Academic Publishers: Dordrecht, 1990; pp 409−424.

[32] Abragam, A. *Principles of Nuclear Magnetism*; International Series of Monographs on Physics, Vol. 32; Oxford University Press: Croydon, 2011; pp 44−53.

[33] Tolstov, G. P. *Fourier Series*; Dover Publications: Mineola, 1976.

[34] Derome, A. E. *Modern NMR Techniques for Chemistry Research*; Pergamon Press: Oxford, 1987, pp 9−29.

[35] Apperley, D. C.; Harris, R. K.; Hodgkinson, P. *Solid State NMR: Basic Principles & Practice*; Momentum Press: New York, 2012; pp 32−35.

[36] Maricq, M. M.; Waugh, J. S. NMR in Rotating Solids. *J. Chem. Phys*. **1979**, *70*, 3300-3316.

[37] Hahn, E. L. Spin Echoes. *Phys. Rev*. **1950**, *80*, 580-594.

[38] Shore, S. E.; Ansermet, J. P.; Slichter, C. P.; Sinfelt, J. H. Nuclear-Magnetic-Resonance Study of the Bonding and Diffusion of Co Chemisorbed on Pd. *Phys. Rev. Lett*. **1987**, *58*, 953-956.

[39] Barrett, S. E.; Durand, D. J.; Pennington, C. H.; Slichter, C. P.; Friedmann, T. A.; Rice, J. P.; Ginsberg, D. M. $^{63}$Cu Knight Shifts in the Superconducting State of YBa$_2$Cu$_3$O$_{7-\delta}$ ($T_c$ = 90 K). *Phys. Rev. B*, **1990**, *41*, 6283-6296.

[40] Larsen, F. H.; Jakobsen, H. J.; Ellis, P. D.; Nielsen, N. C. Sensitivity-Enhanced Quadrupolar-Echo NMR of Half-Integer Quadrupolar Nuclei. Magnitudes and Relative Orientation of Chemical Shielding and Quadrupolar Coupling Tensors. *J. Phys. Chem. A*, **1997**, *101*, 8597-8606.

[41] Kupče, Ē.; Freeman, R. Adiabatic Pulses for Wideband Inversion and Broadband Decoupling. *J. Magn. Reson. Ser. A*, **1995**, *115*, 273-276.

[42] Bhattacharyya, R.; Frydman, L. Quadrupolar Nuclear Magnetic Resonance Spectroscopy in Solids Using Frequency-Swept Echoing Pulses. *J. Chem. Phys*. **2007**, *127*, 194503.

[43] O'Dell, L. A. The WURST Kind of Pulses in Solid-State NMR. *Solid State Nucl. Magn. Reson*. **2013**, *55-56*, 28-41.

[44] Böhlen, J.-M.; Bodenhausen, G. Experimental Aspects of Chirp NMR Spectroscopy. *J. Magn. Reson., Ser. A*, **1993**, *102*, 293-301.

[45] O'Dell, L . A.; Schurko, R. W. QCPMG Using Adiabatic Pulses for Faster Acquisition of Ultra-Wideline NMR Spectra. *Chem. Phys. Lett*. **2008**, *464*, 97–102.

[46] Schurko, R. W. Acquisition of Wideline Solid-State NMR Spectra of Quadrupolar Nuclei. In *NMR of Quadrupolar Nuclei in Solid Materials*; Wasylishen, R. E., Ashbrook, S. E., Wimperis, S., Eds.; Wiley: Chichester, 2012; pp 77-93.

[47] Massiot, D.; Farnan, I.; Gautier, N.; Trumeau, D.; Trokiner, A.; Coutures, J. P. $^{71}$Ga and $^{69}$Ga Nuclear Magnetic Resonance Study of $\beta$-$Ga_2O_3$: Resolution of Four- and Six-Fold Coordinated Ga Sites in Static Conditions. *Solid State Nucl. Magn. Reson*. **1995**, *4*, 241-248.

[48] Medek, A.; Frydman, V.; Frydman, L. Central Transition Nuclear Magnetic Resonance in the Presence of Large Quadrupole Couplings: Cobalt-59 Nuclear Magnetic Resonance of Cobaltophthalocyanines. *J. Phys. Chem. A*, **1999**, *103*, 4830-4835.

[49] Schurko, R. W. Ultra-Wideline Solid-State NMR Spectroscopy. *Acc. Chem. Res*. **2013**, *46*, 1985-1995.

[50] Lipton, A. S.; Wright, T. A.; Bowman, M. K.; Reger, D. L.; Ellis, P. D. Solid-State $^{67}$Zn NMR Spectroscopy in Bioinorganic Chemistry. Spectra of Four- and Six-Coordinate Zinc Pyrazolylborate Complexes Obtained by Management of Proton Relaxation Rates with a Paramagnetic Dopant. *J. Am. Chem. Soc*. **2002**, *124*, 5850-5860.

[51] ADF2012, SCM, Theoretical Chemistry, Vrije Universiteit, Amsterdam, The Netherlands. http://www.scm.com (Accessed October 20, 2015).

[52] te Velde, G.; Bickelhaupt, F. M.; van Gisbergen, S. J. A; Guerra, C. F.; Baerends, E. J.; Snijders, J. G.; Ziegler, T. Chemistry with ADF. *J. Comput. Chem*. **2001**, *22*, 931-967.

[53] Guerra, C. F.; Snijders, J. G.; te Velde, G.; Baerends, E. J.; Towards an Order-N DFT Method. *Theor. Chem. Acc*. **1998**, *99*, 391-403.

[54] Clark, S. J.; Segall, M. D.; Pickard, C. J.; Hasnip, P. J.; Probert, M. J.; Refson, K.; Payne, M. C. First Principles Methods Using CASTEP. *Z. Kristallogr*. **2005**, *220*, 567-570.

[55] Profeta, M.; Mauri, F.; Pickard, C. J. Accurate First Principles Prediction of $^{17}$O NMR Parameters in $SiO_2$: Assignment of the Zeolite Ferrierite Spectrum. *J. Am. Chem. Soc*. **2003**, *125*, 541-548.

[56] Pickard, C. J.; Mauri, F. All-Electron Magnetic Response with Pseudopotentials: NMR Chemical Shifts. *Phys. Rev. B*, **2001**, *63*, 245101.

[57] Yates, J. R.; Pickard, C. J.; Mauri, F. Calculation of NMR Chemical Shifts for Extended Systems Using Ultrasoft Pseudopotentials. *Phys. Rev. B*, **2007**, *76*, 024401.

[58] Perdew, J. P.; Burke, K.; Ernzerhof, M. Generalized Gradient Approximation Made Simple. *Phys. Rev. Lett*. **1996**, *77*, 3865-3868.

[59] Perdew, J. P.; Burke, K.; Ernzerhof, M. Generalized Gradient Approximation Made Simple (vol 77, pg 3865, 1996). *Phys. Rev. Lett*. **1997**, *78*, 1396.

[60] Cohen, E. R.; Cvitaš, T.; Frey, J. G.; Holmström, B.; Kuchitsu, K.; Marquardt, R.; Mills, I.; Pavese, F.; Quack, M.; Stohner, J., et al. *Quantities, Units and Symbols in Physical Chemistry*, 3rd ed.; RSC Publishing: Cambridge, 2007.

[61] Pyykkö, P. Year-2008 Nuclear Quadrupole Moments. *Mol. Phys*. **2008**, *106*, 1965-1974.

[62] Faucher, A.; Terskikh, V. V.; Wasylishen, R. E. Feasibility of Arsenic and Antimony NMR Spectroscopy in Solids: An Investigation of Some Group 15 Compounds. *Solid State Nucl. Magn. Reson*. **2014**, *61-62*, 54-61.

[63] Albert, S.; Ripmeester, J. A. Ionic Reorientations and Phase Transition in Solid $IF_6AsF_6$. *Can. J. Chem*. **1988**, *66*, 3153-3156.

[64] Dharmatti, S. S.; Weaver, H. E., Jr. The Magnetic Moment of $^{75}As$. *Phys. Rev*. **1951**, *84*, 367.

[65] Weaver, H. E., Jr. Magnetic Moments of $Si^{29}$, $S^{33}$, $Zn^{67}$, $As^{75}$, $Se^{77}$, $Te^{123}$, and $Te^{125}$. *Phys. Rev*. **1953**, *89*, 923-930.

[66] Jeffries, C. D.; Loeliger, H.; Staub, H. H. The Nuclear Magnetic Resonance of Titanium and Arsenic. *Phys. Rev*. **1952**, *85*, 478-479.

[67] Proctor, W. G.; Yu, F. C. On the Nuclear Magnetic Moments of Several Stable Isotopes. *Phys. Rev*. **1951**, *81*, 20-30.

[68] Balimann, G.; Pregosin, P. S. Arsenic-75 Nuclear Magnetic Resonance. A Study of Some Arsenic Salts. *J. Magn. Reson*. **1977**, *26*, 283-289.

[69] Arnold, M. St. J.; Packer, K. J. Non-Aqueous Solutions of Electrolytes I. The $^{75}As$ Nuclear Magnetic Spin-Lattice Relaxation Times of the Hexafluoroarsenate Ion. *Mol. Phys*. **1966**, *10*, 141.

[70] Arnold, M. St. J.; Packer, K. J. Non-Aqueous Solutions of Electrolytes II. Temperature and Cation Dependence of $^{75}As$ Nuclear Magnetic Spin-Lattice Relaxation Times of Hexafluoroarsenate Ion. *Mol. Phys*. **1968**, *14*, 249.

[71] Andrew, E. R.; Farnell, L. F.; Gledhill, T. D. Resolved Spin Multiplets in the Nuclear Magnetic Resonance Spectra of Solids. *Phys. Rev. Lett*. **1967**, *19*, 6-7.

[72] Biswal, M.; Body, M.; Legein, C.; Corbel, G.; Sadoc, A.; Boucher, F. Structural Investigation of $\alpha$- and $\beta$-Sodium Hexafluoroarsenate, $NaAsF_6$, by Variable Temperature X-Ray Powder Diffraction and Multinuclear Solid-State NMR, and DFT Calculations. *J. Phys. Chem. C*, **2012**, *116*, 11682-11693.

[73] Andrew, E. R. Nuclear Magnetic Resonance Absorption in $NaSbF_6$. *Phys. Rev*. **1951**, *82*, 443-444.

[74] Dharmatti, S. S.; Weaver, H. E. Nuclear Magnetic Resonance Lines of Antimony in Antimony Hexafluoride Ion. *Phys. Rev*. **1952**, *87*, 675.

[75] Gutowsky, H. S.; McCall, D. W. Nuclear Magnetic Resonance Fine Structure in Liquids. *Phys. Rev*. **1951**, *82*, 748-749.

[76] Gutowsky, H. S.; McCall, D. W.; Slichter, C. P. Coupling Among Nuclear Magnetic Dipoles in Molecules. *Phys. Rev*. **1951**, *84*, 589-590.

[77] McNeil, E. B.; Slichter, C. P.; Gutowsky, H. S. "Slow Beats" in $F^{19}$ Nuclear Spin Echoes. *Phys. Rev*. **1951**, *84*, 1245-1246.

[78] Hahn, E. L.; Maxwell, D. E. Chemical Shift and Field Independent Frequency Modulation of the Spin Echo Envelope. *Phys. Rev*. **1951**, *84*, 1246-1247.

[79] Ramsey, N. F.; Purcell, E. M. Interactions Between Nuclear Spins in Molecules. *Phys. Rev*. **1952**, *85*, 143-144.

[80] Hatton, J. V.; Saito, Y.; Schneider, W. G. Nuclear Magnetic Resonance Investigations of Some Group V Metal Fluorides and Oxyions. *Can. J. Chem*. **1965**, *43*, 47.

[81] Kidd, R. G.; Matthews, R. W. Antimony-121 Nuclear Magnetic Resonance in Some Antimony(V) Compounds. *J. Inorg. Nucl. Chem*. **1975**, *37*, 661-663.

[82] Andrew, E. R.; Firth, M.; Jasinski, A.; Randall, P. J. $^{19}F$ Nuclear Spin Coupling Constants in Solids by High-Speed Rotation Method. *Phys. Lett. A*, **1970**, *31*, 446.

[83] Kozlova, S. G.; Kriger, Yu. G.; Goncharuk, V. K. Quadrupole Interactions and NMR Relaxation in $KSbF_6$. *J. Struct. Chem*. **1987**, *28*, 321-323.

[84] Mazej, Z.; Hagiwara, R. Hexafluoro-, Heptafluoro-, and Octafluoro-Salts, and $[M_nF_{5n-1}]^-$ ($n$ = 2, 3, 4) Polyfluorometallates of Singly Charged Metal Cations, $Li^+$-$Cs^+$, $Cu^+$, $Ag^+$, $In^+$ and $Tl^+$. *J. Fluorine Chem*. **2007**, *128*, 423-437.

[85] Heyns, A. M.; Pistorius, C. W. F. T. Vibrational Spectra, High-Pressure Polymorphism and Force Constants of $KAsF_6$. *Spectrochim. Acta A*, **1975**, *31*, 1293-1301.

[86] Roof, R. B. The Crystal Structure of $KAsF_6$. *Acta Crystallogr*. **1955**, *8*, 739.

[87] Ibers, J. A. A Note on the Least-Squares Method: The Refinement of the Structure of $KAsF_6$. *Acta Crystallogr*. **1956**, *9*, 967-969.

[88] Gafner, G.; Kruger, G. J. Potassium Arsenic Hexafluorine: A Redetermination. *Acta Crystallogr., Sect. B: Struct. Sci*. **1974**, *30*, 250-251.

[89] Peterková, J.; Dušek, M.; Petříček, V.; Loub, J. Structures of Fluoroarsenates $KAsF_{6-n}(OH)_n$, $n$ = 0, 1, 2: Application of the Heavy-Atom Method for Modulated Structures. *Acta Crystallogr., Sect. B: Struct. Sci*. **1998**, *54*, 809-818.

[90] Niemelä, L. Pulsed NMR Studies of Phase Transitions and Reorientation of $AsF_6^-$-Ions in Solid $NaAsF_6$ and $KAsF_6$. *Ann. Univ. Turku. Ser. A1*, **1973**, *162*, 99-105.

[91] Parsonage, N. G.; Staveley, L. A. K. *Disorder in Crystals*; Clarendon Press: Oxford, 1978.

[92] Heyns, A. M.; Pistorius, C. W. F. T. Polymorphism, High-Pressure Phase-Diagram and Vibrational-Spectra of $KSbF_6$. *Spectrochim. Acta A*, **1976**, *32*, 535-545.

[93] Heyns, A. M.; Reynhardt, E. C. A Raman and NMR Study of $KSbF_6$. *J. Phys. Chem. Solids*, **1981**, *42*, 461-471.

[94] Heyns, A. M.; Prinsloo, L. C.; Range, K. J. $KSbF_6$ Revisited Part II. An Infrared Study of the I-II Phase Transition. *Vib. Spectrosc*. **1996**, *11*, 151-157.

[95] Bode, H.; Voss, E. Die Kristallstruktur des Kaliumhexafluoroantimonats(V). *Z. Anorg. Allg. Chem*. **1951**, *264*, 144-150.

[96] Kruger, G. J.; Pistorius, C. W. F. T.; Heyns, A. M. Potassium Hexafluoroantimonate (I). *Acta Crystallogr., Sect. B: Struct. Sci*. **1976**, *32*, 2916-2918.

[97] Niemelä, L. K. E.; Vesanen, O. A. Pulsed NMR Studies of Reorientation and Phase Transitions in Solid $NaSbF_6$ and $KSbF_6$. *Chem. Phys. Lett*. **1975**, *31*, 507-510.

[98] Takahashi, T.; Kawashima, H.; Sugisawa, H.; Baba, T. $^{207}Pb$ Chemical Shift Thermometer at High Temperature for Magic Angle Spinning Experiments. *Solid State Nucl. Magn. Reson*. **1999**, *15*, 119-123.

[99] Wsolids1 simulation software package ver. 1.17.30 was provided by Dr. Klaus Eichele, Institut für Anorganische Chemie, Universität Tübingen, Germany.

[100] Massiot, D.; Fayon, F.; Capron, M.; King, I.; Le Calvé, S.; Alonso, B.; Durand, J.-O., Bujoli, B.; Gan, Z.; Hoatson, G. Modelling One- and Two-Dimensional Solid-State NMR Spectra. *Magn. Reson. Chem*. **2002**, *40*, 70-76.

[101] Sowa, H. Pressure-Induced $Fm\bar{3}m \rightarrow R\bar{3}$ Phase Transition in $NaSbF_6$. *Acta Crystallogr., Sect. B: Struct. Sci*. **1997**, *53*, 25-31.

[102] Gabuda, S. P.; Maifat, M. A.; Zil'berman, B. D.; Panich, A. M.; Ippolitov, E. G. Structural and Dynamic Characteristics in Phase Transitions of Alkali Metal Hexafluoroarsenates. *Koordinats. Khim*. **1979**, *5*, 850-854.

[103] Feindel, K. W.; Wasylishen, R. E. A Relativistic DFT Study of One-Bond Fluorine-X Indirect Spin-Spin Coupling Tensors. *Magn. Reson. Chem*. **2004**, *42*, S158-S167.

[104] Vanderhart, D. L.; Earl, W. L.; Garroway, A. N. Resolution in $^{13}C$ NMR of Organic Solids Using High-Power Proton Decoupling and Magic-Angle Sample Spinning. *J. Magn. Reson*. **1981**, *44*, 361-401.

[105] Jameson, C. J.; Gutowsky, H. S. Systematic Trends in the Coupling Constants of Directly Bonded Nuclei. *J. Chem. Phys*. **1969**, *51*, 2790.

[106] Harris, R. K.; Mann, B. E. *NMR and the Periodic Table*; Academic Press: New York, 1978.

[107] Pettinari, C.; Marchetti, F.; Rafaiani, G. Heteronuclear NMR Applications (As, Sb, Bi). In *Encyclopedia of Spectroscopy and Spectrometry*; Lindon, J. C., Tranter, G. E., Holmes, J. L., Eds.; Academic Press: London, San Diego, 2000; Volume 1, 685-690.

[108] *NMR of Quadrupolar Nuclei in Solid Materials*; Wasylishen, R. E., Ashbrook, S. E., Wimperis, S., Eds.; Wiley: Chichester, 2012.

[109] *Multinuclear NMR*; Mason, J., Ed.; Plenum Press: New York, 1987.

[110] Leung, F.; Cooke, S. A.; Gerry, M. C. L. The Rotational Spectrum and Hyperfine Structure of Arsenic Monophosphide, AsP. *J. Mol. Spectrosc*. **2006**, *238*, 36-41.

[111] Cooke, S. A.; Gerry, M. C. L. The Pure Rotational Spectra and Hyperfine Constants of SbN and SbP. *Phys. Chem. Chem. Phys*. **2004**, *6*, 4579-4585.

[112] Duncan, T. M. *Principal Components of Chemical Shift Tensors: A Compilation*, 2nd Edition; The Farragut Press: Chicago, 1994.

[113] Gerry, M. C. L.; Cooke, S. A. Born-Oppenheimer Breakdown Effects and Hyperfine Structure in the Rotational Spectra of SbF and SbCl. *J. Mol. Spectrosc*. **2005,** *234*, 195-203.

[114] Haiduke, R. L. A.; da Silva, A. B. F.; Visscher, L. The Nuclear Electric Quadrupole Moment of Antimony from the Molecular Method. *J. Chem. Phys*. **2006**, *125*, 064301.

[115] Demovič, L.; Kellö, V.; Sadlej, A. J. The Quadrupole Moment of the As Nucleus from Molecular Microwave Data and Calculated Relativistic Electric Field Gradients. *Chem. Phys. Lett*. **2010**, *498*, 10-13.

[116] Crawford, M. F.; Bateson, S. Nuclear Moments of Antimony Isotopes – Discussion of Landé's Theory. *Can. J. Res*. **1934**, *10*, 693-702.

[117] Crawford, M. F.; Crooker, A. M. Nuclear Moment of Arsenic. *Nature,* **1933**, *131*, 655-656.

[118] Helminger, P.; Beeson, E. L.; Gordy, W. Microwave Spectra and Molecular Constants of Arsine and Stibine. *Phys. Rev. A: At. Mol. Opt. Phys*. **1971**, *3*, 122-126.

[119] Das, T. P.; Hahn, E. L. *Nuclear Quadrupole Resonance Spectroscopy*; Academic Press: New York, 1958.

[120] Mercier, H. P. A.; Sanders, J. C. P.; Schrobilgen, G. J. Hexakis(pentafluorooxotellurato)pnictate(v) Anions, $M(OTeF_5)_6^-$ (M = As, Sb, Bi): A Series of Very Weakly Coordinating Anions. *J. Am. Chem. Soc*. **1994**, *116*, 2921-2937.

[121] Casteel, W. J.; Kolb, P.; LeBlond, N.; Mercier, H. P. A.; Schrobilgen, G. J. Tetrachloro- and Tetrabromostibonium(v) Cations: Raman and $^{19}F$, $^{121}Sb$, and $^{123}Sb$ NMR Spectroscopic Characterization and X-Ray Crystal Structures of $SbCl_4^+Sb(OTeF_5)_6^-$ and $SbBr_4^+Sb(OTeF_5)_6^-$. *Inorg. Chem.* **1996**, *35*, 929-942.

[122] Collins, M. J.; Rao, U. R. K.; Schrobilgen, G. J. $^{75}$Arsenic NMR Study of $[As(OTeF_5)_6]^-$ in Solution. *J. Magn. Reson*. **1985**, *61*, 137-140.

[123] McGarvey, G. B.; Moffat, J. B. An Arsenic-75 Nuclear Magnetic Resonance Study of Heteropoly Oxometalates in Solution. *J. Mag. Res*. **1990**, *88*, 305-310.

[124] Mikhaylov, A. A.; Mel'nik, E. A.; Churakov, A. V.; Novotortsev, V. M.; Howard, J. A. K.; Sladkevich, S.; Gun, J.; Bharathi, S.; Lev, O.; Prikhodchenko, P. V. Synthesis, Crystal Structure and Characterization of Alkali Metal Hydroxoantimonates. *Inorg. Chim. Acta*. **2011**, *378*, 24-29.

[125] Mammadov, E.; Taylor, P. C.; Reyes, A.; Mehdiyeva, S.; Kuhns, P. $^{75}$As NMR Relaxation in Glassy Ge−As−Se. *Phys. Status Solidi .***2010**, *207*, 635-638.

[126] Mammadov, E.; Bobela, D.; Reyes, A.; Mehdiyeva, S.; Taylor, P. C. Magnetic Resonance Study of Arsenic Bonding Sites in Ternary Chalcogenide Glasses. *Solid State Commun.* **2011**, *151*, 1459-1462.

[127] Hari, P.; Taylor, P. C.; Kleinhammes, A.; Kuhns, P. L.; Moulton, W. G.; Sullivan, N. S. Asymmetry in the Local Structural Order in Arsenic Chalcogenide Glasses: High Field NMR in Crystalline and Glassy $As_2Se_3$. *Solid State Commun.* **1997**, *104*, 669-672.

[128] Taylor, P. C.; Su, T.; Hari, P.; Ahn, E.; Kleinhammes, A.; Kuhns, P. L.; Moulton, W. G.; Sullivan, N. S. Structural and Photostructural Properties of Chalcogenide Glasses: Recent Results from Magnetic Resonance Measurements. *J. Non-Cryst. Solids*, **2003**, *326-327*, 193-198.

[129] Potter, L. D.; Wu, Y. NMR Measurements of Homonuclear Indirect Couplings in GaAs. *J. Magn. Reson. A*, **1995**, *116*, 107-112.

[130] Potter, L. D.; Guzelian, A. A.; Alivisatos, A. P.; Wu, Y. Structure of Chemically Synthesized Nanophase GaAs Studied by Nuclear Magnetic Resonance and X-Ray Diffraction. *J. Chem. Phys.* **1995**, *103*, 4834-4840.

[131] Suemitsu, M.; Nakajo, N. Charged Point Defects in GaAs Crystals Evaluated by NMR Spin Echo. *J. Appl. Phys.* **1989**, *66*, 3178-3186.

[132] Schurko, R. W.; Wi, S.; Frydman, L. Dynamic Effects on the Powder Line Shapes of Half-Integer Quadrupolar Nuclei: A Solid-State NMR Study of $XO_4^-$ Groups. *J. Phys. Chem. A*, **2002**, *106*, 51-62.

[133] Bowers, G. M.; Kirkpatrick, R. J. High-Field [75]As NMR Study of Arsenic Oxysalts. *J. Magn. Reson.* **2007**, *188*, 311-321.

[134] Lehmann-Horn, J. A.; Miljak, D. G.; Bastow, T. J. [75]As, [63]Cu NMR and NQR Characterization of Selected Arsenic Minerals. *Solid State Nucl. Magn. Reson.* **2013**, *54*, 8-12.

[135] Cannon, J. R.; Edmonds, J. S.; Francesconi, K. A.; Raston, C. L.; Saunders, J. B.; Skelton, B. W.; White, A. H. Isolation, Crystal Structure and Synthesis of Arsenobetaine, a Constituent of the Western Rock Lobster, the Dusky Shark, and Some Samples of Human Urine. *Aust. J. Chem.* **1981**, *34*, 787-798.

[136] Lawrence, J. F.; Michalik, P.; Tam, G.; Conacher, H. B. S. Identification of Arsenobetaine and Arsenocholine in Canadian Fish and Shellfish by High-Performance Liquid Chromatography with Atomic Absorption Detection and Confirmation by Fast Atom Bombardment Mass Spectrometry. *J. Agric. Food. Chem.* **1986**, *34*, 315-319.

[137] *Encyclopedia of Inorganic Chemistry*, 2nd Edition; King, B. R., Ed.; Wiley: Chichester, 2005; Volume 1.

[138] Chernov'yants, M. S.; Burykin, I. V.; Aleshina, N. V. Crystal and Molecular Structure of Tetraphenylarsonium Diiodobromide. *Russ. J. Gen. Chem.* **2008**, *78*, 1345-1349.

[139] Wells, A. F. *Structural Inorganic Chemistry*, 5th Edition; Oxford: New York, 1984.

[140] Cotton, F. A.; Wilkinson, G. *Advanced Inorganic Chemistry*, 5th Edition; Wiley: New York, 1988.

[141] Vega, A. J. Quadrupolar Nuclei in Solids. In *NMR of Quadrupolar Nuclei in Solid Materials*; Wasylishen, R. E., Ashbrook, S. E., Wimperis, S., Eds.; Wiley: Chichester, West Sussex, 2012; pp 17-44.

[142] Siegel, R.; Nakashima, T. T.; Wasylishen, R. E. Signal-to-Noise Enhancement of NMR Spectra of Solids Using Multiple-Pulse Spin-Echo Experiments. *Concepts Magn. Reson. A.* **2005**, *26*, 62-77.

[143] Frisch, M. J.; Trucks, G. W.; Schlegel, H. B.; Scuseria, G. E.; Robb, M. A.; Cheeseman, J. R.; Scalmani, G.; Barone, V.; Mennucci, B.; Petersson, G. A., et al. Gaussian 09, Revision C.01; Gaussian, Inc.: Wallingford CT, 2009.

[144] Ferguson, G.; Glidewell, C.; Lloyd, D.; Metcalfe, S. Effect of the Counter-Ion on the Structures of Tetraphenylantimony(v)-Stibonium Compounds: Crystal and Molecular Structures of Tetraphenylantimony(v) Bromide, Perchlorate, and Tetraphenylborate. *J. Chem. Soc. Perkin Trans. II.* **1988**, *5*, 731-735.

[145] Knop, O.; Vincent, B. R.; Cameron, T. S. Pentacoordination and Ionic Character: Crystal Structure of Ph$_4$SbBr. *Can. J. Chem.* **1989**, *67*, 63-70.

[146] Bryce, D. L.; Wasylishen, R. E. Quadrupolar Nuclei in Solids: Influence of Different Interactions on Spectra. In *NMR of Quadrupolar Nuclei in Solid Materials*, Wasylishen, R. E., Ashbrook, S. E., Wimperis, S., Eds.; Wiley: Chichester, 2012; pp 63-74.

[147] Alcock, N. W.; Pennington, M.; Willey, G. R. Structure of Tetraphenylphosphonium Bromide. *Acta Crystallogr. C.* **1985**, *41*, 1549-1550.

[148] Schweizer, E. E.; Baldacchini, C. J.; Rheingold, A. L. Tetraphenylphosphonium Chloride Monohydrate, Tetraphenylphosphonium Bromide and Tetraphenylphosphonium Iodide. *Acta Crystallogr. C*, **1989**, *45*, 1236-1239.

[149] Dean, P .A. W.; Craig, D. C.; Scudder, M. L.; Dance, I. G. Tetraphenylarsonium Iodide, A New Determination. *Acta Crystallogr.* C, **2003**, *59*, m484-m486.

[150] Van der Kelen, G. P.; de Ketelaere, R. F. Organo Group VB Chemistry. Part IV: On the NQR Spectra of Tertiary Aryl Group VB Compounds ($^{35}$Cl, $^{75}$As, $^{121}$Sb, $^{209}$Bi). *J. Mol. Struct.* **1974**, *23*, 329-335.

[151] Bryukhova, E. V.; Ginzburg, A. G.; Khotsyanova, T. L.; Saatsazov, V. V.; Semin, G. K. Nuclear Quadrupole Resonance Spectra on $^{55}$Mn, $^{75}$As, $^{121}$Sb, $^{123}$Sb Atoms of C$_5$H$_5$Mn(CO)$_2$ – Ligand Complexes. *Izvestiya Akademii Nauk SSSR, Seriya Khimicheskay*, **1973**, *3*, 681-683.

[152] Asai, T. Refinement of Crystal-Structure of Sodium Hexahydroxoantimonate(v), $NaSb(OH)_6$. *Bull. Chem. Soc. Jpn.* **1975**, *48*, 2677-2679.

[153] Conrad, E.; Pickup, J.; Burford, N.; McDonald, R.; Ferguson, M. J. Prototypical Arsine-Triel Adducts ($R_3AsEX_3$ for E = B, Al, and Ga). *Can. J. Chem*. **2010**, *88*, 797-803.

[154] Wi, S.; Frydman, V.; Frydman, L. Residual Dipolar Couplings Between Quadrupolar Nuclei in Solid State Nuclear Magnetic Resonance at Arbitrary Fields. *J. Chem. Phys*. **2001**, *114*, 8511-8519.

[155] Jones, A. C.; O'Brien, P. *CVD of Compound Semiconductors: Precursor Synthesis, Development and Applications*; VCH: Weinheim, 1997.

[156] Maury, F. Organometallic Molecular Precursors for Low-Temperature MOCVD of III-V Semiconductors. *Adv. Mater*. **1991**, *3*, 542-548.

[157] Wi, S.; Frydman, L. Residual Dipolar Couplings Between Quadrupolar Nuclei in High Resolution Solid State NMR: Description and Observations in the High-Field Limit. *J. Chem. Phys*. **2000**, *112*, 3248-3261.

[158] Wu, G.; Yamada, K. Residual Dipolar Couplings in MAS and MQMAS NMR Spectra of Quadrupolar Nuclei. *Chem. Phys. Lett*. **1999**, *313*, 519-524.

[159] Facey, G.; Gusev, D.; Morris, R. H.; Macholl, S.; Buntkowsky, G. $^2H$ MAS NMR of Strongly Dipolar Coupled Deuterium Pairs in Transition Metal Dihydrides: Extracting Dipolar Coupling and Quadrupolar Tensor Orientations from the Lineshape of Spinning Sidebands. *Phys. Chem. Chem. Phys*. **2000**, *2*, 935-941.

[160] Harris, R. K.; Olivieri, A. C. Quadrupolar Effects Transferred to Spin-1/2 Magic-Angle Spinning Spectra of Solids. *Prog. Nucl. Magn. Reson. Spectrosc*. **1992**, *24*, 435-456.

[161] Wasylishen, R. E. Dipolar and Indirect Coupling: Basics. In *NMR Crystallography*; Harris, R. K., Wasylishen, R. E., Duer, M. J., Eds.; Wiley: Chichester, 2009; pp 127-136.

[162] Alarcón, S. H.; Olivieri, A. C.; Harris, R. K. Quadrupole Effects of Spin-3/2 Nuclei on the Solid-State Magic-Angle Spinning Nuclear Magnetic Resonance Spectra of Spin-1/2 Nuclei. Deviations from First-Order Theory and Implications Concerning the Sign of the Indirect Coupling Constant. *Solid State Nucl. Magn. Reson*. **1993**, *2*, 325-334.

[163] Eichele, K.; Wasylishen, R. E.; Grossert, J. S.; Olivieri, A. C. The Influence of Chlorine-Carbon Dipolar and Indirect Spin-Spin Interactions on High-Resolution Carbon-13 Spectra of Chloroketosulfones in the Solid State. *J. Phys. Chem*. **1995**, *99*, 10110-10113.

[164] Perras, F. A.; Bryce, D. L. Residual Dipolar Coupling Between Quadrupolar Nuclei Under Magic-Angle Spinning and Double-Rotation Conditions. *J. Magn. Reson*. **2011**, *213*, 82-89.

[165] Gusev, A. A.; Reznik, I. M.; Tsitrin, V. A. Electron-Electron Interaction and Antishielding Constants of Core Shells of Atoms. *J. Phys.: Condens. Mat*. **1995**, *7*, 4855-4863.

[166] Lide, D. R., Jr. Microwave Spectrum of Trimethyarsine. *Spectrochim. Acta*, **1959**, *15*, 473-476.

[167] Townes, C. H.; Dailey, B. P. Determination of Electronic Structure of Molecules from Nuclear Quadrupole Effects. *J. Chem. Phys*. **1949**, *17*, 782-795.

[168] Brill, T. B.; Long, G. G. Studies of Pentavalent Organoarsenic, -antimony, and -bismuth Halide Compounds by Nuclear Quadrupole Resonance Spectroscopy. *Inorg. Chem*. **1970**, *9*, 1980-1985.

[169] Ege, O.; Hamai, S.; Negita, H. Zeeman NQR Studies on Polycrystals of Copper Compounds, Arsenic Compounds, and Chlorine Compounds. *Z. Naturforsch*. **1992**, *47a*, 401-408.

[170] Zakirov, D. U.; Savdur, V. I.; Gamayurova, V. S.; Chernokal'skii, B. D.; Safin, I. A. $^{75}$As NQR Spectra of Some Tetracoordinated Arsenic Acids. *B. Acad. Sci. USSR Ch+*. **1977**, *26*, 834-836.

[171] Goswami, M.; Knijn, P. J.; Bauhuis, G. J.; Janssen, J. W. G.; van Bentum, P. J. M.; de Wijs, G. A.; Kentgens, A. P. M. Stripline $^{75}$As NMR Study of Epitaxial III-V Semiconductor Al$_{0.5}$Ga$_{0.5}$As. *J. Phys. Chem. C*, **2014**, *118*, 13394-13405.

[172] Knijn, P. J.; van Bentum, P. J. M.; van Eck, E. R. H.; Fang, C.; Grimminck, D. L. A. G.; de Groot, R. A.; Havenith, R. W. A.; Marsman, M.; Meerts, W. L.; de Wijs, G. A., et al. A Solid-State NMR and DFT Study of Compositional Modulations in Al$_x$Ga$_{1-x}$As. *Phys. Chem. Chem. Phys*. **2010**, *12*, 11517-11535.

[173] Cossairt, B. M.; Cummins, C. C.; Head, A. R.; Lichtenberger, D. L.; Berger, R. J. F.; Hayes, S. A.; Mitzel, N. W.; Wu, G. On the Molecular and Electronic Structures of AsP$_3$ and P$_4$. *J. Am. Chem. Soc*. **2010**, *132*, 8459-8465.

[174] Egorov, A.; Mukhamedshin, I. R.; Suzuki, H. NMR Powder Spectra in Case of Strong Quadrupole Interaction. *Physica B*. **2003**, *329-333*, 1397-1398.

[175] Hari, P.; Guzel, S.; Su, T.; Taylor, P. C.; Kuhns, P. L.; Moulton, W. G.; Sullivan, N. S. Photodarkening Effect in Glassy As$_2$S$_3$ and As$_2$O$_3$. *J. Non-Cryst. Solids*, **2003**, *326-327*, 199-204.

[176] Blinc, R.; Apih, T. NMR in Multidimensionally Modulated Incommensurate and CDW Systems. *Prog. Nucl. Magn. Reson. Spectrosc*. **2002**, *41*, 49-82.

[177] Bastow, T. J. Arsenic-75 NMR: Knight Shifts in Arsenic Metal. *J. Phys.: Condens. Matter*, **1999**, *11*, 569-574.

[178] Taylor, P. C.; Hari, P.; Kleinhammes, A.; Kuhns, P. L.; Moulton, W. G. Asymmetries in Local Bonding Sites in Amorphous Semiconductors: Very High Field NMR of [75]As. *J. Non-Cryst. Solids*, **1998**, *227-230*, 770-774.

[179] Takeuchi, J.; Nakamura, H.; Yamada, H.; Kita, E.; Tasaki, A.; Erata, T. Quadrupolar Nutation NMR on a Compound Semiconductor Gallium-Arsenide. *Solid State Nucl. Magn. Reson.* **1997**, *8*, 123-128.

[180] Newitt, D. C.; Hahn, E. L. Detection of Two-Quantum Nuclear Coherence by Nuclear-Quadrupole-Induced Electric Polarization. *J. Magn. Reson. A*, **1994**, *106*, 140-143.

[181] Harbison, G. S.; Slokenbergs, A.; Barbara, T. M. Two-Dimensional Zero-Field Nutation Nuclear-Quadrupole Resonance Spectroscopy. *J. Chem. Phys*. **1989**, *90*, 5292-5298.

[182] Bain, A. D. A Simple Proof that Third-Order Quadrupole Perturbations of the NMR Central Transition of Half-Integral Spin Nuclei are Zero. *J. Magn. Reson*. **2006**, *179*, 308-310.

[183] Gan, Z.; Srinivasan, P.; Quine, J. R.; Steuernagel, S.; Knott, B. Third-Order Effect in Solid-State NMR of Quadrupolar Nuclei. *Chem. Phys. Lett*. **2003**, *367*, 163-169.

[184] Wolf, F.; Kline, D.; Story, H. S. [93]Nb and ^{23}Na NMR in Polycrystalline Sodium Niobate. *J. Chem. Phys*. **1970**, *53*, 3538-3543.

[185] Menger, E. M.; Veeman, W. S. Quadrupole Effects in High-Resolution ^{31}P Solid-State NMR Spectra of Triphenylphosphine Copper(I) Complexes. *J. Magn. Reson.* **1982**, *46*, 257-268.

[186] Bain, A. D. Exact Calculation, Using Angular Momentum, of Combined Zeeman and Quadrupolar Interactions in NMR. *Mol. Phys*. **2003**, *101*, 3163-3175.

[187] Widdifield, C. M.; Bryce, D. L. Solid-State [127]I NMR and GIPAW DFT Study of Metal Iodides and their Hydrates: Structure, Symmetry, and Higher-Order Quadrupole-Induced Effects. *J. Phys. Chem*. **2010**, *114*, 10810-10823.

[188] Widdifield, C. M.; Bain, A. D.; Bryce, D. L. Definitive Solid-State [185/187]Re NMR Spectral Evidence for and Analysis of the Origin of High-Order Quadrupole-Induced Effects for *I* = 5/2. *Phys. Chem. Chem. Phys*. **2011**, *13*, 12413-12420.

[189] Hamaed, H.; Laschuk, M. W.; Terskikh, V. V.; Schurko, R. W. Application of Solid-State [209]Bi NMR to the Structural Characterization of Bismuth-Containing Materials. *J. Am. Chem. Soc*. **2009**, *131*, 8271-8279.

[190] Perras, F. A.; Bryce, D. L. Direct Investigation of Covalently Bound Chlorine in Organic Compounds by Solid-State $^{35}$Cl NMR Spectroscopy and Exact Spectral Line-Shape Simulations. *Agnew. Chem.* **2012**, *124*, 4303-4306.

[191] Bryce, D. L. Tensor Interplay. In *Encyclopedia of Nuclear Magnetic Resonance*; Harris, R. K., Wasylishen, R. E., Eds.; Wiley: Chichester, 2012; pp 5039-5049.

[192] Wasylishen, R. E. Dipolar and Indirect Coupling Tensors in Solids. In *Encyclopedia of Nuclear Magnetic Resonance*; Harris, R. K., Wasylishen, R. E., Eds.; Wiley: Chichester, 2012; 1066-1076.

[193] Chen, F.; Ma, G; Bernard, G. M.; Cavell, R. G.; McDonald, R.; Ferguson, M. J.; Wasylishen, R. E. Solid-state $^{115}$In and $^{31}$P NMR Studies of Triarylphosphine Indium Trihalide Adducts. *J. Am. Chem. Soc.* **2010**, *132*, 5479-5493.

[194] Jakobsen, H. J.; Bildsøe, H.; Brorson, M.; Gan, Z.; Hung, I. Direct Observation of $^{17}$O-$^{185/187}$Re $^{1}J$-Coupling in Perrhenates by Solid-State $^{17}$O VT MAS NMR: Temperature and Self-Decoupling Effects. *J. Magn. Reson.* **2013**, *230*, 98-110.

[195] Goetze, R.; Nöth, H. Contributions to the Chemistry of Boron, LXXII. Some Studies on Arsine Boranes. *Z. Naturforsch.* **1975**, *30B*, 343-349.

[196] Chase, P. A.; Parvez, M.; Piers, W. E. Trimethylphosphine-tris(pentafluorophenyl)borane. *Acta Crystallogr. Sect. E: Struct. Rep. Online*, **2006**, *62*, o5181-o5183.

[197] Jacobsen, H.; Berke, H.; Döring, S.; Kehr, G.; Erker, G.; Fröhlich, R.; Meyer, O. Lewis Acid Properties of Tris(pentafluorophenyl)borane. Structure and Bonding in L−B(C$_6$F$_5$)$_3$ Complexes. *Organometallics*. **1999**, *18*, 1724-1735.

[198] Huffman, J. C.; Skupinski, W. A.; Caulton, K. G. Structure of Triphenylphosphine Borane at −165 Degrees C$_{18}$H$_{18}$BP. *Cryst. Struct. Commun.* **1982**, *11*, 1435-1440.

[199] Sobolev, A. N.; Belsky, V. K.; Chernikova, N. Yu.; Akhmadulina, F. Yu. Structure Analysis of Triaryl Derivatives of the Group V Elements. VIII. The Crystal and Molecular Structure of Triphenylarsine, C$_{18}$H$_{15}$As. *J. Organomet. Chem.* **1983**, *244*, 129-136.

[200] Hayashi, S.; Hayamizu, K. Shift References in High-Resolution Solid-State NMR. *Bull. Chem. Soc. Jpn.* **1989**, *62*, 2429-2430.

[201] Brill, T. B.; Long, G. G. Substituent Transmission Effects in Some Substituted Triphenylarsines and -stibines Using Nuclear Quadrupole Resonance Spectroscopy. *Inorg. Chem.* **1972**, *11*, 225-228.

[202] Wiegand, T.; Eckert, H.; Ekkert, O.; Fröhlich, R.; Kehr, G.; Erker, G.; Grimme, S. New Insights Into Frustrated Lewis Pairs: Structural Investigations of Intramolecular Phosphane-

Borane Adducts by Using Modern Solid-State NMR Techniques and DFT Calculations. *J. Am. Chem. Soc*. **2012**, *134*, 4236-4249.

[203] Power, W. P. Phosphorus-31 Solid-State NMR of a Phosphine-Borane Adduct: Phosphorus Chemical Shielding Trends in the Isoelectronic Series $R_3PX$, where $X = BH_3$, $CH_2$, NH, O. *J. Am. Chem. Soc*. **1995**, *117*, 1800-1806.

[204] Antušek, A.; Jaszuński, M.; Olejniczak, M. Ab Initio Study of NMR Shielding Constants and Spin-Rotation Constants in N, P and As Diatomic Molecules. *Comp. Theor. Chem*. **2011**, *970*, 54-60.

[205] Bryce, D. L.; Wasylishen, R. E.; Gee, M. Characterization of Tricoordinate Boron Chemical Shift Tensors: Definitive High-Field Solid-State NMR Evidence for Anisotropic Boron Shielding. *J. Phys. Chem. A*. **2001**, *105*, 3633-3640.

[206] Durig, J. R.; Hudgens, B. A.; Odom, J. D. Microwave, Infrared, Raman, and Nuclear Magnetic Resonance Spectra and Structure of Trimethylarsine-Borane. *Inorg. Chem*. **1974**, *13*, 2306-2312.

[207] Durig, J. R.; Li, Y. S.; Carreira, L. A.; Odom, J. D. Microwave Spectrum, Structure, Dipole Moment, and Barrier to Internal Rotation of Phosphine-Borane. *J. Am. Chem. Soc*. **1973**, *95*, 2491-2496.

[208] Lutz, M.; Spek, A. L.; Azghay, A.; Slootweg, J. C. CCDC 745335: Experimental Crystal Structure Determination, 2009.

[209] Chen, F.; Ma, G.; Bernard, G. M.; Wasylishen, R. E.; Cavell, R. G.; McDonald, R.; Ferguson, M. J. An Investigation of 1:1 Adducts of Gallium Trihalides with Triarylphosphines by Solid-State [69/71]Ga and ^{31}P NMR Spectroscopy. *Chem. Eur. J*. **2013**, *19*, 2826-2838.

[210] Bradley, D. C.; Hawkes, G. E.; Haycock, P. R.; Sales, K. D.; Zheng, D. H. Intermolecular Exchange in a Triarylborane-Phosphine Complex: A Multinuclear Magnetic Resonance Study. *Phil. Trans. R. Soc. Lond. A*, **1994**, *348*, 315-322.

[211] Bradley, D. C.; Harding, I. S.; Keefe, A. D.; Motevalli, M.; Zheng, D. H. Reversible Adduct Formation Between Phosphines and Triarylboron Compounds. *J. Chem. Soc., Dalton Trans.*, **1996**, 3931-3936.

[212] Sivaev, I. B.; Bregadze, V. I. Lewis Acidity of Boron Compounds. *Coordin. Chem. Rev*. **2014**, *270-271*, 75-88.

[213] Odom, J. D.; Moore, T. F. Nuclear Magnetic Resonance Studies of Boron Compounds XVI. Carbon-13 Studies of Organoboranes: Phenylboranes and Boron-Substituted Aromatic Heterocycles. *J. Organomet. Chem*. **1979**, *173*, 15-32.

[214] Paterson, A. S.; Raja, B.; Garvey, G.; Kolhatkar, A.; Hagström, A. E. V.; Kourentzi, K.; Lee, T. R.; Willson, R. C. Persistent Luminescence Strontium Aluminate Nanoparticles as Reporters in Lateral Flow Assays. *Anal. Chem*. **2014**, *86*, 9481-9488.

[215] Reginster, J.-Y.; Brandi, M.-L.; Cannata-Andía, J.; Cooper, C.; Cortet, B.; Feron, J.-M.; Genant, H.; Palacios, S.; Ringe, J. D.; Rizzoli, R. The Position of Strontium Ranelate in Today's Management of Osteoporosis. *Osteoporos. Int*. **2015**, *26*, 1667-1671.

[216] Rabiee, S. M.; Nazparvar, N.; Azizian, M.; Vashaee, D.; Tayebi, L. Effect of Ion Substitution on Properties of Bioactive Glasses: A Review. *Ceram. Int*. **2015**, *41*, 7241-7251.

[217] Maeno, Y.; Rice, T. M.; Sigrist, M. The Intriguing Superconductivity of Strontium Ruthenate. *Phys. Today*. **2001**, *54*, 42-47.

[218] Maeno, Y.; Nohara, M.; Nakamura, F.; Suzuki, T.; Fujita, T. Structural Instabilities and Superconductivity in La-214 Compounds. *J. Supercond*. **1994**, *7*, 39-43.

[219] Umemura, T.; Egawa, K.; Kinouchi, S.; Utsunomiya, S.; Nojiri, M. Synthesis and Superconducting Properties of BSCCO Including Precipitates with High Density. *Phase Transitions*, **1993**, *42*, 47-51.

[220] Gervais, C.; Veautier, D.; Smith, M. E.; Babonneau, F.; Belleville, P.; Sanchez, C. Solid State $^{47,49}$Ti, $^{87}$Sr, and $^{137}$Ba NMR Characterization of Mixed Barium/Strontium Titanate Perovskites. *Solid State Nucl. Magn. Reson*. **2004**, *26*, 147-152.

[221] Chung, H. J.; Kim, J. H.; Woo, S. I. (Pb,Sr)TiO$_3$ thin films for a ULSI DRAM capacitor prepared by liquid source misted chemical deposition. *Chem. Mater*. **2001**, *13*, 1441-1443.

[222] Yang, G.; Feng, J.; Sun. W.; Dai, N.; Hou, M.; Hao, X.; Qiao, J.; Sun, K. The characteristic of strontium-site deficient perovskites Sr$_x$Fe$_{1.5}$Mo$_{0.5}$O$_{6-\delta}$ ($x$ = 1.9-2.0) as intermediate-temperature solid oxide fuel cell cathodes. *J. Power Sources*, **2014**, *268*, 771-777.

[223] Bera, A.; Wu, K.; Sheikh, A.; Alarousu, E.; Mohammed, O. F.; Wu, T. Perovskite oxide SrTiO$_3$ as an efficient electron transporter for hybrid perovskite solar cells. *J. Phys. Chem. C*. **2014**, *118*, 28494-28501.

[224] Bonhomme, C.; Gervais, C.; Folliet, N.; Pourpoint, F.; Diogo, C. C.; Lao, J.; Jallot, E.; Lacroix, J.; Nedelec, J.-M.; Iuga, D., et al. $^{87}$Sr Solid-State NMR as a Structurally Sensitive Tool for the Investigation of Materials: Antiosteoporotic Pharmaceuticals and Bioactive Glasses. *J. Am. Chem. Soc*. **2012**, *134*, 12611-12628.

[225] USGS Minerals Information: Publications and Data Products. http://minerals.usgs.gov/minerals/pubs/ (accessed September 22, 2015).

[226] Heyden, M.; Kopfermann, H.; About the MRI Changes During Radioactive Beta-Decay Process $^{87}$Rb → $^{87}$Sr. *Z. Physik*, **1938**, *108*, 232-243.

[227] Jeffries, C. D.; Sogo, P. B. The Nuclear Magnetic Moment of $^{53}$Cr and $^{87}$Sr. *Phys. Rev.* **1953**, *91*, 1286.

[228] Weber, M. J.; Allen. R. R. Nuclear Magnetic Resonance Study of the Phase Transition in Strontium Titanate. *J. Chem. Phys.* **1963**, *38*, 726.

[229] Banck, J.; Schwenk, A. $^{87}$Strontium NMR Studies. *Z. Physik*, **1973**, *265*, 165-171.

[230] Larsen, F. H.; Skibsted, J.; Jakobsen, H. J.; Nielsen, N. C. Solid-State QCPMG NMR of Low-γ Quadrupolar Metal Nuclei in Natural Abundance. *J. Am. Chem. Soc.* **2000**, *122*, 7080-7086.

[231] Bowers, G. M.; Mueller, K. T. Electric Field Gradient Distributions about Strontium Nuclei in Cubic and Octahedrally Symmetric Crystal Systems. *Phys. Rev. B*, **2005**, *71*, 224112.

[232] Bastow, T. J. Electric Field Gradients at the M-Site in MCO$_3$: M = Mg, Ca, Sr and Ba. *Chem. Phys. Lett.* **2002**, *354*, 156-159.

[233] Bowers, G. M.; Ravella, R.; Komarneni, S.; Mueller, K. T. NMR Study of Strontium Binding by a Micaceous Mineral. *J. Phys. Chem. B*, **2006**, *110*, 7159-7164.

[234] Bowers, G. M.; Lipton, A. S.; Mueller, K. T. High-Field QCPMG NMR of Strontium Nuclei in Natural Minerals. *Solid State Nucl. Magn. Reson.* **2006**, *29*, 95-103.

[235] Blom, C. E.; Hedderich, H. G.; Lovas, F. J.; Suenram, R. D.; Maki, A. G. Infrared and Microwave Spectra of SrO and BaO. *J. Mol. Spectrosc.* **1992**, *152*, 109-118.

[236] Etchison, K. C.; Dewberry, C. T.; Cooke, S. A. Born-Oppenheimer Breakdown Effects and Hyperfine Structure in the Rotational Spectrum of Strontium Monosulfide, SrS. *Chem. Phys.* **2007**, *342*, 71-77.

[237] Kye, Y.-S.; Zhao, X.; Harbison, G. S. Orientation of Single Crystals Using Linear Approximations to NMR Transits. *J. Magn. Reson.* **2005**, *174*, 54-59.

[238] Antušek, A.; Rodziewicz, P.; Kędziera, D.; Kaczmarek-Kędziera, A.; Jaszuński, M. Ab Initio Study of NMR Shielding of Alkali Earth Metal Ions in Water Complexes and Magnetic Moments of Alkali Earth Metal Nuclei. *Chem. Phys. Lett.* **2013**, *588*, 57-62.

[239] Briggman, B.; Oskarsson, Å. The Crystal Structures of Calcium Malonate Dihydrate and Strontium Malonate. *Acta Crystallogr., Sect. B: Struct. Sci.* **1977**, *33*, 1900-1906.

[240] Abrahams, S. C.; Liminga, R.; Marsh, P.; Loiacono, G. M. Strontium Nitrite Monohydrate: A New Pyroelectric Nonlinear Optic Material. *J. Appl. Phys.* **1983**, *54*, 6776-6778.

[241] Fischer, K. Neues Verfahren zur maßanalytischen Bestimmung des Wassergehaltes von Flüssigkeiten und festen Körpern. *Angew. Chem*. **1935**, *48*, 394-396.

[242] R. W. G. Wyckoff, *Crystal Structures*, 2nd ed.; Interscience: New York, 1963; Vol. 1, pp 239-244.

[243] Liu, G.; Eick, H. A. The Structure of a Metastable Form of SrI$_2$ by the X-Ray Rietveld Procedure. *J. Less-Common Met*. **1989**, *156*, 237-245.

[244] Gürmen, E.; Daniels, E.; King, J. S. Crystal Structure Refinement of SrMoO$_4$, SrWO$_4$, CaMoO$_4$, and BaWO$_4$ by Neutron Diffraction. *J. Chem. Phys*. **1971**, *55*, 1093-1097.

[245] Schulze, A. R.; Müller Buschbaum, Hk. Zur Verbindungsbildung von MeO: M$_2$O$_3$. IV. Zur Struktur von Monoklinem SrAl$_2$O$_4$. *Z. Anorg. Allg. Chem*. **1981**, *475*, 205-210.

[246] Nowotny, H.; Heger, G. Structure Refinement of Strontium Nitrate, Sr(NO$_3$)$_2$, and Barium Nitrate, Ba(NO$_3$)$_2$. *Acta Crystallogr., Sect. C: Cryst. Struct. Commun*. **1983**, *39*, 952-956.

[247] Lundgren, J.-O.; Kvick, Å.; Liminga, R.; Abrahams, S. C. Neutron Diffraction Structural Study of Pyroelectric Sr(NO$_2$)$_2$·H$_2$O at 294, 100, and 20 K. *J. Chem. Phys*. **1985**, *83*, 2426-2432.

[248] Effenberger, H.; Pertlik, F. Four Monazite Type Structures: Comparison of SrCrO$_4$, SrSeO$_4$, PbCrO$_4$ (Crocoite), and PbSeO$_4$. *Z. Kristallogr*. **1986**, *176*, 75-83.

[249] Agron, P. A.; Busing, W. R. Calcium and Strontium Dichloride Hexahydrates by Neutron Diffraction. *Acta Crystallogr., Sect. C: Cryst. Struct. Commun*. **1986**, *42*, 141-143.

[250] Jacobsen, S. D.; Smyth, J. R.; Swope, R. J.; Downs, R. T. Rigid-Body Character of the SO$_4$ Groups in Celestine, Anglesite, and Barite. *Can. Mineral*. **1998**, *36*, 1053-1060.

[251] Abrahams, I.; Vordemvenne, E. Strontium Dibromide Hexahydrate. *Acta Crystallogr., Sect. C: Cryst. Struct. Commun*. **1995**, *51*, 183-185.

[252] Price, D. J.; Powell, A. K.; Wood, P. T. Hydrothermal Crystallisation and X-Ray Structure of Anhydrous Strontium Oxalate. *Polyhedron*, **1999**, *18*, 2499-2503.

[253] Mitchell, R. H.; Chakhmouradian, A. R.; Woodward, P. M. Crystal Chemistry of Perovskite-Type Compounds in the Tausonite-Loparite Series, (Sr$_{1-2x}$Na$_x$La$_x$)TiO$_3$. *Phys. Chem. Miner*. **2000**, *27*, 583-589.

[254] Ahtee, A.; Ahtee, M.; Glazer, A. M.; Hewat, A. W. The Structure of Orthorhombic SrZrO$_3$ by Neutron Powder Diffraction. *Acta Crystallogr., Sect. B: Struct. Sci*. **1976**, *32*, 3243-3246.

[255] Rutt, O. J.; Williams, G. R.; Clarke, S. J. Reversible Lithium Insertion and Copper Extrusion in Layered Oxysulfides. *Chem. Commun*. **2006**, 2869-2871.

[256] Aleksovska, S.; Dimitrovska, S.; Kuzmanovski, I. Crystal Structure Prediction in Orthorhombic $ABO_3$ Perovskites by Multiple Linear Regression and Artificial Neural Networks. *Acta Chim. Slov*. **2007**, *54*, 574-582.

[257] Antao, S. M.; Hassan, I. The Orthorhombic Structure of $CaCO_3$, $SrCO_3$, $PbCO_3$ and $BaCO_3$: Linear Structural Trends. *Can. Mineral*. **2009**, *47*, 1245-1255.

[258] Verbraeken, M. C.; Suard, E.; Irvine, J. T. S. Structural and Electrical Properties of Calcium and Strontium Hydrides. *J. Mater. Chem*. **2009**, *19*, 2766-2770.

[259] Christensen, A. N.; Hazell, R. G. Thermal Analysis and Crystal Structure of Tetragonal Strontium Oxalate Dihydrate and of Triclinic Strontium Oxalate Hydrate. *Acta. Chem. Scand*. **1998**, *52*, 508-512.

[260] Ferrari, A.; Braibanti, A.; Bigliardi, G.; Lanfredi, A. M. M. The Crystal Structure of Strontium Permanganate Trihydrate. *Acta Crystallogr*. **1966**, *21*, 681-685.

[261] Hull, S.; Norberg, S. T.; Ahmed, I.; Eriksson, S. G.; Mohn, C. E. High Temperature Crystal Structures and Superionic Properties of $SrCl_2$, $SrBr_2$, $BaCl_2$, and $BaBr_2$. *J. Solid State Chem*. **2011**, *184*, 2925-2935.

[262] Hennings, E.; Schmidt, H.; Voigt, W. Crystal Structures of $Sr(ClO_4)_2 \cdot 3H_2O$, $Sr(ClO_4)_2 \cdot 4H_2O$ and $Sr(ClO_4)_2 \cdot 9H_2O$. *Acta Crystallogr., Sect. E: Struct. Rep. Online*, **2014**, *70*, 510-514.

[263] Bonhomme, C.; Gervais, C.; Babonneau, F.; Coelho, C.; Pourpoint, F.; Azaïs, T.; Ashbrook, S. E.; Griffin, J. M.; Yates, J. R.; Mauri, F., et al. First-Principles Calculation of NMR Parameters Using the Gauge Including Projector Augmented Wave Method: A Chemist's Point of View. *Chem. Rev*. **2012**, *112*, 5733-5779.

[264] Charpentier, T. The PAW/GIPAW Approach for Computing NMR Parameters: A New Dimension Added to NMR Study of Solids. *Solid State Nucl. Magn. Reson*. **2011**, *40*, 1-20.

[265] Haeberlen, U. High Resolution NMR in Solids: Selective Averaging; Academic Press: London, 1976; p 18.

[266] Kroeker, S.; Eichele, K.; Wasylishen, R. E.; Britten, J. F. Cesium-133 NMR Study of $CsCd(SCN)_3$: Relative Orientation of the Chemical Shift and Electric Field Gradient Tensors. *J. Phys. Chem. B*, **1997**, *101*, 3727-3733.

[267] Clavier, N.; Podor, R.; Dacheux, N. Crystal Chemistry of the Monazite Structure. *J. Eur. Ceram. Soc*. **2011**, *31*, 941-976.

[268] Stahl, K.; Frankaer, C. G.; Raffalt, A. C.; Sørensen, S. R.; Andersen, J. E. T. Polymeric Strontium Ranelate Nonahydrate. *Acta Crystallogr., Sect. E: Struct. Rep. Online*, **2011**, *67*, m471-m472.

[269] Horvath, S.; Demuynck, I.; Damien, G. Alpha Crystalline Form of Strontium Ranelate. US 7,459,568 B2, December 2, 2008.

[270] Jameson, C. J.; De Dios, A. C. Theoretical and physical aspects of nuclear shielding. In *Nuclear Magnetic Resonance*; Kamieńska-Trela, K., Wójcik, J., Eds.; RSC Publishing: Cambridge, 2015; Volume 44.

[271] Varga, Z.; Lanza, G.; Minichino, C.; Hargittai, M. Quasilinear Molecule par Excellence, $SrCl_2$: Structure from High-Temperature Gas-Phase Electron Diffraction and Quantum-Chemical Calculations – Computed Structures of $SrCl_2$·Argon Complexes. *Chem. Eur. J.* **2006**, *12*, 8345-8357.

[272] Laurencin, D.; Smith, M. E. Development of $^{43}Ca$ Solid State NMR Spectroscopy as a Probe of Local Structure in Inorganic and Molecular Materials. *Prog. Nucl. Magn. Reson. Spectrosc*. **2013**, *68*, 1-40.

[273] Pallister, P. J.; Moudrakovski, I. L.; Ripmeester, J. A. Mg-25 Ultra-High Field Solid State NMR Spectroscopy and First Principles Calculations of Magnesium Compounds. *Phys. Chem. Chem. Phys*. **2009**, *11*, 11487-11500.

[274] Gemmi, M.; La Placa, M. G. I.; Galanis, A. S.; Rauch, E. F.; Nicolopoulos, S. Fast Electron Difftraction Tomography. *J. Appl. Crystallogr*. **2015**, *48*, 718-727.

[275] Macavei, J.; Schulz, H. The Crystal Structure of Wolframite Type Tungstates at High Pressure. *Z. Kristallogr*. **1993**, *207*, 193-208.

[276] Abrahams, S. C.; Marsh, P.; Liminga, R.; Lundgren, J.-O. Pyroelectric $Sr(NO_2)_2 \cdot H_2O$: Room Temperature Crystal Structure. *J. Chem. Phys*. **1983**, *79*, 6237-6241.

[277] Müller, U. *Inorganic Structural Chemistry*, 2nd Edition; Wiley: Chichester, 2007; pp 3−7.

[278] Moudrakovski, I. L. Recent Advances in Solid-State NMR of Alkaline Earth Elements. In *Annual Reports on NMR Spectroscopy*; Webb, G. A., Ed.; Academic Press: Oxford, 2013; Volume 79, pp 129-240.

[279] Jameson, C. J. The Chemical Shift. In *Multinuclear NMR*; Mason, J., Ed.; Plenum Press: New York, 1987; pp 61-62.

[280] Bryce, D. L.; Wasylishen, R. E. Beryllium-9 NMR Study of Solid Bis(2,4-pentanedionato-O,O')beryllium and Theoretical Studies of $^9Be$ Electric Field Gradient and Chemical Shielding

Tensors. First Evidence for Anisotropic Beryllium Shielding. *J. Phys. Chem. A*, **1999**, *103*, 7364-7372.

[281] Widdifield, C. M.; Moudrakovski, I.; Bryce, D. L. Calcium-43 Chemical Shift and Electric Field Gradient Tensor Interplay: A Sensitive Probe of Structure, Polymorphism, and Hydration. *Phys. Chem. Chem. Phys*. **2014**, *16*, 13340-13359.

[282] Burgess, K. M. N.; Perras, F. A.; Moudrakovski, I. L.; Xu, Y.; Bryce, D. L. High Sensitivity and Resolution in ⁴³Ca Solid-State NMR Experiments. *Can. J. Chem*. **2015**, *93*, 799-807.

[283] Hung, I.; Schurko, R. W. Solid-State ²⁵Mg QCPMG NMR of Bis(cyclopentadienyl)magnesium. *Solid State Nucl. Magn. Reson*. **2003**, *24*, 78-93.

[284] MacKenzie, K. J. D.; Smith, M. E. *Multinuclear Solid-State NMR of Inorganic Materials*; Pergamon: Oxford, 2002.

[285] Hamaed, H.; Ye, E.; Udachin, K.; Schurko, R. W. Solid-State ¹³⁷Ba NMR Spectroscopy: An Experimental and Theoretical Investigation of ¹³⁷Ba Electric Field Gradient Tensors and their Relation to Structure and Symmetry. *J. Phys. Chem. B*, **2010**, *114*, 6014-6022.

[286] O'Dell, L. A.; Moudrakovski, I. L. A Combined Ultra-Wideline Solid-State NMR and DFT Study of ¹³⁷Ba Electric Field Gradient Tensors in Barium Compounds. *Chem. Phys. Lett*. **2013**, *565*, 56-60.

[287] MacKenzie, K. J. D.; Meinhold, R. H. Prospects for ¹³⁷Ba MAS NMR Spectroscopy of Ceramics and Related Inorganic Materials. *Ceram. Int*. **2000**, *26*, 87-92.

[288] Dec, S. F.; Davis, M. F.; Maciel, G. E.; Bronnimann, C. E.; Fitzgerald, J. J.; Han, S.-S. Solid-State Multinuclear NMR Studies of Ferroelectric, Piezoelectric, and Related Materials. *Inorg. Chem*. **1993**, *32*, 955-959.

[289] Malkin, E.; Komorovsky, S.; Repisky, M.; Demissie, T. B.; Ruud, K. The Absolute Shielding Constants of Heavy Nuclei: Resolving the Enigma of the ¹¹⁹Sn Absolute Shielding. *J. Phys. Chem. Lett*. **2013**, *4*, 459-463.

[290] Xiao, Y.; Zhang, Y.; Liu, W. New Experimental NMR Shielding Scales Mapped Relativistically from NSR: Theory and Application. *J. Chem. Theory Comput*. **2014**, *10*, 600-608.

[291] Bonhomme, C.; Gervais, C.; Smith, M.; Laurencin, D. Solid State NMR Studies of Alkaline Earth Metal Ions. Presented at the 9th Alpine Conference on Solid-State NMR, Chamonix-Mont Blanc, France, Sept 13-17, 2015; T 27.

[292] Autschbach, J.; Zheng, S.; Schurko, R. W. Analysis of Electric Field Gradient Tensors at Quadrupolar Nuclei in Common Structural Motifs. *Concepts Magn. Reson., Part A*, **2010**, *36*, 84-126.

[293] Sele, V.; Sloth, J. J.; Holmelid, B.; Valdersnes, S.; Skov, K.; Amlund, H. Arsenic-Containing Fatty Acids and Hydrocarbons in Marine Oils – Determination Using Reversed-Phase HPLC–ICP-MS and HPLC–qTOF-MS. *Talanta*, **2014**, *121*, 89-96.

[294] Erickson, B. E. Reducing Arsenic Exposure. *Chem. Eng. News*, **2015**, *93*, 27-28.

[295] Lougheed, T. Arsenic – A Foe with Many Faces. *Can. Chem. News*, **2015**, *67*, 30-33.

[296] Gundert-Remy, U.; Damm, G.; Foth, H.; Freyberger, A.; Gebel, T.; Golka, K.; Röhl, C.; Schupp, T.; Wollin, K.-M.; Hengstler, J. G. High Exposure to Inorganic Arsenic by Food: The Need for Risk Reduction. *Arch. Toxicol.* **2015**, *89*, 2219-2227.

[297] Meyer, S.; Raber, G.; Ebert, F.; Taleshi, M. S.; Francesconi, K. A.; Schwerdtle, T. Arsenic-Containing Hydrocarbons and Arsenic-Containing Fatty Acids: Transfer Across and Presystemic Metabolism in the Caco-2 Intestinal Barrier Model. *Mol. Nutr. Food Res*. **2015**, *59*, 2044-2056.

[298] Park, B.-K.; Kim, D.-W.; Song, R.-H.; Lee, S.-B.; Lim, T.-H.; Park, S.-J.; Park, C.-O.; Lee, J.-W. Design of a Dual-Layer Ceramic Interconnect based on Perovskite Oxides for Segmented-in-Series Solid Oxide Fuel Cells. *J. Power Sources*, **2015**, *300*, 318-324.

[299] Burye, T. E.; Nicholas, J. D. Nano-Ceria Pre-Infiltration Improves $La_{0.6}Sr_{0.4}Co_{0.8}Fe_{0.2}O_{3-x}$ Infiltrated Solid Oxide Fuel Cell Cathode Performance. *J. Power Sources*, **2015**, *300*, 402-412.

[300] Jacobsson, T. J. Pazoki, M.; Hagfeldt, A.; Edvinsson, T. Goldschmidt's Rules and Strontium Replacement in Lead Halogen Perovskite Solar Cells: Theory and Preliminary Experiments on $CH_3NH_3SrI_3$. *J. Phys. Chem. C*, **2015**, *119*, 25673-25683.

[301] Harris, K. J.; Lupulescu, A.; Lucier, B. E. G.; Frydman, L.; Schurko, R. W. Broadband Adiabatic Inversion Pulses for Cross Polarization in Wideline Solid-State NMR Spectroscopy. *J. Magn. Reson.* **2012**, *224*, 38-47.

[302] Harris, K. J.; Veinberg, S. L.; Mireault, C. R.; Lupulescu, A.; Frydman, L.; Schurko, R. W. Rapid Acquisition of [14]N Solid-State NMR Spectra with Broadband Cross Polarization. *Chem. Eur. J*. **2013**, *19*, 16469-16475.

[303] Lucier, B. E. G.; Johnston, K. E.; Xu, W.; Hanson, J. C.; Senanayake, S. D.; Yao, S.; Bourassa, M. W.; Srebro, M.; Autschbach, J.; Schurko, R. W. Unravelling the Structure of Magnus' Pink Salt. *J. Am. Chem. Soc*. **2014**, *136*, 1333-1351.

[304] Veinberg, S. L.; Friedl, Z. W.; Harris, K. J.; O'Dell, L. A.; Schurko, R. W. Ultra-Wideline $^{14}N$ Solid-State NMR as a Method for Differentiating Polymorphs: Glycine as a Case Study. *CrystEngComm*, **2015**, *17*, 5225-5236.

[305] Overhauser, A. W. Polarization of Nuclei in Metals. *Phys. Rev.* **1953**, *92*, 411-415.

[306] Carver, T. R.; Slichter, C. P. Polarization of Nuclear Spins in Metals. *Phys. Rev.* **1953**, *92*, 212-213.

[307] Maly, T.; Debelouchina, G. T.; Bajaj, V. S.; Hu, K.-N.; Joo, C.-G.; Mak-Jurkauskas, M. L.; Sirigiri, J. R.; van der Wel, P .C. A.; Herzfeld, J.; Temkin, R. J.; Griffin, R. G. Dynamic Nuclear Polarization at High Magnetic Fields. *J. Chem. Phys.* **2008**, *128*, 052211.

[308] Perras, F. A.; Kobayashi, T.; Pruski, M. PRESTO Polarization Transfer to Quadrupolar Nuclei: Implications for Dynamic Nuclear Polarization. *Phys. Chem. Chem. Phys.* **2015**, *17*, 22616-22622.

[309] National High Magnetic Field Laboratory. https://nationalmaglab.org/ (Accessed January 26, 2016).

# Appendix A: Example Input Files for ADF Calculations

## A.1 Electric Field Gradient

```
#! /bin/sh
mkdir AsP_efg
cd AsP_efg

$ADFBIN/adf -n 4 << eor> AsP_efg_out.txt
Atoms
As     0.000000000     0.000000000     0.000000000
P      0.000000000     0.000000000     2.001623730
End

qtens

relativistic spinorbit zora
symmetry NOSYM
xc
 lda vwn
gga becke perdew
end

integration 6

Basis
 Type ZORA/QZ4P
 Core None
End
End input
eor

rm TAPE21 logfile
```

## A.2 Magnetic Shielding

```
#! /bin/sh
mkdir AsP_csa
cd AsP_csa

$ADFBIN/adf -n 4 << eor> AsP_csa_out.txt
Atoms
As    0.000000000    0.000000000    0.000000000
P     2.001623730    0.000000000    0.000000000
End

relativistic spinorbit zora
symmetry NOSYM
xc
 lda vwn
gga becke perdew
end

integration 6

Basis
 Type ZORA/QZ4P
 Core None
End

save TAPE10

End input
eor

$ADFBIN/nmr -n 4 << eor

NMR
 U1K Best
 OUT tens
 NUC 1 2
END
eor

rm TAPE21 logfile TAPE10
```